

ADVERTIMENT. L'accés als continguts d'aquesta tesi queda condicionat a l'acceptació de les condicions d'ús establertes per la següent llicència Creative Commons:  http://cat.creativecommons.org/?page_id=184

ADVERTENCIA. El acceso a los contenidos de esta tesis queda condicionado a la aceptación de las condiciones de uso establecidas por la siguiente licencia Creative Commons:  <http://es.creativecommons.org/blog/licencias/>

WARNING. The access to the contents of this doctoral thesis it is limited to the acceptance of the use conditions set by the following Creative Commons license:  <https://creativecommons.org/licenses/?lang=en>



**Universitat Autònoma
de Barcelona**

**Department of Chemistry
Faculty of Science**

Synthesis and electronic characterization of triphenylene-based materials

Noemí Contreras Pereda

PhD Thesis
PhD in Material Science
2021

Supervisor:

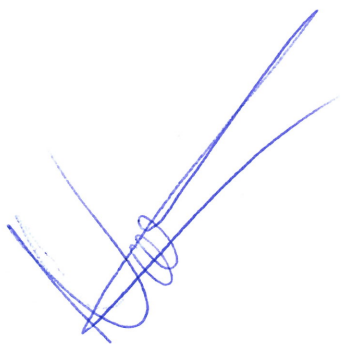
Dr. Daniel Ruiz-Molina

Tutor:

Prof. Jordi Sort Viñas



Memòria presentada per aspirar al Grau de Doctora per Noemí Contreras Pereda



Noemí Contreras Pereda

Vist i plau,



Dr. Daniel Ruiz Molina

Bellaterra, 23 de juny del 2021

Acknowledgements

First, I would like to thank my thesis supervisor, Daniel Ruiz-Molina for offering me the opportunity of performing this PhD. Thank you not only for guiding me during this project but also to involving me in the decisions as in a partnership. I have learnt a lot in the latest years in the many areas concerned in research thanks to your advice.

Further, I would like to thank the financial support to this thesis, mainly the “La Caixa” Foundation for my fellowship for Doctoral Studies. Moreover, I would like to acknowledge the support of the European COST action MP1407, who has financially supported my Short-Term Scientific Mission in the ETH of Zürich for three months. That experience has increased both my knowledge and the quality of this thesis.

To all my colleagues of Nanosfun group, you are the most valuable gaining of this thesis. Specially to Salvi, for all the support, cheering and help I got from you since the day I arrived to the lab. To Miguel Àngel as well, for all the support and scientific discussions in the daily life of the lab. Thanks to all the labmates and group members who have being there bringing joy and fun during this thesis: Eva, José, Junda, Meri (Maria), Pau, Àlex, Ivana, Jaume, Héctor, Claudio, Fernando, Aleix, Ferran, Olga, Paula, Nahia, Meritxell and Mario. Also to all the members of Nanosfun who are not in the group anymore: Bea, Caro, Xiao, Carol, Josep, Faezeh, Alexis, Roger, Guillem, Nuria, Pablo, Payam, Verónica, Àlex Ayala, Gianluca, Christian and Antón. I would like to thank specially Javier Baselga and Belén Pepió as well, who have not only supported me as group members during their stay in the group but also accepted me as their bachelor and master thesis director respectively. Guiding you and see you grow as scientists has been a great pleasure.

I would like to also thank Dr. Josep Sedó for his help and advice on chemistry during this thesis. Thanks as well for all the help and guidance from the members of *Core Research Facilities* and *Electron Microscopy Division*: Dr. Javier Saiz-Poseu, Dr. Jessica Padilla, Marcos Rosado and Francisco Belarre.

I would like to acknowledge the many collaborations as well that have participated in this thesis and enriched it. First of them to Prof. Josep Puigmartí-Luis for allowing me to perform my research stay in the *ETH Zurich* under his supervision. Your help and guidance during the stay and the following months of my thesis have been key for our fruitful collaboration. Thanks to Dr. David Rodriguez San Miguel and Dr. Carlos Franco Pujante from

ETH for all their help and support within the collaboration. I acknowledge Prof. Salvador Pané i Vidal from *ETH* as well for his help in the research stay. Thank you as well to Dr. Eduardo Solano for *ALBA synchrotron* for his guidance in the crystallography synchrotron measurements.

Thanks as well to Dr. Raphael Pfattner from *Institut de Ciències de Materials de Barcelona* for the help in the electrical characterization of thin films developed in this thesis.

I would like to also thank Prof. Aitor Mugarza from *ICN2* and members of this group Dr. Markos Paradinas and Dr. Amina Kimouche for the collaboration in UHV deposition of MOFs. I also acknowledge Dr. Roberto Robles from *Centro de Física de Materiales CFM/MPC (CSIC-UPV/EHU)* for the DFT calculations in magnetic properties of MOF.

Thanks as well to other collaborations that have taken place during my thesis giving rise to many interesting projects: Dr. Faezeh Moghzi from *University of Tehran*, Dr. Samia Benmansour from *Instituto de Ciencia Molecular, Universidad de Valencia* and Dr. Haixia Zhong and Dr. Renhao Dong from *Technische Universität Dresden*.

Further than the boundaries of science, part of my deepest gratitude is towards my friends spread all around the globe: Martí Raya, Jesús, Cristina, Verónica, Sophie, Märta, Ana, Giulia, Adrián, Licia, Laura, Martí Gibert, Jan, María, Jana and Iván. Borders, different time-zones and pandemics have not been rivals for your unequal source of support, cheer and love.

Finally, I am truly indebted towards my family. Papá y Maman mil gracias por todo lo que habéis hecho por mí y seguís haciendo. Os debo todo cuanto soy: me habéis apoyado incondicionalmente en cada etapa de mi vida incluyendo mi aventura en el mundo científico a la par que erais mis modelos. A mis abuelos Pepe y Carmen, por todo su apoyo y su amor constantes. Gracias Abuela por empujarme a coger todas las oportunidades que decías a ti no se te pudieron presentar y gracias Abuelo por hacerme reír cada día y hacerme feliz. Abuelo Domingo y Abueli, no he podido compartir esta etapa con vosotros, pero cuánto sé y aprendí de vosotros me ha acompañado de cerca. A mis tíos/tías y mis primis, por su paciencia conmigo, fuerza incesante y contagio de la alegría por la vida. Primis mayores, habéis sido mis guardianes y primis pequeños me habéis enseñado mucho. Y por último, pero no menos importante, gracias a mi hermana Ana por estar ahí siempre y hacer todo la una por la otra sin reservas. Eres el mejor deseo cumplido que podría haber tenido.

¡Muchas gracias a todos! Merci beaucoup à tous! Thank you all!

Abstract

Triphenylene (TP) based materials have been living a great expansion in the latest years. TP molecules have interesting optoelectronic properties arising from the aromatic core which have been exploited in functional two-dimensional (2D) Metal-Organic Frameworks (MOFs) and Covalent Organic Frameworks (COFs) aside other organic polymers. Morphology, crystallinity and orientation, among others (which are defined by the synthetic methodology) have proven to have great impact on the properties and performance of these materials in functional devices. Thus, development of synthetic approaches that allow for control and fine-tuning of these characteristics is crucial to fully enhance the applications of these materials.

With this aim, in this Thesis different morphologies have been explored: supported MOF monolayer and multilayer crystals and supported and free-standing thin films. The approaches used are totally new and on the frontier of current knowledge, in search of new formats that allow the properties of these materials to be exploited. Additionally, impact of physico-chemical properties as crystal domain and orientation or wettability on the electronic characterization have been established. Furthermore, deep studies on the obtained materials has paved the way to their potential application in some cases showcasing the interdisciplinary character of this thesis.

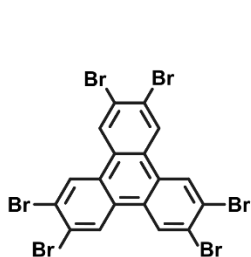
In a first Chapter, the deposition of cobalt-based TP 2D MOFs monolayers and bulk crystals in ultra-high vacuum (UHV) conditions is aimed. For this, work in this chapter includes optimization on the synthetic procedure of starting TP molecule (aiming for high purity for monolayer and bulk synthesis), on the bulk synthesis of the related MOF and its surface deposition using UHV techniques, specifically with the novel atomic layer injection (ALI). In a second Chapter, synthesis of centimeter large, supported MOF thin films on different substrates (insulating, conducting, flexible and hybrid) is introduced using microfluidics as microgravity simulated environment. The slow diffusion of reagents in the gas phase allowed to control the growth of the thin film and its crystalline orientation, having a great impact on the film electrical conductivity and charge carrier transfer. Finally, in the last Chapter, TP-based melanin-inspired free standing thin films were developed. The synergy between the adhesive and conductive properties under humid and sweat-like conditions indicated the good performance of the free-standing film as active material for wearable electronic artificial skin devices.

List of abbreviations

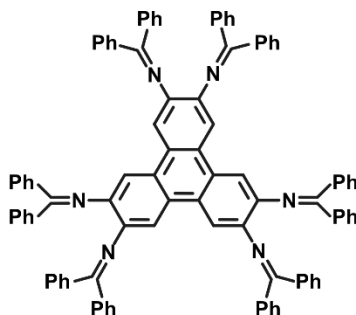
AC	Alternating Current	IMMP	Interfacial Microfluidic
AcO⁻	Acetate Ion CH ₃ COO ⁻		Membrane Processing
AFM	Atomic Force Microscopy	IPA	Isopropanol
ALI	Atomic Layer Injection	I-V	Intensity-Voltage
COF	Covalent Organic Framework	LbL	Layer-by-layer
DC	Direct Current	LSG	Laser Scribed Graphene
DFT	Density Functional Theory	MALDI-MS	Matrix-Assisted Laser Desorption/Ionization Mass Spectroscopy
DF-STEM	Dark-Field Scanning Transmission Electron Microscopy	MAE	Magnetic Anisotropy Energy
DLC	Discotic Liquid Crystal	MeOH	Methanol
DLS	Dynamic Light Scattering	MOF	Metal-Organic Framework
DMSO	Dimethyl sulfoxide	OM	Optical Microscopy
E-skin	Artificial Electronic Skin	ORR	Oxygen Reduction Reaction
E_a	Activation Energy	PBS	Phosphate Buffer Solution
ECG	Electrocardiogram	PDMS	Polydimethylsiloxane
EDX	Energy Dispersive X-ray	PDOS	Projected Density of States
EELS	Electron Energy Loss Spectroscopy	PEEK	Polyether Ether Ketone
E_F	Fermi Energy	PEG	Polyethylene glycol
EtOH	Ethanol	PMMA	Poly(methyl methacrylate)
FFT	Fast-Fourier Transform	PVA	Polyvinyl alcohol
FT-IR	Fourier-Transformed Infrared Spectroscopy	PXRD	Powder X-Ray Diffraction
GDY	Graphdyine	RH	Relative Humidity
GF	Gauge Factor	RMS	Root Mean Squared roughness
GIWAXS	Grazing Incident Wide Angle X-ray Scattering	RT	Room Temperature
GIXRD	Grazing Incident X-Ray Diffraction	SAED	Selected Area Electron Diffraction
H-NMR	Proton Nuclear Magnetic Resonance	SAM	Self-Assembled Monolayer
HER	Hydrogen Evolution Reaction	SEM	Scanning Electron Microscopy
HR-TEM	High resolution Transmission Electron Microscopy	STM	Scanning Tunneling Microscopy

STS	Scanning Tunneling Spectroscopy	UV-vis-NIR	Ultraviolet-visible-Near Infrared spectroscopy
TGA	Thermogravimetric Analysis	vdP	Van der Pauw
TLC	Thin Layer Chromatography	WAXS	Wide Angle X-ray Scattering
TP	Triphenylene	XMCD	X-ray Magnetic Circular Dichroism
UHV	Ultra-High Vacuum	XG	Xanthan Gum
UV-vis	Ultraviolet-visible spectroscopy	XPS	X-Ray Photoelectron Spectroscopy
		XRD	X-Ray Diffraction

List of molecules



1
(2,3,6,7,10,11 hexabromo-triphenylene)



2
(2,3,6,7,10,11 hexabenzophenoneimine-triphenylene)

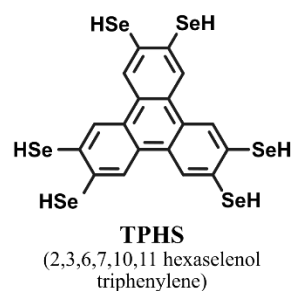
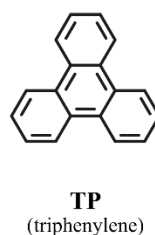
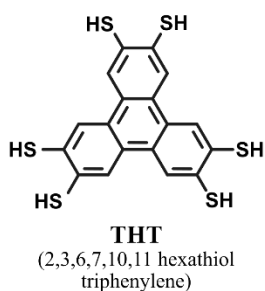
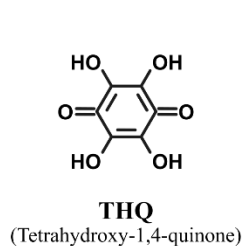
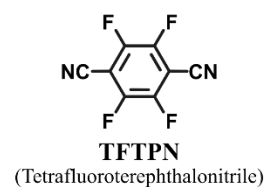
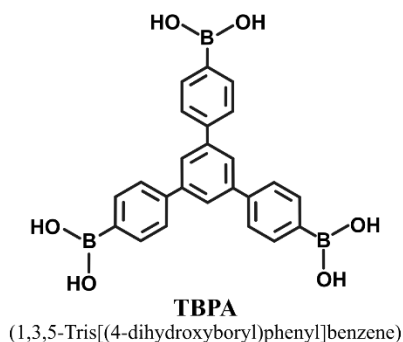
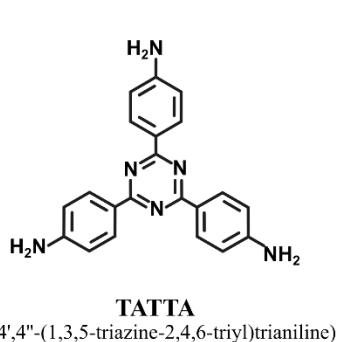
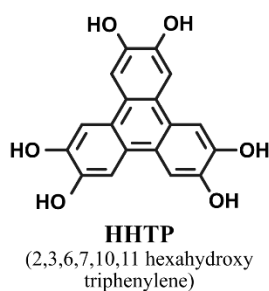
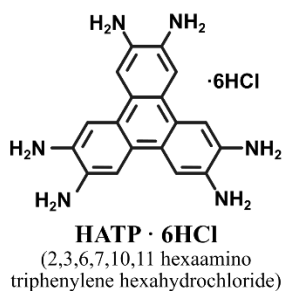
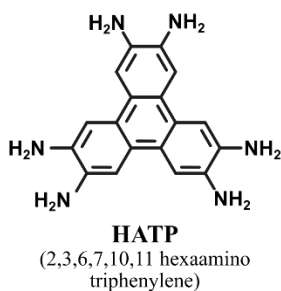
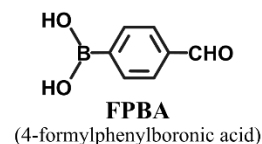
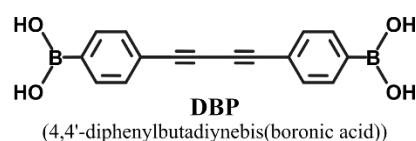
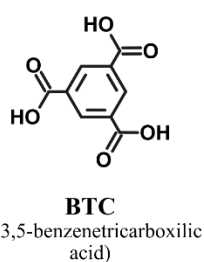
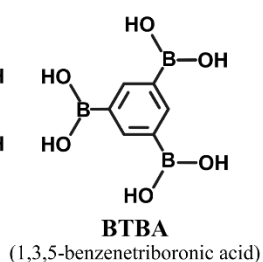
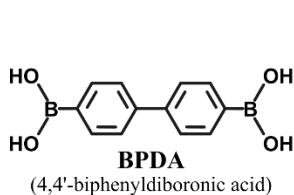
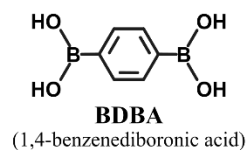


Table of contents

Chapter 1 General Introduction to triphenylene-based polymers	1
1.1 Molecular characteristics and supramolecular properties	2
1.2 Synthetic methodologies	6
1.2.1 Bulk syntheses	6
Solvothermal reactions.....	6
Sonochemical reactions	7
1.2.2 Template-assisted syntheses	8
Layer-by-Layer	9
Vapor assisted conversion.....	10
1.2.3 Interfacial syntheses of thin films	10
1.2.4 Microfluidic devices	12
Capillary force mimicking reactions.....	12
Continuous flow.....	12
1.2.5 On-surface Ultra-High Vacuum evaporation.....	13
1.3 Triphenylene-based 2D MOFs.....	13
1.3.1. Chemical families.....	13
HHTTP triphenylene ligand	14
HATP triphenylene ligand	16
THT triphenylene ligand.....	18
Other structures	20
1.3.2. Applications of triphenylene-based 2D MOFs.....	22
Chemiresistive sensor	23
Batteries/Supercapacitor	25
Electrocatalyst.....	26
Spintronics	27
Optoelectronics	28
Others	28
1.4 Triphenylene-based 2D COFs.....	30
1.4.1. Chemical families.....	30
HHTTP triphenylene ligand	30
HATP triphenylene ligand	33
Others.....	34
1.4.2. Applications of triphenylene-based 2D COFs	34
Photovoltaics and photocurrent.....	35
Li-ion battery	36
Electrocatalysis	37
1.5 Future perspectives	37

1.6 Tables.....	41
Table 1.1 Conductivities of HHTP based MOFs	41
Table 1.2 Conductivities of HATP based MOFs	42
Table 1.3 Conductivities of THT based MOFs.....	42
Table 1.4 Described boronic COFs.....	43
1.7 References.....	49
Chapter 2 Objectives	55
Chapter 3 Monolayers on surfaces	57
3.1 Introduction	58
3.1.1 TP-based monolayers on surfaces: interest and state-of-the-art	58
3.1.2 MOF of choice and experimental approach	61
3.1.3 Scope of this chapter.....	65
3.2 Results and discussion	65
3.2.1. Optimization on the synthesis of HATP·6HCl	65
Reproducibility of the reported protocol	66
Modification of column chromatography	68
Modification of reagents stoichiometry	68
3.2.2. Synthesis of Co ₃ (HITP) ₂	70
3.2.2.1. First attempts to obtain Co ₃ (HITP) ₂	70
3.2.2.2. Synthesis and characterization of Co ₃ (HITP) ₂ particles by acetate addition	74
3.2.3. Controlled deposition on surfaces with ALI	77
Effect of suspension concentration	79
Effect of the pulse time	80
Effect of the number of pulses	81
Temperature effect	82
Effect of distance between sample and injector.....	83
3.2.4. Synthesis of monolayers using UHV	88
3.3 Conclusions.....	92
3.4 Materials and methods	92
3.5 References.....	96
Chapter 4 Synthesis of 2D TP MOF Thin Films under simulated microgravity conditions .	99
4.1 Introduction	100
4.1.1 Conductive triphenylene-based 2D MOFs thin films	100

4.1.2 Microfluidics as simulated microgravity synthetic conditions	100
4.1.3 Our microfluidic approach	104
4.1.4 Scope of this chapter	108
4.2 Results and discussion	108
4.2.1 Aqueous synthesis of $\text{Ni}_3(\text{HITP})_2$ thin films	108
a.- Aqueous synthesis of $\text{Ni}_3(\text{HITP})_2$ thin films with the microfluidic device	108
b.- $\text{Ni}_3(\text{HITP})_2$ crystals synthesized according to the published protocol.....	111
c.- $\text{Ni}_3(\text{HITP})_2$ thin films synthesized by diffusion of ammonia.....	114
4.2.2 Synthesis in DMSO of $\text{Ni}_3(\text{HITP})_2$ thin films with confined spaces	118
a.- $\text{Ni}_3(\text{HITP})_2$ powder bulk synthesis in DMSO.....	118
b.- Control on the synthesis of $\text{Ni}_3(\text{HITP})_2$ thin films in double slide confined spaces	120
c.- Synthesis and characterization of $\text{Ni}_3(\text{HITP})_2@ \text{Glass}$, $\text{Ni}_3(\text{HITP})_2@ \text{Quartz}$ and $\text{Ni}_3(\text{HITP})_2@ \text{Glass-SAM}$ thin films	126
d.- Synthesis and characterization of $\text{Ni}_3(\text{HITP})_2@ \text{Au}$ and $\text{Ni}_3(\text{HITP})_2@ \text{Au-SAM}$ thin films	129
e.- Electronic anisotropy	136
f.- Synthesis and characterization of $\text{Ni}_3(\text{HITP})_2@ \text{PDMS}$	143
g.- Synthesis and characterization of $\text{Ni}_3(\text{HITP})_2@ \text{Graphene}$	145
4.3 Conclusions.....	147
4.4 Materials and methods	148
4.5 References.....	155
Chapter 5 Melanin-inspired HHTP-based thin films for wearable on-skin electronics .	157
5.1 Introduction	158
5.1.1 e-skin: state-of-the-art	158
5.1.2 Thin films	160
5.1.3 Eumelanin-like approach	162
5.1.4 Scope of this chapter	165
5.2 Results and discussion	165
5.2.1 Attempts to obtain HHTP-based thin-films by reaction with different amine .	165
a.- Ammonia	165
b.- Flexible amines.....	169
c.- Rigid amines	169
5.2.2 Film formation optimization	172
5.2.3 Conductive properties of optimized films.....	176
5.2.4 Interaction of the films with skin	179

5.2.5 Use in a wearable e-skin devices.....	184
5.2.5.1 Measurements under pure water: sensitivity to skin-bending	184
5.2.5.2 Measurements sweat-like buffer	185
a.- Sweat and bending sensitivity.....	185
b.- Sensitivity to skin stretching.....	186
c.- Temperature sensing	187
5.3 Conclusions.....	187
5.4 Materials and methods	188
5.5 References.....	191
Chapter 6 General Conclusions.....	193

Chapter 1: General introduction to triphenylene-based polymers

1.1. Molecular characteristics and supramolecular properties

Triphenylene (TP) is a polycyclic aromatic hydrocarbon consisting in three benzene rings fused to a fourth one in an alternate fashion, characterized by a large π -electron cloud (see Figure 1.1a).¹ R_1 and R_2 can be different groups, but the most relevant for this work are those where $R_1=R_2=$ -OH (henceforth HHTP), -NH₂ (henceforth HATP) or -SH (henceforth THT). TPs exhibit a supramolecular packing mainly through π - π stacking with the help of further nonspecific interactions arising upon hexasubstitution of these positions with long alkyl chains, which do not disturb neither planarity nor electronic relocation. The remarkable electronic delocalization of the resulting supramolecular structures has made them suitable for different applications, among them sensors for neutral aromatic or cationic guests,² molecular rotors¹ whose ON to OFF switching can be detected through the emission or in applications where redox reactions are relevant, as for instance in high-stable organic-oxygen cells batteries.³ Nevertheless one of the areas where these materials have shown greater impact is that of discotic liquid crystals (DLCs).

DLCs are mesophase supramolecular materials, as liquid crystals, formed by the columnar stacking of disk-like moieties (see Figure 1.1b).^{4,5} The lack of intrinsic charge carriers leads to the obtaining of broad energetic band gaps so conduction occurs mainly due to hopping of charge carriers rather than a band-like effect, relying on the interplanar distance between TP molecules.⁶ Therefore, DLCs often require of electrochemical or photochemical doping or charge injection from metallic surfaces moieties for enhanced electronic conductivity.⁷ In this case, large electronic delocalization leads to strong charge carrier percolation along the columnar axis constituting hence one-dimensional organic semiconductor.⁵ One example of this is the use of nitrogen-doped planar moieties as electron acceptor to obtain an intercalated donor-acceptor system. The obtained material DLC material proved good capacities and was implemented as working cathode in Li batteries.⁸ Furthermore, DLCs are characterized by their easy processability into thin films⁴ enabling their introduction into electronic devices, making them thus suitable for optoelectronic applications as organic photovoltaics or OLEDs.⁶

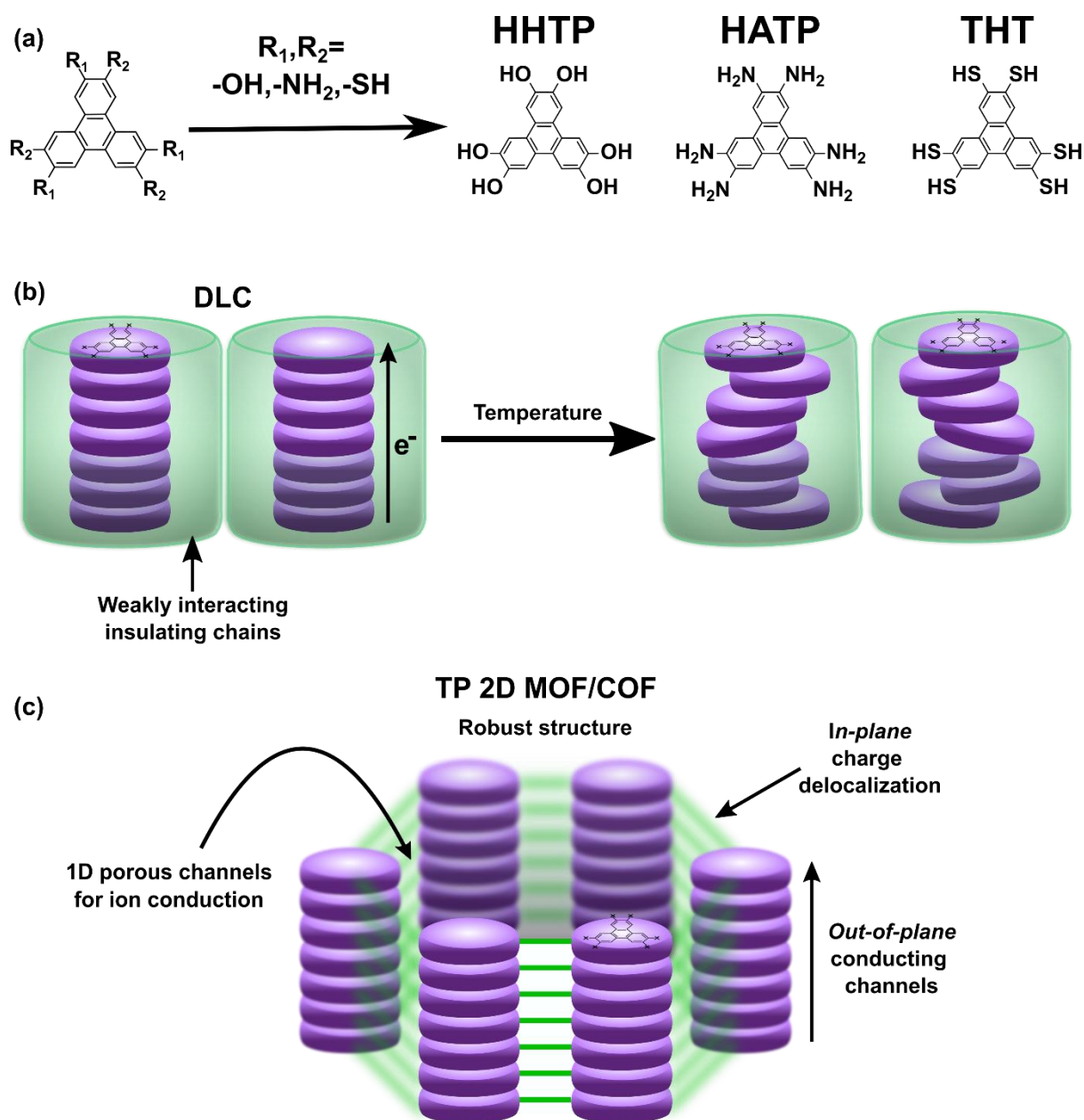


Figure 1.1: (a) Chemical structure of a TP molecule. When having identical hexasubstitutions different ligand arise being HHTP for hexahydroxy triphenylene, HATP for hexaamino triphenylene and THT for triphenylene hexathiol. (b) Schematic of stacking of TP moieties in DLCs forming 1D conducting channels. The supramolecular mesophase structure relies on weak interactions that can be broken upon external stimuli as temperature. (c) Schematic of the stacking of TP moieties in TP 2D MOFs and COFs. The crystalline packing ensures a robust structure formed by several hexagonally distributed 1D conducting channels. Furthermore, large *in-plane* delocalization can be obtained along the 2D layers depending on the coordination or covalent bonds used. Moreover, the structure defines 1D pores suitable for host-guest interactions or ionic conduction.

According to all the preceding evidence, these conductive 1D structures represented a great advance towards the manufacture of new optoelectronic devices though some of its possible applications are still hardly available due to the lack of reproducibility and the required consistency. The reason for this is that charge carrier mobility is strongly dependent

on the crystallinity of the mesophase,^{6,9} which can vary considerably in a DLC modifying the interaction between TP moieties of these 1D semiconductors. Alternatively, DLCs can also be obtained with linear and flexible covalent polymers bearing TP moieties that stack into columnar phases positioning the bended side chains in the outer surface of the column.¹⁰ Though, still control over the crystallinity is strongly dependent on the nature and bendable character of building blocks.¹¹ Therefore, in the recent years TP-based 2D Metal-Organic Frameworks (MOFs) and Covalent-Organic Frameworks (COFs) have been sought to take advantage of controlled crystallinity while aiming for broad electronic bands for enhanced electronic conduction.

COF and MOF are polymeric crystalline porous network materials that can be rationally designed and synthesized involving the bonding between one or different organic building blocks that polymerize through covalent (COFs) or coordination bonds (MOFs).^{12–14} While covalent bonds ensure a larger thermal and pH stability,^{14,15} the incorporation of metallic ions can add novel optical, magnetic and /or specially electrical properties.¹⁶ In any case, both covalent or coordination bonds provide a long range, stable and robust structures that do not depend on external factors such as temperature, as DLCs do (Figure 1.1c). Moreover, the configuration and dimensionality of the polymer can be predicted by the selective use of the metal nodes and the organic linkers, giving rise to a wide variety of 2D structures.¹⁷ These planar polymeric layers can further form a 3D supramolecular structure by interlayer interactions as for instance π - π stacking, Hydrogen bonding or Van der Waals.

The incorporation of TP moieties within MOFs and COFs is schematically represented in Figure 1.2. The 2D layers present honeycomb graphitic structures that result in interesting band structures and properties. Regarding the electronic properties, two main components arise: conduction of charge carriers along the 2D layers (*in-plane*) and interlayer charge transfer (*out-of-plane* conduction).¹⁸ On one hand, coordination bonds of TP MOF typically lead to large electron delocalization and conjugation pathways along the 2D layers, pointing to very high *in-plane* conductivities. Strong delocalizations can be a direct consequence of strong coordination d- π bonds (normally arising by the rational choosing of suitable metallic center and TP substitution).¹⁹ Contrarily, covalent bonds formed in TP COF structures need to maintain the conjugation in order to lead to such conductivities.²⁰ Thus,

very few examples of conductive COFs have been reported and commonly require of either chemical (including donor atoms in their chemical structure) or external doping to aim for electronic applications.¹⁴ On the other hand, *out-of-plane* conductivities are determined by the supramolecular stacking of the 2D layers. In a similar fashion to DLCs, stacking of the TP moieties (obtained through the packing of the layers) can lead to one-dimensional charge transfer channels, where charge transfer occurs in through-space pathways.¹⁸ However, different stacking geometries (being mostly eclipsed, nearly-eclipsed or slipped-parallel) can be found, being always determined by the chemical structure of TP 2D MOF/COF. Hence, the crystalline structure has great impact in the *in-plane* and *out-of-plane* contributions of the optoelectronic properties of TP MOFs/COFs. In the following sections, impact of chemical structures of TP MOFs/COFs in the final *in-plane* and *out-of-plane* charge transfer properties electronic properties will be discussed.

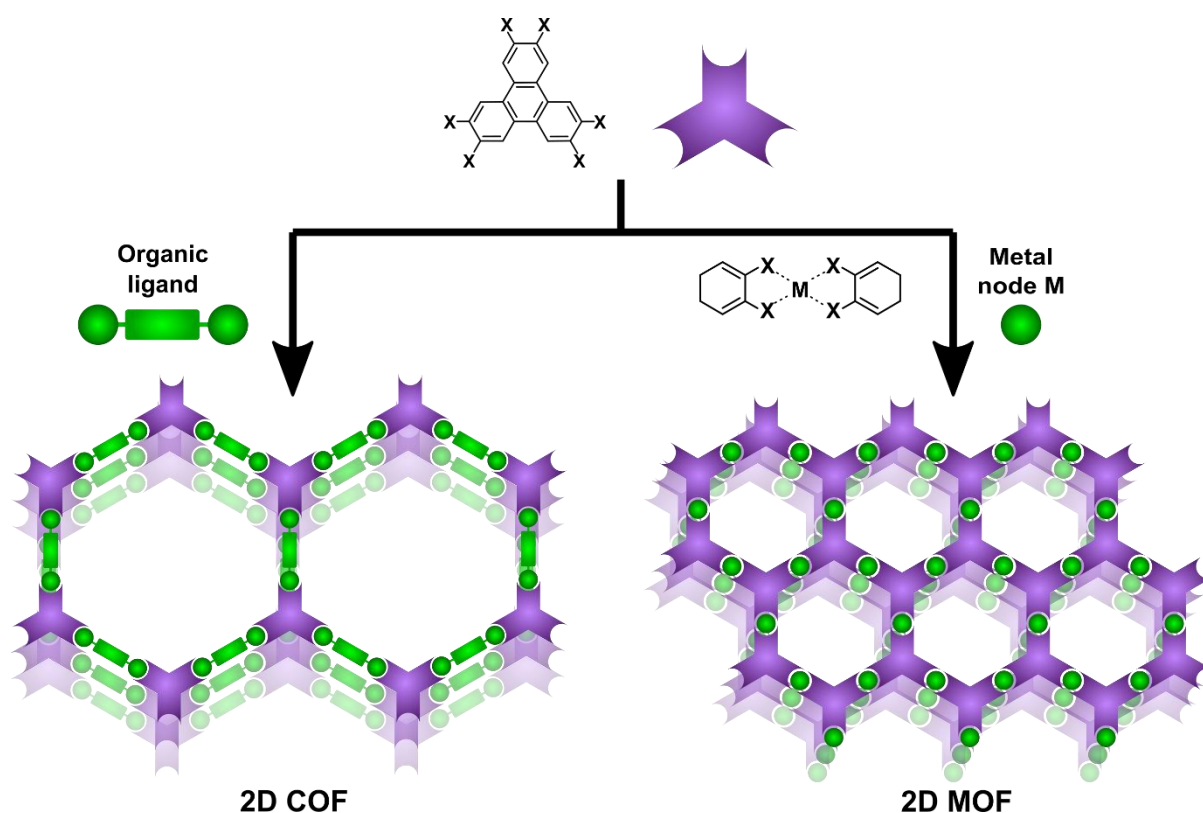


Figure 1.2: Scheme of formation of TP 2D MOFs and TP 2D COFs. TP 2D MOFs are typically formed by coordination of a metallic ion with the electron donor heteroatoms from TP functionalization. On the other hand, TP 2D COFs are formed by covalent bond formation of the TP functionalities with other organic ligands. The three-fold geometry of TP leads to the previously mentioned honeycomb hexagonal structures.

1.2. Synthetic methodologies

Characteristics of the MOFs and COFs such as crystallinity, crystallite size, material processing can have a direct and relevant impact on the conductivity.^{18,21} Therefore, control over these parameters, and therefore the synthetic methodology, have become very relevant. Most representative examples of the different methodologies used are given next.

1.2.1. Bulk syntheses

Solvothermal reactions. The most followed approach for the synthesis of TP 2D MOFs and COFs is the solvothermal synthesis. For this, reactants are dispersed or solubilized in a common solvent and heated up either in a sealed or opened glassware (depending on the need of oxygen in the reaction). A schematic representation of this approach is shown in Figure 1.3a.

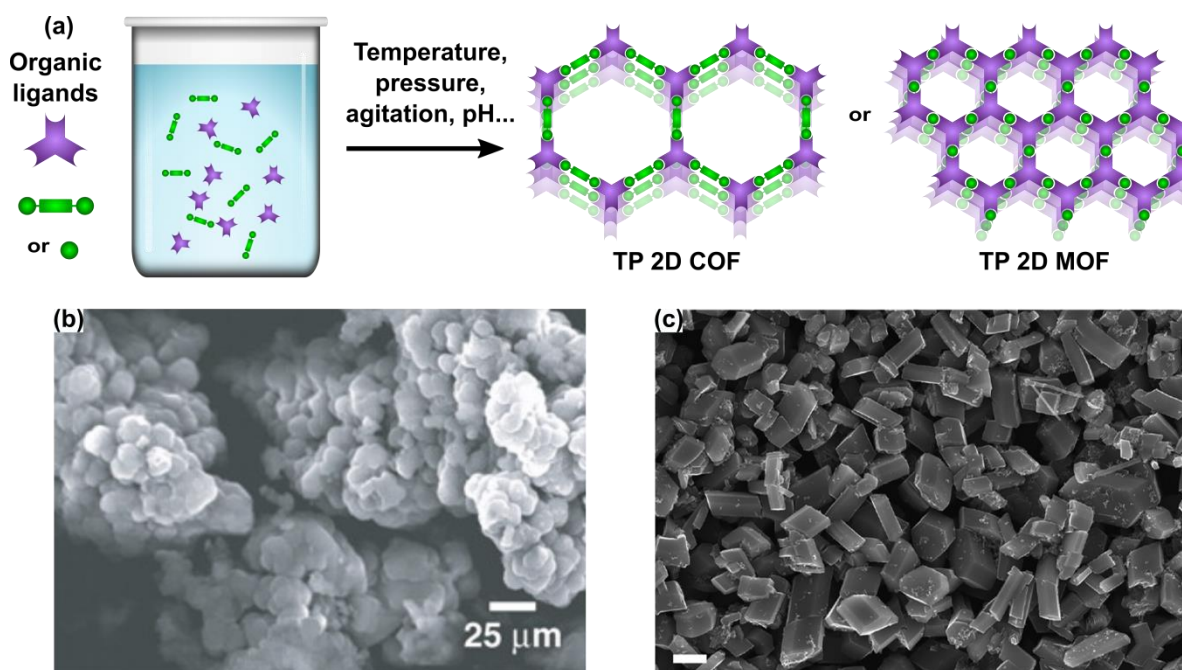


Figure 1.3: (a) Scheme of solvothermal reaction syntheses of TP 2D MOF and COF. (b) Scanning Electron Microscopy (SEM) image of crystals of typical TP 2D COF obtained with solvothermal methods. Image extracted from ref. 25. (c) SEM image of crystals of TP 2D MOF obtained with solvothermal methods. Scale bar represents 1 μm. Image extracted from ref. 24.

TP-based solvothermal reactions of MOFs are characterized by a fast uncontrollable crystallization, leading to several nucleation points. Studies to enhance the crystallinity and particle size were attempted by changing the order of addition or modifying the amount of

additives.^{22,23} In any case, the largest TP 2D MOFs reported with this approach lengths in the order of few micrometers (Figure 1.3c).²⁴ In the case of COFs, long reaction times are required to ensure the crystallization of the covalent polymers, which are obtained anyway mostly in the form of insoluble powders (Figure 1.3b), as first described by Yaghi and co-workers for COF-5 (see structure in the following section).²⁵ Heterogeneous reaction mixtures are obtained characterized by the occlusion of reagents within the precipitated material and low synthetic yields.^{26,27} Thus, studies on homogeneous polymerization have been seek reducing the crystallization to minutes.²⁷ For instance, the formation rate dependence of COF-5 with temperature, concentration and presence of additives allowed the obtaining of micrometer-long polycrystalline aggregates.

Sonochemical reactions. The reaction between monomers assisted by ultrasound in solution is highly modulated by parameters such as used solvent, sonication times or sonication powers, which are used to modulate the crystallinity, dimensions and porosity of the obtained particles (Figure 1.4). Moreover, sonochemical syntheses pointed the way to faster crystallizations lowering the reaction time to minutes or hours.²⁶ Noteworthy, large surface areas significantly higher than the ones reported by the solvothermal methods can be achieved using this approach. Whereas sonochemical syntheses are widely used approach for COF, they are rarely applied in MOF synthesis as small sized crystals are already obtained.

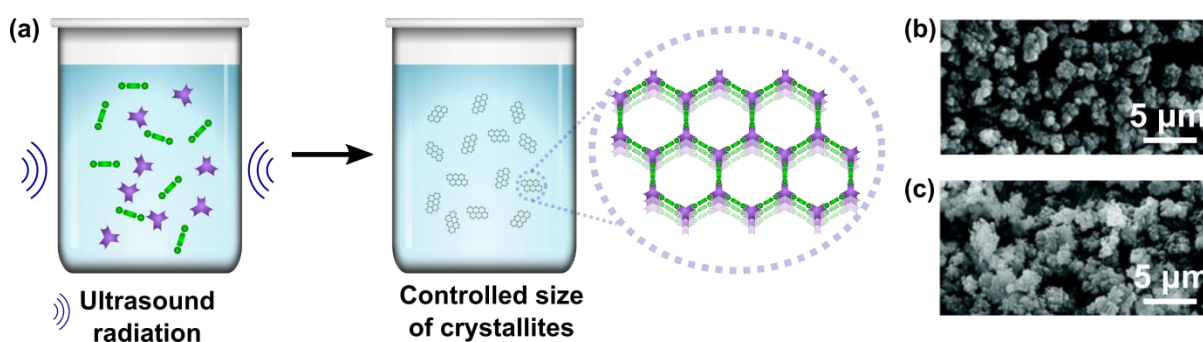


Figure 1.4: Scheme of sonochemical reaction of TP 2D COF. (b) and (c) SEM images of crystals of the same TP 2D COF obtained with sonochemical reactions obtained under different conditions. As observed, small and narrow size distribution of particles is obtained. Images extracted from ref. 26.

1.2.2. Template-assisted syntheses

Top-down techniques have been described in the recent years regarding post-synthetic on-substrate deposition as for example drop-casting of colloidal suspensions of TP 2D MOFs (either as-synthesized²⁸ or after sonication²⁹) and also of TP 2D COFs.³⁰ Other examples are spin-coating,³¹ ball-milling blending and abrasion of powders onto substrates³² or spray-coating of colloidal suspension onto flexible substrates with a high control on the coverage area and patterning.²³ Though, most of the time crystalline powder is not always suitable for device fabrication.³³ So, to facilitate the incorporation of TP MOFs on surfaces, one of the approaches followed is the incorporation of the substrates while the reaction takes place (Figure 1.5a). With this aim, a wide variety of substrates has been described (Figure 1.5c) including flat substrates for thin film formation³⁴ and coating of textiles³⁵, carbon paper³⁶, shrinkable flexible substrates³⁷ or core-shell materials.^{38–40}

Solvothermal or sonochemical reactions were also used to induce the epitaxial on-substrate growth of COFs taking advantage of initial interactions between monomers and the immersed substrate (Figure 1.5b). As an example, Dichtel *et al.* grew COF thin films with nanometered thicknesses on single layer graphene by dipping it into the reaction mixture.⁴¹ The highly dense TP COF films showcased smooth surfaces and long-range order with a *c*-axis preferential orientation independently on the supporting substrate used for the single layer graphene. Variability of the substrate has been also reported for TP 2D COF, covering materials such as carbon nanotubes and free standing graphene.^{42,43} This technique has also been used to growth TP COF on the inner surface of polydopamine coated capillars.⁴⁴ The capillary was filled with the reaction mixture, sealed and subjected to high temperature as in a solvothermal synthesis. Higher quality and scalable thin films can be obtained also by combination of template-assisted method with approaches as colloidal template.⁴⁵ Upon the addition of co-solvents, undesired COF nanoparticles obtained in solution remain a stable colloidal suspension. Thus, irregular deposition of COF is disabled and only heterogeneous nucleation and growth on the substrate occurs.

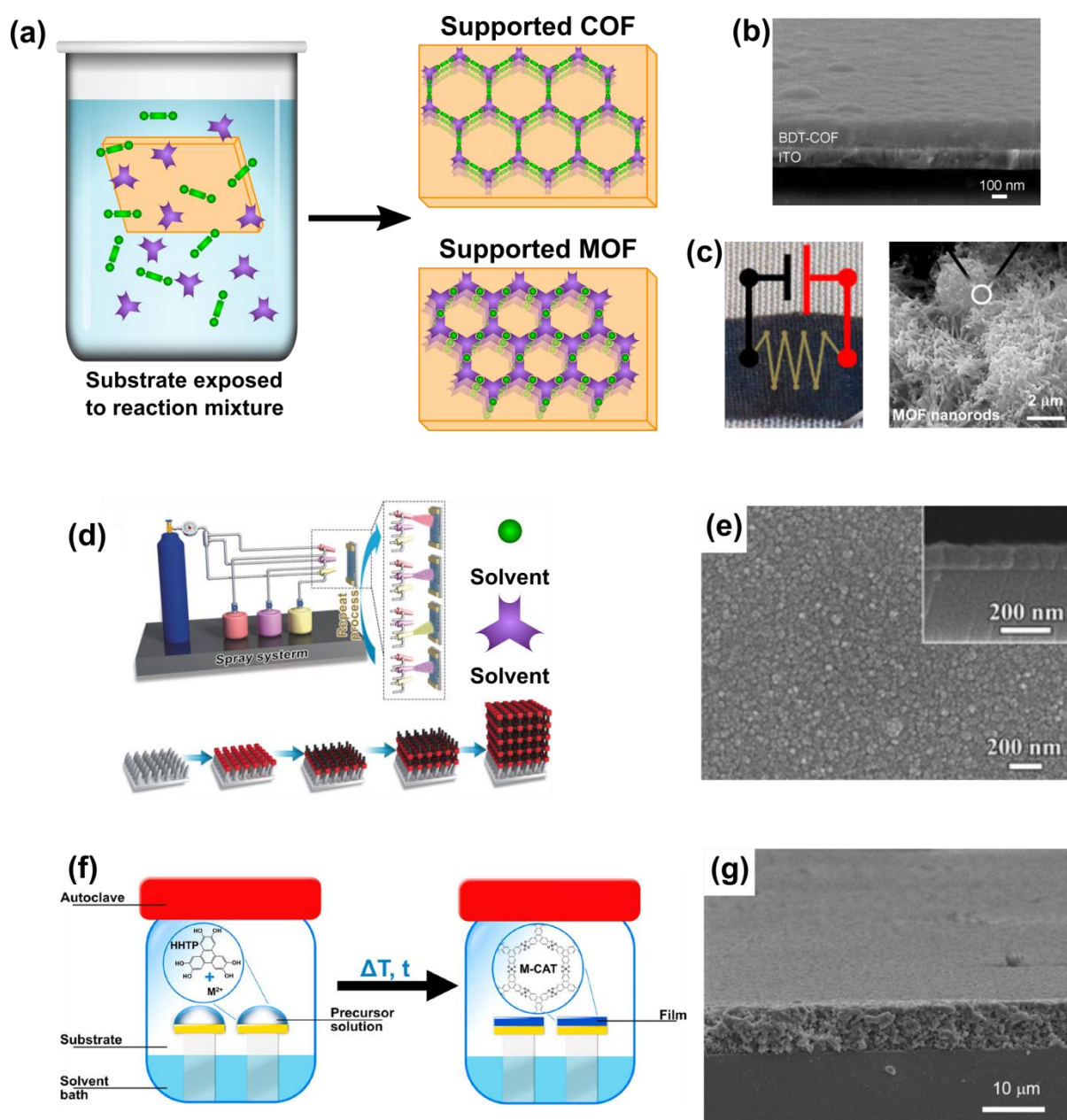


Figure 1.5: (a) Schematic of template-assisted synthesis upon the immersion of a substrate in a solvothermal reaction mixture. (b) Cross-section SEM image of a TP COF thin film grown on top of a rigid metallic substrate through template-assisted method. Image extracted from ref. 46. (c) Picture and SEM image of a TP MOF grown on flexible textile through template-assisted method, proving the wide range of available substrates. Images extracted from ref. 35. (d) and (e) Schematic of a layer-by-layer growth of TP MOF using spray-drying of the TP and metallic moieties and SEM image of the obtained TP MOF, respectively. Images adapted from ref. 47. (f) Schematic of the vapor assisted conversion method. Image extracted from ref. 48. (g) SEM image of a TP COF grown with vapor assisted conversion. Image extracted from ref. 49.

Layer-by-Layer (LbL). This approach has been explored principally for TP 2D MOFs. Typically, substrates are functionalized with active sites to entrap the metal ion on the surface (Figure 1.5d). Afterwards, the metal-loaded substrate is exposed to TP substituted moiety

saturating all the available metallic centers through coordination bonds and leaving coordination sites available. Further, the substrate is exposed again to a metallic solution. This procedure is repeated in a cyclic fashion inducing a homogeneous and layered growth of thin films of large lateral sizes. This approach is characterized by the large control of thickness which is directly related to the number of cycles performed. Also, the obtained thin films grow epitaxially having highly oriented crystallites (Figure 1.5e). Remarkably, the deposition can be performed with different methods as for instance substrate immersion in solutions⁵⁰ or by spraying the solutions onto the substrate.⁴⁷ The main drawback of this technique is the long reaction time.

Vapor-assisted conversion. This methodology has been recently reported for TP 2D MOFs,⁴⁸ and relies on the reaction between starting monomers on a wet surface at the solvent gas pressure conditions (Figure 1.5f). This leads to a saturated reaction environment nearby the substrate's surface. This method allowed to growth highly oriented centimeter-long thin films on different substrates both insulating and conducting. However, optimization from substrate to substrate was required. For some samples, some acidic modulators were needed in the synthesis in order to obtain homogeneous and large covering of the substrate. In the case of COFs, Vapor-assisted conversion was introduced by Bein and co-workers as a scalable approach to obtain TP 2D COFs in 2015. Notoriously, the approach allows to form COF thin films at room temperature with a high control on their thicknesses ranging from hundred nanometers to micrometer scale (Figure 1.5g).⁴⁹

1.2.3. Interfacial syntheses of thin films

In the case of liquid-liquid interfaces, the metallic salt and the organic ligand are dissolved in different immiscible solvents so the reaction takes place at the interface upon slow diffusion of the reactants (Figure 1.6a and 1.6c).^{51,52} Following this approach, thin films with sub-millimeter lateral sizes can be obtained though reaching nanometer thicknesses still remains a challenge due to the lack of homogeneity along the film.⁵¹ On the other side, one of the most representative approaches used at liquid-gas interface is the Langmuir-Blodgett technique, resulting in the growth of sub-millimeter films with nanometer scale thicknesses, with main achievements being the growth of a 2D monolayer⁵³ or even high preferential orientation (Figure 1.6d).⁵¹ Remarkably, growth and stamping can be repeated leading to a controlled increase of the thickness.⁵¹ Another approach is the use of reagents in the gas state

as for instance ammonia vapors⁵⁴ or atmospheric oxygen.⁵⁵ The thin film formed at the interface grows upon diffusion of the gas reagent into the liquid phase. Hence, control on the thickness is achieved upon the control of the reaction time. Notoriously, in some cases lateral dimensions of hundreds of microns are obtained leading to lower conductivities than the previously reported in compressed pellets.⁵⁴ Moreover, polycrystalline random orientations were obtained. Interfacial syntheses have been largely exploited for TP MOFs whereas regarding TP COF structures, Glass-coupling reactions are the main example of interfacial synthesis, where the starting monomer is in one phase and the copper catalyzer in another (Figure 1.6b).⁵⁶

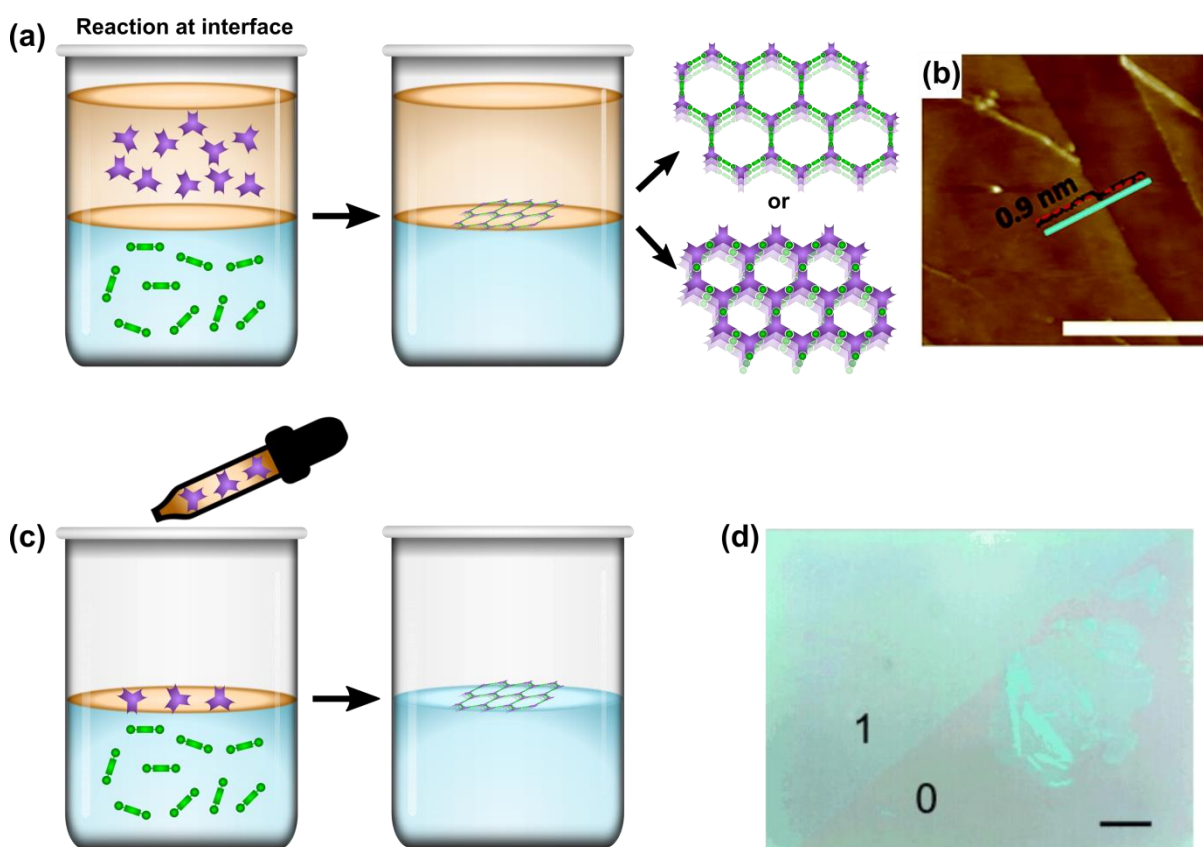


Figure 1.6: (a) Schematic of liquid-liquid interfacial synthesis. The starting monomers are in different liquid phases and the reaction between them occurs at the interface. Growth and reaction are mediated by the migration of the monomers towards the interface. (b) Atomic Force Microscopy (AFM) image of a TP COF obtained in a liquid-liquid interface. Image extracted from ref. 56. (c) Schematic of liquid-gas interfacial synthesis. One monomer meets the reaction mixture at the liquid-air interface, it can be added in a gas form. (d) Optical microscopy (OM) image of a TP MOF thin film grown through liquid-air interface. Image extracted from ref. 53.

1.2.4. Microfluidic devices

Capillary force mimicking reactions. To avoid turbulent flows or fast precipitation, which usually lead to polycrystalline materials, a novel approach mimicking capillary forces has been reported.^{57,58} Reaction occurs between two substrates pressed one against the other, where the organic ligand and the metallic ion were previously incorporated (TP needs to be deposited through Ultra-High Vacuum (UHV) thermal evaporation for a planar deposition on the surface).⁵⁷ The confinement between substrates enhances the MOF growth along the *c*-axis with hexagonal plate-like and lateral sizes of 1-10 μm (in sharp contrast to the needle-like crystals typically obtained in *in situ* reactions) (Figure 1.7a and 1.7b). Alternatively, the pressed substrates can be previously functionalized with hydroxyl groups by piranha or Ultraviolet (UV)-ozone treatment and subjected to a layer-by-layer growth.⁵⁸ Centimeter-scaled thin films with very controlled thicknesses were obtained on top of commercial silicon wafers with a preferential orientation.

Continuous flow. Less explored methods to obtain 2D TP COFs have been occasionally reported. This is the case of growing 2D TP COF thin films under continuous flow conditions.⁵⁹ In a work reported by Ditchel and co-workers, monomers solutions are pumped and passed over a substrate under heating conditions. The continuous flow prevents the irregular deposition on substrate of COF colloids grown in the solution. The technique is characterized by a constant rate growth, allowing a high control on the thickness of the thin film. Crystallinity studies on the thin film proved that growth relies not only on the flow of monomeric species over the substrate but also pre-polymerized oligomers.

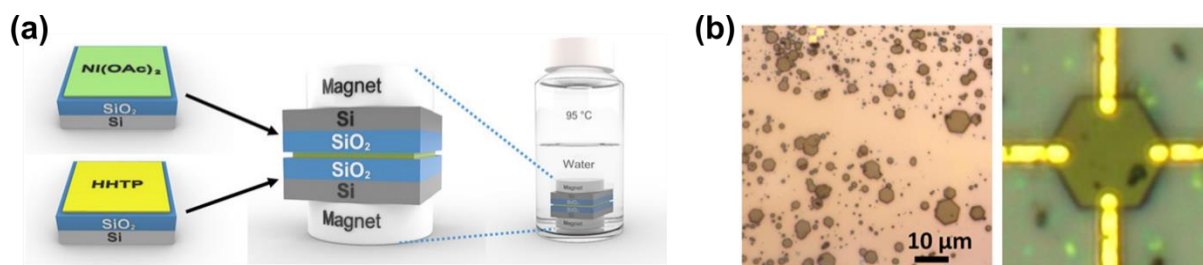


Figure 1.7: (a) Schematic of a capillary force mimicking reaction. The two substrates containing a starting monomer each are pressed together and exposed to the solvent. The space between substrates was filled by capillary force. (b) Optical microscope images of the TP MOF crystals obtained with capillary force mimicking systems. Images extracted from ref. 57.

1.2.5. On-surface UHV evaporation

UHV evaporation and deposition has opened the way to large and relevant information on the synthesis of supported 2D TP MOF/COF single-layers. A more detailed description on the state-of-the-art of UHV techniques can be found on the Introduction (Section 3.1) of Chapter 3.

1.3. Triphenylene-based 2D MOFs

Below we will review the different examples of TP-based MOFs described to date paying special attention to the synthetic methods used, chemical families and conductive properties.

1.3.1. Chemical families

TP ligands coordinate with either square planar or orthogonal (with unavailable axial positions to keep the planar coordination along the 2D layers) metal ions, most often Ni^{2+} , Co^{2+} or Cu^{2+} (see Figure 1.8).⁶⁰ The resulting honeycomb graphitic structures (having hexagonal porous of 2 nm) with large electron delocalization point to very high *in-plane* conductivities along the 2D coordinated layer.¹⁹ In this sense, the radius of the donor atom in the TP moiety and the electronic configuration of the metallic ion have great impact on the π -d orbital hybridization of the material, determining bond distance and strength of the MX_4 moieties.¹⁹ So, the electronic conductivity can be tailored by using different combination of TP substitutions and metallic centers.²¹ These features are key factors to ensure the *in-plane* charge conduction. For instance, MO_4 based TP MOFs typically showcase lower charge transport than homologous MN_4 TP MOFs. Moreover, the Kagomé lattice arrangement of the metallic centers may originate band structures with the presence of Dirac points, where ultrafast charge carrier mobilities and non-trivial physical properties as topological states can arise.^{19,61} On top of that, TP can be oxidized during the MOF formation reaching up to a total charge of -3, some of the intermediate species being stable radicals.⁶¹ Concerning the *out-of-plane* contribution to conductivity, different stacking of the layers and crystalline arrangements can modify the MOF bulk physical properties and electron conduction arising from the differences in the overlap of TP moieties within the structure. Further, extended 1D pore channels arise in the case of eclipsed or nearly-eclipsed stacking of the layers that can be used to modify the properties.⁶⁰ Next, a summary of TP 2D MOFs and the corresponding conductivity properties grouped according to the donor heteroatom is given.

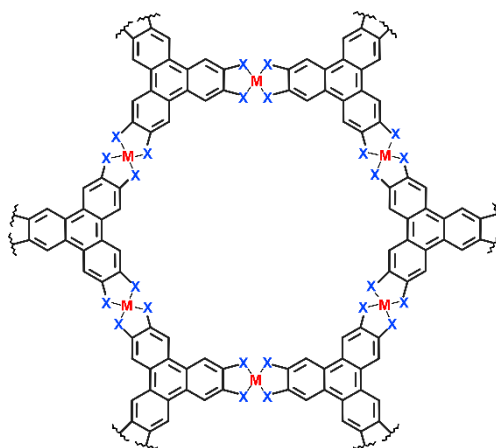


Figure 1.8: Structure of TP 2D MOFs layers. The planar coordination centers MX_4 defines the honeycomb graphitic structure.

HHTP triphenylene ligand

In 2012, Yaghi and co-workers reported the first TP 2D MOFs using HHTP and Ni^{2+} , Co^{2+} and Cu^{2+} metal ions.⁶² X-Ray Diffraction (XRD) of the Co-based MOF revealed extended layered honeycomb networks combining cobalt ions and HHTP molecules (Figure 1.9a and 1.9b). The metallic center showcased octahedral geometries with two terminal water ligands in the axial positions and the HHTP molecules in equatorial positions. These 2D coordination layers pile up by π - π stacking of the triphenylene units in an alternated ABAB stacking pattern, leading to a 3D supramolecular structure. Additionally, the coordination layers are intercalated with layers of molecules with formula $[(\text{H}_2\text{O})_4\text{Co}]_3\text{HHTP}$. Hence the final formula of the Co-based MOF resulted in $\text{Co}_9(\text{HHTP})_4$ excluding the coordinated water molecules. Hexagonal rod-like Ni-based crystals resulted isostructural according to powder XRD and High-Resolution Transmission Electron Microscopy (HR-TEM) images (Figure 1.9c). Conductivity measurements of $\text{M}_9(\text{HHTP})_4$ ($\text{M}=\text{Co}$ and Ni) pressed pellets showed low conductivities on the order of $10^{-3} \text{ S cm}^{-1}$ as the discrete molecular coordination units disrupt the staggering of TP units, decreasing the charge interlayer delocalization.⁶² Very recently, in a significant work Dincă and co-workers grew single crystals of $\text{Ni}_9(\text{HHTP})_4$ large enough to provide the *in-plane* (0.4 S cm^{-1}) and *out-of-plane* conductivities ($10^{-4} \text{ S cm}^{-1}$) (Figure 1.9d).⁵⁷ The remarkable difference up to three orders of magnitude highlights the relevant charge transport mediated by the conjugated 2D layers. On the other hand, interlayer charge transport hardly contributes to the conductivity due to the large distance and disrupted stacking of the layers and hence of the TP moieties.

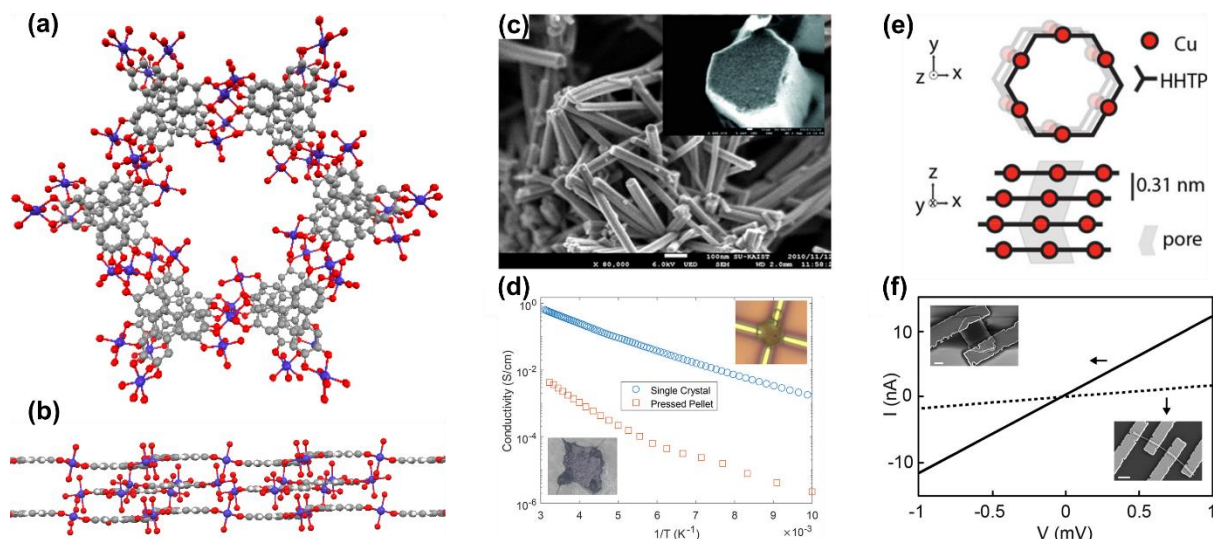


Figure 1.9: (a) and (b) Top and side view respectively of the 2D layers in the $\text{Co}_9(\text{HHTP})_4$ structure. The discrete molecular units can be easily appreciated between layers in (b) showing their disruption of the TP stacking. (c) SEM images of rod-like $\text{Ni}_9(\text{HHTP})_4$ crystals. Image extracted from ref. 62. (d) Temperature dependence of electrical conductivity of a single crystal and of a pressed pellet. Defects arising from polycrystalline pressed pellet led to lower conductivities and different temperature dependance with comparison to single crystal devices. Insets: optical microscope images of single-crystal and pressed-pellet devices. Image extracted from ref. 57. (e) Schematic of the structure of $\text{Cu}_3(\text{HHTP})_2$ crystals. The structure is characterized by a continuous shifting of the layers. (f) Intensity-Voltage (I-V) curves of plate-like and rod-like $\text{Cu}_3(\text{HHTP})_2$ crystals respectively taken at room temperature. Each shape allowed to assess the *in-plane* and *out-of-plane* contributions to electrical conductivity. Images extracted from ref. 24.

Interestingly, the powder XRD pattern of the Cu-based MOF indicated the presence of a different crystalline phase, as confirmed later on by Dincă and co-workers using powder XRD and HR-TEM. In this case, the layers are stacked in an almost eclipsed fashion (Figure 1.9e), with a slight continuous shift along the c direction, without any occlusion of molecular coordination units, and an expected formula of $\text{Cu}_3(\text{HHTP})_2$.²⁴ Single crystal conductivity by Yaghi et al showed a values as high as 0.1 S cm^{-1} ,⁶² as confirmed later on by Dincă and co-workers on plate-like crystals with the 2D layers oriented along the crystal plane synthesized using sonication assisted synthesis (Figure 1.9f).²⁴ *In-plane* and *out-of-plane* conductivities of the 2D layers were 0.5 S cm^{-1} and 1.5 S cm^{-1} , respectively, confirming equal contribution of intralayer and interlayer charge transport (arising from the large planar conjugation and eclipsed stacking of the TP molecules respectively). As expected, polycrystalline systems of $\text{Cu}_3(\text{HHTP})_2$ TP MOF have provided conductivities in the range of 10^{-1} to $10^{-3} \text{ S cm}^{-1}$ depending on the synthetic method proving the impact of morphology on the charge transport properties (see Table 1.1 for more information). Relevance of the stacking interaction between TP in the conductivity properties were assessed as well studying a series of

lanthanide $\text{Ln}_{x+1}(\text{HHTP})$ MOFs.⁶³ In the described structures, Ln centers ($\text{Ln} = \text{La}^{3+}, \text{Nd}^{3+}, \text{Ho}^{3+}, \text{Yb}^{3+}$) coordinate to HHTP molecules forming a 3D coordination network, where HHTP molecules are located along 2D planes and Ln centers in between layers. Stacking between HHTP moieties remain close to graphitic π - π interactions having interlayer distances of ~ 3 Å. Notoriously, larger interlayer distances were obtained with larger lanthanide ions which could be directly correlated to a decrease of the conductivity. Finally, essays on crystallization of TP 2D MOFs with Fe ions were attempted by Mirica and co-workers.³² Despite the lack of crystallinity of the material, the Fe-based MOF displayed similar polycrystalline conductivities of $10^{-3} \text{ S cm}^{-1}$.

HATP triphenylene ligand

One of the first imino substituted TP-based MOFs reported was $\text{Ni}_3(\text{HITP})_2$ by Dincă and co-workers in 2014.³⁴ The 2D coordination layers display a honeycomb network with a slipped-parallel structure with a minimal offset direction (see Figure 1.10a and 1.10b). Hence, an almost eclipsed stacking of TP moieties is obtained, converging to large charge delocalization along the material. The resulting conductivities were as high as 40 S cm^{-1} in polycrystalline thin films, even when grain boundaries dramatically limits the percolation of charge carriers between crystallites.^{34,60} A linear increase of the conductivity with the temperature indicated a semiconducting behavior of the material, sustained by the oxidation of the amines into iminosemiquinones and the formation of a hole rich p-type semiconductor. Controversial results were obtained in a more recent study by Day *et al.* on micrometer-long rod-like crystals using hydrothermal synthesis with single crystal conductivities as 150 S cm^{-1} with non-nullar conductivities at 0 K, indicating a metallic behavior (Figure 1.10c and 1.10d).²⁴ DFT calculations by Foster *et al.* already demonstrated in a manuscript published in 2018 that such differences may arise from interface defects as grain boundaries or stacking displacements, which not only break the conjugation of the graphitic layers or the charge delocalization across them but also can open a band gap in the otherwise metallic $\text{Ni}_3(\text{HITP})_2$ MOF.⁶⁴ In fact, DFT anticipated a semiconductor behavior for a $\text{Ni}_3(\text{HITP})_2$ monolayer whereas the bulk material is metallic. A related DFT study anticipated an increase of the band gap upon increasing the intralayer distance.⁶⁵ Worth-to-mention, strong band dispersion is not only obtained in the *in-plane* direction but orthogonally to the 2D layers as well, underlining the strong charge delocalization across the layers. Therefore, relevance of the synthetic

protocol is highlighted providing different conductivities depending on the used approach as shown in Table 1.2.

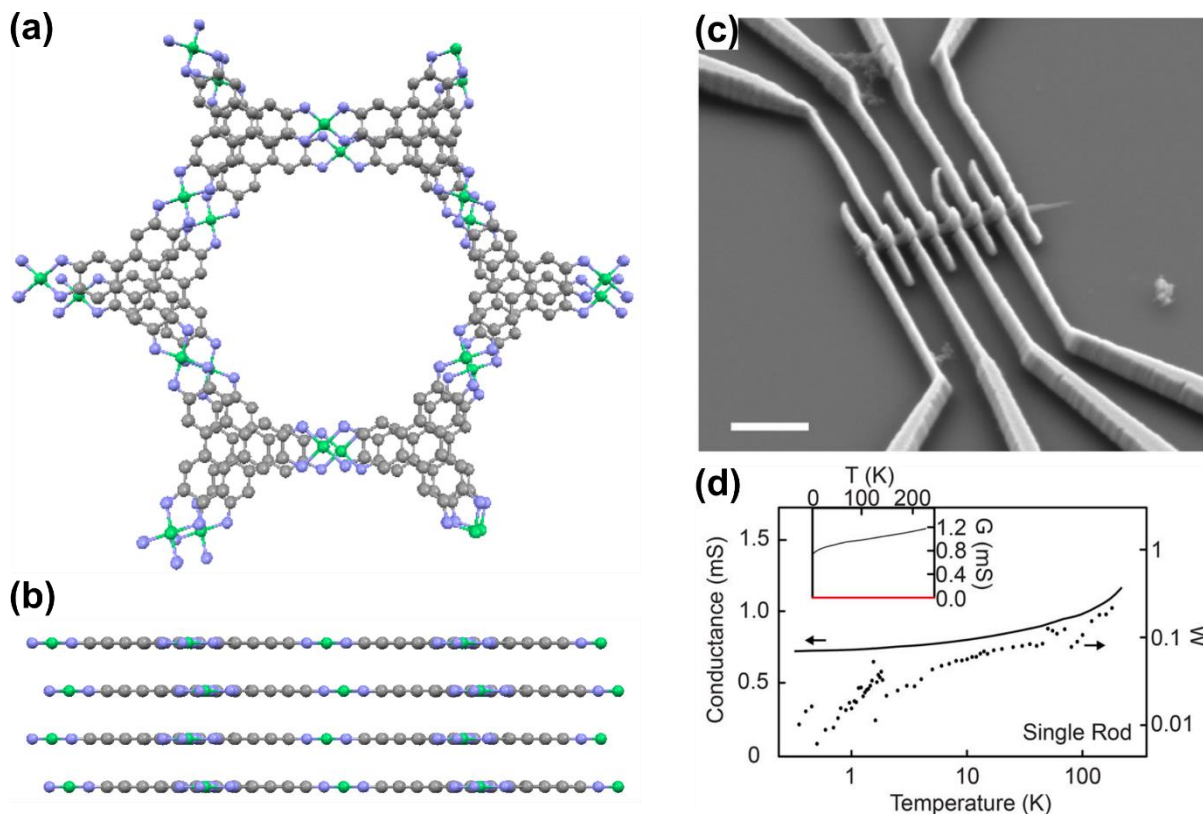


Figure 1.10: (a) and (b) Top and side view respectively of the 2D layers in the Ni₃(HITP)₂ structure. (c) SEM image of rod-like Ni₃(HITP)₂ single crystal device. (d) Temperature dependence of electrical conductivity of a Ni₃(HITP)₂ single crystal proving the metallic behavior. Images extracted from ref. 24.

TP-based MOFs Cu₃(HITP)₂⁶⁶ and Co₃(HITP)₂ structures,²² were also synthesized and isostructural showcasing similar powder crystalline patterns. However, slight variations on the interlayer distance with the metallic center, being these 3.30, 3.16 and 3.29 Å for Ni₃(HITP)₂, Cu₃(HITP)₂ and Co₃(HITP)₂ structures, respectively, were determined.²² Consequently, different pressed pellet conductivity values of 55.4, 0.75 and 0.024 S cm⁻¹ were obtained. Controlled modifications of the conductivity and band gap were also achieved by tuning the metallic ratio in a series of alloys M_nM'_{3-n}(HITP)₂ containing pairs of metallic ions (Ni/Co, Ni/Cu, Cu/Co). Differences on the MOFs behavior depending on the incorporating metal atom have been predicted by DFT calculations. As previously commented, calculations on Ni₃(HITP)₂ monolayer structure proved a semiconducting band structure with a band gap of 0.13 eV.⁶⁷ The metallic Ni²⁺ center showcase a dsp²

hybridization with the HITP ligand leading to a perfect square planar geometry and 2D layers. On the other hand, upon substitution from Ni^{2+} to Cu^{2+} lead to sp^3 hybridization due to the extra electron when comparing the electronic configuration between both ions. Consequently, square-grid coordination geometry is obtained inducing a distortion in the 2D layers. This change in the crystallographic network induces a metallic behavior of the 2D monolayer. However, direct correlation of the crystalline structure variations with the conductivity remains however a challenge due to the different degree of crystallinity of the pressed pellets, especially in the case of $\text{Co}_3(\text{HITP})_2$ crystals.²² Properties modification as these ones arising from the variability of the chemical formula of the MOF will have a direct impact in the possible applications of the materials (see *vide infra*).

THT triphenylene ligand

The first report of a 2D MOF were crystals grown through an *in situ* reaction between a metallic salt containing the Pt ion and THT derivative in the presence of oxygen.⁶⁸ After the MOF formation, the THT ligand showcased a -4 oxidation state, hence, sodium ions were uptaken in the final formula for charge balance reaching the final formula of $\text{Na}_{1.8}\text{Pt}_3(\text{THT})_2$. The square planar coordination geometry favored the formation of hexagonal layered networks with a staggered stacking due to the large ionic radius of Pt ions (see Figure 1.11a and 1.11b). Remarkably, the THT ligands could be further oxidized upon I_2 treatment reaching a neutral formula of $\text{Pt}_3(\text{THT})_2$ without no relevant structural changes and a final conductivity of the order of $10^{-6} \text{ S cm}^{-1}$. This low value arises from the lack of *out-of-plane* contribution as staggered packing alternates the TP moieties, disabling their interaction. Further, Pt is a very large metallic ion that can form not strong enough d- π bonds leading to a weak intralayer charge delocalization.

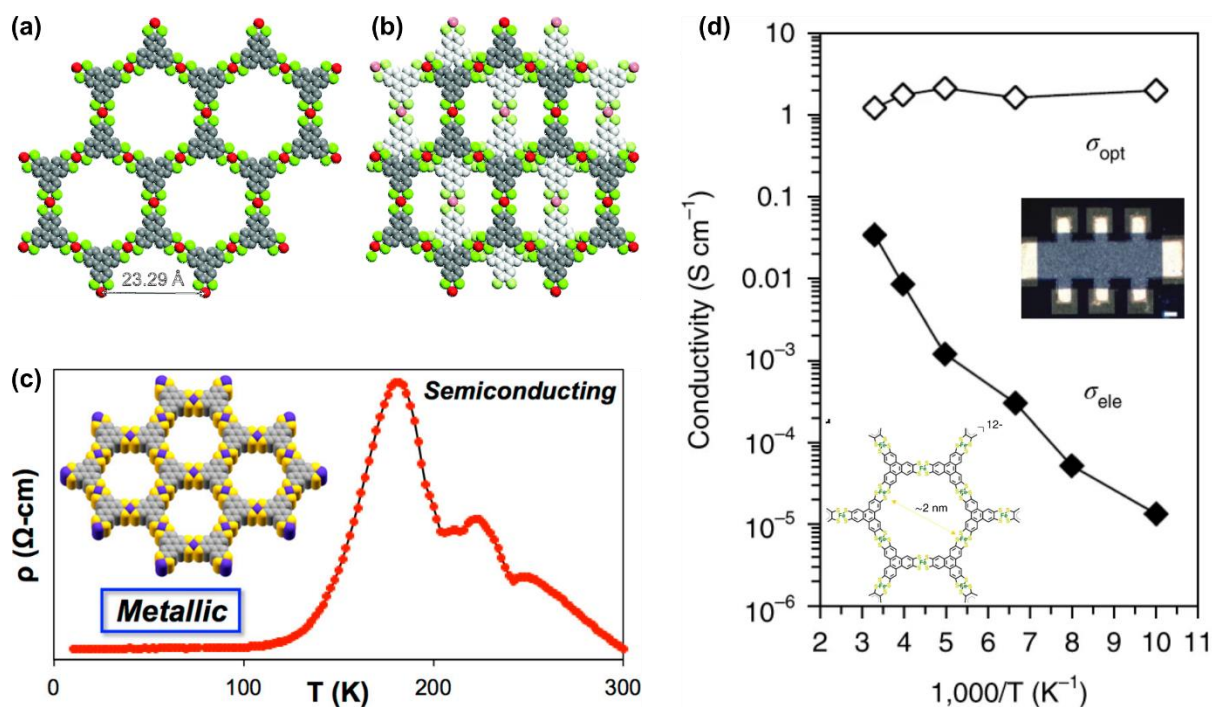


Figure 1.11: (a) and (b) Single layer and layer packing structures of Pt₃(THT)₂ crystals. Images extracted from ref. 68. (c) Temperature dependence of the electrical resistivity of Co₃(THT)₂ samples passing from a semiconducting to metallic behavior. The eclipsed honeycomb structure of Co₃(THT)₂ is shown in the inset. Image extracted from ref. 69. (d) Electrical and optoelectrical conductivity of Fe₃(THT)₂ thin films. The thin film device and structure of Fe₃(THT)₂ are shown in inset. Images adapted from ref. 70.

To overcome this low conductivity other smaller metallic ions were tested, among them Co and Ni whose bis(dithiolene) complexes have proved a strong bonding with large carrier mobilities and several accessible redox-active states.^{18,52} Hence, in 2015, Marinescu and co-workers reported the Co₃(THT)₂ MOF with honeycomb 2D layers stacked with an eclipsed conformation that resulted in conductivities of $1.4 \cdot 10^{-3}$ S cm⁻¹ for pressed pellets and $3.2 \cdot 10^{-2}$ S cm⁻¹ for thin films formed through an interfacial reaction method, without any further treatment.⁵² DFT calculations suggested that these conductivities were associated with an *out-of-plane* mobility, with low *in-plane* conductivities arising from the mixed-valence character of the metallic centers (two Co³⁺ per Co²⁺ center). Remarkably, the Co₃(THT)₂ MOF goes from a semiconducting state, attributed to a scattering of charge carriers, at high temperatures to a metallic state transition upon decreasing the temperature, being strongly dependent on the pellet/film thickness (Figure 1.11c). Dong *et al.* also reported the growth of a 2D monolayer of the related complex Ni₃(THT)₂ using the Langmuir-Blodgett technique. The single-layer exhibited a hexagonal pattern with porous of ~2 nm and large stability, with large lateral area of the order of millimeters and thicknesses of 0.7 nm.

In 2017, Mirica and co-workers reported the hydrothermal synthesis of $\text{Co}_3(\text{THT})_2$, $\text{Cu}_3(\text{THT})_2$ and $\text{Ni}_3(\text{THT})_2$ MOFs under basic conditions.⁷¹ The spectroscopic characterization proved the mixed valence character for cobalt and copper ($\text{Co}^{2+}/\text{Co}^{3+}$ and $\text{Cu}^{1+}/\text{Cu}^{2+}$) whereas only the Ni^{2+} state was found. Pressed pellets of the resulting polycrystalline material showed very low conductivities of $2.4 \cdot 10^{-9}$, $2.4 \cdot 10^{-8}$ and $3.6 \cdot 10^{-4} \text{ S cm}^{-1}$ for $\text{Co}_3(\text{THT})_2$, $\text{Cu}_3(\text{THT})_2$ and $\text{Ni}_3(\text{THT})_2$, respectively. Thin films of the $\text{Fe}_3(\text{THT})_2(\text{NH}_4)_3$ MOF with good control on the thickness were reported by Feng and co-workers in 2018 using a liquid-liquid interfacial approach (Figure 1.11d).⁷⁰ The Fe ions were found in its Fe^{3+} state, in spite using Fe^{2+} ions as reactive materials, so to compensate the charge of the fully anionic THT ligand ammonia ions were incorporated in the structure. Crystallographic analysis revealed hexagonal layers packed in a near-eclipsed inclined structure with conductivities of $3.4 \cdot 10^{-2} \text{ S cm}^{-1}$ and semiconductor behavior with optical band gaps of 245 meV. Hence, time-resolved photoconductivity measurements were performed, reaching mobilities up to $220 \text{ cm}^2 \text{ V}^{-1} \text{ s}^{-1}$. Marinescu and co-workers proved similar semiconductor to metallic transitions in this material with as synthesized conductivities of $\sim 0.2 \text{ S cm}^{-1}$.⁷² More notoriously, upon oxidation to atmospheric air, temperature transition got shifted to higher values, reaching room temperature metallic behavior and final conductivities of to $8.0 \cdot 10^{-4} \text{ S cm}^{-1}$.

Other structures

Interest on the development of new structures were pointed out firstly by DFT calculations on combination of dual ligands or different hetero-atom substitutions in ortho position of Pt and Pd-based TP MOFs.^{73,74} These variations on previously described structures proved to have great impact on the band structure of the material as different band gap openings were obtained. These indications were further experimentally explored by developing novel hetero-atom substitution or combining different ligands.

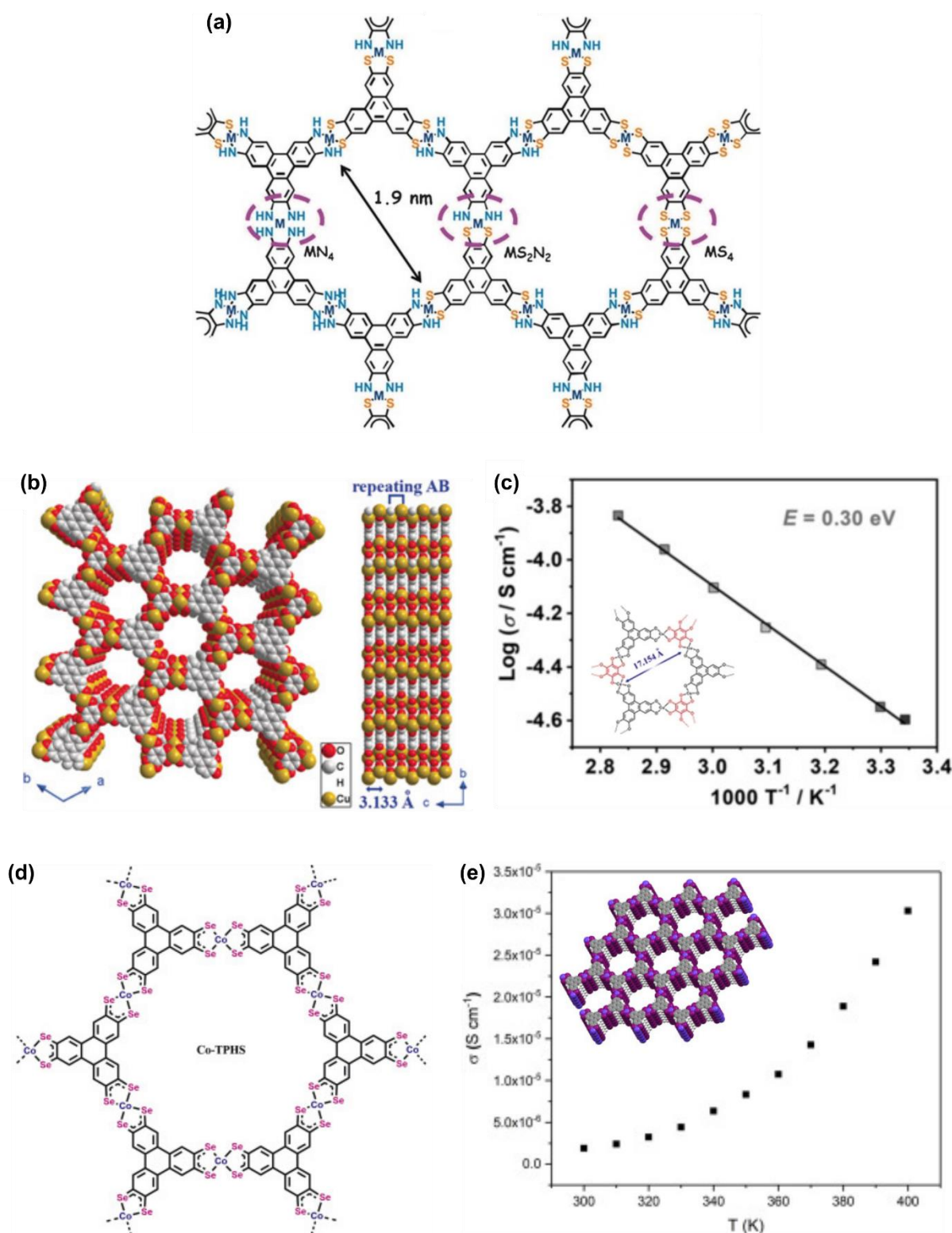


Figure 1.12: (a) Structure of the honeycomb structure incorporating both THT and HATP molecules. The different available coordination spheres (CoN_4 , CoN_2S_2 , CoS_4) are shown. Image extracted from ref. 75. (b) Top view and side view of the layers of the structure of $\text{Cu}_3(\text{HHTP})(\text{THQ})$. (c) Temperature dependence of the electrical conductivity of $\text{Cu}_3(\text{HHTP})(\text{THQ})$. Inset: Structure of a single layer of $\text{Cu}_3(\text{HHTP})(\text{THQ})$. Images extracted from ref. 76. (d) structure of a single layer of $\text{Co}_3(\text{TPHS})_2$. (e) Temperature dependence of electrical conductivity of $\text{Co}_3(\text{TPHS})_2$. Inset: Eclipsed packing structure of the layers in $\text{Co}_3(\text{TPHS})_2$. Images extracted from ref. 77.

One of the approaches followed on the quest for novel structures is the combination of two or more ligands within a single structure. For instance, Feng and co-workers reported the simultaneous incorporation of HATP and THT ligands into a honeycomb structure obtained as a crystalline powder or thin films (either monolayer or supported on graphene).⁷⁵ Control on coordination spheres is hardly achieved obtaining randomly distributed CoN_2S_2 , CoN_4 and CoS_4 coordination units along the material (Figure 1.12a). The CoN_2S_2 center contributed to an enhanced catalytic activity due to the combination of donor atoms contributing each to the absorption and desorption of analytes. Kitagawa and co-workers reported the combination of alternating HHTP and tetrahydroxy-1,4-quinone (THQ) ligand within the semiconducting $\text{Cu}_3(\text{HHTP})(\text{THQ})$ MOF.⁷⁶ Presence of ethylenediamine in the synthesis was needed as chelating agent of the metallic center to ensure the balance of coordination between the two units while avoiding the precipitation of $\text{Cu}_3(\text{HHTP})_2$ or $\text{Cu}_3(\text{THQ})_2$ MOFs. All in all resulted in hexagonal layers further piled in a slipped parallel fashion (pores of 1.7 nm) and conductivities of $2.53 \cdot 10^{-5} \text{ S cm}^{-1}$ (Figure 1.12b and 1.12c). Finally, a selenol-based triphenylene (TPHS) ligand was used to synthesize the semiconducting $\text{Co}_3(\text{TPHS})_2$ TP 2D MOF, with an eclipsed packing of hexagonal honeycomb 2D layered (Figure 1.12d and 1.12e).⁷⁷ The conductivity of a pressed pellet of the order of $10^{-6} \text{ S cm}^{-1}$ due to the poor crystallinity of the material in the stacking direction. DFT calculations on the structure revealed a poor electronic coupling of the d and π -orbitals of the Co and ligand respectively, probably due to the large radius of the Se donor atom. This led to larger interlayer contribution to the electronic coupling. Notoriously, $\text{Co}_3(\text{TPHS})_2$ showed glassy magnetic properties with low intralayer antiferromagnetic coupling.

1.3.2. Applications of triphenylene-based 2D MOFs

In this section, some of the most characteristic applications found for these materials are listed, giving if possible, a correlation of the chemical structure on the performance of the material.

TP 2D MOFs have proved to be largely sensitive to ambience conditions.⁷⁸ Conductivity of TP 2D MOFs in vacuum can reach larger values by several orders of magnitudes than in ambience or inert conditions and much higher values than when exposed to acidic/basic entities. Thus, this property has opened the way to chemiresistive gas sensing applications for TP 2D MOF. Many examples of TP 2D MOF sensing devices can be found in the literature, as for instance sensing different solvent humidity²³ or toxic gases (NH₃, NO or H₂S).^{32,35,37,66} Furthermore, devices have been adapted to a wide variety of platforms, occluding MOF in electronic textiles,³⁵ flexible polymers^{23,37} or pressed pellets.³² Notoriously, all devices showcase ppm range detection limits and sensitivity and fast responses (both detecting and recovery). Choosing an appropriate combination of metal and ligand has proved to be critical as different responses to the analytes are obtained for each MOF (Figure 1.13a and 1.13b). Most frequently used ligands used in this application are HITP or HHTP with Ni or Cu metallic center.

In a very recent study, Mirica and co-workers demonstrated that different host guest interactions between MOF and ammonia gas were occurring depending on the used ligand and metal.⁷⁹ Remarkably, in all cases, the MOF electronic structure was altered upon the interaction with ammonia preserving the crystallinity of the material. In the case of amino-substituted TP MOFs, NH₃ is absorbed at Lewis acid sites without causing structural changes. However, in the case of hydroxyl-substituted TP MOFs, ammonia coordinates at Brönsted acid sites inducing structural changes in the TP aromatic ring, affecting the MOF's conductivity (Figure 1.13c). Moreover, Cu-based MOFs seemed to have larger redox reactivity by coordination to ammonia than Ni-based ones. Thus Cu-based MOFs seem to be more suitable materials for chemiresistive sensors of basic acids than Ni-based. On the other hand, Ni-based MOFs seem more suitable to detect neutral volatile organic compounds as for instance ethanol, acetone or aromatic volatile molecules (Figure 1.13d).⁸⁰ This has enable using Cu-based MOFs for highly selective sensing of ammonia traces in interference gases as ethanol or acetone.⁴⁷ Worth-to-mention, apolar volatile molecules are hardly detected by TP 2D MOFs chemiresistive devices. Driven by the success on chemiresistive sensor application, use of TP 2D MOFs for other analytes has arisen in the form of potentiometric²⁸ (ionic salt concentration) and neurochemical voltammetry sensors.²⁹

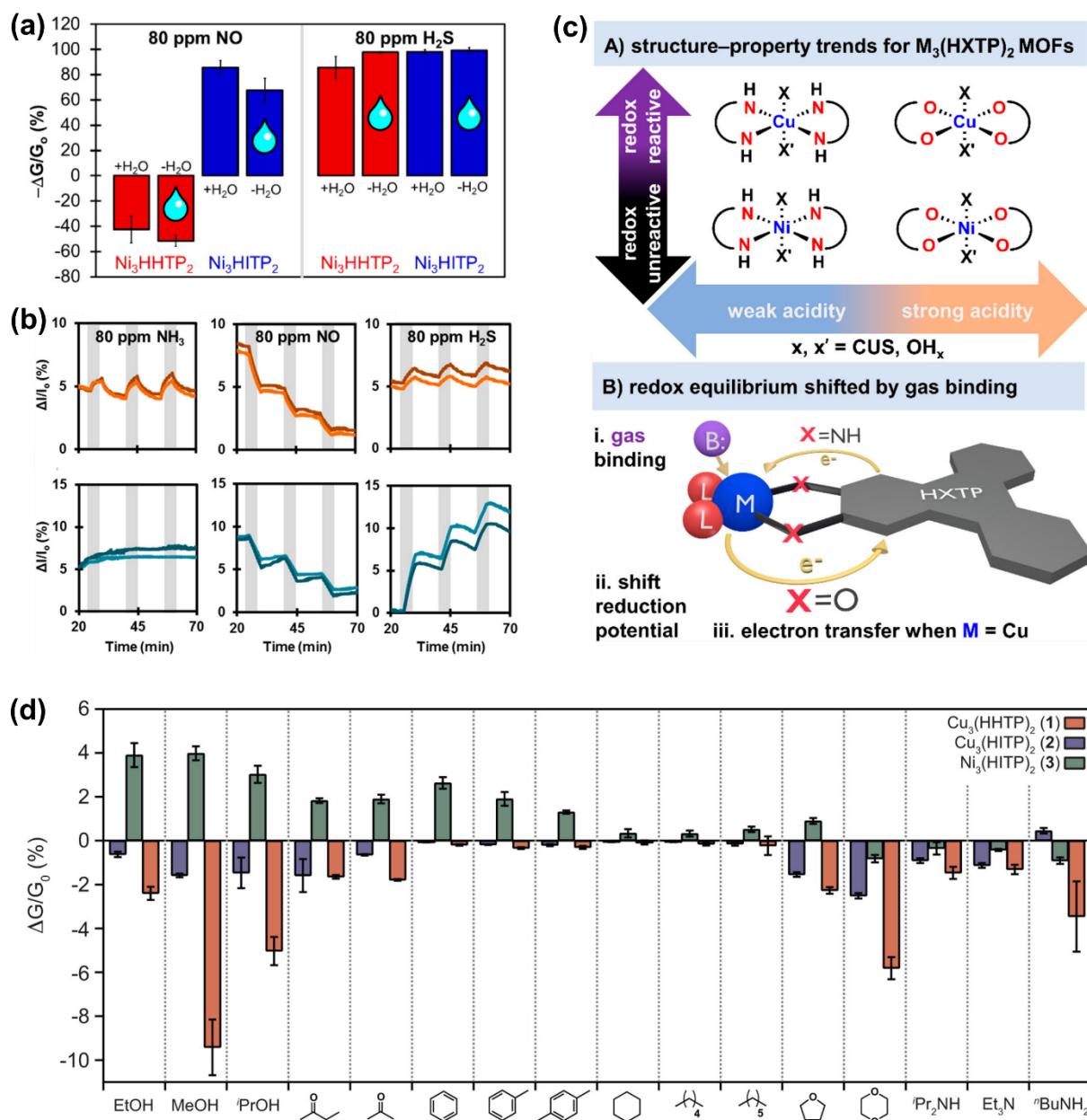


Figure 1.13: (a) Saturation sensor response for electronic textiles containing $\text{Ni}_3(\text{HHTP})_2$ (red) and $\text{Ni}_3(\text{HITP})_2$ (blue) exposed to 80 ppm of NO and H_2S in dry nitrogen (solid bars) and in the presence of 5000 ppm water (with water droplet). Relevance of the used ligand in the MOF is shown, as different responses are obtained between the two systems having the same metallic ion. Image extracted from ref. 35. (b) Sensing traces of toxic gases NH_3 , NO and H_2S at 80 ppm using $\text{Cu}_3(\text{HHTP})_2$ (orange) and $\text{Ni}_3(\text{HHTP})_2$ (blue) grown on flexible devices. Grey areas represent the exposure of the devices to the respective gas. Relevance of the used metal in the MOF is highlighted in this figure as different responses are obtained for a same analyte. Image extracted from ref. 37. (c) Summary of the general trends in acidity and redox activity of MOFs probed by basic gases and proposed mechanism for the shift of oxidation states in Cu-containing species upon binding of a basic gas. Image extracted from ref. 79. (d) Sensor responses of chemiresistor arrays of $\text{Cu}_3(\text{HHTP})_2$, $\text{Cu}_3(\text{HITP})_2$ and $\text{Ni}_3(\text{HITP})_2$ to different analytes. Image extracted from ref. 80.

The large conductivity and surface area of TP 2D MOFs led to large capacitance when incorporating them in pressed pellets electrodes. Further, their large 1D pores allow to host large and solvated ionic structures making them suitable for supercapacitor or ion batteries.^{81,82} In 2017, Dincă and co-workers reported the first TP MOF electrode for supercapacitors using pressed pellets of $\text{Ni}_3(\text{HHTP})_2$ achieving capacities of $18 \mu\text{F cm}^{-2}$, exceeding values found for some other carbon based materials.⁸¹ Moreover, the electrodes proved large stability, retaining almost 90% of the capacitance after 5000 charge and discharge cycles. Worth-to mention, the MOF-based supercapacitor was used as battery for flashlight. Similar capacitive values were obtained in $\text{Cu}_3(\text{HHTP})_2$ electrodes for zinc batteries, retaining also 75% of the initial capacity after 500 cycles.⁸² Notoriously, $\text{Cu}_3(\text{HHTP})_2$ electrodes possessed two redox-active sites (the copper ion and the quinoid structure) to increase the specific capacity of the material in a reversible way, storing the Zn^{2+} ions in the 1D pores. Nevertheless, pelletization of TP 2D MOFs dramatically decreases the available surface area, hindering the internalization of ions into the structure.^{36,40} Thus, nanostructuration of TP MOF based electrodes has been recently reported as an approach to increase available surface area. In a first example, $\text{Cu}_3(\text{HHTP})_2$ nanowires were grown on carbon paper by template assisted method leading to large surface areas of $540 \text{ m}^2 \text{ g}^{-1}$ without need of further treatment (Figure 1.14a and 1.14b).³⁶ Remarkably, the supported carbon paper electrodes were suitable electrodes showcasing capacities of $22 \mu\text{F cm}^{-2}$ which were retained up to 80% of the initial value after 5000 cycles. Furthermore, larger capacitive responses of 3200 mF cm^{-2} were obtained by combination of $\text{Ni}_3(\text{HHTP})_2$ nanorods grown on top of NiCo layered double hydroxide nanosheets in a Ni foam forming a hybrid nanostructured porous array.⁴⁰ Other example of hybrid material was the growth of $\text{Ni}_9(\text{HHTP})_4$ on 3D porous laser scribed graphene (LSG) interdigitated electrodes on polyimide substrates (Figure 1.14e-g).⁸³ LSG was patterned applying a CO_2 laser and a O_2 -plasma prior to the on-surface growth of the MOF. Notoriously, the hybrid MOF/LSG material provided large areal capacitance, energy density and power density (15.2 mF cm^{-2} , $4.1 \mu\text{W h cm}^{-2}$ and 7 mW cm^{-2} respectively). Another strategy to increase charge percolation and available surface area has been growing TP 2D MOFs on top of flexible structured substrates as polypropylene separators⁸⁴ (Figures 1.14b-d) or cellulose nanofiber papers (Figures 1.14h-k).⁸⁵ The obtained composites showcased large conductivities along with large areal capacities which were retained after several charge –discharge cycles.

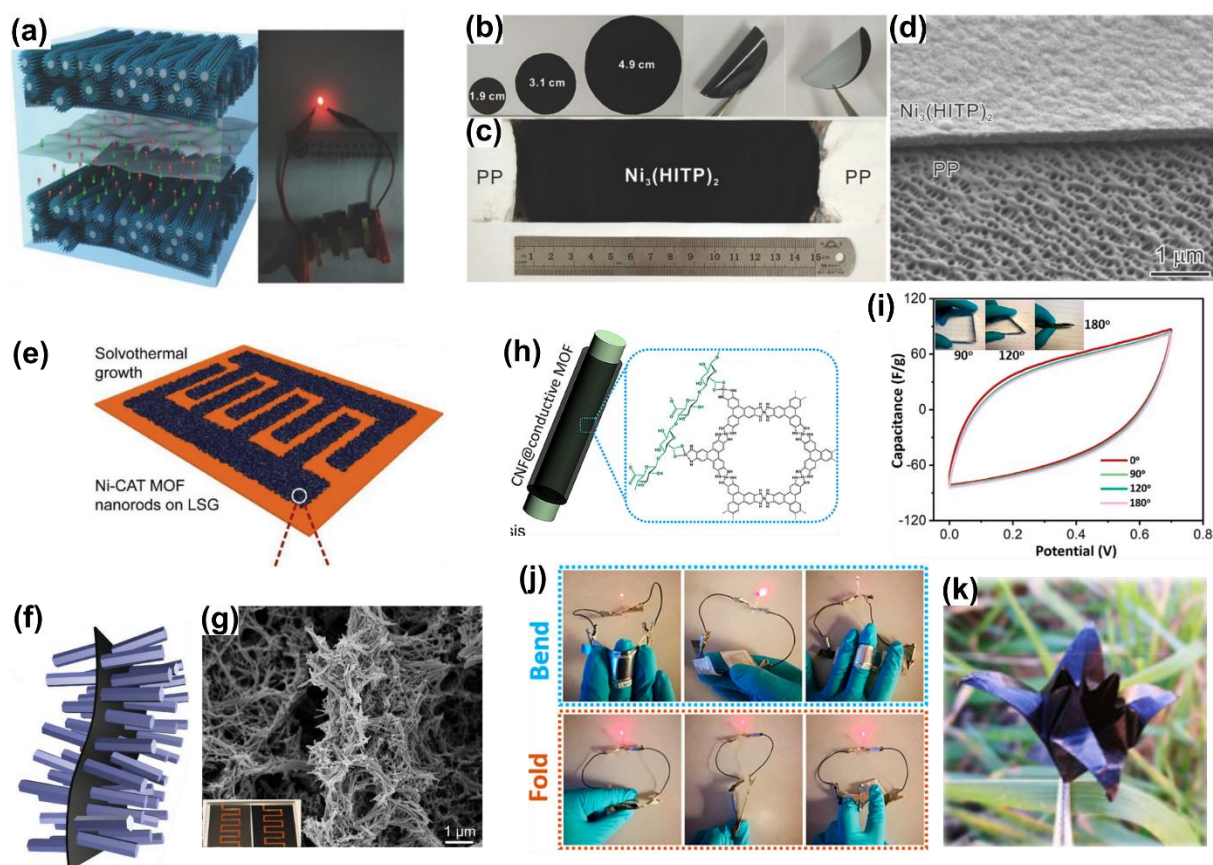


Figure 1.14: (a) Schematic structure of $\text{Cu}_3(\text{HHTP})_2$ on carbon paper supercapacitor (left) and photograph of a red light-emitting-diode powered by the three supercapacitors connected in series (right). Image extracted from ref. 36. (b) and (c) Photographs of the $\text{Ni}_3(\text{HITP})_2$ grown on polypropylene separators showing their different shape and sizes and their flexibility. (d) SEM cross-section image of $\text{Ni}_3(\text{HITP})_2$ films on polypropylene. Images extracted from ref. 84. (e) Schematic and structural illustrations of the interdigital pattern of LSG/ $\text{Ni}_9(\text{HHTP})_4$ hybrid and (f) solvothermal growth of $\text{Ni}_9(\text{HHTP})_4$ nanorods. (g) SEM image of the structure of LSG/ $\text{Ni}_9(\text{HHTP})_4$ hybrid showing the large available porosity. Images extracted from ref. 83. (h) Schematic of the growth of $\text{Ni}_3(\text{HITP})_2$ and $\text{Ni}_9(\text{HHTP})_4$ on cellulose nanofiber papers. (i) Cyclic voltammetry measurements of $\text{Ni}_3(\text{HITP})_2$ on cellulose paper at different folding angles. (j) Photographs of red light-emitting diodes powered by $\text{Ni}_3(\text{HITP})_2$ on cellulose paper capacitors under different folding or bending geometries. (k) Photograph of origami folded $\text{Ni}_3(\text{HITP})_2$ on cellulose paper capacitors in flower shape. Images extracted from ref. 85.

Electrocatalyst

The large conductivity and porosity of TP 2D MOFs aside their large metallic active site density enabled their use in electrocatalytic activity. Notoriously, they have been reported to effectively perform electrochemical redox reactions typical in fuel cell batteries as Hydrogen Evolution Reaction (HER) or Oxygen Reduction Reaction (ORR). Regarding HER, Co dithiolene structures previously proved to have large catalytic activity for HER. Thus, in 2015 Marinescu *et al.* reported the used of $\text{Co}_3(\text{THT})_2$ thin films as electrocatalytic cathode for hydrogen generation from water.⁵² The film was synthesized by interfacial

method and deposited onto a variety of substrates (HOPG, glassy carbon...). Remarkably, the electrode showed high acidic stability and large cobalt active site density suitable for HER reaction, reaching Tafel slopes of 189 mV/dec at pHs of 4.2.

On the other hand, ORR reactions seemed to be less efficiently catalyzed depending on the used structure. In a primary study, $\text{Ni}_3(\text{HITP})_2$ film grown on glassy carbon electrodes proved to have large ORR activity under O_2 atmosphere.⁸⁶ Worth-to-mention, the electrodes remained largely stable as 88% of the initial current in potentiostatic measurement was retained over 8 h. However, the reaction proved to be strongly dependent on pHs of the media, suggesting different mechanism electron transfer were occurring. Theoretical insights on the catalytic mechanism for the oxygen reduction reaction on $\text{M}_3(\text{HITP})_2$ ($\text{M} = \text{Ni}, \text{Cu}$) proved that generation of H_2O_2 under acidic conditions is more favorable in both structures due to the complicated multipath generation of H_2O .⁸⁷ A deeper study was followed consequently studying the effectivity of different TP 2D MOFs for ORR.⁸⁸ In this work, Dincă and co-workers reported the higher catalytic activity of hexagonal crystalline systems as $\text{Ni}_3(\text{HITP})_2$, $\text{Cu}_3(\text{HITP})_2$ and $\text{Cu}_3(\text{HHTP})_2$ derived from their higher electrical conductivity and redox activity facilitating electron transfer to O_2 . On the other hand, trigonal crystallized MOFs as $\text{Ni}_3(\text{HHTP})_2$ and $\text{Co}_3(\text{HHTP})_2$ have a disruption of the π - π stacking of the triphenylene cores which strongly affects to the electron transfer kinetics. Hence, crystalline structure has proven to be critical to determine electrocatalytic properties of TP 2D MOFs. Interestingly, large electronic density of $\text{M}_3(\text{HITP})_2$ structures has even proved to be suitable for O_2 generation⁸⁹ (enhanced by doping of the structure with iron catalytic centers) and CO_2 reduction, mimicking photosynthesis processes.^{90,91} Notoriously, large photocatalytic performance was obtained under light irradiation when using $\text{Ni}_3(\text{HITP})_2$ as co-catalyzer along with a photosensitizer.⁹¹

Spintronics

Cu-based MOFs have been the widest explored materials for these properties due to their electronic configuration with an odd number of d electrons. In a recent study published by Dincă *et al.*, single crystals of trinuclear molecular models of $\text{Cu}_3(\text{HHTP})_2$ and $\text{Cu}_3(\text{HITP})_2$ MOFs were obtained.⁹² Magnetic measurements on this analogous systems proved neighboring spins couple antiferromagnetically which would effectively lead to spin frustration if occurring in the TP 2D MOFs. This effect has been deeper studied recently by Awaga and co-workers, proving thin films of $\text{Cu}_3(\text{HHTP})_2$ had antiferromagnetic interactions

between neighboring atoms and were reaching a quantum spin liquid state at ultralow temperature (38 mK).⁹³ This property has paved the way to novel spintronic applications as their use in organic spin valves.⁵⁰ Highly oriented thin films of $\text{Cu}_3(\text{HHTP})_2$ were implemented on vertical spin valves devices between LMSO and Co ferromagnetic electrodes. The chemical structure and rational *c*-axis growth of the film allowed the spin-polarized transport through the MOF. The devices showcased low magnetoresistances at cryostat temperatures that were retained upon changing the film thickness and increasing the temperature up to 200K.

Optoelectronics

Thanks to their large conjugation, this family of MOFs exhibit a strong light absorption with chemically-tunable band gaps of relevance in optoelectronic applications such as photodetectors or solar cells. In 2019, Bein and co-workers implemented highly oriented $\text{Ni}_3(\text{HHTP})_2$ thin films grown on ITO through vapor-assisted conversion into basic photovoltaic devices.⁴⁸ Interestingly, photoinduced charge generation and separation could be observed in the MOF material, making suitable for solar cell devices. The devices showcased open-circuit voltages of 156 mV under irradiation. Furthermore, Feng and co-workers reported recently a $\text{Fe}_3(\text{THT})_2$ photodetector capable of detecting radiation ranging from UV to the Near Infrared (NIR) (400-1575 nm) (Figure 1.15a).⁹⁴ Due to the narrow IR band gap of the material, room-temperature detection was limited, requiring cryogenic temperatures for a good performance reaching specificities of $7 \cdot 10^8 \text{ cm Hz}^{1/2} \text{ W}^{-1}$ (Figure 1.15b and 1.15c).

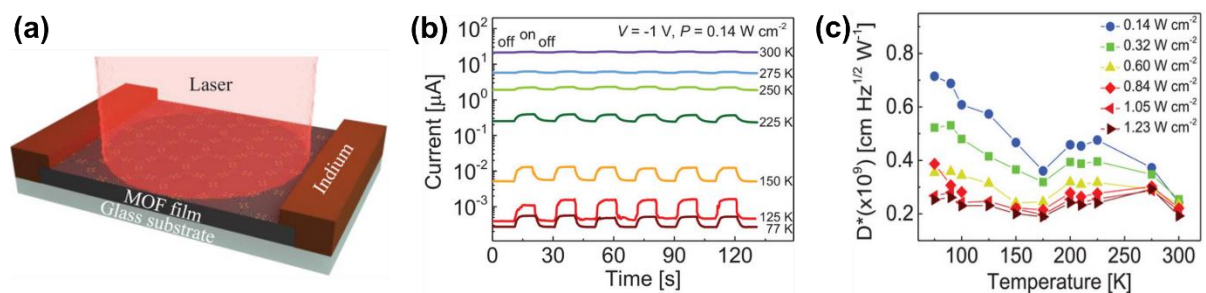


Figure 1.15: (a) Schematic of $\text{Fe}_3(\text{THT})_2$ thin film photodetector device with indium electrodes. (b) Temperature- dependent photoswitching behavior under pulsed illumination of 785 nm laser (c) Temperature dependence of photodetection at different power densities. Images extracted from ref. 94.

Others

Tactile sensor. The template-assisted growth of the $\text{Cu}_3(\text{HHTP})_2$ MOF on $\text{Cu}(\text{OH})_2$ microwires grown on a flexible Cu mesh substrate was used to develop a tactile sensor.³⁹ The

rationally designed flexible sensor allowed the modulation of the contact area as a function of the applied pressure, having a direct impact on the measured intensity (Figure 1.16). This was used to monitor human motion and pulse, recognizing music through machine learning algorithms and displaying pressure maps when using an array of multiple sensors. Remarkably, the sensor showcased a large durability, retaining nearly all the initial signal after 2700 pressure and release cycles.

FET logic. In 2014, Xu et al reported porous FET transistors based thin films of $\text{Ni}_3(\text{HITP})_2$.⁵⁵ The highly smooth and compact thin films were obtained by interfacial liquid-air method and recovered by stamping on a silicon wafer for its integration into FET transistor. Notoriously, the transistor showcased p-type behavior with large hole mobilities up to $48.6 \text{ cm}^2 \text{ V}^{-1} \text{ s}^{-1}$. Other electronic features of the device as large on/off ratios pointed to future possible applications as voltage-gated ion channels.

Thermoelectric. The combination of low thermal conductivity due to strong phonon scattering of the porous with the high electrical conductivity of this family of MOFs paves the way for their use in thermoelectric applications. Nanostructuration and grain boundaries also avoid phonon propagation, decreasing thus the thermal conductivity. However, so far only the thermoelectric properties of $\text{Ni}_3(\text{HITP})_2$ pressed pellets have been reported with an ultralow thermal conductivity of $0.21 \text{ W m}^{-1} \text{ K}^{-1}$ and a large electrical conductivity of 58.8 S cm^{-1} .⁹⁵ Remarkably, $\text{Ni}_3(\text{HITP})_2$ pellets provided. This led to negative Seebeck coefficients, indicating an n-type thermoelectric behavior, and high thermoelectric figure of merit (ZT) of $1.19 \cdot 10^{-3}$ at room temperature. In complementary studies, crystallinity of the material proved to be as well crucial as it had a deep impact on the electrical conductivity and hence on the thermoelectric efficiency.⁹⁶

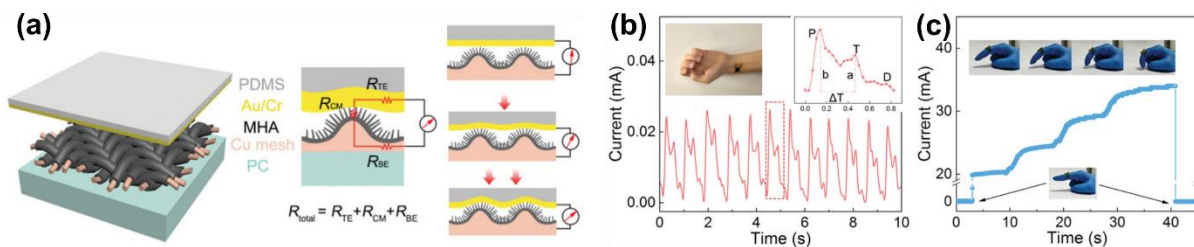


Figure 1.16: (a) Schematic illustration of working principle of the MOF-based tactile sensor. The larger applied pressure larger contact dimension between the MOF-containing mesh and the top electrode film and therefore the lower measured resistance. (b) Heart-beat monitoring using the MOF-based tactile sensor. (c) Current monitoring at different finger bending angles. Images extracted from ref. 39.

1.4. Triphenylene-based 2D COFs

1.4.1. Chemical families

Next, we will describe the different families of TP-based COFs so far reported grouped according to the ligand use, as previously done for the MOF family.

HHTP triphenylene ligand

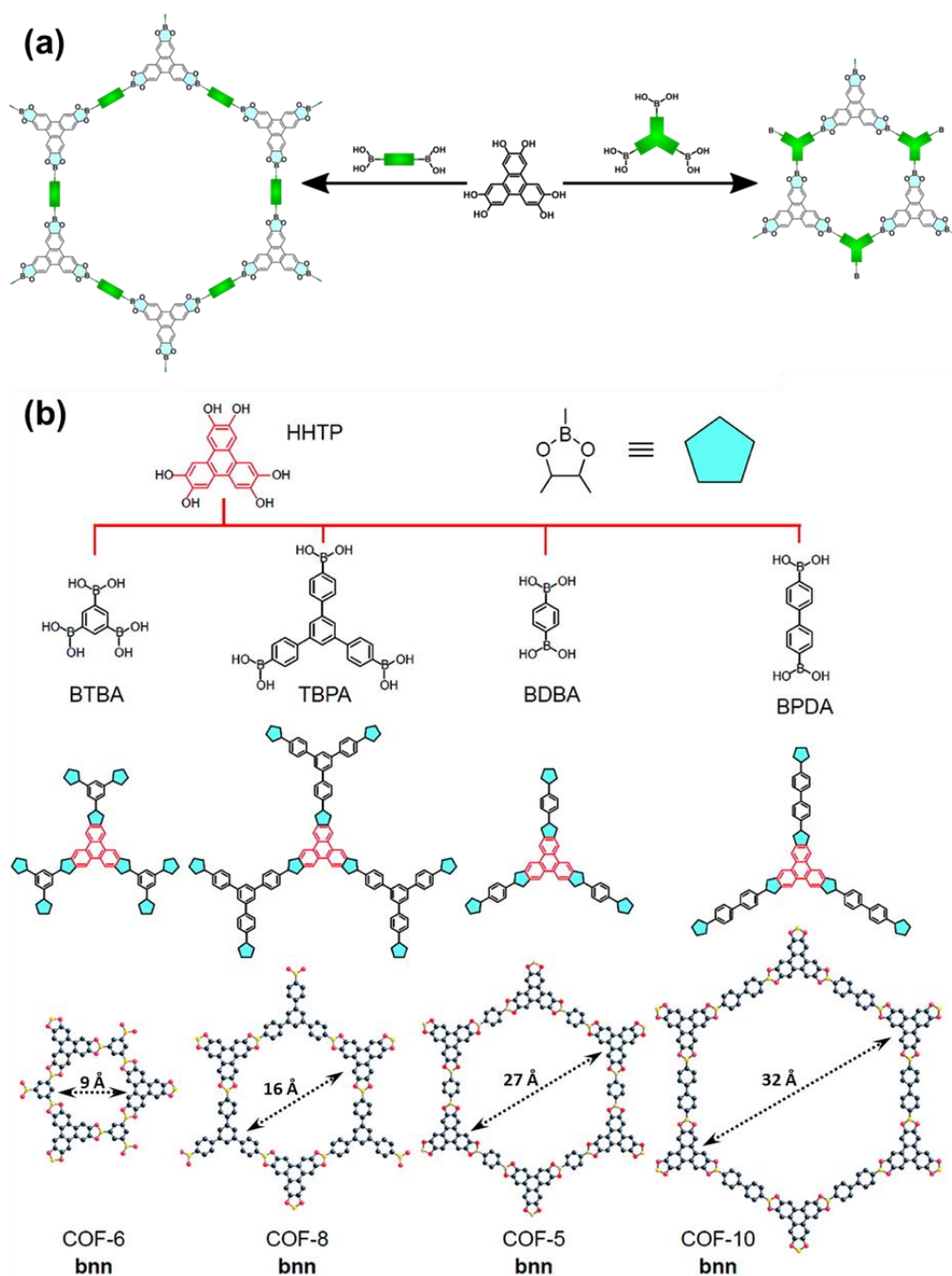


Figure 1.17: (a) Schematic of the structures of ester-boronate TP COFs condensing di- or tri-boronic acids with HHTP. (b) Condensation reactions between boronic acids and HHTP to give rise to different triphenylene-based 2D-COF with different porosities. B, orange; O, red; C, black. All 2D-COFs have a boron-nitride layer packaging. Image adapted from ref. 98.

The most common family of HHTP based COFs, and probably of all TP-based COFs, is that formed from boronic acids that covalently react upon dehydrogenation generating five-membered BO_2C_2 rings. A prototype structure of one of such ester-boronate COFs is the COF-5 reported by Yaghi and co-workers by condensing the hydroxyl derivative triphenylene HHTP and 1,4-benzenediboronic acid (BDBA) in a three-day solvothermal synthesis (Figure 1.17).^{25,33} Crystallographic characterization revealed a hexagonal unit cell forming layers stacked in an eclipsed boron nitride arrangement with interlayer distances of 0.34 nm as in graphitic structures. This structure leads to a large porosity showcasing 1D mesopores of 27 Å in diameter. Interestingly, the eclipsed layer stacking is attributed to the presence of triphenylene cores, as they interact by π - π stacking. Afterwards, the synthesis protocol has been extended to a wide variety of boronic acid derivatives giving rise to numerous TP ester-boronate COFs, named after COF-5 as COF-6, COF-8, COF-5 and COF-10, most of them summarized in Figure 1.17.⁹⁷ Most of them retain the crystalline space group of COF-5 with planar layers and porous diameters ranging from the angstrom to the few nanometers and therefore variable adsorption surface areas.⁹⁸

Worth to mention, ester-boronate TP bonding can be combined with other condensation reactions in a same synthesis opening the way to rational design and polymerization of novel COFs. Jiang and co-workers reported numerous structures TP COFs combining boron-ester and imine condensation reactions⁹⁹ in tri-ligand fused synthesis as the one seen in Figure 1.18a. Remarkably, different functionalities could be achieved modifying the used boronic acid. Simultaneously, Zeng *et al.* reported the synthetic study of the same structure.¹⁰⁰ Despite the efforts, crystallization could only be achieved in one-pot reaction with all three ligands present, sequential condensations would lead to other boronic structures or lack of precipitate. However, the obtained triphenylene-based COF showcased a large H_2 and CO_2 uptake with BET surface areas of 1619 m^2/g . On a second hand, polyarylether TP 2D COF structures have been recently developed by nucleophilic aromatic substitution between ortho-difluoro benzene derivatives and HHTP.¹⁰¹ Two layered structures, JUC-505 and JUC-506 (Figure 1.18b) were obtained using tetrafluoroterephthalonitrile and 2,3,6,7-tetrafluoroanthraquinone respectively. Both structures showcase hexagonal pores of 16.8 and 28.4 Å respectively and large chemical stability in strong acid, basic, reductive or oxidant media. Incorporation of cyano groups in JUC-505 as shown in Figure 1.18b allowed post-synthetic functionalization with carboxyl or amino groups forming JUC-505-COOH and

JUC-505-NH₂ structures, respectively. The same strategy was performed by Yaghi and co-workers achieving rare functionalization of COFs such as amide and amidoxime groups.¹⁰²

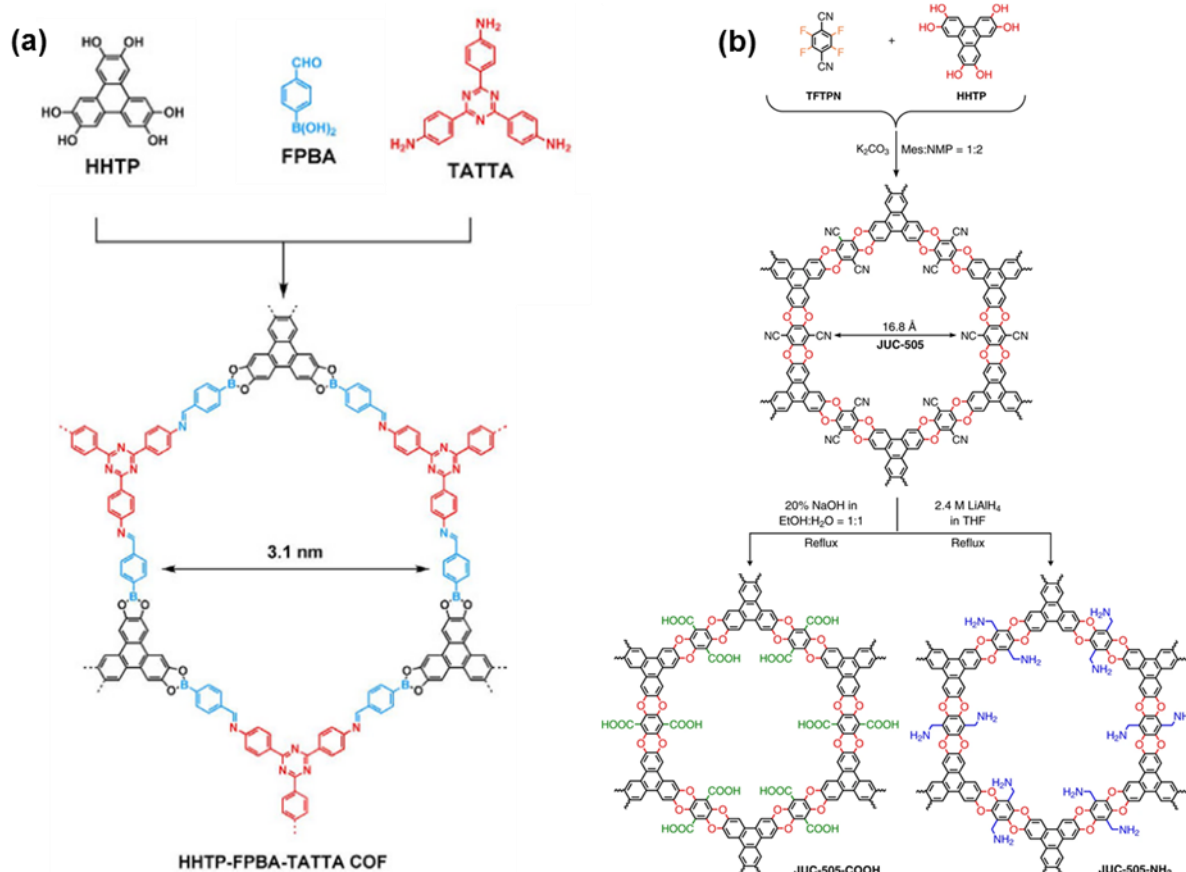


Figure 1.18: (a) Synthesis of multi-valent hexagonal TP COF using boron-ester and imine condensation reactions. Image reproduced from ref. 99. (b) Synthesis of JUC-505 through the condensation of tetrafluorobenzenes and HHTP. The present CN groups in the structure allowed post-synthesis modifications forming JUC-505-COOH and JUC-505-NH₂ structures. Image adapted from ref. 101.

A wide variety of 2D TP COFs with ester and ether bonds using HHTP can be found depending on the targeting application. Novel structures or structure modifications have been studied seeking gas storage applications (H₂, CH₄, CO₂...) above all, especially in the case of boronic ester COFs, as the used boronic acid determines the porous size and surface area and therefore the gas uptake capability.^{25,98} Moreover, all this premises crystallized into examples have been extended to a wide study of triphenylene-based boronic ester-linked COFs that are summarized in Table 1.4. Analogously, pore size modifications and chemistry surface functionalizations on polyarylether structures has enabled the tunability of molecular uptake into the pores, allowing water treatment applications and filtrations at various pHs.^{101,103} Worth-to-mention, electronic application of these structures are hardly explored

since ester and ether bonds break the conjugation along the 2D layer. A clear example of this is their recent use in low-k dielectrics.⁴⁵ Thus, charge transfer occurs mainly in the *out-of-plane* direction through the one-dimensional stacking of TP moieties as occurred for DLCs. Hence, doping is often required for the optoelectronic applications, either by incorporation of electron donor/acceptor atoms into the ester/ether structure,¹⁰⁴ use of conjugated ligands (creating electron donor-acceptor systems along with TP)¹⁰⁵ or external optoelectronic doping.⁴² A deeper description on the properties and applications of the structures described with different acids can be found on 1.4.2.

HATP triphenylene ligand

Inspired by the successful synthesis and application of ester/ether COFs, very recently other TP 2D COFs have been reported, obtained with different condensation reactions. TP phenazine-fused COFs are a main example of novel structures obtained by imine condensation reaction. Phenazine-fused TP COFs are characterized by constituting nitrogen-doped graphitic porous structures suitable for *in-plane* charge transfer. These tailored structures are suitable for electronic applications due to their large electronic conjugation (see Section 1.4.2 for more information). Typically, they are formed by condensation of HATP with *ortho*-planar tetraketones in solvothermal conditions.^{31,106,107} Notoriously, as previously for ester/ether COFs, different ketones can be used as starting monomers leading to different porous size as shown in Figure 1.19. In the case of Figure 20b, CS-COF structure was obtained by Guo *et al.* in a reaction between HATP and tert-butylpyrene tetraone leading to an extended π -conjugated system with pores of 1.6 nm.³¹ On the other hand, the structure shown in Figure 1.19a, reported by Meng *et al.* condensing HATP and hexaketonecyclohexane into a layered 2D COF with 1D pores of diameter ~ 1 nm. Worth-to-mention, this structure could also be obtained inverting the functional groups of the starting materials, condensing thus HHTP molecules with planar tetraamines.¹⁰⁸ More remarkably, nitrogen-doped TP 2D COFs with larger pores can be obtained upon the reaction between HHTP and HATP as reported by Jhulki *et al.*¹⁰⁹ with the structure of C2P-5 COF. Worth-to-mention, all the structures here described present eclipsed packing of the layers, thus *out-of-plane* contribution is expected as well, either by delocalization of the electrons in the TP moieties or by proton conduction along the one-dimensional porous.

Furthermore, research on different polymerized triphenylene structures has opened the way to new carbon allotropes as for instance TP graphdiyne (TP-GDY) analogues, containing both sp and sp^2 carbon atoms. This structure is well characterized as well for the large electronic conjugation suitable for electronic applications. Nishihara and co-workers reported the synthesis of TP-GDY through Glaser-Hay homo-cross coupling catalyzed by copper in a liquid-liquid interfacial system obtaining thin films of 220 nm thickness.¹¹⁰ Later, Tan and co-workers reported modifications on the synthesis obtaining control on both nanosheets and thin film forms, obtaining few monolayers thick films (0.9 nm) with good mechanical strength.⁵⁶

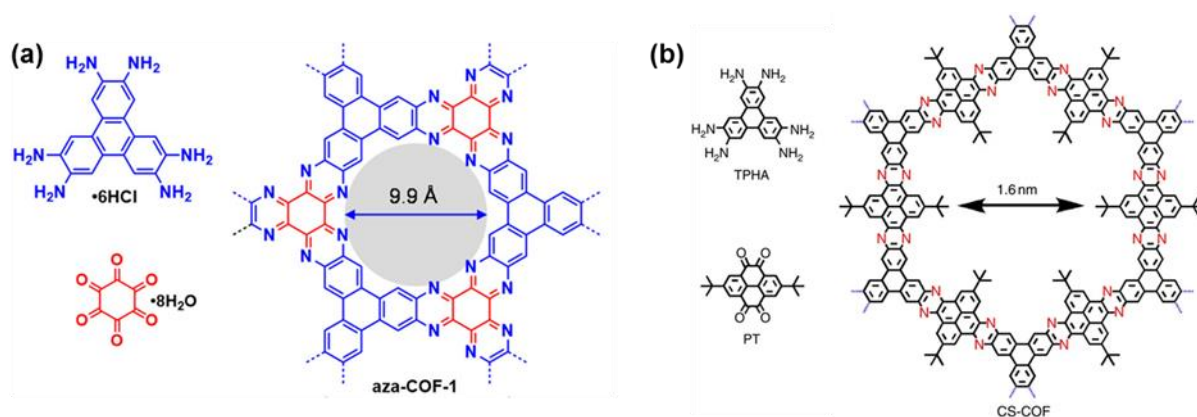


Figure 1.19: (a) and (b) Examples of nitrogen-doped graphitic COFs obtained through condensation of HATP with ortho-planar ketones. Images adapted from refs. 31 and 106 respectively.

1.4.2. Applications of TP-based 2D COFs

A particular property of layered COFs is their large π -orbital overlap in the stacking direction conferring them high exciton and charge conductions interesting for optoelectronic applications. Furthermore, their large and extended porosity enable chemical encapsulation or electrochemical doping for complementary functionalities. Finally, their high thermal stability avoids phase transitions disabling their electronic properties. However, to aim to given properties or applications one might tailor the structure of the COF or shape it in a given fashion.

Photovoltaics and photocurrent

Free TP molecules exhibit a characteristic blue emission fluorescence that is usually shifted upon integration in a COF structure as a result of a higher delocalization degree when conjugated co-ligands.^{111–113} These structures are characterized by the overlap of the triphenylene emission band with the co-ligand absorption one, acting as a donor-acceptor systems (where the TP is an electron donor and the co-ligand an electron-acceptor). Interlayer distance has proven to be critical in some cases as well, enabling on to off phosphorescence at cryogenic temperatures upon its reduction.¹¹³ Interestingly, photoluminescent kinetics have proved to be highly dependent on crystallites size in other studies, obtaining shorter exciton life times with in smaller particle suspension.^{114,115}

These results on the control of charge transfer and donor-acceptor systems point out already to possible photovoltaics applications. Several ester-boronate COFs have been described including TP and the boronic acid as electron donor and acceptor respectively.^{105,116,117} The eclipsed stacking of the layers in these structures led to bicontinuous electron donor-acceptor ordering: upon light irradiation hole charge transfer is conducted through the one dimensional stacking of TP moieties whereas electron conduction is ensured by the eclipsed packing of the acceptor units. For instance, in a study reported by Jiang and co-workers, a boronic ester COF is reported using a benzothiadiazole boronic acid as electron acceptor.¹⁰⁵ This structure provided large photocurrents with hole and electron mobilities of 0.01 and 0.04 cm² V⁻¹ s⁻¹ respectively. This same principle was used by Bein and co-workers in a TP-porphyrin based COF as donor –acceptor system (Figure 1.20b and 1.20c). Highly oriented thin film of the COF was incorporated in a photovoltaic device, reaching open-circuit voltages of 312 meV.¹¹⁶ Worth-to-mention, external doping agents as fullerene derivatives can be used as an acceptor when hosted in the one-dimensional pores of the electron donor COF (Figure 1.20a).¹¹⁸ Nonetheless, such heterojunctions can limit the charge separation and mobility and hence the photovoltaics performance.

Large *in-plane* conjugation of TP-based COFs may also allow the generation of photocurrents. A clear example is the previously introduced phenazine-fused CS-COF structure seen in Figure 1.20d and 1.20e. The extended π -conjugated system showcased large hole photocurrent mobility (4.2 cm²V⁻¹s⁻¹).³¹ However, faster photoconductive kinetics were obtained by hosting C₆₀ fullerenes molecules in the pores of CS-COF as a donor-acceptor system as happening for the previously described structures. Further, the CS-COF $\text{\textcircled{C}}_{60}$ system

was successfully integrated into functional photoswitches and photovoltaic cells. Similarly, previously introduced C2P-5 thin films showcased intrinsic large hole mobility resulting into conductivities of 1.75 S cm^{-1} .¹⁰⁹ This conductivity is significantly increased upon irradiation with light especially after hybridization of the C2P-5 films with graphene. Larger photocurrents were recorded when applying larger powder light sources. Thus, the hybrid device proved to be a suitable photodetector for UV, visible and NIR light.

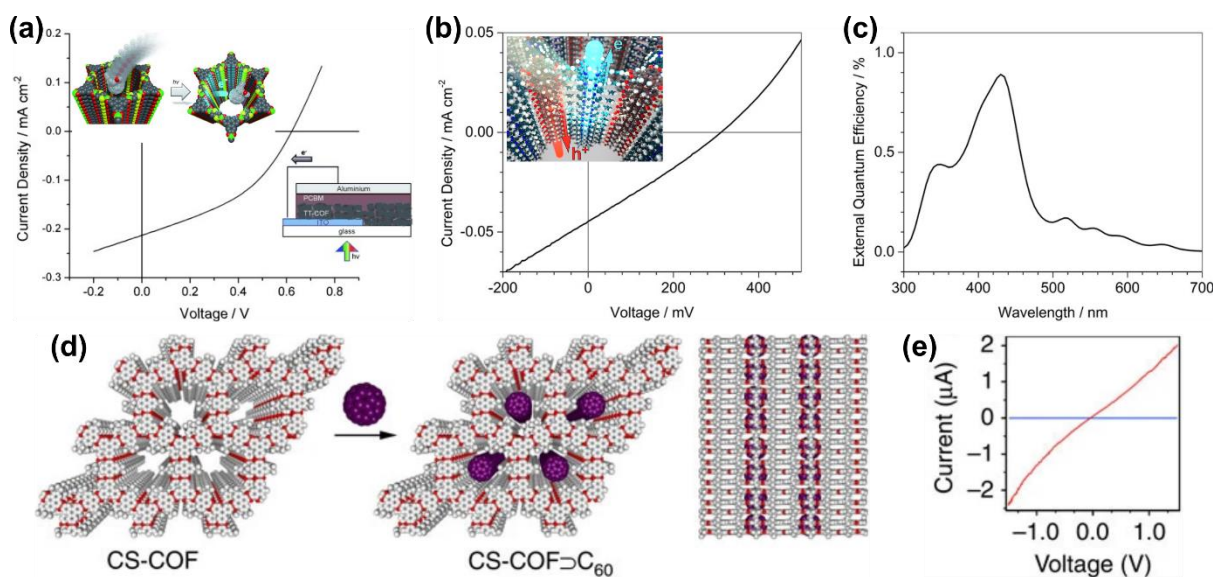


Figure 1.20: (a) I–V characteristics of a fullerene-doped thiophene-based TP COF (TT-COF) photovoltaic cell measured under illumination with simulated solar light. Insets: Schematic of the host-guest interaction between the TT-COF and the fullerene derivative (left) and schematic of the photovoltaic device (right). Images adapted from ref. 118. (b) I–V characteristics under irradiation of a porphyrin-based TP COF acting as a donor-acceptor system. Inset: Schematic of electron and hole charge transfer along the one-dimensional conduction paths defined by the TP and porphyrin moieties. (c) External quantum efficiency of the porphyrin-TP COF. Images adapted from ref. 116. (d) Schematic representation of CS-COF and its doping with fullerenes upon host-guest interactions in the open one-dimensional porous channels of the CS-COF (white: C; red: N; purple: fullerene). (e) I–V measurements of the fullerene-doped CS-COF in the dark (blue) and under irradiation (red). Images extracted from ref. 31.

Li-ion battery

As a result of the large conjugation and porosity, the phenazine-fuse COF shown in Figure 1.20a showcased large proton conduction, enhanced in aqueous and acidic media making it suitable for inclusion in a battery cell.¹⁰⁶ Performance of this material as anode in Li-ion batteries was also studied by Shi and co-workers achieving high reversible capacities of $701 \text{ mA} \cdot \text{h} \cdot \text{g}^{-1}$ and long cycling performance (4500 cycles).¹¹⁹ Other conjugated graphitic structures as TP-GDY can be considered as suitable candidates for working anodes in Li-ion

batteries. Due to lower electronic conductivity of TP-GDY, hybridization of the structure with CNTs through π - π stacking was performed obtaining free-standing films.⁵⁶ The films exhibited good electrochemical properties as reversible capacity of 1624 mA·h·g⁻¹, good rate performance and recyclability, and were incorporated as the anode of a lithium battery. Ester-boronate COFs are rarely used in electronic applications such as this one as the boron ester bond breaks the conjugation along the 2D layer. However, one may reach these properties by external doping.^{42,43,120} In a recent study, differently charged 2D-COF (COF-5 among them) were doped with low molecular weight polyethylene glycol (PEG) by including it into the 1D channels.¹²⁰ Interestingly, PEG significantly enhanced the Li⁺ ion conduction along the pores of COF due to the large donor number in the PEG structure.

Electrocatalysis

Another interesting electronic application of nitrogen-doped COF are as electrocatalysts. In a work reported by Zhang and co-workers, phenazine-fused COF shown in 1.20 is used as ORR catalyst.⁹² DFT calculations proved that the large nitrogen density, crystallinity and stability of the material display high availability of electrocatalytic sites. Consequently, low overpotentials of 349 mV at 10 mA cm⁻² and Tafel slopes of 64 mV dec⁻¹ were obtained. Notoriously, the same nitrogen-doped COF has been applied in composite core-shell structures covering Fe/Fe₃C nanoparticles to improve the long-term stability and performance.¹⁰⁷ Worth-to-mention, the composite showcased a good electrocatalytic behavior along with retention of 92% of the initial current after 10000 chronoamperometric cycles.

1.5. Future perspectives

There is no doubt that MOFs, and to a lesser extent COFs, based on ligands of the TP family have opened a whole new world of exploration as regards the conductivity of molecular materials. In a relatively few years, there has been a blossoming of research with very promising results. Proof of this are the numerous examples described above and the different fields of application where these materials are finding their niche. TP structures could be ideal candidates not only because of their electronic properties but also because of their porosity. For instance, benzene ligands provide conductivities within the same range or even larger than TP ligands due to their larger density of ligands and metals within the

structure. However, they showcase very small porosity or inexistent, which hindered the use of these structures in applications such as chemiresistor. Nonetheless, despite the potential of TP structures variability of reported structures is still limited. Rational design has enabled large π -conjugation along the 2D layers and interlayer π - π interactions enabling charge transport pathways, but chemical ligand design is still in its infancy. We have here reported novel structures using novel TP substitutions (as for example selenol) or ligand combinations but novel extended ligands containing TP or TP derivative moieties are also arising for both MOF and COF structures,^{121–124} pointing to an exciting route to explore.

Even more interesting is the fact that most of the conductivities found for these materials are on polycrystalline systems that are far from being optimal in terms of conductivity. Indeed, polycrystalline samples are formed by several finite crystalline domains exhibiting grain boundaries. These boundaries and small domains disrupt carrier paths or charges transfers affecting the conductive properties and can even mislead to unexpected properties as for instance opening a band gap in otherwise metallic materials. On the contrary, a single crystal is a continuous and defect-free (aside monomer vacancies) structure formed by the infinite repetition of a unit cell, so the conductive properties are more closely related to the intrinsic properties of the material. Hence, single crystals are commonly aimed for the study of anisotropic properties as for instance the *in-plane* and *out-of-plane* contributions. Some examples have been reported in the last years specially in the case of TP 2D MOFs. In these, measurements of rod-like or plate-like single crystals have allowed to assess the correlation of the anisotropy of conductivity with the crystalline structure. However, deeper insights on this correlation are needed as only anisotropy of two structures have been reported in single crystal up to our knowledge.

In fact, the ultimate measure would be on a single-layer as the thickness plays a key role in the appearance of quantum confinement effects and interlayer interactions. This has already been seen in other 2D materials as for instance transition metal dichalcogenides: the band gap of MoS₂ can be tuned from 1.23 eV in the bulk form to 1.8 eV in the monolayer.¹²⁵ The obtaining of a single layer has been faced using top-down methodologies, mainly the exfoliation of a single crystal, an approach that has already been successfully used for the delamination of 2D coordination polymers.^{126–128} However, this requires the growth of

crystals large enough which is not always an easy task. Thus, some few examples on exfoliation of TP 2D COFs¹²⁹ can be found whereas it is not the case of TP 2D MOFs. Otherwise, bottom-up techniques represent an alternative that attracts more interest every day. Among them, two main methods: interfacial liquid synthesis⁵³ and UHV evaporation, the latter being more suitable to obtain monolayers as the deposition rate allows for the specific control. The reported studies of the UHV formation of TP 2D MOFs and COFs have demonstrated the relevance of several key parameters as the deposition order or stoichiometry between the evaporated monomers.^{130–132} However, despite the numerous studies, nanodomains have been obtained only, leading to a finite polymeric array that may be subjected to in-plane quantum confinement.¹³¹ Thus the extracted properties may differ from the ones obtained in an infinite layer. In future, long range single layers should be obtained and deeply studied.

Advantages of single crystals prevail for fundamental studies while in terms of applications polycrystalline materials are so far postulated due to the geometrical restrictions to adapt a crystal to a specific device. So, development of methodologies that allow for the controlled deposition of the polycrystalline material on substrates to achieve homogenous and flat interfaces that avoid charge entrapment have been pursued. Pressing the powder into pellets can provide less rough surfaces and easily manageable systems is one of the most used ones. However, application of high pressures can induce a crystalline phase transition, crystal breaking or to occluded porous. As an alternative to post-synthetic treatment, direct growth of the polycrystalline material on supported thin films has been proposed. This approach can lead to thin films with preferential crystalline orientations that minimize grain boundaries and energetic defects while defining the parallel arrangement of the one-dimensional porous, charge conduction channels and orbitals leading to enhanced performances in applications such as photovoltaics^{30,46} or spin-valves⁵⁰. Unfortunately, most of current synthetic methods are characterized by sub-millimeter lateral sizes or randomly oriented thin films. Few examples of oriented TP 2D MOF/COF thin films (mostly limited to HHTP) have been reported, using layer-by-layer⁴⁷ or interfacial approaches⁵¹ (as Langmuir-Blodgett or Vapor-Assisted Conversion). Therefore, development of novel synthetic methods of highly oriented thin film morphologies is urgently required. This would include the need to incorporate different compatible substrates aimed at each specific target application. For instance, optically transparent or insulating substrates are typically needed for optoelectronic devices

whereas flexible or wearable electronics are more suitable for biological applications. Hence, synthesis protocols need to be compatible with a wide variety of substrates, being the ideal situation the obtaining of flexible free-standing thin-films that can be easily manipulated even in the absence of a support substrate, which has been only achieved in one occasion up to our knowledge.⁷⁰

In addition to all of the above, there are two other relevant areas that deserve further studies. The first one is to improve the stability in water. 2D materials are finding a wide resonance in the field of bioapplications due as a substitute for already used biomaterials but above all because of the new perspectives that they have opened. However, the poor stability of TP MOFs in water arising from the decrease of conductivity (due to swelling effect of water) and possible redox activity of both ligand and metal has prevented their use in this area. TP COF structures may have more impact as more they are more stable in water and exhibit proton conductivities in aqueous conditions. But still the conductive properties are not as developed as they are for MOFs so bioelectronic applications of TP COFs remain at earlier stage of development (being the need of doping and lack of intrinsic charge carrier conduction the main limitation in COF) and further exploration is required to improve the stability of MOFs in water and/or the conductivity of COFs. And the second one is the study in more detail of their magnetic properties. Indeed, TP 2D MOFs are formed by Kagomé lattice structures where metallic ions are coordinated in trinuclear arrangements.^{50,92,93} Hence, TP 2D MOFs structures can be candidates for geometrically frustrated spin systems. Nonetheless, the intrinsic and in depth study of the magnetic properties is still unexplored. So far, a few examples of Cu-based MOFs have been studied with this aim and successfully implemented in spin valves but no detailed studies to understand, and if possible to control, the magnetic properties of these materials with the proper choice of ligands and metals, and its interaction with the conductive properties have been reported. Therefore we can anticipate an important deal of investigation in this area over the years to come.

1.6 Tables

Table 1.1: Conductivities of HHTP based MOFs

MOF	Measuring technique	Conditions	Conductivity ($S\ cm^{-1}$)	Orientation	Ref
Ni₉(HHTP)₄	Single crystal (4-probe)	Vacuum	0.4	<i>ab</i> -axis	57
	Single crystal (2-probe)	Vacuum	$1 \cdot 10^{-4}$	<i>c</i> -axis	57
	Thin film (vdP)	-	$1.1 \cdot 10^{-3}$	<i>ab</i> -axis	48
	Pellet (4-probe)	Vacuum	$3.6 \cdot 10^{-3}$	Random	57
	Pellet (4-probe)	-	$1 \cdot 10^{-1}$	Random	32
	Pellet (4-probe)	-	$1 \cdot 10^{-2}$	Random	37
	Pellet (4-probe)	-	0.26	Random	85
	Pellet (2-probe)	-	$6.0 \cdot 10^{-3}$	Random	88
	Pellet (vdP)	-	$6.8 \cdot 10^{-3}$	Random	48
Cu₃(HHTP)₂	Single crystal (4-probe)	Vacuum	0.2	<i>c</i> -axis	62
	Single crystal (4-probe)	Vacuum	1.5	<i>ab</i> -axis	24
	Single crystal (2-probe)	Vacuum	0.5	<i>c</i> -axis	24
	Film (4-probe)	Vacuum	0.29	<i>ab</i> -axis	50
	Film (4-probe)	Vacuum	10^{-4}	<i>ab</i> -axis	51
	Film (4-probe)	Argon	$2.3 \cdot 10^{-2}$	<i>ab</i> -axis	23
	Film (2-probe)	-	$2 \cdot 10^{-2}$	<i>ab</i> -axis	47
	Pellet (4-probe)	Argon	$4.5 \cdot 10^{-2}$	Random	23
	Pellet (4-probe)	-	$2.0 \cdot 10^{-2}$	Random	32
	Pellet (4-probe)	-	$7.6 \cdot 10^{-3}$	Random	37
	Pellet (4-probe)	-	$8.0 \cdot 10^{-3}$	Random	93
	Pellet (2-probe)	-	$1.0 \cdot 10^{-2}$	Random	82
	Pellet (2-probe)	-	$3.0 \cdot 10^{-3}$	Random	36
	Pellet (vdP)	-	$2.7 \cdot 10^{-2}$	Random	48
	Pellet (vdP)	-	$3.2 \cdot 10^{-2}$	Random	48
Co₉(HHTP)₄	Thin film (vdP)	-	$3.3 \cdot 10^{-3}$	<i>ab</i> -axis	48
	Pellet (vdP)	-	$3.2 \cdot 10^{-2}$	Random	48
	Pellet (4-probe)	-	$2.7 \cdot 10^{-6}$	Random	32
	Pellet (2-probe)	-	$2.0 \cdot 10^{-3}$	Random	88
Fe₃(HHTP)₂	Pellet (4-probe)	Amorphous	$3.0 \cdot 10^{-3}$	Random	32
Zn₃(HHTP)₂	Pellet (4-probe)	Amorphous	$5.7 \cdot 10^{-6}$	Random	93

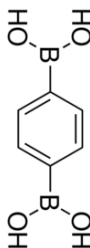
Table 1.2: Conductivities of HATP based MOFs

MOF	Measuring technique	Conditions	Conductivity (S cm ⁻¹)	Orientation	Ref
Ni₃(HITP)₂	Single crystal (4-probe)	Vacuum	150	<i>c</i> -axis	24
	Film (Lock-in)	Ambient	39.7	<i>ab</i> -axis	
	Film (Lock-in)	Ambient	$7.5 \cdot 10^{-4}$	<i>c</i> -axis	
	Film (vdP)	Vacuum	40	Random	34
	Film (-)	-	37.2	Random	84
	Film (2-probe)	-	$8.5 \cdot 10^{-3}$ - 0.23	Random	54
	Pellet (vdP)	Vacuum	50	Random	81
	Pellet (vdP)	Vacuum and previous annealing	58.8	Random	95
	Pellet (4-probe)	Ambient	55.4	Random	22
	Pellet (4-probe)	-	39	Random	85
	Pellet (4-probe)	Ambient	1.896	Random	133
	Pellet (4-probe)	-	1	Random	96
	Pellet (2-probe)	Vacuum	2	Random	34
	Pellet (2-probe)	Ambient	0.2	Random	66
	Pellet (4-probe)	Ambient	0.75	Random	22
Co₃(HITP)₂	Pellet (4-probe)	Ambient	$8 \cdot 10^{-4}$	Random	133
	Pellet (4-probe)	Ambient	0.024	Random	22

Table 1.3: Conductivities of THT based MOFs

MOF	Measuring technique	Conditions	Conductivity (S cm ⁻¹)	Orientation	Ref
Ni₃(THT)₂	Pellet (-)	-	$3.6 \cdot 10^{-4}$	Random	71
Cu₃(THT)₂	Pellet(-)	-	$2.4 \cdot 10^{-8}$	Random	71
Co₃(THT)₂	Film (vdP)	-	$3.2 \cdot 10^{-2}$	Random	69
	Pellet (vdP)	-	$1.4 \cdot 10^{-3}$	Random	69
	Pellet (-)	-	$2.4 \cdot 10^{-9}$	Random	71
Fe₃(THT)₂	Film (vdP)	Vacuum	$3.4 \cdot 10^{-2}$	Random	70
	Film (vdP)	Vacuum	0.2	Random	72
Pt₃(THT)₂	Pellet (2-probe)	-	$3.86 \cdot 10^{-4}$	Random	68

Table 1.4: Described boronic COFs

COF /Boronic acid used	Form	Synthesis method	Pore size (Å)	BET Surface area (m ² /g)	Properties and application	Ref
COF-5 	Powder	Solvothermal	27	1590	Porosity and H ₂ uptake	25,134
	Powder	Solvothermal	-	1990	H ₂ , CH ₄ , CO ₂ uptake	98
	Powder	Solvothermal	-	2000	Shorter reaction times	27
	Powder	Solvothermal	-	1517	-	135
	Powder	Solvothermal	2.274-1.248	1421-36	Inclusion of BDBA with side azide groups at different percentages and different functionalization with click-chemistry. Tunable porosity	136
	Powder	Solvothermal	27	1670	Mechanistic studies of synthesis with Lewis acid mediation	137
	Powder	Solvothermal	-	-	Growth kinetic study in homogenous reaction	138
	Powder and oriented pressed pellets	Solvothermal and high pressure pelletization	-	-	Li-Ion battery	139
	Powder	Microwaved assisted synthesis	-	2019-2027	Shorter reaction times	140

Powder	Microwaved assisted synthesis	-	1200	Addition of a modulator at different percentages to control growth	141
Powder	Sonochemistry	-	-	Starting material for B-doped molten salt synthesis	142
Powder	Sonochemistry	-	-	Stability of in different pyridine percentages	143
Powder and supported thin film	Sonochemistry with substrate imbedded in solution	-	2122	Shorter reaction times	26
Powder and free-standing thin film	Solvothermal and solvent evaporation for thin film	-	840 (Thin film)	Change of synthetic conditions for colloidal suspension	144
Supported thin film	Vapor-assisted conversion	27	-	Preferential orientation, control of thickness and different substrates	49
COF coating of CNTs and graphene	Sonochemistry with substrate imbedded in solution	-	57.6/9.83	Large CO2 uptake	43
COF coating on polydopamine coated glass	Solvothermal	-	-	Capillar for electrochromatography of small molecules	44
COF coating on CNTs	Solvothermal with substrate imbedded in solution	-	-	Li-Ion battery	42
Supported monolayer	UHV evaporation	29.8	-	-	145

COF-10	Powder	Solvothermal	34.1	2080	Porosity	97
	Powder	Solvothermal	32	1320	Mechanistic studies of synthesis with Lewis acid mediation	137
	Powder	Solvothermal	34	1200	Ammonia uptake	146
	Powder	Sonochemistry	-	-	Stability of in different pyridine percentages	143
	Powder	Solvothermal	-	2080	H ₂ , CH ₄ , CO ₂ uptake	98
	Powder	Solvothermal	-	-	Growth kinetic study in homogenous reaction	138
	Powder	Solvothermal	-	-	Change of synthetic conditions for colloidal suspension	144
	Supported monolayer	Solvothermal with substrate imbedded in solution	-	-	-	131
COF-6	Powder	Solvothermal	6.4	980	Porosity	97
	Powder	Solvothermal	-	960	H ₂ , CH ₄ , CO ₂ uptake	98
COF-8	Powder	Solvothermal	18.7	1400	Porosity	97
	Powder	Solvothermal	-	1400	H ₂ , CH ₄ , CO ₂ uptake	98

	Nanosheets	Liquid phase exfoliation of powder assisted by sonication	17	-	Nanostructuration	129
TP-COF	Powder	Solvothermal	32	868	Porosity, Fluorescence and Conductivity	112
	Powder	Solvothermal	-	-	Growth kinetic study in homogenous reaction	138
	Powder	Solvothermal	-	-	Change of synthetic conditions for colloidal suspension	144
	Supported thin film	Solvothermal with substrate imbedded	32	-	Photoemission	41
BDT-COF	Powder	Solvothermal	25.7	904	Compared to other tiophene based COFs and doping with oxidizing agents	104
	Powder	Solvothermal	29 with ethoxys	1844 with ethoxys	Partial or full substitution with side ethoxy groups for pore modification. Growth studies.	147
	Powder	Solvothermal	-	1125 (S) 1056 (Se) 302-352 (Te)	Substitution of sulfur for other chalcogenides with changing conductivities	148
	Powder and thin film	Solvothermal and spin- coating for film	30	1810	Photovoltaics: Adsorption of fullerenes as host- guest for photoluminescent quenching	118
	Powder and oriented thin films	Vapor-assisted conversion	32	1946 (powder) 175-145 cm ² /cm ² (thin films)	Photovoltaics: Adsorption of fullerenes as host- guest for photoluminescent quenching	46
	Powder and supported thin film	Solvothermal with substrate imbedded	-	1376 (powder)	Both randomly and oriented films. Photoconductivity: Faster response in oriented.	30

	Oriented thin films	Vapor-assisted conversion	32	-	Conductivity anisotropy measurements and hole photoconductivity	149
	Thin film	Vapor-assisted conversion	32	990	Preferential orientation, control of thickness and different substrates	49
HHTP-DBP-COF	Powder	Solvothermal	-	2400	Growth kinetic study in homogenous reaction	138
	Powder	Solvothermal	-	-	Change of synthetic conditions for colloidal suspension	144
Azo-COF	Powder	Solvothermal	30	810	Isomerization with UV radiation with retention of porosity and structure	150
	Supported monolayer	UHV evaporation	36	-	-	130
2D D-A COF	Powder and supported thin film	Solvothermal with substrate imbedded	28	2021	Photoconductivity	105
Dione-COF	Powder	Solvothermal	32	1510	Large interlayer interaction with antiparallel building blocks	151
HHTP-DBP COF	Powder and supported thin film	Solvothermal with substrate imbedded	47	2640	Large porosity, oriented films and blue emission	111
DTP-A_{NDI}-COF	Powder and coating of CNTs	Solvothermal with presence CNTs	50.6	1583 (powder) 676 (CNT)	Li-ion battery	152
DTP-A_{NDI}-COF	Powder	Solvothermal	53	1504	Photoluminescence kinetic study	117
DTP-A_{PyrDI}-COF			53	1910		
TDB (1)	Powder	Solvothermal	20.6 (1)	972	Control on the phase by presence of water.	104

TDB (2)			13.8 (2)	562	Conductivity study by doping with oxidizing agents	
BTDB (3)			32.4 (3)	544		
T-COF-OH	Powder	Solvothermal	41	2000 560 (post-functionalization)	Post-synthesis chemical modification with fluorescein	153
Porphyrin	Powder and supported thin film	Solvothermal with substrate imbedded	46	8.9	Photovoltaics	116
Combination of different acids	Powder	Solvothermal	-	-	Multifunctional COFs	154

1.7. References

1. D. Sonet, B. Bibal, *Tetrahedron Lett.* **2019**, 60, 872.
2. S. Ibáñez, E. Peris, *Angew. Chemie - Int. Ed.* **2019**, 58, 6693.
3. G. Cong, W. Wang, N. C. Lai, Z. Liang, Y. C. Lu, *Nat. Mater.* **2019**, 18, 390.
4. S. Kumar, *NPG Asia Mater.* **2014**, 6, e82.
5. F. J. M. Hoeben, P. Jonkhøj, E. W. Meijer, A. P. H. J. Schenning, *Chem. Rev.* **2005**, 105, 1491.
6. S. Laschat, A. Baro, N. Steinke, F. Giesselmann, C. Hägele, G. Scalia, R. Judele, E. Kapatsina, S. Sauer, A. Schreivogel, M. Tosoni, *Angew. Chemie - Int. Ed.* **2007**, 46, 4832.
7. T. Wöhrle, I. Wurzbach, J. Kirres, A. Kostidou, N. Kapernaum, J. Litterscheidt, J. C. Haenle, P. Staffeld, A. Baro, F. Giesselmann, S. Laschat, *Chem. Rev.* **2016**, 116, 1139.
8. K. Nakashima, T. Shimizu, Y. Kamakura, A. Hinokimoto, Y. Kitagawa, H. Yoshikawa, D. Tanaka, *Chem. Sci.* **2020**, 11, 37.
9. Y.-F. Zhu, X.-L. Guan, Z. Shen, X.-H. Fan, Q.-F. Zhou, *Macromolecules* **2012**, 45, 3346.
10. H. N. Gayathri, B. Kumar, K. A. Suresh, H. K. Bisoyi, S. Kumar, *Phys. Chem. Chem. Phys.* **2016**, 18, 12101.
11. M. Saleh, M. Baumgarten, A. Mavrinskiy, T. Schäfer, K. Müllen, *Macromolecules* **2010**, 43, 137.
12. W. Zheng, C. S. Tsang, L. Y. S. Lee, K. Y. Wong, *Mater. Today Chem.* **2019**, 12, 34.
13. H. C. Zhou, J. R. Long, O. M. Yaghi, *Chem. Rev.* **2012**, 112, 673.
14. M. S. Lohse, T. Bein, *Adv. Funct. Mater.* **2018**, 28, 1705553.
15. J. L. Segura, M. J. Mancheño, F. Zamora, *Chem. Soc. Rev.* **2016**, 45, 5635.
16. G. Givaja, P. Amo-Ochoa, C. J. Gómez-García, F. F. Zamora, C. J. Gomez-Garcia, F. F. Zamora, *Chem. Soc. Rev.* **2012**, 41, 115.
17. R. Mas-Ballesté, C. Gómez-Navarro, J. Gómez-Herrero, F. Zamora, *Nanoscale* **2011**, 3, 20.
18. L. S. Xie, G. Skorupskii, M. Dincă, *Chem. Rev.* **2020**, 120, 8536.
19. M. Wang, R. Dong, X. Feng, *Chem. Soc. Rev.* **2021**, 50, 2764.
20. X. Zhuang, Y. Mai, D. Wu, F. Zhang, X. Feng, *Adv. Mater.* **2015**, 27, 403.
21. M. Ko, L. Mendecki, K. A. Mirica, *Chem. Commun.* **2018**, 54, 7873.
22. A. P. Côté, A. I. Benin, N. W. Ockwig, M. O'Keeffe, A. J. Matzger, O. M. Yaghi, *Science* **2005**, 310, 1166.
23. R. W. Day, D. K. Bediako, M. Rezaee, L. R. Parent, G. Skorupskii, M. Q. Arguilla, C. H. Hendon, I. Stassen, N. C. Gianneschi, P. Kim, M. Dincă, *ACS Cent. Sci.* **2019**, 5, 1959.
24. T. Chen, J.-H. Dou, L. Yang, C. Sun, N. J. Libretto, G. Skorupskii, J. T. Miller, M. Dincă, *J. Am. Chem. Soc.* **2020**, 142, 12367.
25. B. Hoppe, K. D. J. Hindricks, D. P. Warwas, H. A. Schulze, A. Mohmeyer, T. J. Pinkvos, S. Zailskas, M. R. Krey, C. Belke, S. König, M. Fröba, R. J. Haug, P. Behrens, *CrystEngComm* **2018**, 20, 6458.
26. S. T. Yang, J. Kim, H. Y. Cho, S. Kim, W. S. Ahn, *RSC Adv.* **2012**, 2, 10179.
27. B. J. Smith, W. R. Dichtel, *J. Am. Chem. Soc.* **2014**, 136, 8783.
28. L. Mendecki, K. A. Mirica, *ACS Appl. Mater. Interfaces* **2018**, 10, 19248.
29. M. Ko, L. Mendecki, A. M. Eagleton, C. G. Durbin, R. M. Stolz, Z. Meng, K. A. Mirica, *J. Am. Chem. Soc.* **2020**, 142, 11717.
30. Y. Chen, H. Cui, J. Zhang, K. Zhao, D. Ding, J. Guo, L. Li, Z. Tian, Z. Tang, *RSC Adv.* **2015**, 5, 92573.
31. J. Guo, Y. Xu, S. Jin, L. Chen, T. Kaji, Y. Honsho, M. A. Addicoat, J. Kim, A. Saeki, H. Ihee, S. Seki, S. Irle, M. Hiramoto, J. Gao, D. Jiang, *Nat. Commun.* **2013**, 4, 2736.
32. M. Ko, A. Aykanat, M. K. Smith, K. A. Mirica, *Sensors* **2017**, 17, 2192.
33. J. W. Colson, W. R. Dichtel, *Nat. Chem.* **2013**, 5, 453.
34. D. Sheberla, L. Sun, M. A. Blood-Forsythe, S. Er, C. R. Wade, C. K. Brozek, A. Aspuru-Guzik, M. Dincă, *J. Am. Chem. Soc.* **2014**, 136, 8859.
35. M. K. Smith, K. A. Mirica, *J. Am. Chem. Soc.* **2017**, 139, 16759.
36. W. H. Li, K. Ding, H. R. Tian, M. S. Yao, B. Nath, W. H. Deng, Y. Wang, G. Xu, *Adv. Funct. Mater.* **2017**, 27, 1.
37. M. K. Smith, K. E. Jensen, P. A. Pivak, K. A. Mirica, *Chem. Mater.* **2016**, 28, 5264.
38. Y. Yue, S. Y. Yang, Y. L. Huang, B. Sun, S. W. Bian, *Energy and Fuels* **2020**, 34, 16879.
39. K. Zhou, C. Zhang, Z. Xiong, H. Y. Chen, T. Li, G. Ding, B. Yang, Q. Liao, Y. Zhou, S. T. Han, *Adv. Funct. Mater.* **2020**, 30, 1.
40. Y. L. Li, J. J. Zhou, M. K. Wu, C. Chen, K. Tao, F. Y. Yi, L. Han, *Inorg. Chem.* **2018**, 57, 6202.
41. J. W. Colson, A. R. Woll, A. Mukherjee, M. P. Levendoff, E. L. Spitler, V. B. Shields, M. G. Spencer, J. Park, W. R. Dichtel, *Science* **2011**, 332, 228.
42. J. Yoo, S.-J. Cho, G. Y. Jung, S. H. Kim, K.-H. Choi, J.-H. Kim, C. K. Lee, S. K. Kwak, S.-Y. Lee, *Nano Lett.* **2016**, 16, 3292.

43. J. T. Yoo, S. H. Lee, S. Hirata, C. R. Kim, C. K. Lee, T. Shiraki, N. Nakashima, J. K. Shim, *Chem. Lett.* **2015**, 44, 560.
44. T. Bao, P. Tang, D. Kong, Z. Mao, Z. Chen, *J. Chromatogr. A* **2016**, 1445, 140.
45. A. M. Evans, A. Giri, V. K. Sangwan, S. Xun, M. Bartnof, C. G. Torres-Castanedo, H. B. Balch, M. S. Rahn, N. P. Bradshaw, E. Vitaku, D. W. Burke, H. Li, M. J. Bedzyk, F. Wang, J.-L. Brédas, J. A. Malen, A. J. H. McGaughey, M. C. Hersam, W. R. Dichtel, P. E. Hopkins, *Nat. Mater.* **2021**, DOI 10.1038/s41563-021-00934-3.
46. D. D. Medina, V. Werner, F. Auras, R. Tautz, M. Dogru, J. Schuster, S. Linke, M. Döblinger, J. Feldmann, P. Knochel, T. Bein, *ACS Nano* **2014**, 8, 4042.
47. M.-S. Yao, X.-J. Lv, Z.-H. Fu, W.-H. Li, W.-H. Deng, G.-D. Wu, G. Xu, *Angew. Chemie* **2017**, 129, 16737.
48. A. Mahringer, A. C. Jakowetz, J. M. Rotter, B. J. Bohn, J. K. Stolarczyk, J. Feldmann, T. Bein, D. D. Medina, A. Mähringer, A. C. Jakowetz, J. M. Rotter, B. J. Bohn, J. K. Stolarczyk, J. Feldmann, T. Bein, D. D. Medina, *ACS Nano* **2019**, 13, 6711.
49. D. D. Medina, J. M. Rotter, Y. Hu, M. Dogru, V. Werner, F. Auras, J. T. Markiewicz, P. Knochel, T. Bein, *J. Am. Chem. Soc.* **2015**, 137, 1016.
50. X. Song, X. Wang, Y. Li, C. Zheng, B. Zhang, C. Di, F. Li, C. Jin, W. Mi, L. Chen, W. Hu, *Angew. Chemie* **2020**, 132, 1134.
51. V. Rubio-Giménez, M. Galbiati, J. Castells-Gil, N. Almora-Barrios, J. Navarro-Sánchez, G. Escorcia-Ariza, M. Mattera, T. Arnold, J. Rawle, S. Tatay, E. Coronado, C. Martí-Gastaldo, *Adv. Mater.* **2018**, 30, 1704291.
52. A. J. Clough, J. W. Yoo, M. H. Mecklenburg, S. C. Marinescu, *J. Am. Chem. Soc.* **2015**, 137, 118.
53. R. Dong, M. Pfeiffermann, H. Liang, Z. Zheng, X. Zhu, J. Zhang, X. Feng, *Angew. Chemie - Int. Ed.* **2015**, 54, 12058.
54. K. Yuan, T. Song, X. Zhu, B. Li, B. Han, L. Zheng, J. Li, X. Zhang, W. Hu, *Small* **2019**, 15, 1804845.
55. G. Wu, J. Huang, Y. Zang, J. He, G. Xu, *J. Am. Chem. Soc.* **2017**, 139, 1360.
56. X.-L. Ye, Y.-Q. Huang, X.-Y. Tang, J. Xu, C. Peng, Y.-Z. Tan, *J. Mater. Chem. A* **2019**, 7, 3066.
57. D.-G. Ha, M. Rezaee, Y. Han, S. A. Siddiqui, R. W. Day, L. S. Xie, B. J. Modtland, D. A. Muller, J. Kong, P. Kim, M. Dincă, M. A. Baldo, *ACS Cent. Sci.* **2021**, 7, 104.
58. Y. Liu, Y. Wei, M. Liu, Y. Bai, X. Wang, S. Shang, C. Du, W. Gao, J. Chen, Y. Liu, *Adv. Mater.* **2021**, 33, 2007741.
59. R. P. Bisbey, C. R. DeBlase, B. J. Smith, W. R. Dichtel, *J. Am. Chem. Soc.* **2016**, 138, 11433.
60. L. Sun, M. G. Campbell, M. Dincă, *Angew. Chemie Int. Ed.* **2016**, 55, 3566.
61. V. Rubio-Giménez, S. Tatay, C. Martí-Gastaldo, *Chem. Soc. Rev.* **2020**, 49, 5601.
62. M. Hmadeh, Z. Lu, Z. Liu, F. Gándara, H. Furukawa, S. Wan, V. Augustyn, R. Chang, L. Liao, F. Zhou, E. Perre, V. Ozolins, K. Suenaga, X. Duan, B. Dunn, Y. Yamamoto, O. Terasaki, O. M. Yaghi, *Chem. Mater.* **2012**, 24, 3511.
63. G. Skorupskii, B. A. Trump, T. W. Kasel, C. M. Brown, C. H. Hendon, M. Dincă, *Nat. Chem.* **2020**, 12, 131.
64. M. E. Foster, K. Sohlberg, M. D. Allendorf, A. A. Talin, *J. Phys. Chem. Lett.* **2018**, 9, 481.
65. M. E. Foster, K. Sohlberg, C. D. Spataru, M. D. Allendorf, *J. Phys. Chem. C* **2016**, 120, 15001.
66. M. G. Campbell, D. Sheberla, S. F. Liu, T. M. Swager, M. Dincă, *Angew. Chemie Int. Ed.* **2015**, 54, 4349.
67. S. Chen, J. Dai, X. C. Zeng, *Phys. Chem. Chem. Phys.* **2015**, 17, 5954.
68. J. Cui, Z. Xu, *Chem. Commun.* **2014**, 50, 3986.
69. A. J. Clough, J. M. Skelton, C. A. Downes, A. A. De La Rosa, J. W. Yoo, A. Walsh, B. C. Melot, S. C. Marinescu, *J. Am. Chem. Soc.* **2017**, 139, 10863.
70. R. Dong, P. Han, H. Arora, M. Ballabio, M. Karakus, Z. Zhang, C. Shekhar, P. Adler, P. S. Petkov, A. Erbe, S. C. B. Mannsfeld, C. Felser, T. Heine, M. Bonn, X. Feng, E. Cánovas, *Nat. Mater.* **2018**, 17, 1027.
71. L. Mendecki, M. Ko, X. Zhang, Z. Meng, K. A. Mirica, *J. Am. Chem. Soc.* **2017**, 139, 17229.
72. A. J. Clough, N. M. Orchanian, J. M. Skelton, A. J. Neer, S. A. Howard, C. A. Downes, L. F. J. Piper, A. Walsh, B. C. Melot, S. C. Marinescu, *J. Am. Chem. Soc.* **2019**, 141, 16323.
73. Q. Zhou, J. Wang, T. S. Chwee, G. Wu, X. Wang, Q. Ye, J. Xu, S. W. Yang, *Nanoscale* **2015**, 7, 727.
74. Y. He, C. D. Spataru, F. Léonard, R. E. Jones, M. E. Foster, M. D. Allendorf, A. Alec Talin, *Phys. Chem. Chem. Phys.* **2017**, 19, 19461.
75. R. Dong, Z. Zheng, D. C. Tranca, J. Zhang, N. Chandrasekhar, S. Liu, X. Zhuang, G. Seifert, X. Feng, *Chem. - A Eur. J.* **2017**, 23, 2255.
76. M. Yao, J. Zheng, A. Wu, G. Xu, S. S. Nagarkar, G. Zhang, M. Tsujimoto, S. Sakaki, S. Horike, K. Otake, S. Kitagawa, *Angew. Chemie* **2020**, 132, 178.

77. Y. Cui, J. Yan, Z. Chen, W. Xing, C. Ye, X. Li, Y. Zou, Y. Sun, C. Liu, W. Xu, D. Zhu, *iScience* **2020**, 23, 100812.
78. V. Rubio-Giménez, N. Almora-Barrios, G. Escorcía-Ariza, M. Galbiati, M. Sessolo, S. Tatay, C. Martí-Gastaldo, *Angew. Chemie Int. Ed.* **2018**, 57, 15086.
79. R. M. Stolz, A. Mahdavi-Shakib, B. G. Frederick, K. A. Mirica, *Chem. Mater.* **2020**, 32, 7639.
80. M. G. Campbell, S. F. Liu, T. M. Swager, M. Dincă, *J. Am. Chem. Soc.* **2015**, 137, 13780.
81. D. Sheberla, J. C. Bachman, J. S. Elias, C.-J. Sun, Y. Shao-Horn, M. Dincă, *Nat. Mater.* **2017**, 16, 220.
82. K. W. Nam, S. S. Park, R. dos Reis, V. P. Dravid, H. Kim, C. A. Mirkin, J. F. Stoddart, *Nat. Commun.* **2019**, 10, 1.
83. H. Wu, W. Zhang, S. Kandambeth, O. Shekhah, M. Eddaoudi, H. N. Alshareef, *Adv. Energy Mater.* **2019**, 9, 1900482.
84. Y. Zang, F. Pei, J. Huang, Z. Fu, G. Xu, X. Fang, *Adv. Energy Mater.* **2018**, 8, 1.
85. S. Zhou, X. Kong, B. Zheng, F. Huo, M. Strømme, C. Xu, *ACS Nano* **2019**, 13, 9578.
86. E. M. Miner, T. Fukushima, D. Sheberla, L. Sun, Y. Surendranath, M. Dincă, *Nat. Commun.* **2016**, 7, 10942.
87. Y. Tian, Z. Zhang, C. Wu, L. Yan, W. Chen, Z. Su, *Phys. Chem. Chem. Phys.* **2018**, 20, 1821.
88. E. M. Miner, L. Wang, M. Dincă, *Chem. Sci.* **2018**, 9, 6286.
89. W. H. Li, J. Lv, Q. Li, J. Xie, N. Ogiwara, Y. Huang, H. Jiang, H. Kitagawa, G. Xu, Y. Wang, *J. Mater. Chem. A* **2019**, 7, 10431.
90. Y. Tian, Y. Wang, L. Yan, J. Zhao, Z. Su, *Appl. Surf. Sci.* **2019**, 467, 98.
91. W. Zhu, C. Zhang, Q. Li, L. Xiong, R. Chen, X. Wan, Z. Wang, W. Chen, Z. Deng, Y. Peng, *Appl. Catal. B Environ.* **2018**, 238, 339.
92. L. Yang, X. He, M. Dincă, *J. Am. Chem. Soc.* **2019**, 141, 10475.
93. Y. Misumi, A. Yamaguchi, Z. Zhang, T. Matsushita, N. Wada, M. Tsuchiizu, K. Awaga, *J. Am. Chem. Soc.* **2020**, 142, 16513.
94. H. Arora, R. Dong, T. Venanzi, J. Zscharschuch, H. Schneider, M. Helm, X. Feng, E. Cánovas, A. Erbe, *Adv. Mater.* **2020**, 32, 1907063.
95. L. Sun, B. Liao, D. Sheberla, D. Kraemer, J. Zhou, E. A. Stach, D. Zakharov, V. Stavila, A. A. Talin, Y. Ge, M. D. Allendorf, G. Chen, F. Léonard, M. Dincă, *Joule* **2017**, 1, 168.
96. Y. Nonoguchi, D. Sato, T. Kawai, *Polymers* **2018**, 10, 962.
97. H. Furukawa, O. M. Yaghi, *J. Am. Chem. Soc.* **2009**, 131, 8875.
98. A. P. Côté, H. M. El-Kaderi, H. Furukawa, J. R. Hunt, O. M. Yaghi, *J. Am. Chem. Soc.* **2007**, 129, 12914.
99. X. Chen, M. Addicoat, E. Jin, H. Xu, T. Hayashi, F. Xu, N. Huang, S. Irle, D. Jiang, *Sci. Rep.* **2015**, 5, 14650.
100. Y. Zeng, R. Zou, Z. Luo, H. Zhang, X. Yao, X. Ma, R. Zou, Y. Zhao, *J. Am. Chem. Soc.* **2015**, 137, 1020.
101. X. Guan, H. Li, Y. Ma, M. Xue, Q. Fang, Y. Yan, V. Valtchev, S. Qiu, *Nat. Chem.* **2019**, 11, 587.
102. B. Zhang, M. Wei, H. Mao, X. Pei, S. A. Alshimmri, J. A. Reimer, O. M. Yaghi, *J. Am. Chem. Soc.* **2018**, 140, 12715.
103. W. Ji, Y. S. Guo, H. M. Xie, X. Wang, X. Jiang, D. S. Guo, *J. Hazard. Mater.* **2020**, 397, 122793.
104. G. H. V. Bertrand, V. K. Michaelis, T.-C. Ong, R. G. Griffin, M. Dincă, *Proc. Natl. Acad. Sci.* **2013**, 110, 4923.
105. X. Feng, L. Chen, Y. Honsho, O. Saengsawang, L. Liu, L. Wang, A. Saeki, S. Irle, S. Seki, Y. Dong, D. Jiang, *Adv. Mater.* **2012**, 24, 3026.
106. Z. Meng, A. Aykanat, K. A. Mirica, *Chem. Mater.* **2019**, 31, 819.
107. I. Ahmad, F. Li, C. Kim, J.-M. Seo, G. Kim, J. Mahmood, H. Y. Jeong, J.-B. Baek, *Nano Energy* **2019**, 56, 581.
108. Y. Ma, X. Liu, X. Guan, H. Li, Y. Yusran, M. Xue, Q. Fang, Y. Yan, S. Qiu, V. Valtchev, *Dalt. Trans.* **2019**, 48, 7352.
109. S. Jhulki, J. Kim, I.-C. Hwang, G. Haider, J. Park, J. Y. Park, Y. Lee, W. Hwang, A. A. Dar, B. Dhara, S. H. Lee, J. Kim, J. Y. Koo, M. H. Jo, C.-C. Hwang, Y. H. Jung, Y. Park, M. Kataria, Y.-F. Chen, S.-H. Jhi, M.-H. Baik, K. Baek, K. Kim, *Chem* **2020**, 6, 2035.
110. R. Matsuoka, R. Toyoda, R. Shiotsuki, N. Fukui, K. Wada, H. Maeda, R. Sakamoto, S. Sasaki, H. Masunaga, K. Nagashio, H. Nishihara, *ACS Appl. Mater. Interfaces* **2019**, 11, 2730.
111. E. L. Spitler, B. T. Koo, J. L. Novotney, J. W. Colson, F. J. Uribe-Romo, G. D. Gutierrez, P. Clancy, W. R. Dichtel, *J. Am. Chem. Soc.* **2011**, 133, 19416.
112. S. Wan, J. Guo, J. Kim, H. Ihee, D. Jiang, *Angew. Chemie Int. Ed.* **2008**, 47, 8826.
113. S. Wang, L. Ma, Q. Wang, P. Shao, D. Ma, S. Yuan, P. Lei, P. Li, X. Feng, B. Wang, *J. Mater. Chem. C* **2018**, 6, 5369.

114. A. M. Evans, L. R. Parent, N. C. Flanders, R. P. Bisbey, E. Vitaku, M. S. Kirschner, R. D. Schaller, L. X. Chen, N. C. Gianneschi, W. R. Dichtel, *Science* **2018**, *361*, 52.
115. N. C. Flanders, M. S. Kirschner, P. Kim, T. J. Fauvell, A. M. Evans, W. Helweh, A. P. Spencer, R. D. Schaller, W. R. Dichtel, L. X. Chen, *J. Am. Chem. Soc.* **2020**, *142*, 14957.
116. M. Calik, F. Auras, L. M. Salonen, K. Bader, I. Grill, M. Handloser, D. D. Medina, M. Dogru, F. Löbermann, D. Trauner, A. Hartschuh, T. Bein, *J. Am. Chem. Soc.* **2014**, *136*, 17802.
117. S. Jin, K. Furukawa, M. Addicoat, L. Chen, S. Takahashi, S. Irle, T. Nakamura, D. Jiang, *Chem. Sci.* **2013**, *4*, 4505.
118. M. Dogru, M. Handloser, F. Auras, T. Kunz, D. Medina, A. Hartschuh, P. Knochel, T. Bein, *Angew. Chemie Int. Ed.* **2013**, *52*, 2920.
119. L. Meng, S. Ren, C. Ma, Y. Yu, Y. Lou, D. Zhang, Z. Shi, *Chem. Commun.* **2019**, *55*, 9491.
120. Z. Guo, Y. Zhang, Y. Dong, J. Li, S. Li, P. Shao, X. Feng, B. Wang, *J. Am. Chem. Soc.* **2019**, *141*, 1923.
121. J.-H. Dou, M. Q. Arguilla, Y. Luo, J. Li, W. Zhang, L. Sun, J. L. Mancuso, L. Yang, T. Chen, L. R. Parent, G. Skorupskii, N. J. Libretto, C. Sun, M. C. Yang, P. V. Dip, E. J. Brignole, J. T. Miller, J. Kong, C. H. Hendon, J. Sun, M. Dincă, *Nat. Mater.* **2021**, *20*, 222.
122. R. Dong, X. Feng, *Nat. Mater.* **2021**, *20*, 122.
123. M. Yu, R. Dong, X. Feng, *J. Am. Chem. Soc.* **2020**, *142*, 12903.
124. Z. Meng, K. A. Mirica, *Nano Res.* **2021**, *14*, 369.
125. H. Zhang, *ACS Nano* **2015**, *9*, 9451.
126. N. Contreras-Pereda, P. Hayati, S. Suárez-García, L. Esrafil, P. Retailleau, S. Benmansour, F. Novio, A. Morsali, D. Ruiz-Molina, *Ultrason. Sonochem.* **2019**, *55*, 186.
127. N. Contreras-Pereda, F. Moghzi, J. Baselga, H. Zhong, J. Janczak, J. Soleimannejad, R. Dong, D. Ruiz-Molina, *Ultrason. Sonochem.* **2021**, *70*, 105292.
128. B. Pepió, N. Contreras-Pereda, S. Suárez-García, P. Hayati, S. Benmansour, P. Retailleau, A. Morsali, D. Ruiz-Molina, *Ultrason. Sonochem.* **2021**, *72*, 105425.
129. I. Berlanga, M. L. Ruiz-González, J. M. González-Calbet, J. L. G. Fierro, R. Mas-Ballesté, F. Zamora, *Small* **2011**, *7*, 1207.
130. C. Liu, Y. Yu, W. Zhang, Q. Zeng, S. Lei, *Chem. - A Eur. J.* **2016**, *22*, 18412.
131. L. Yu, Z. B. Li, D. Wang, *Chem. Commun.* **2016**, *52*, 13771.
132. M. Lischka, R. Dong, M. Wang, N. Martsinovich, M. Fritton, L. Grossmann, W. M. Heckl, X. Feng, M. Lackinger, *Chem. – A Eur. J.* **2019**, *25*, 1975.
133. Y. Lian, W. Yang, C. Zhang, H. Sun, Z. Deng, W. Xu, L. Song, Z. Ouyang, Z. Wang, J. Guo, Y. Peng, *Angew. Chemie Int. Ed.* **2020**, *59*, 286.
134. S. H. Sang, H. Furukawa, O. M. Yaghi, W. A. Goddard, *J. Am. Chem. Soc.* **2008**, *130*, 11580.
135. H. Yang, Y. Du, S. Wan, G. D. Trahan, Y. Jin, W. Zhang, *Chem. Sci.* **2015**, *6*, 4049.
136. A. Nagai, Z. Guo, X. Feng, S. Jin, X. Chen, X. Ding, D. Jiang, *Nat. Commun.* **2011**, *2*, 536.
137. E. L. Spitler, M. R. Giovino, S. L. White, W. R. Dichtel, *Chem. Sci.* **2011**, *2*, 1588.
138. B. J. Smith, N. Hwang, A. D. Chavez, J. L. Novotney, W. R. Dichtel, *Chem. Commun.* **2015**, *51*, 7532.
139. D. A. Vazquez-Molina, G. S. Mohammad-Pour, C. Lee, M. W. Logan, X. Duan, J. K. Harper, F. J. Uribe-Romo, *J. Am. Chem. Soc.* **2016**, *138*, 9767.
140. N. L. Campbell, R. Clowes, L. K. Ritchie, A. I. Cooper, *Chem. Mater.* **2009**, *21*, 204.
141. M. Calik, T. Sick, M. Dogru, M. Döblinger, S. Datz, H. Budde, A. Hartschuh, F. Auras, T. Bein, *J. Am. Chem. Soc.* **2016**, *138*, 1234.
142. Y. B. Huang, P. Pachfule, J. K. Sun, Q. Xu, *J. Mater. Chem. A* **2016**, *4*, 4273.
143. Y. Du, K. Mao, P. Kamakoti, B. Wooler, S. Cundy, Q. Li, P. Ravikovitch, D. Calabro, *J. Mater. Chem. A* **2013**, *1*, 13171.
144. B. J. Smith, L. R. Parent, A. C. Overholts, P. A. Beaucage, R. P. Bisbey, A. D. Chavez, N. Hwang, C. Park, A. M. Evans, N. C. Gianneschi, W. R. Dichtel, *ACS Cent. Sci.* **2017**, *3*, 58.
145. N. A. A. Zwaneveld, R. Pawlak, M. Abel, D. Catalin, D. Gimes, D. Bertin, L. Porte, *J. Am. Chem. Soc.* **2008**, *130*, 6678.
146. C. J. Doonan, D. J. Tranchemontagne, T. G. Glover, J. R. Hunt, O. M. Yaghi, *Nat. Chem.* **2010**, *2*, 235.
147. M. S. Lohse, J. M. Rotter, J. T. Margraf, V. Werner, M. Becker, S. Herbert, P. Knochel, T. Clark, T. Bein, D. D. Medina, *CrystEngComm* **2016**, *18*, 4295.
148. S. Duhović, M. Dincă, *Chem. Mater.* **2015**, *27*, 5487.
149. D. D. Medina, M. L. Petrus, A. N. Jumabekov, J. T. Margraf, S. Weinberger, J. M. Rotter, T. Clark, T. Bein, *ACS Nano* **2017**, *11*, 2706.
150. J. Zhang, L. Wang, N. Li, J. Liu, W. Zhang, Z. Zhang, N. Zhou, X. Zhu, *CrystEngComm* **2014**, *16*, 6547.
151. L. M. Salonen, D. D. Medina, E. Carbó-Argibay, M. G. Goesten, L. Mafra, N. Guldris, J. M. Rotter, D. G. Stroppa, C. Rodríguez-Abreu, *Chem. Commun.* **2016**, *52*, 7986.

- 152.** F. Xu, S. Jin, H. Zhong, D. Wu, X. Yang, X. Chen, H. Wei, R. Fu, D. Jiang, *Sci. Rep.* **2015**, *5*, 8225.
- 153.** S. Rager, M. Dogru, V. Werner, A. Gavryushin, M. Götz, H. Engelke, D. D. Medina, P. Knochel, T. Bein, *CrystEngComm* **2017**, *19*, 4886.
- 154.** N. Huang, L. Zhai, D. E. Coupry, M. A. Addicoat, K. Okushita, K. Nishimura, T. Heine, D. Jiang, *Nat. Commun.* **2016**, *7*, 12325.

Chapter 2:

Objectives

The main objective set for this thesis is the use of new synthetic approaches for the fabrication of TP-based thin films with enhanced conductive properties.

To achieve this main objective, the following specific objectives were set:

- i. Synthesis and characterization of TP 2D MOFs on surfaces using UHV conditions, both as a monolayer or dispersed microcrystals (studied for comparison purposes).
- ii. Synthesis and characterization of TP 2D MOFs crystalline thin films on surfaces under simulated microgravity environments using a microfluidic approach.
- iii. Study of the conductive properties of the resulting supported substrates.
- iv. Synthesis and characterization of TP-based melanin-inspired amorphous polymer free-standing thin films.
- v. Study of the conductive properties of the free-standing thin films under different conditions (atmospheric air, inert ambiance, humidity...) and study of potential applications.

To achieve this, the following sub-objectives were set:

- To optimize the synthesis and purification of $\text{HATP} \cdot 6\text{HCl}$ to ensure large monolayers and bulk crystals.
- Synthesis and characterization of $\text{Co}_3(\text{HITP})_2$ and $\text{Ni}_3(\text{HITP})_2$ in different environments (different solvents, turbulent flows, basic media...).
- Deposition of the synthesized crystals in UHV using novel techniques.
- To control the crystallization of $\text{Ni}_3(\text{HITP})_2$.
- To establish a synthetic procedure for free-standing thin films, optimizing the starting reagents and approach.
- To evaluate the potential bioelectronic application of free-standing films as wearable on-skin devices.

Chapter 3:

Monolayers on surfaces

In the following chapter, protocols on the synthesis of **HATP·6HCl** and derived cobalt-based MOFs are studied aiming for a large degree of purity. Use of large reagent stoichiometry and the use of alumina as static phase during purification process are introduced as modifications on the reported protocol for **HATP·6HCl**. The large purity of the organic ligand allowed to obtain high quality **Co₃(HITP)₂** structures in bulk and supported monolayers obtained by solvothermal and ultra-high vacuum (UHV) techniques respectively. Further deposition of bulk structures on surfaces with UHV technique Atomic Layer Injection was optimized for the future study and comparison of the magnetic properties of bulk and monolayer structures.

Manuscript in preparation

3.1. Introduction

3.1.1. TP-based monolayers on surfaces: interest and state-of-the-art

Over the last years, the synthesis of coordination polymers on surfaces using UHV evaporation techniques has attracted raising interest thanks to the high control and tailoring of the resulting MOFs and COFs. A very schematic representation of the experimental approach and the resulting monolayers on surfaces is shown in Figure 3.1. This allows for unique UHV spectroscopies on surface 2D monolayer MOFs giving rise to the determination of their electronic band structure and hence attributed electronic properties.⁵ On top of that, additional information on how the structure is influenced by epitaxial effects of the substrate,² the nature of the ligand used or the evaporation rates³ of the metal/ligand components,⁴ can also be obtained.

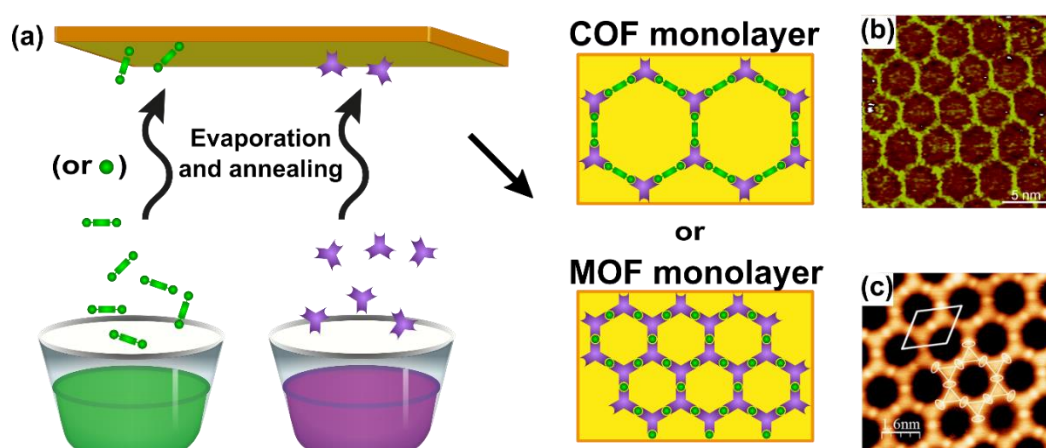


Figure 3.1: (a) Schematic of the UHV evaporation synthesis. The monomers are evaporated onto a substrate which will catalyze their reaction to form COF or MOF monolayers. (b) and (c) Scanning Tunneling Microscopy (STM) of TP COF and MOF monolayers respectively. Both materials showcase the characteristic honeycomb structure and porous within the nanometer range. Images extracted from refs. 1 and 2 respectively.

Specifically, UHV evaporation and deposition of TP and derivatives on metallic surfaces has provided large and relevant basic information on the synthesis of supported 2D TP MOF/COF layers.^{3,4} Worth-to-mention, TP molecules are planarly adsorbed on the surface in organized and oriented domains. Geometry of the packaging is determined by the interaction between TP molecules, typically repulsive and leading to two closed-packed orientations

rotated 60° one from the other.³ Interestingly, the introduction of functional groups (as hydroxyl ones) has great impact on the available packing geometries as strong interactions between the functional groups can arise depending on the evaporation conditions achieving honeycomb structures typical in 2D TP MOFs and COFs.⁴ Supported monolayered domains of 2D TP COFs could be obtained by thermal evaporation of the starting organic monomers in UHV and deposition on metallic surfaces.⁵ Catalyzed by the substrate and upon annealing treatment, covalent bonds between the deposited monomers occur, creating the porous organized network. This approach leads to the formation of molecular down to the atomic thickness very useful for fundamental studies.⁶

Led by the success of these studies, synthesis of 2D TP MOFs monolayers was pursued by the sequential evaporation of the TP based ligand and a metallic center (see Figure 3.2). Synthesis of HATP-based MOF monolayers using UHV evaporation have been the widely studied. Remarkably, the direct evaporation of HATP molecules onto surfaces containing possible coordinators (for instance copper substrates) did not lead to an extended coordination but to discrete coordination clusters (Figure 3.2a).⁷ Thus, after the thermal evaporation of the TP molecule, co-deposition of Ni metallic center with electron beam evaporation and annealing are required to obtain unit cells of TP 2D MOF $\text{Ni}_3(\text{HITP})_2$ (Figure 3.2b). These results lead to a more robust protocol where the thermal evaporation of $\text{HATP} \cdot 6\text{HCl}$ is sequentially followed by the evaporation of metallic cluster, giving rise to single-layer structures of $\text{Ni}_3(\text{HITP})_2$ ⁸ and $\text{Fe}_3(\text{HITP})_2$ ² (Figures 3.2c-f). Notoriously, small lateral domains within the nanometer range were obtained. Despite their small size, preliminary studies of the density of states on such structures have already pointed to interesting properties as extended conjugation or non-trivial topological or spin-orbit coupling induced gaps. However, studies on the magnetic properties of these systems are still in its infancy.

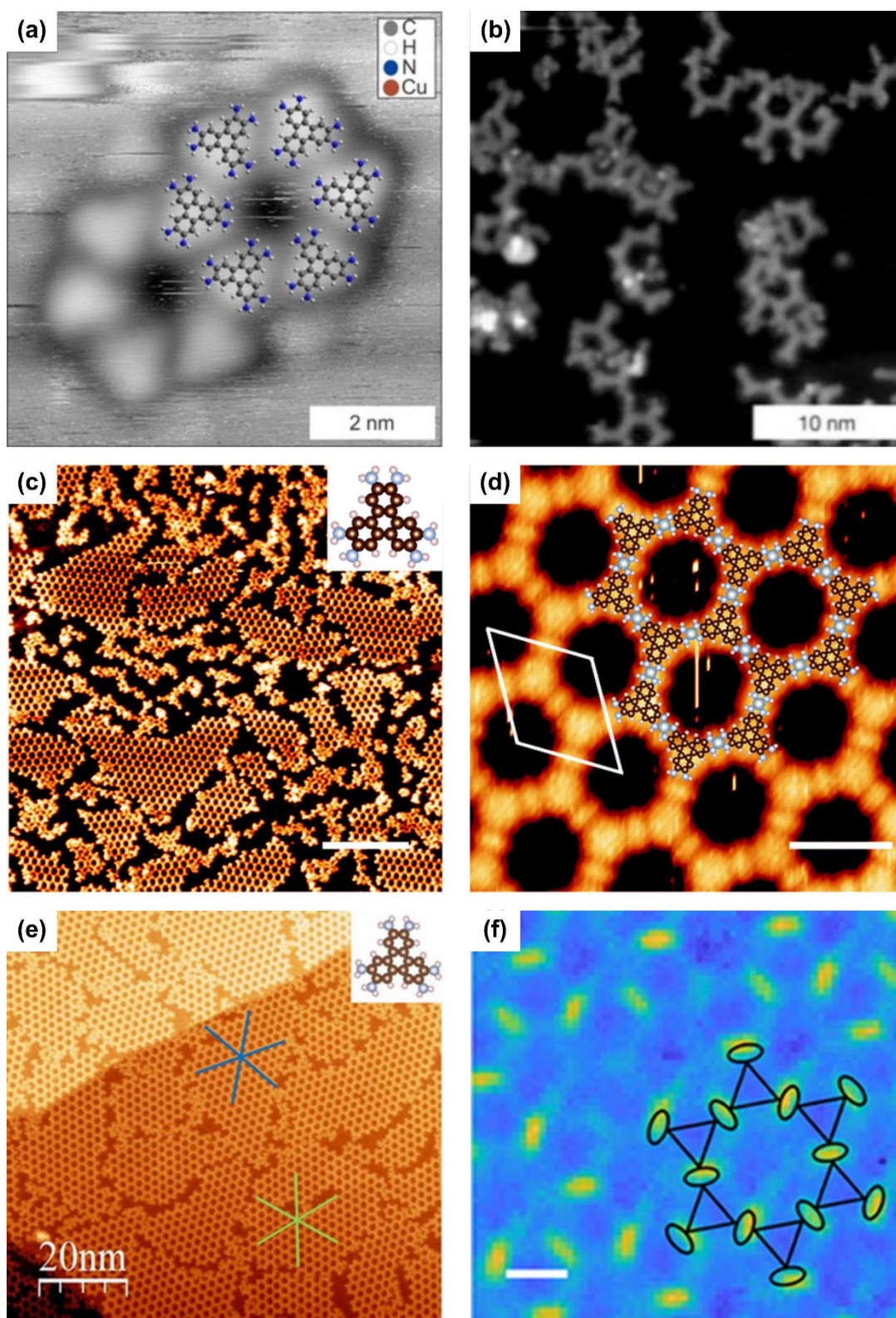


Figure 3.2: (a) STM of room-temperature deposition of HATP onto Cu(111). (b) STM images of HATP on Cu(111) acquired after deposition of Ni and subsequent annealing to 200 °C. Images adapted from ref. 7. (c-d) STM images of single-layer $\text{Ni}_3(\text{HITP})_2$ networks self-assembled on Au(111). Scale bars: 20 nm and 2 nm respectively. Image (d) is overlaid with a molecular model (Ni: large blue balls). Images adapted from ref. 8. (e) Overview STM image of the single layer of the $\text{Fe}_3(\text{HITP})_2$ framework self-assembled on Au(111). (f) dI/dV map of $\text{Fe}_3(\text{HITP})_2$ framework acquired at -0.48 V showing a larger electron density at the iron centers at these biases. Images adapted from ref. 2.

3.1.2. MOF of choice and experimental approach

Though of representing an area of high interest, magnetic properties of TP based MOF have been rarely studied. Indeed, TP 2D MOFs are formed by Kagomé lattice structures where metallic ions are coordinated in trinuclear arrangements.^{9–11} Hence, TP 2D MOFs structures can be candidates for geometrically frustrated spin systems. Nonetheless, the intrinsic and in deep study of the magnetic properties is still unexplored. So far, a few examples of Cu-based MOFs have been studied with this aim and successfully implemented in spin valves¹¹ but no detailed studies to understand, and if possible to control, the magnetic properties of these materials with the proper choice of ligands and metals, and its interaction with the conductive properties have been reported.

The ultimate purpose of such study would be the comparison of magnetic properties of single-layer and multilayer bulk materials, as the thickness plays a key role in the appearance of quantum confinement effects and interlayer interactions.¹² The reported studies of the UHV formation of TP 2D MOFs have demonstrated the relevance of several key parameters as the deposition order or stoichiometry between the evaporated monomers.^{1,6,7} However, despite the numerous studies, nanodomains have been obtained only, leading to a finite polymeric array that may be subjected to in-plane quantum confinement.¹ Hence the extracted properties may differ from the ones obtained in an infinite layer.

Thus, the last of the objectives foreseen for this Thesis was the manufacture of monolayers and the study of their spectroscopic properties of UHV conditions. These experiments were planned in collaboration with *Atomic Manipulation and Spectroscopy Group*, led by Dr Aitor Mugarza, at the ICN2. The group, in addition to have all the required equipment, is well-recognized for investigating the interplay between structural, electronic and magnetic properties of materials at the atomic/molecular scale combining STM techniques with synchrotron radiation spectroscopy.^{13–15} As regards the materials used for these studies, we aimed to synthesize monolayers of **Fe₃(HITP)₂** and **Co₃(HITP)₂** monolayers supported on gold substrates. At the time of starting these studies, these compounds had not been described to us, although they were described in a recent study by Dincă et al. only in bulk as microcrystalline materials.¹⁶ The reason for the choice of these systems were the previous theoretical studies carried out by the group of Dr. Roberto Robles working at the *Centro de Física de Materiales CFM/MPC* (CSIC-UPV/EHU). Density Functional Theory (DFT) calculations were performed on HATP-based MOF structures supported on gold substrate

using different metals, assessing their possible magnetic coupling. Among the tried metals, two candidates revealed interesting magnetic properties: iron and cobalt (Figure 3.3a and 3.3b). Remarkably, calculated Projected Density of States (PDOS) of **Fe₃(HITP)₂** and **Co₃(HITP)₂** monolayers supported on gold substrates indicate a surface magnetization due to the Dirac cones close to the Fermi level (Figure 3.3c and 3.3d). It should be notice that this cone arises mainly from the metallic contribution as it corresponds to d orbital states of the transition metals.

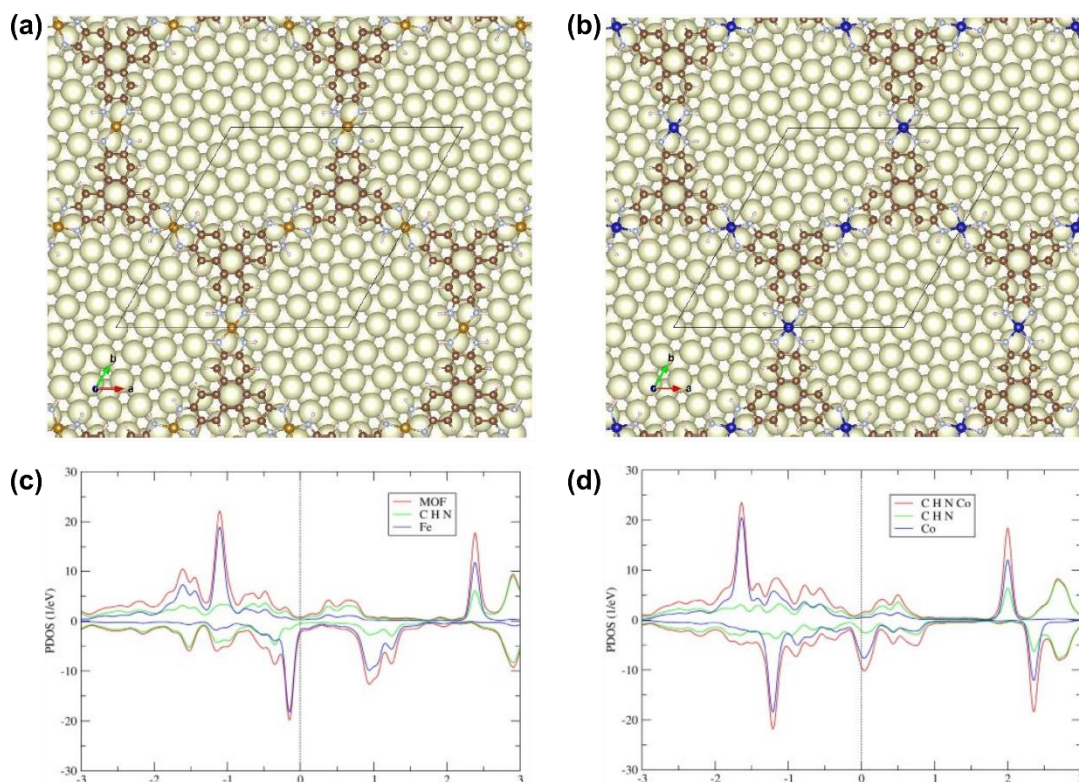


Figure 3.3: (a) and (b) Simulated monolayers of **Fe₃(HITP)₂** and **Co₃(HITP)₂** respectively supported on gold substrates. (c) and (d) Corresponding simulated band structure.

These d bands lead to a higher spin density located in the metallic centers in both structures (Figure 3.4). The magnetism is therefore robust because it is related only to d bands and not hybridizing with the Au. Differences between anti-ferromagnetic and ferromagnetic energies indicate that both monolayers should showcase anti-ferromagnetic coupling between metals. Larger exchange interaction and hence larger coupling are expected in the Fe-based layer as higher densities can be observed according to the spin map.

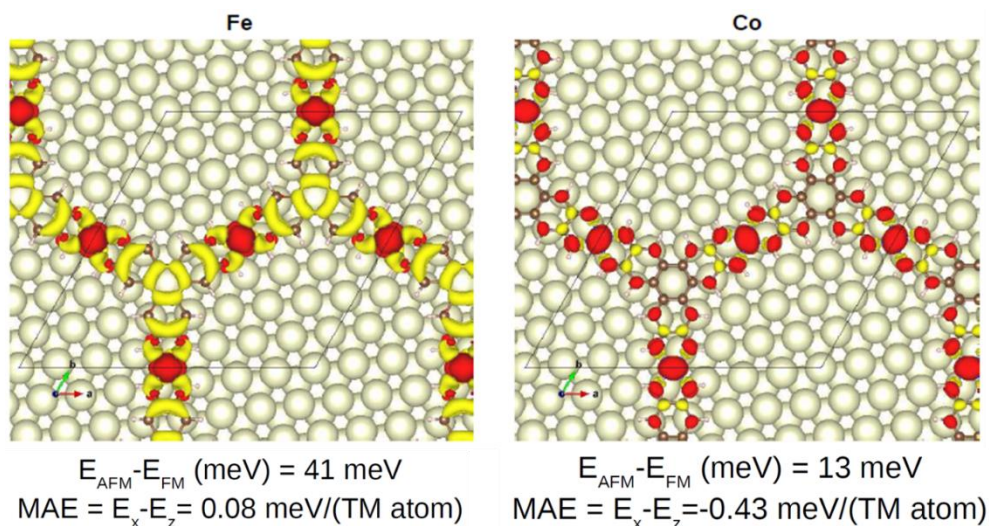


Figure 3.4: Simulated spin density in **Fe₃(HITP)₂** and **Co₃(HITP)₂** monolayers with corresponding magnetic anisotropy energies (MAE) underneath.

The main task of this doctoral thesis was initially the synthesis of the precursor **HATP·6HCl** as pure as possible for the synthesis of MOFs on surfaces under UHV conditions. However, these works went beyond those originally planned since additional experiments were proposed for the synthesis of these materials in bulk. If feasible, the objective would be the deposition of the microcrystals on silicon surfaces, as isolated as possible, for their study as a model with Synchrotron light of under the same conditions than those used for the monolayers. To obtain this objective, two main challenges were faced. The bulk synthesis of the materials, as it had not been described before at the moment of starting these studies. And second, the controlled deposition of the microcrystals on surfaces under UHV conditions avoiding as much as possible any side impurity. For this, Atomic Layer Injection (ALI) was the technique of choice. ALI is a versatile technique for deposition of macromolecules and nanoparticles in solution using UHV conditions. The injection system relies in a pulse valve connecting both a UHV and a pre-injection chambers, which opening and closing can be controlled with high precision, allowing the flow of controlled amounts of solution. The solution containing the aimed nanoparticles is introduced in the pre-injection chamber with argon as carrier gas at a given pressure. During the opening of the pulse valve, the over-pressure of the carrier gas in the pre-injection chamber leads to the injection of microdroplets of the solution into the UHV chamber with a ballistic trajectory. Over this one, the microdroplet slowly evaporates due to the UHV conditions leading to deposition of the solute into substrates (Figure 3.5 left). Injection of liquids is monitored by the pressure in the UHV chamber as it increases with every pulse but rapidly recovers the UHV conditions (Figure 3.5 right).

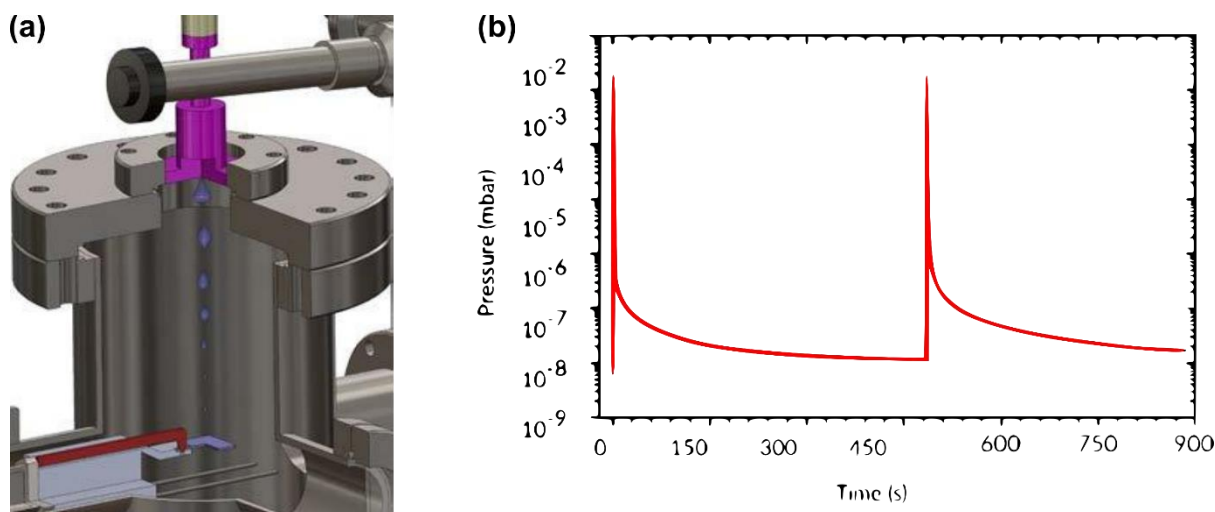


Figure 3.5: (a) Schematic illustration ALI showing the deposition system. Droplets get injected by pulses generated with and opening and closing valve and a high pre-injection chamber pressure. (b) Pulses are controlled by the pressure variation in the main chamber. Different parameters can be varied to optimize the deposition: number of pulses, time of valve opening, pre-injection chamber's pressure, sample to injector distance, solvent and concentration of the suspension, temperature etc.

Being a versatile technique, several parameters can be tuned in the equipment to ensure an optimum deposition:

- **Pre-injection chamber pressure:** Pressure of the carrier gas in the pre-injection chamber can be adjusted between 25 mbar and atmospheric pressure. Larger pressures will result into larger injection of solution.
- **Solvent for the suspension:** Many solvents can be injected into the chamber regardless of its polarity. However, a good dispersion of nanoparticles is highly recommended to avoid precipitation in the pre-injection chamber.
- **Concentration:** Concentration of the suspension should be as well taken into account. Higher concentrated solutions will lead to larger depositions over the substrates. Nevertheless, too concentrated solutions can cause obstruction of the pulse valve depending on the valve size.
- **Time pulse:** It is defined as the time during which the pulse valve is opened. It can be lowered to the ms range with high precision up to 10 min. The time pulse will determine the size of the injected microdroplets, being these bigger using longer pulses and carrying thus larger amounts of nanoparticles.

- **Number of pulses:** Pulses can be repeated sequentially after recovering the UHV pressure in chamber to enlarge the amount of nanoparticles deposited in the substrate.
- **Temperature:** The chamber and substrate's temperature can be regulated between 4 and 80 °C to ensure the evaporation of the solvent in the microdroplets depending on its polarity and boiling point.
- **Valve to substrate distance:** The distance between the valve and the substrate can be modified from 100 mm to 200 mm. Larger distances lead to larger trajectories for the microdroplets allowing a better drying of the solutes before the deposition. However, shorter distances allow larger material densities in the substrate.

3.1.3. Scope of this chapter

Considering the aforementioned, the specific objectives of this Chapter are:

- To optimize the synthesis of **HATP·6HCl** organic ligand aiming for a large degree of purity needed in the subsequential single-layer MOF UHV evaporation synthesis.
- To synthesize in solution of high-quality crystalline **Co₃(HITP)₂** MOF without impurities or by-products with potential magnetic properties.
- To optimize the deposition of the obtained **Co₃(HITP)₂** MOF in UHV conditions using ALI technique

3.2 Results and discussion

3.2.1 Optimization on the synthesis of 2,3,6,7,10,11-hexaamino triphenylene (HATP·6HCl)

The synthesis of **HATP·6HCl** was faced following a synthetic protocol already described in the literature,¹⁷ although some experimental modifications were introduced to improve the reproducibility and yield of the reaction. This step is very important to subsequently obtain the desired MOF single-layers with the largest lateral sizes as possible.

Reproducibility of the reported protocol. Synthesis of **HATP·6HCl** was reproduced as described (Figure 3.6a). The approach is characterized by a two-step reaction: the palladium catalyzed amination of a halogen substituted TP moiety and the acidic hydrolysis of the obtained product after purification. In a first step, palladium catalyzed amination of **1** led to synthesis of **2**. Thin layer chromatography (TLC) of the crude of this first reaction and the starting reagents can be found in Figure 3.6b. Figure 3.6b.

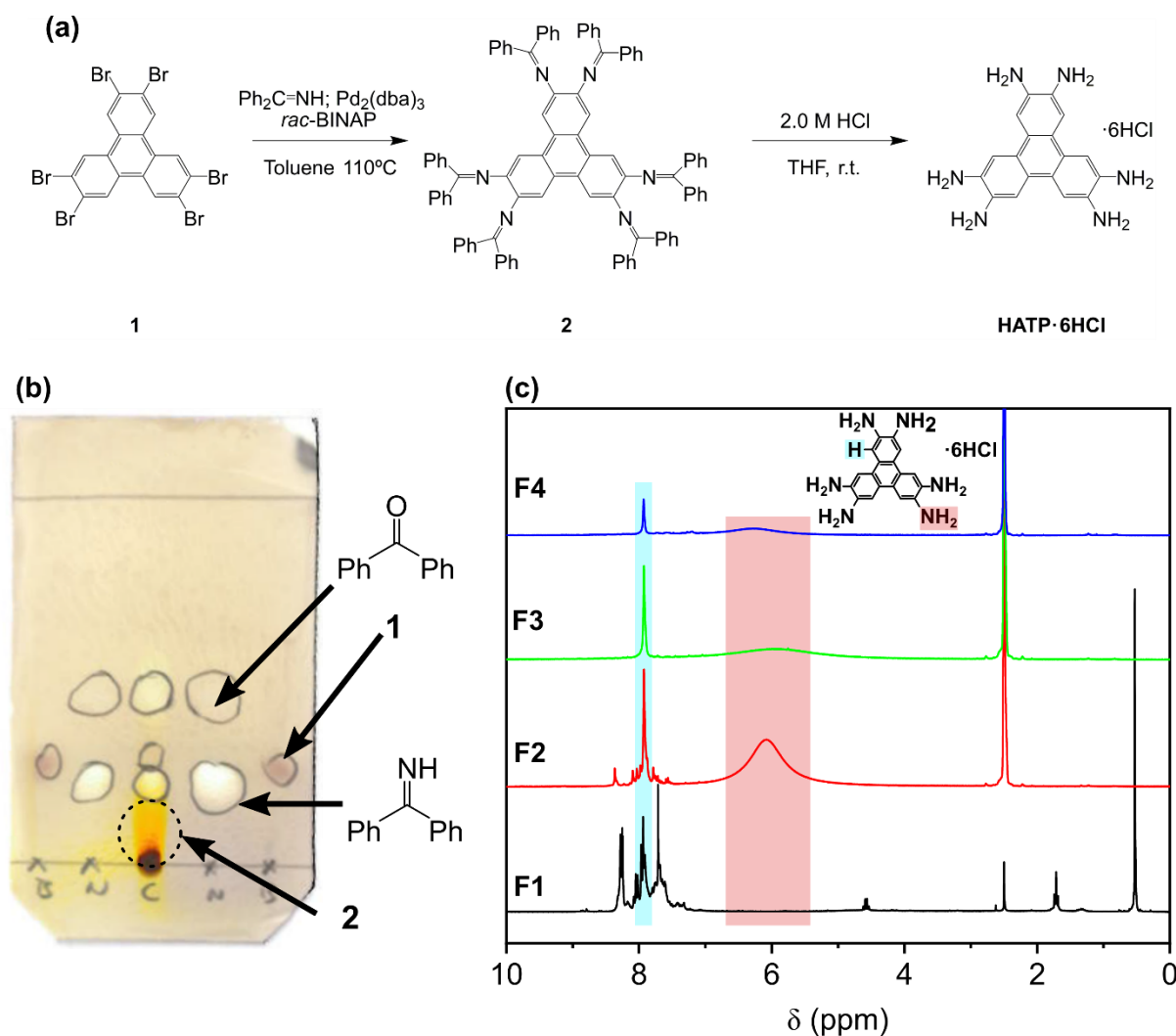


Figure 3.6: (a) Scheme of the reaction of **HATP·6HCl**. (b) TLC on silica of the crude of synthesis reaction of **2** before purification. Chromatography of the starting reagents **1** and benzophenone imine at 95% was performed for comparison. The yellow compound corresponds to the synthesized **2** which seems to be retained in the silica. (c) Proton Nuclear Magnetic Resonance (^1H -NMR) of products obtained after hydrolysis of the different fractions from purification step of **2** in deuterated Dimethyl Sulfoxide (d -DMSO). **HATP·6HCl** is shown as an inset with signals assigned to the molecule.

As seen there, the yellow spot corresponding to **2** has a lower mobility. Thus **2** would be collected as the last fraction in the purification. However, **2** seems to be largely retained in the silica. Consequently, collection of **2** in the purification step was split in four fractions.

Acidic hydrolysis of the four fractions was performed separately obtaining four brown powders representing each less than a 5% of yield. H-NMR (Figure 3.6c) in *d*-DMSO indicates that the first two fractions collected have a large quantity of impurities with peaks with shifts close to the singlet corresponding to the TP core (highlighted in blue). Only hydrolysis of the two last collected fractions led to high pure **HATP·6HCl** as only singlet at 7.92 ppm corresponding to the TP core and a band at ~6 ppm corresponding to amine groups (highlighted in red) are observed. Nevertheless, pure **HATP·6HCl** was obtained in a very low amount. Large retentions of **2** and impurities from its reaction in silica suggest a lack of stability in the stationary phase. Due to the slight acidic character of silica, possible hydrolysis of **2** and its by-products can occur during the purification. Therefore, mobilities change during the chromatography, leading to mixing of the impurities with the fraction of **2**. Thus, modification of chromatography is needed to ensure the stability of **2** during the purification.

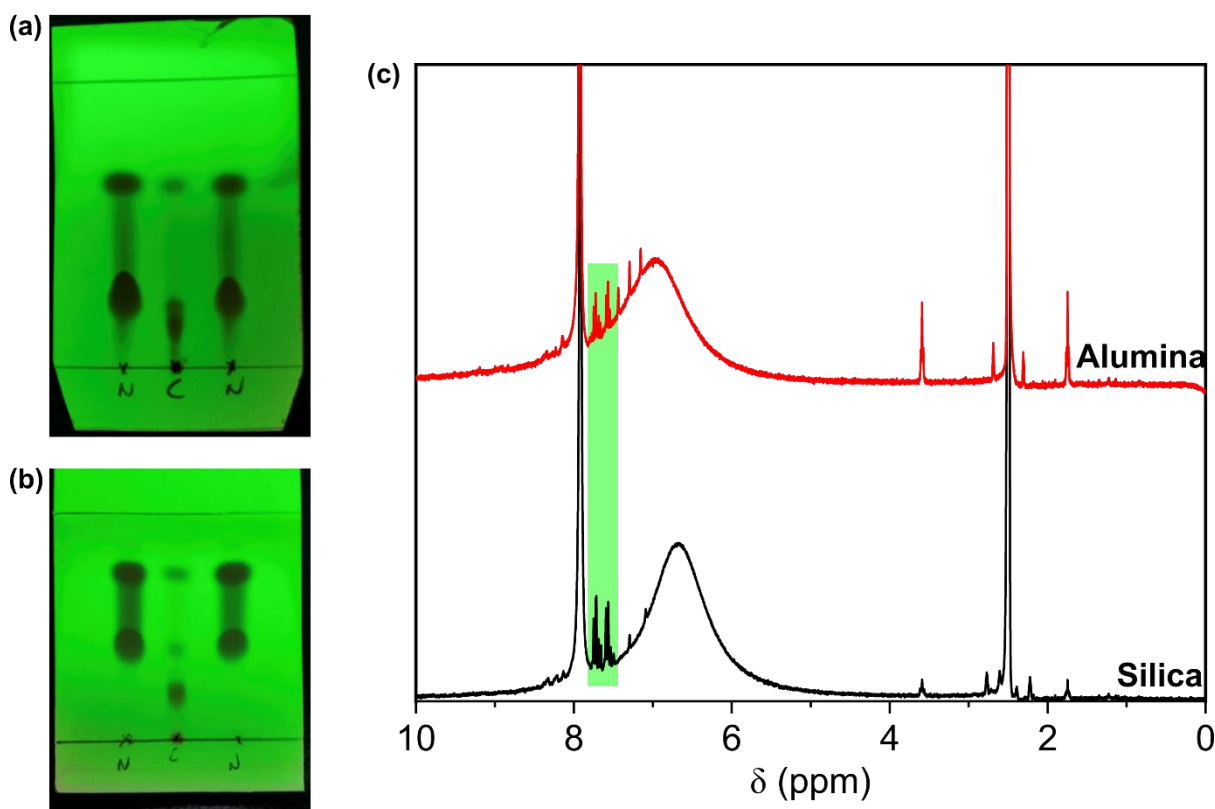


Figure 3.7: (a) TLC on silica of the crude of synthesis reaction of **2** previous to purification (central spot) and benzophenone imine at 95% (side spots) with a 3% v/v of triethylamine in the eluent. (b) TLC on alumina of the crude of synthesis reaction of **2** (central spot) previous to purification and benzophenone imine at 95% (side spots). (c) H-NMR in *d*-DMSO of products obtained after hydrolysis of the last fraction from purification step of **2** in silica and alumina respectively. Signals corresponding to impurities from reaction are highlighted in green.

Modification of column chromatography. To avoid decomposition due to acidity of the silica two solutions were proposed: running chromatography with 3% v/v of triethylamine in the eluent or using neutral alumina as static phase. To assess their efficacy, TLCs on the same crude were performed under these conditions (Figure 3.7a and 3.7b).

TLC on silica with triethylamine did not show any improvement with the previously run TLCs. **2** seems to be retained in the TLC and thus decomposed in the silica. On the other hand, TLC on alumina provided a clear spot of **2** without retention. Thus, purification was henceforth performed using neutral alumina as static phase. Figure 3.7c compares the H-NMRs in *d*-DMSO of **HATP·6HCl** obtained after hydrolysis of **2** purified from the same crude in alumina or silica. The amount of impurities seems to be slightly lower using alumina for purification. However, it is still considerable. The multiplicity of the signals and the position near the triphenylene singlet suggest that it may come from partial amination of **1** instead of a hexasubstitution. This is in agreement with the presence of benzophenone imine in the crude of reaction (as the TLCs indicate) since it was added in a six-fold stoichiometric ratio with **1**.

Modification of reagents stoichiometry. To ensure the large yield of hexasubstitution, the reaction protocol was modified regarding the synthesis of **2**. A 9-fold stoichiometry with **1** of benzophenone imine was used instead of adding it in a 6-fold stoichiometry with **1**. H-NMR of **HATP·6HCl** obtained using larger amount of benzophenone imine (Figure 3.8a) indicated that **HATP·6HCl** is obtained with very high purity. Thus, the synthesis of **HATP·6HCl** is henceforth performed using a 9-fold stoichiometry of benzophenone imine with respect to **1** for the palladium catalyzed amination and using neutral alumina as static phase in the purification process before acidic hydrolysis. This optimized protocol allowed to obtain **HATP·6HCl** with a large yield of 63%.

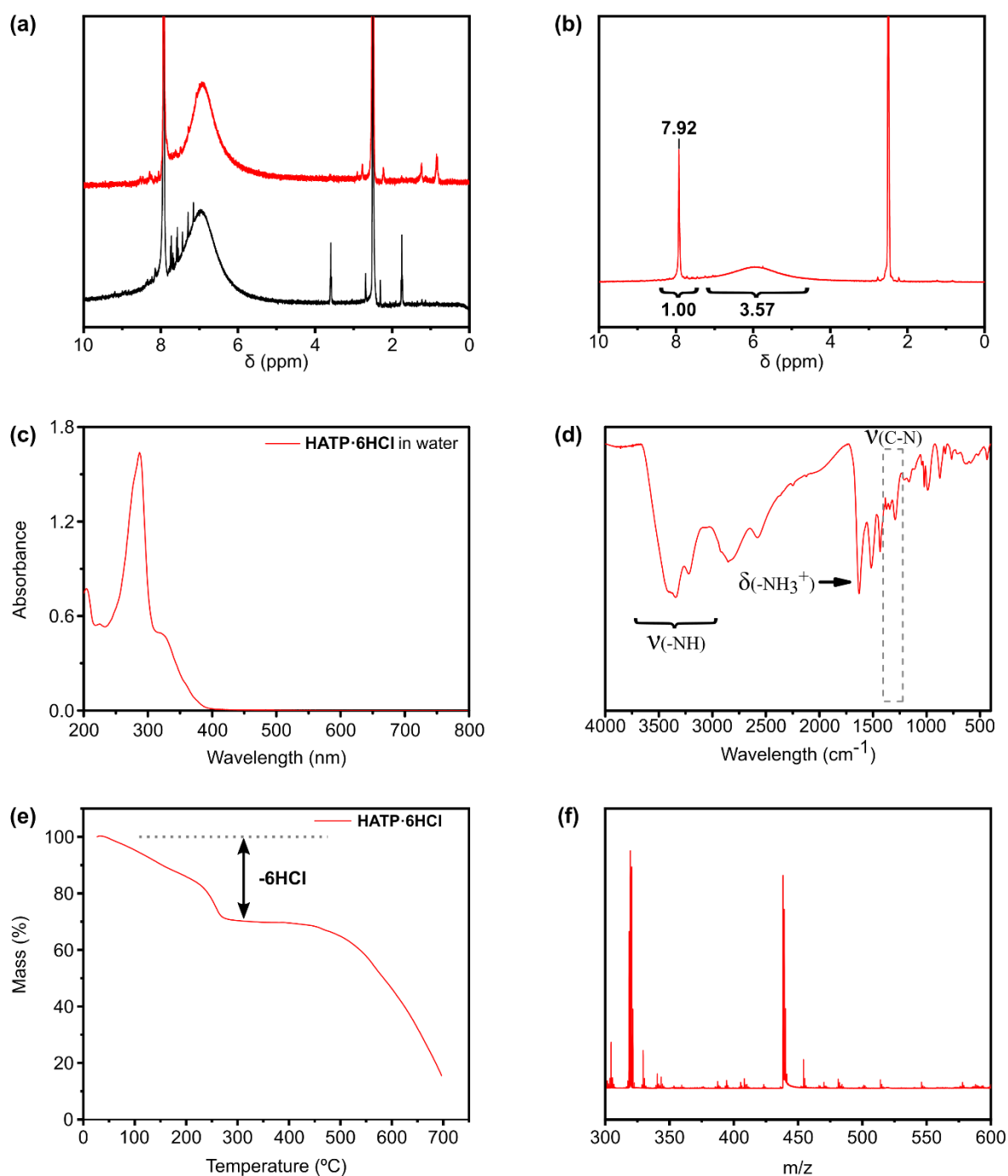


Figure 3.8: (a) ^1H -NMR in d -DMSO of **HATP·6HCl** obtained from reaction using a 6-fold stoichiometry of benzophenone imine (black) and 9-fold stoichiometry (red). (b) ^1H -NMR in d -DMSO of **HATP·6HCl** synthesized with the optimized protocol. Position of the singlet corresponding to the triphenylene core is labeled on top of it. Normalized area integrated from the peaks is labeled underneath. (c) UV-vis spectrum of **HATP·6HCl** in water synthesized with the optimized protocol. (d) FT-IR of **HATP·6HCl** synthesized with the optimized protocol. (e) TGA of **HATP·6HCl** synthesized with the optimized protocol. (f) MALDI-MS spectrum of **HATP·6HCl** ligand.

Full characterization of the obtained **HATP·6HCl** (Figure 3.8) was performed to ensure the quality of this. H-NMR indicated again the high purity of **HATP·6HCl**, showing a singlet at 7.92 ppm corresponding to the proton from the triphenylene core and a broad band at ~6 ppm corresponding to protons from hydrochloride amine groups (Figure 3.8b). Further, normalized areas under the peaks indicated a ratio close to 1:3 between the two types of protons which is in agreement with the **HATP·6HCl** chemical formula. Fourier-Transformed Infrared (FT-IR) spectroscopy confirmed the presence of characteristic bonds of **HATP·6HCl** (Figure 3.8d). A broad band corresponding to the $\nu(\text{N-H})$ stretching vibration can be found at ~3400 cm^{-1} . Further, an intense peak corresponding to the $\delta(\text{N-H})$ vibration can be seen at ~1630 cm^{-1} along with an intense peak corresponding to the $\nu(\text{C-N})$ vibration located at ~1300 cm^{-1} . Further, thermogravimetric analysis (TGA) under argon flux was carried to assess the thermal stability of the obtained **HATP·6HCl**. As seen in Figure 3.8e, a progressive loss of weight is observed until a plateau is reached at 250°C. The plateau, which can be found after 30% of loss weight, corresponds to the thermal desorption of the hydrochloride groups. After this, the remaining **HATP** is stable until high temperatures (~500°C) are reached. Ultraviolet-visible absorbance spectroscopy (UV-vis) revealed a strong absorption at 287 nm (Figure 3.8c), corresponding to the aromatic triphenylene core of the molecule. To avoid saturation of the peak, **HATP·6HCl** aqueous solution had to be diluted to 50 ppm. Matrix-Assisted Laser Desorption/Ionization Mass Spectroscopy (MALDI-MS) spectrum provided two main multiple signals at ~318 corresponding to protonated/ionic species of **HATP** without the hydrochloride groups (Figure 3.8f).

3.2.2. Synthesis of $\text{Co}_3(\text{HITP})_2$

3.2.2.1. First attempts to obtain $\text{Co}_3(\text{HITP})_2$

When this work began, the synthesis of $\text{Co}_3(\text{HITP})_2$ had not yet been described in the literature, so it was necessary to establish a new synthetic protocol (Figure 3.9a). For this, initially we selected a protocol similar to that used for the synthesis of $\text{Ni}_3(\text{HITP})_2$ and using DMSO as a solvent instead of water (see Chapter 4). The reason for this was based on previous studies by Bao *et al.* showing that the synthesis of cobalt-based MOFs using related amino-based ligands in water lead to the precipitation of $\text{Co}(\text{OH})_2$ as main impurity.¹⁸

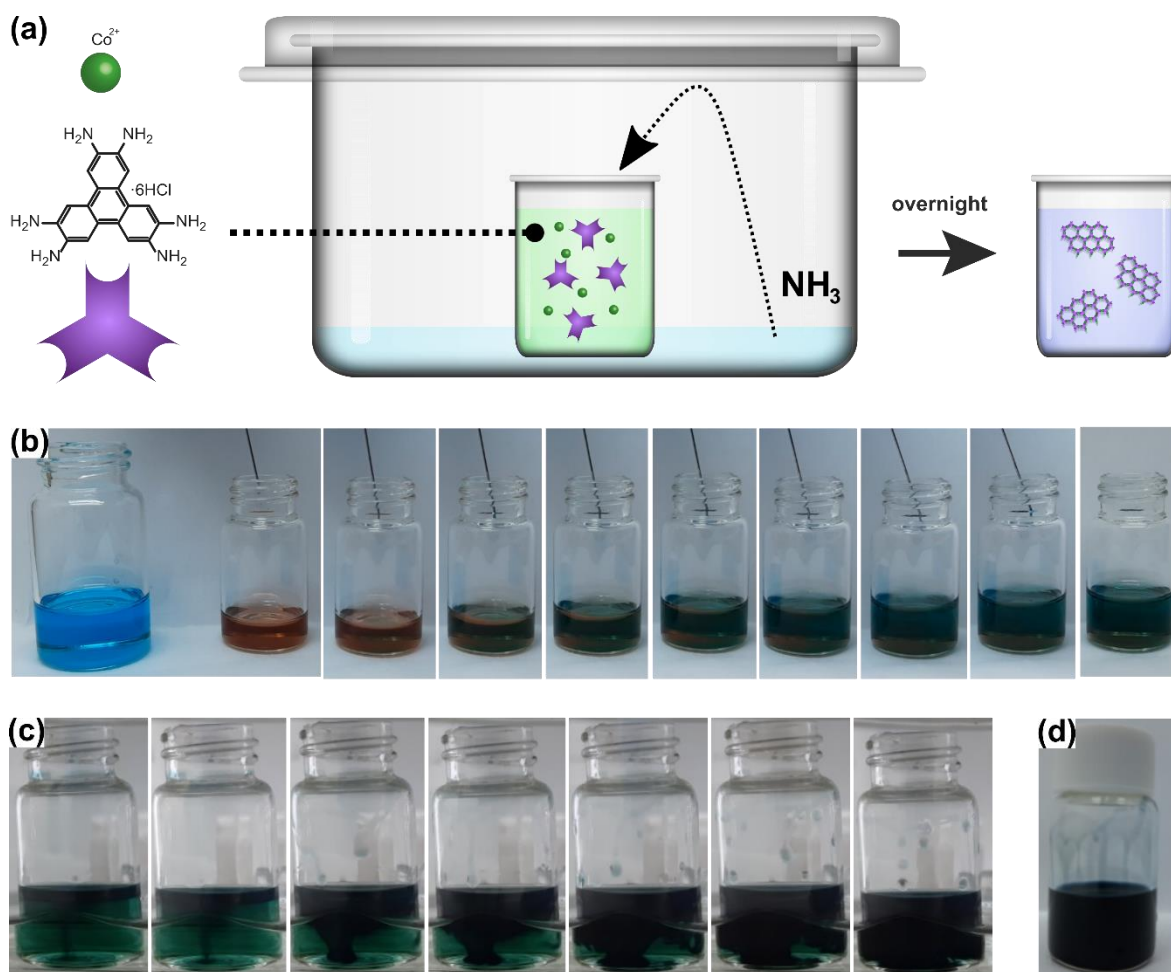


Figure 3.9: (a) Schematic illustration of attempted bulk synthesis of $\text{Co}_3(\text{HITP})_2$ through ammonia diffusion. (b) Sequential images of a $\text{HATP} \cdot 6\text{HCl}$ solution in DMSO (brown) upon dropwise addition of a solution of CoCl_2 in DMSO (blue). The mixture becomes green suggesting coordination between the ligand and the metal. Images were taken every ten seconds. (c) Sequential images of $\text{HATP} \cdot 6\text{HCl}$ and CoCl_2 mixture upon exposure to ammonia vapor. Images were taken every two minutes. (d) Final blue suspension of particles after overnight exposure to ammonia.

Specifically, our reaction consisted in the addition of a solution of CoCl_2 in DMSO (light blue color) over an $\text{HATP} \cdot 6\text{HCl}$ solution also in DMSO (brown color). The resulting solution acquired immediately a light green color tentatively indicating a possible coordination between the $\text{HATP} \cdot 6\text{HCl}$ ligand and the Co metal (Figure 3.9b). Then, the green mixture was placed in a saturated ammonia ambiance for its diffusion overnight. A dark blue precipitate appeared within minutes which remained stable as a colloidal suspension in the vial even for weeks (Figure 3.9c-d).

Dynamic light scattering (DLS) measurements of the as-obtained suspension indicated a narrow particle size distribution with mean sizes around 100 nm while UV-vis of the suspension showed a characteristic broad band around 600 nm attributed to the metal-ligand coordination (Figures 3.10b-c). Attempts to isolate the particles by centrifugation were unsuccessful, which was achieved with the use of a solvent exchange with ethanol. SEM images of the precipitate revealed aggregates of small disk-like particles with dimensions within the range of those found by DLS (Figures 3.10a). FT-IR spectroscopy on the powder revealed a shift of $\sim 30\text{ cm}^{-1}$ on the spectrum of the isolated particles on the peak at 1600 cm^{-1} , corresponding to the $\delta\text{N-H}$ vibration, with respect to the **HATP·6HCl** spectrum (Figure 3.10d). This suggests again the coordination between the ligand and the metallic center. Further presence of peaks at 2920 and 2860 cm^{-1} indicates the presence of DMSO solvent occluded in the material.

$^1\text{H-NRM}$ of the powder dissolved in *d*-DMSO and after treatment with deuterium chloride provided a singlet 7.92 ppm matching with the signal of **HATP·6HCl** (Figure 3.11a). The singlet at 7.98 ppm was attributed to the formation of ketone bonds in the **HATP·6HCl** upon exposure to deuterium chloride with water molecules. HR-TEM imaging of the powder indicated a homogeneous size distribution of disk-like nanoparticles as previously reported by SEM. However, no periodicity associated to the porosity of the material was imaged due to the large energies of the electron beam (Figure 3.11b). Crystallinity was assessed by means of 2D Wide Angle X-ray Scattering (2D WAXS) with synchrotron radiation. Azimuthal integration of the obtained pattern is compared to XRDs of previously reported MOFs (Figure 3.11c). The principal reflection at 3.4 nm^{-1} could not be observed in the experimental pattern because of background scattering. Nonetheless, the matching of peaks at 5.7 nm^{-1} , 6.6 nm^{-1} and 8.8 nm^{-1} suggests that the structure of as synthesized powder in here would be to be isostructural to the **Ni₃(HITP)₂** MOF. In our case however, large interplanar distance between 2D layers would be obtained (maybe because of solvent occlusion), around 3.5 \AA .

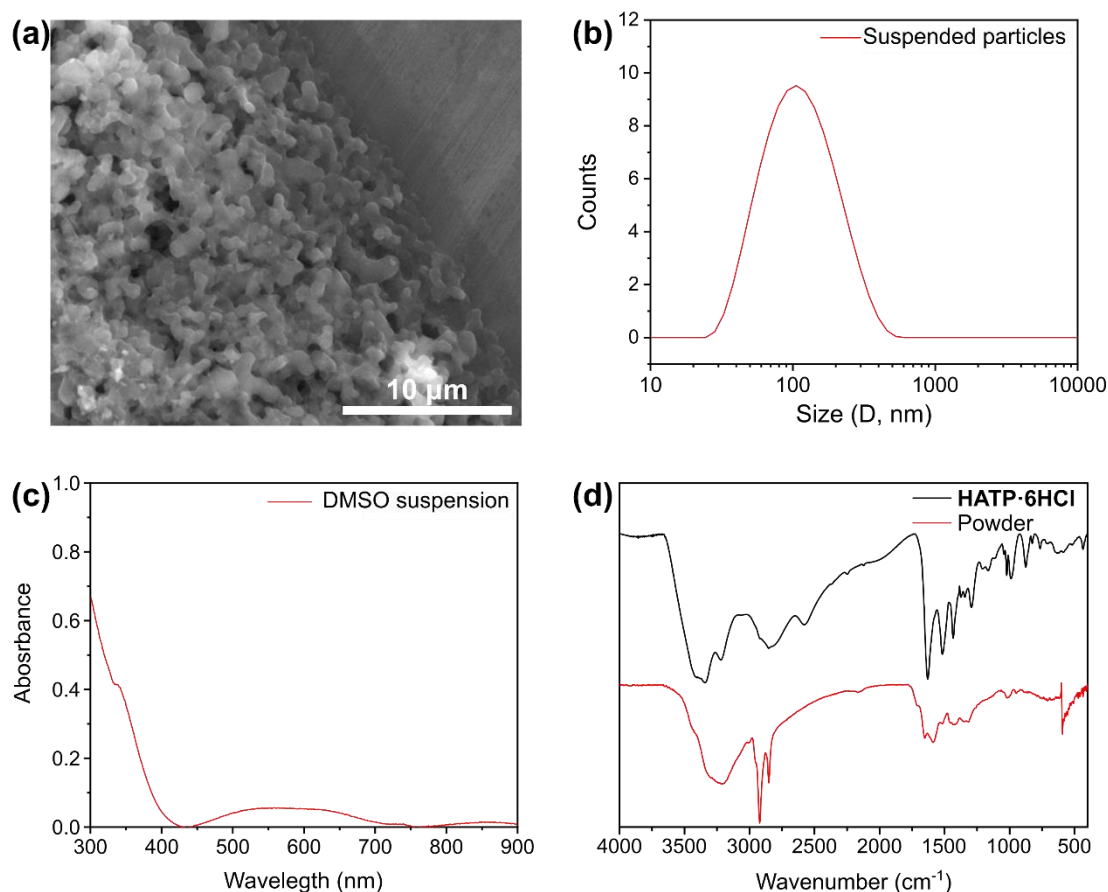


Figure 3.10. (a) SEM image of the $\text{Co}_3(\text{HITP})_2$ particles. (b) Average DLS measurement of $\text{Co}_3(\text{HITP})_2$ suspension in DMSO. (c) UV-vis spectrum of $\text{Co}_3(\text{HITP})_2$ particles suspension in DMSO. (d) Comparison of IR spectra of $\text{HATP} \cdot 6\text{HCl}$ and $\text{Co}_3(\text{HITP})_2$.

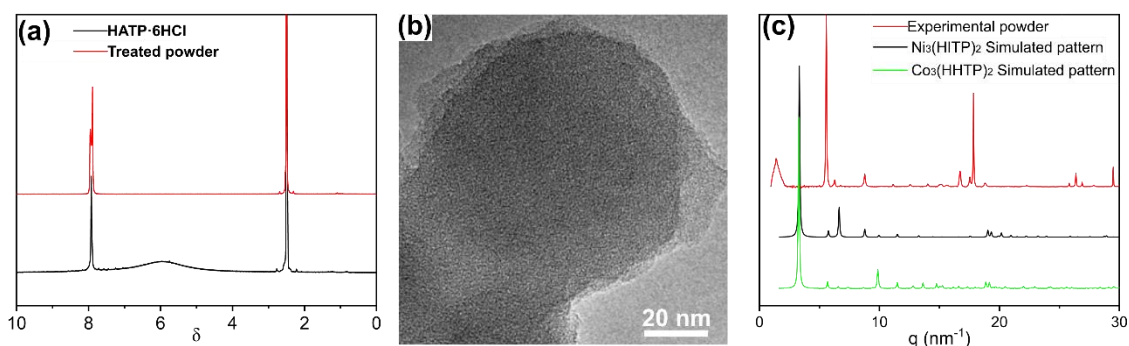


Figure 3.11: (a) Comparison of ^1H -NMR of $\text{HATP} \cdot 6\text{HCl}$ in *d*-DMSO with ^1H -NMR of powder treated with DCl in *d*-DMSO. (b) HR-TEM image of obtained powder. (c) Comparison of azimuthal integration of 2D WAXS measurement of the obtained powder with theoretical XRD patterns of $\text{Ni}_3(\text{HITP})_2$ and $\text{Co}_3(\text{HITP})_2$ MOFs

3.2.2.2. Synthesis and characterization of $\text{Co}_3(\text{HITP})_2$ particles by acetate addition.

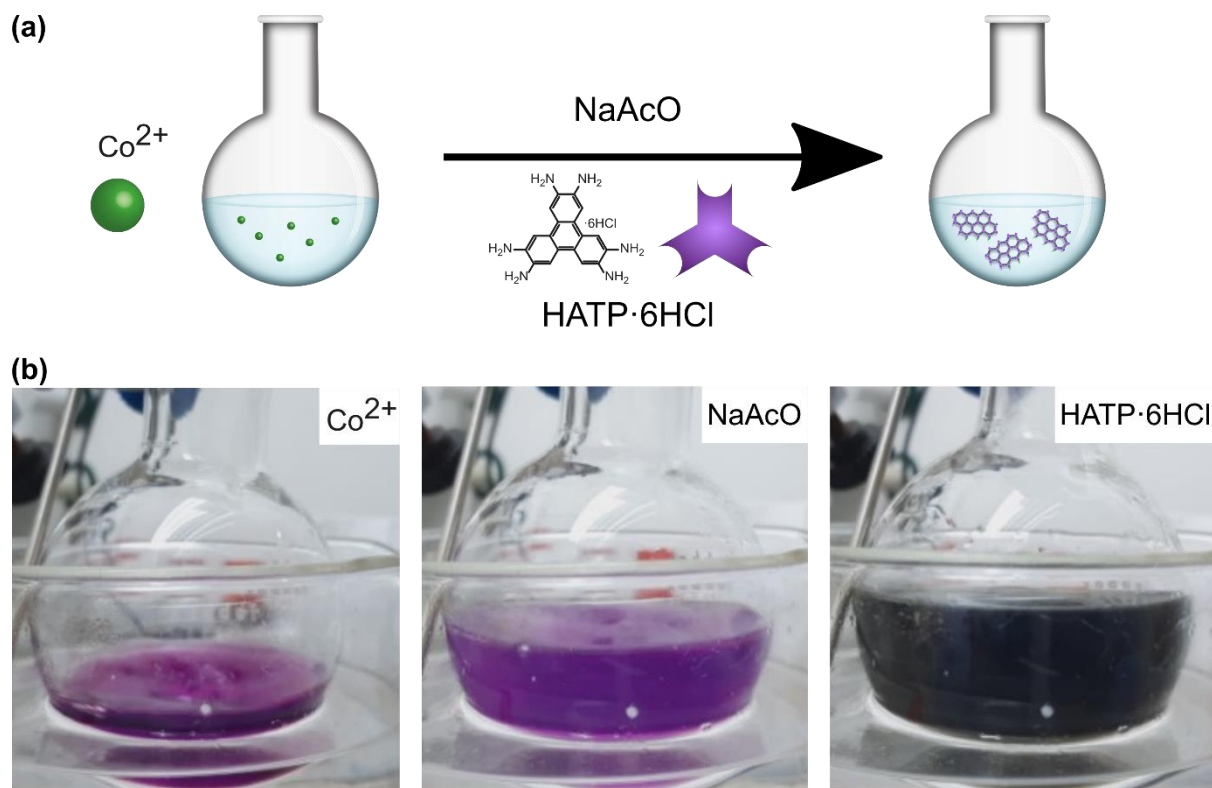


Figure 3.12: (a) Schematic illustration of bulk synthesis of $\text{Co}_3(\text{HITP})_2$ with (b-d) images of reaction at different stages.

While the work described in the previous section was being carried out, Dincă *et al.* reported a novel protocol for the synthesis of $\text{Co}_3(\text{HITP})_2$ MOF using acetate salt as basic agent and in oxidizing environment (Figure 3.12). In short, an aqueous solution of $\text{Na}(\text{CH}_3\text{COO})$ (henceforth NaAcO) was added to a preheated violet solution of $\text{Co}(\text{NO}_3)_2$ in DMF, resulting in a turbid lighter lavender colour. Subsequent addition of adding an aqueous solution of $\text{HATP} \cdot 6\text{HCl}$ resulted in the formation and precipitation of a black powder within a minute, that was isolated after different centrifugation and washing steps. Thus, we decided to stop our synthetic approach to try to reproduce Dincă's one, which was done following the experimental details described in the methodology. Though, an important factor that was not detailed was the addition speed of the reagents, which was proven to be critical to obtain a pure $\text{Co}_3(\text{HITP})_2$ MOF, as described next.

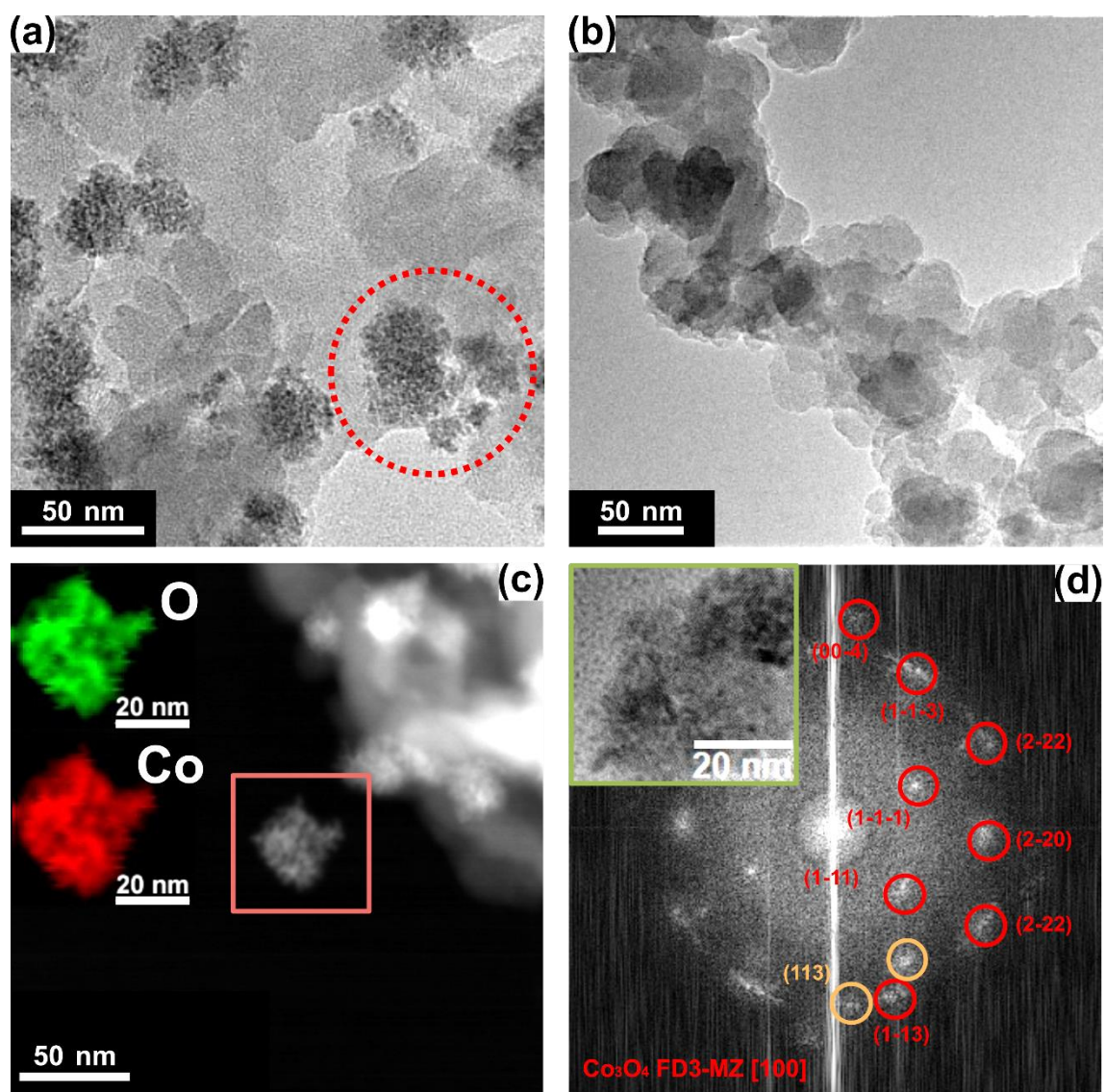


Figure 3.13: (a) Representative HR-TEM image of $\text{Co}_3(\text{HITP})_2$ MOF obtained upon slow addition. Darker aggregate areas as the one encircled in red to a co-precipitated impurity identified as nanoparticles of spinel Co_3O_4 . (b) Representative HR-TEM image of $\text{Co}_3(\text{HITP})_2$ MOF obtained upon fast addition. No impurities are observed. (c) DF-STEM image of the $\text{Co}_3(\text{HITP})_2$ MOF (in grey color) and Co_3O_4 nanoparticles (in white color) obtained in image a. Insets correspond to the EELS color map of the Co_3O_4 aggregate indicated with a square. Large presence of Co and O elements confirm the cobalt oxide composition of the impurities. (d) FFT transformation of Co_3O_4 aggregates imaged along the [100] as shown in the inset. The diffraction spots confirm the spinel form and crystalline phase of the Co_3O_4 aggregate. The diffraction spots labelled in red correspond to monocrystals oriented along the [100] whereas the orange ones correspond to randomly oriented polycrystalline Co_3O_4 .

If spaced additions of the NaAcO and $\text{HATP} \cdot 6\text{HCl}$ aqueous solutions are done, aggregates of nanometered particles were co-precipitated along with $\text{Co}_3(\text{HITP})_2$ as indicated by HR-TEM (Figure 3.13a). In these images, large aggregates can be identified next to porous and crystalline MOF. Dark-Field Scanning-Transmission Electron Microscopy (DF-STEM) was performed on the same sample along with electron energy loss spectroscopy (EELS) analysis

to assess the composition of these aggregates (Figure 3.13c). The elemental analysis shows that the byproduct is composed of Co and O, suggesting it can be cobalt oxide nanoparticles typically obtained in basic aqueous solution of cobalt ions. Fast-Fourier Transform (FFT) on the imaged aggregates revealed a crystalline pattern corresponding to spinel Co_3O_4 structure with a preferential orientation along the [100] direction (Figure 3.13d). Elongated spots in the FFT labelled in red indicated a coherent ordering of monocrystals aggregated in a preferential orientation. On the other hand, some few signals (labelled in orange) suggested the presence of randomly oriented aggregates. Interestingly, Co_3O_4 co-product was not obtained upon fast and sequential addition of the NaAcO and **HATP·6HCl** solution as shown in Figure 3.13b. These conditions are more suitable for the **$\text{Co}_3(\text{HITP})_2$** synthesis as presence of Co impurities. After optimization of the synthesis, physico-chemical characterization on the obtained **$\text{Co}_3(\text{HITP})_2$** MOF was performed. After centrifuging and washing, particles could be isolated for their study.

SEM images revealed aggregates of small disk-like particles sizing around 100 nm (Figure 3.14a). DLS measurements on aqueous suspension after washing showcased a wide particle size distribution with mean sizes around 300 nm (Figure 3.14b). Thus, small aggregates seem to result in the suspension in water. Further the presence of few micrometered sized aggregates suggested the lack of long-term stability of the suspension. Coordination between metal and ligand was confirmed by means of UV-vis by measuring the absorption of the aqueous suspension and observing the characteristic band at 600 nm as previously (Figure 3.14c).

Crystallinity of the obtained **$\text{Co}_3(\text{HITP})_2$** particles was studied by HR-TEM imaging. HR-TEM images revealed particles with disk-like morphology and thin thicknesses as indicated previously in the SEM images (Figure 3.14d). Remarkably, some porosity could be observed during the imaging despite large energies of the electron beam did not allow to fully assess the expected honeycomb structure. FFT on the imaged particles showed a bright diffraction ring of $\sim 1 \text{ nm}^{-1}$ of diameter which corresponds to the 2 nm porosity of the **$\text{Co}_3(\text{HITP})_2$** reported structure. Synchrotron integrated 2D WAXS measurements confirmed the Kagomé crystalline structure as the obtained patterns match the previously reported (Figure 3.14f). Having fully characterized the synthesized MOF, UHV deposition into surfaces was now faced using the ALI technique.

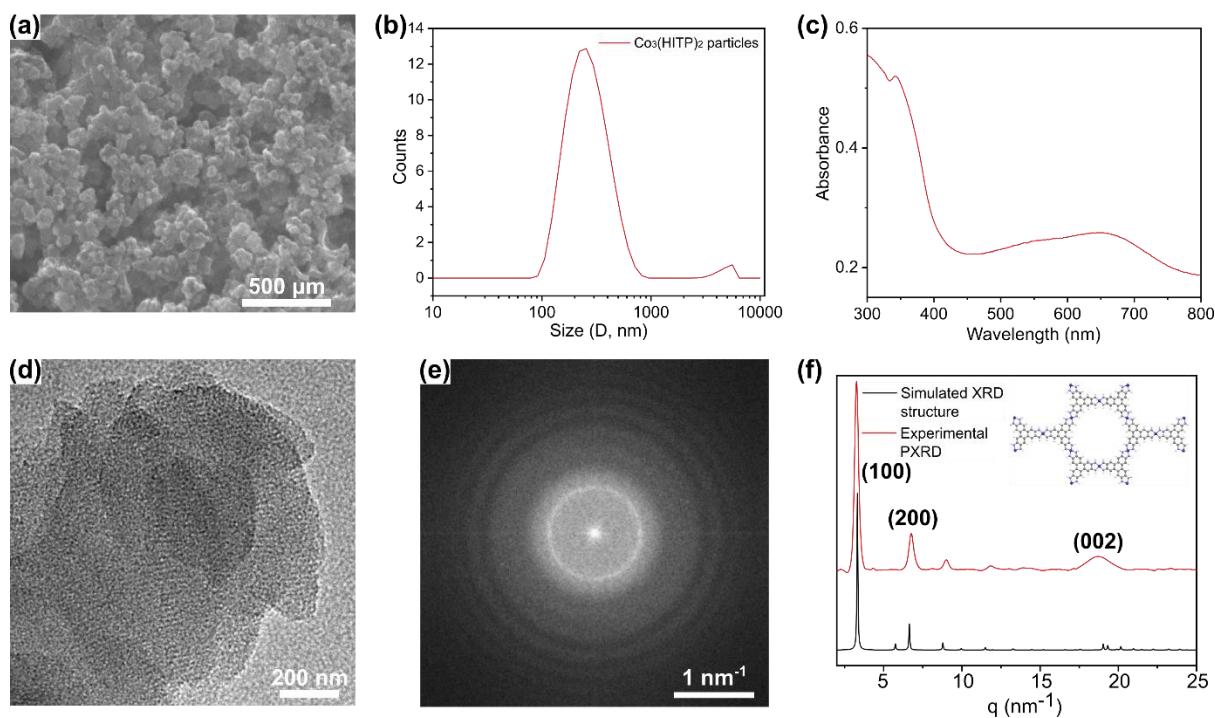


Figure 3.14: Characterization of the crystalline $\text{Co}_3(\text{HITP})_2$ powder: (a) SEM image of the $\text{Co}_3(\text{HITP})_2$ particles, (b) Average DLS measurement of $\text{Co}_3(\text{HITP})_2$ suspension in water suspension. (c) UV-vis spectrum of $\text{Co}_3(\text{HITP})_2$ particles suspension in water. (d) HR-TEM image of the $\text{Co}_3(\text{HITP})_2$ particles showing periodic porosity. (e) FFT transformation of the HR-TEM image. (f) Synchrotron integrated WAXS of the $\text{Co}_3(\text{HITP})_2$ crystalline powder.

3.2.3 Controlled deposition on surfaces with ALI

Once crystals of MOF were obtained and characterized, next step was its deposition on native silicon and the corresponding X-ray Magnetic Circular Dichroism (XMCD) studies. This work comprises three main steps: I) optimization of the deposition parameters, aiming for large and dense depositions of MOFs into the surface in UHV conditions, II) preparation of the samples with the knowledge gained in step I and III) XMCD studies. The three different steps are described in detail next.

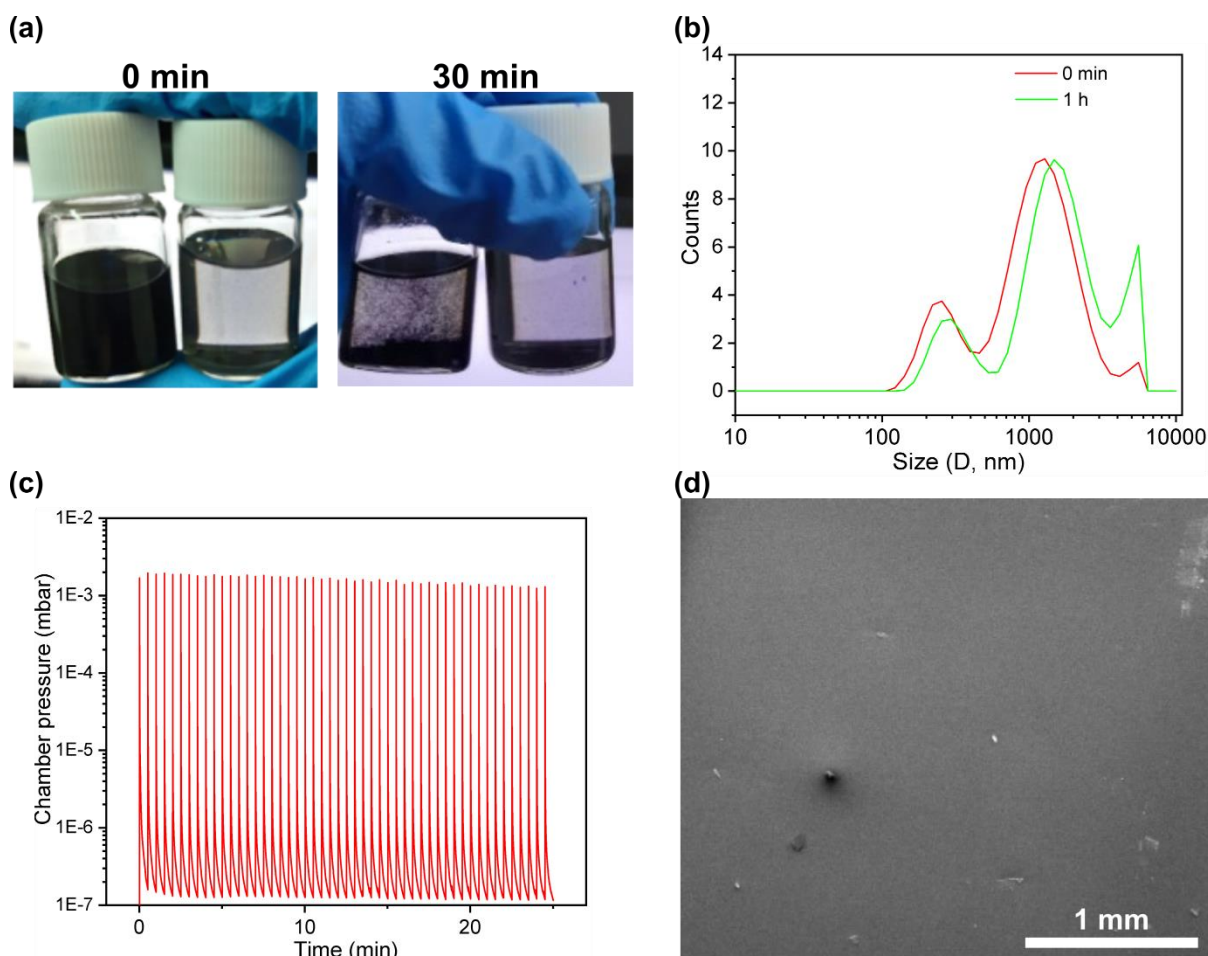


Figure 3.15: (a) Images of as-prepared suspensions in IPA at 0.3 mg/mL (left) and 0.03 mg/mL concentrations (right) and 30 min after. Aggregates of particles are immediately obtained upon dilution and precipitate in short times. (b) DLS measurements of the IPA suspension at 1 mg/mL at different times. (c) ALI Chamber pressure along the deposition of particles suspended in IPA at 0.3 mg/mL. Increases in the pressure indicate the injection of solution. (d) SEM images of ALI depositions on Si substrates using 0.3 mg/mL concentrated suspension in IPA.

First attempts to the direct injection of the as-synthesized $\text{Co}_3(\text{HITP})_2$ using an isopropanol (IPA) were not successful as large micrometer sized aggregates were measured in DLS leading to a fast aggregation and precipitation (Figure 3.17a-b), with only few particles hundred nanometer size remain as a stable colloidal dispersion. Accordingly, independently of the fast injection times and high reproducibility of the pulses only few aggregates of particles are observed on the sample, (Figure 3.17d). First, remarkably, $\text{Co}_3(\text{HITP})_2$ particles seem to not be stabilized by methanol since immediate precipitation is obtained upon solvent addition and sonication. Thus, methanol is not a suitable solvent either. Therefore, DMSO was used as the solvent of choice as large colloidal stabilities were obtained.

Next we describe the different optimized parameters for an optimal deposition:

- Effect of suspension concentration

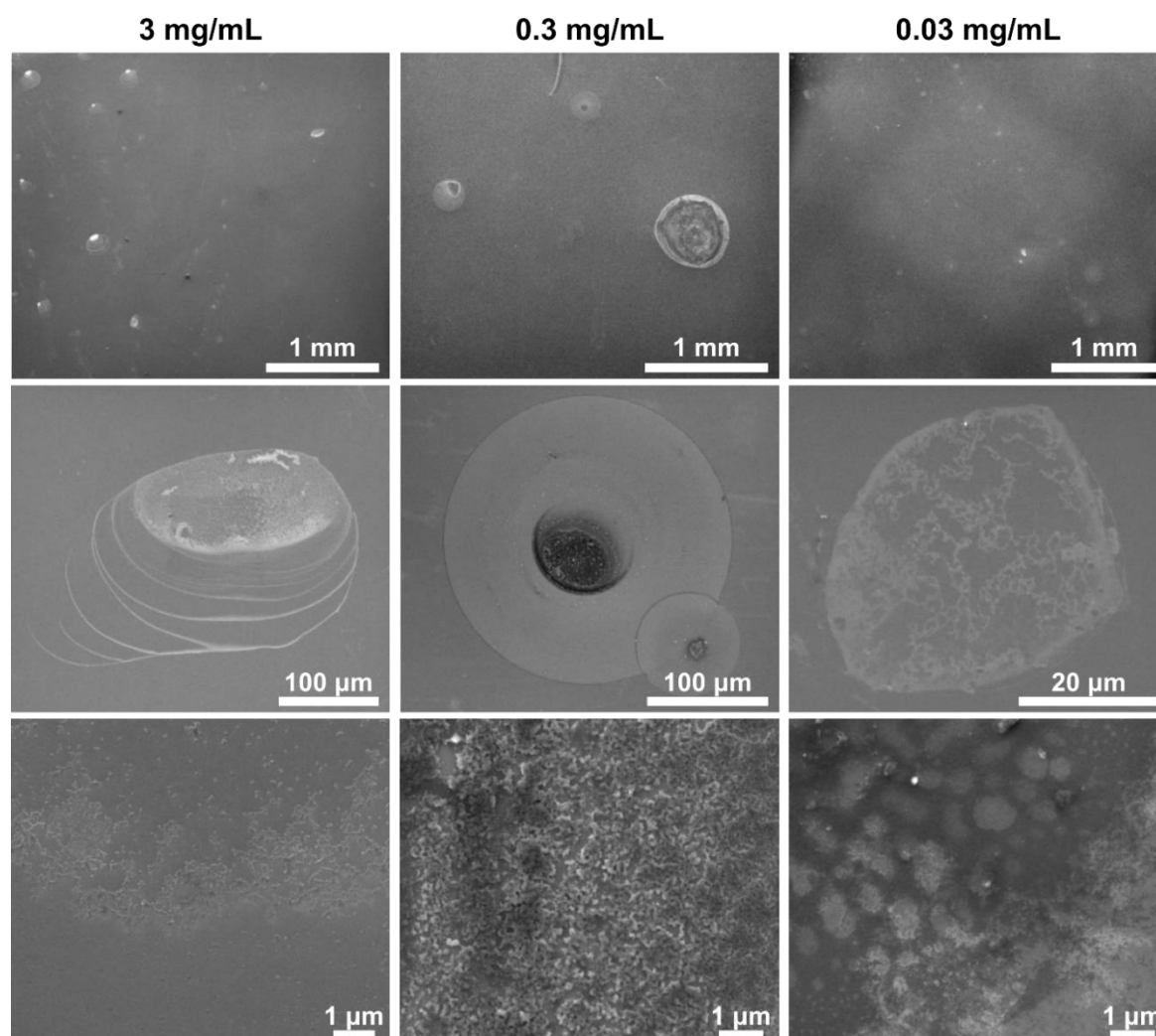


Figure 3.16: SEM images of ALI depositions on Si substrates using different concentrations of DMSO suspensions. All other parameters remained unchanged: 5 pulses of 5 ms at a pressure of 800 mbar and room temperature.

Three injections using the same parameters were performed with the DMSO suspension at ~3 mg/mL, 0.3 mg/mL and 0.03 mg/mL. SEM images of the three depositions revealed large covering of the substrates independently on the suspension concentration (Figure 3.16). However, differences in the droplet size and density arise. Larger concentration (3 and 0.3 mg/mL) led to ~200 μm diameter droplets deposited on the Si/SiO₂ substrate with a large density of particles. On the other hand, concentration of 0.03 mg/mL led to tiny droplets of ~50 μm diameter with a less compact distribution of particles. Interestingly, larger contrasts are seen when imaging the samples obtained with more diluted suspensions. This suggests a faster drying of the sample using larger concentrations.

Hence, larger concentrations seemed to be indicated for large deposition of $\text{Co}_3(\text{HITP})_2$ particles onto substrates through ALI technique. However, pulses seemed to not be reproducible when using higher concentrations: the vacuum in the UHV chamber was hardly recovered between pulses as the pressure remained close to 10^{-5} mbar after the first pulse (Figure 3.17). Further the following pulses (signalized with an arrow in the graph) did not achieve large pressures during the valve opening and showcase decreasing heights, suggesting fewer droplets got injected at every pulse. This may arise by obstruction of the valve with excess of material, as cleaning by injection of pure solvent was required after this deposition in order to recover UHV conditions. After dilution to 0.3 mg/mL of the as synthesized suspension, UHV conditions were easily recovered after every injection pulse as indicated by the graph. However, the pressure was stabilized at different times and peaks show a variety of shape, making them not reproducible. Remarkably, pulses of more diluted samples are widely reproduced, with equidistant peaks of similar shape. Thus, 0.03 mg/mL concentration is used in further experiments for deposition optimization. Variation of other parameters is required to avoid wetting layers on the substrate arising from solvent injection.

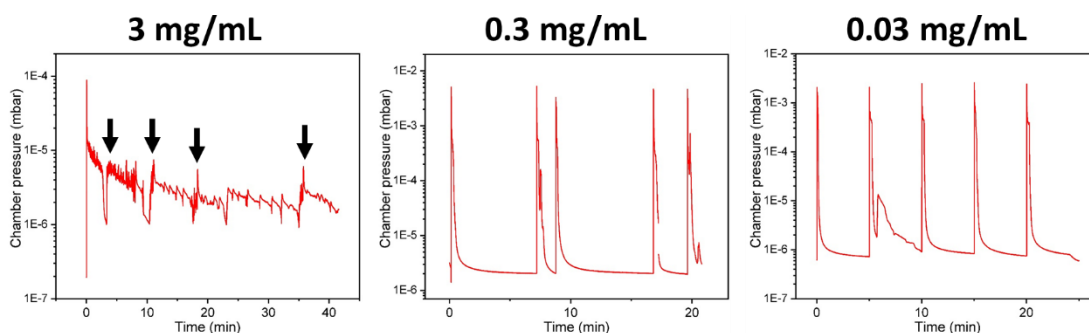


Figure 3.17: ALI Chamber pressure along the deposition of particles suspended in DMSO at three different concentrations. Increases in the pressure indicate the injection of material. In the case of the as synthesized suspension, the four latest pulses are indicated with a row.

- Effect of the pulse time

In a first attempt of getting considerable deposition rates, pulse time were enlarged from 5 ms to 10 ms conserving all other parameters unchanged. SEM images indicated the deposition of very large droplets of ~ 500 μm diameter that can be seen at naked eye with a high density of deposited particles when using 10 ms pulses (Figure 3.18d and e). On the contrary, shorter pulses of 5 ms seem to result into a similar amount of droplets but with smaller size and concentration (Figure 3.18a and b). Nevertheless, notorious amounts of sulfur arising from remaining DMSO were detected in Energy dispersive X-ray (EDX) spectrum at large pulse

times. Hence larger wetting is also obtained at 10 ms. Thus, other approach needed to be used for dry and large deposition.

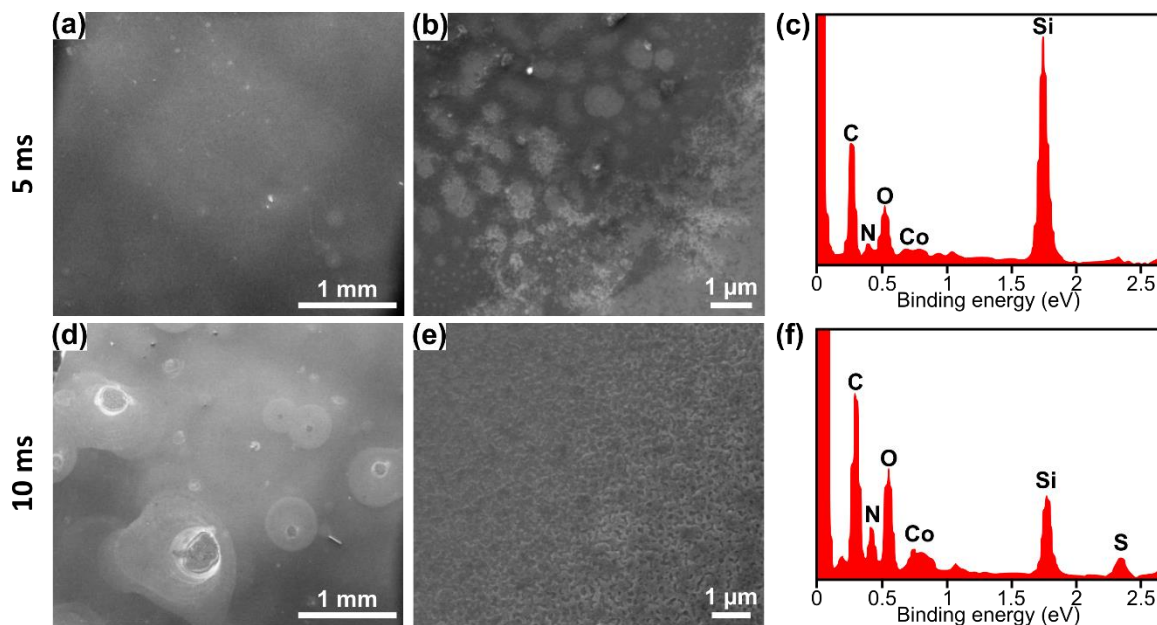


Figure 3.18: SEM images of ALI depositions of DMSO suspension of particles on Si substrates using different pulse's length: (a-b) 5 pulses of 5 ms and (d-e) 5 pulses of 10 ms. (c and f) EDX on both samples are respectively shown. All other parameters remained unchanged: pressure of 800 mbar and room temperature.

- Effect of the number of pulses

As a second approach, increase on the number of pulses was tried in order to accumulate material over sequential depositions of small 5 ms pulses. SEM images revealed small 200 μm droplets in samples obtained with 5 and 10 pulses respectively (Figure 3.19a and d) despite more droplets are observed when applying more pulses. Worth-to-mention, pulse peaks while recording chamber pressure seemed to be quite similar in shape (Figure 3.19c and f). Noticeably, some punctual massive droplets can be observed in the sample obtained with 10 pulses. These may arise from the landing of wet solutes into the substrate coalescing into large droplets and from unexpected injections as the one signalized in Figure 3.19f. EDX confirmed the presence of reminiscence of DMSO on the substrate as large amounts of sulfur are detected with large number of pulses (Figure 3.19b and e). Hence, other approaches were needed to avoid the wetting of the of particles onto substrates.

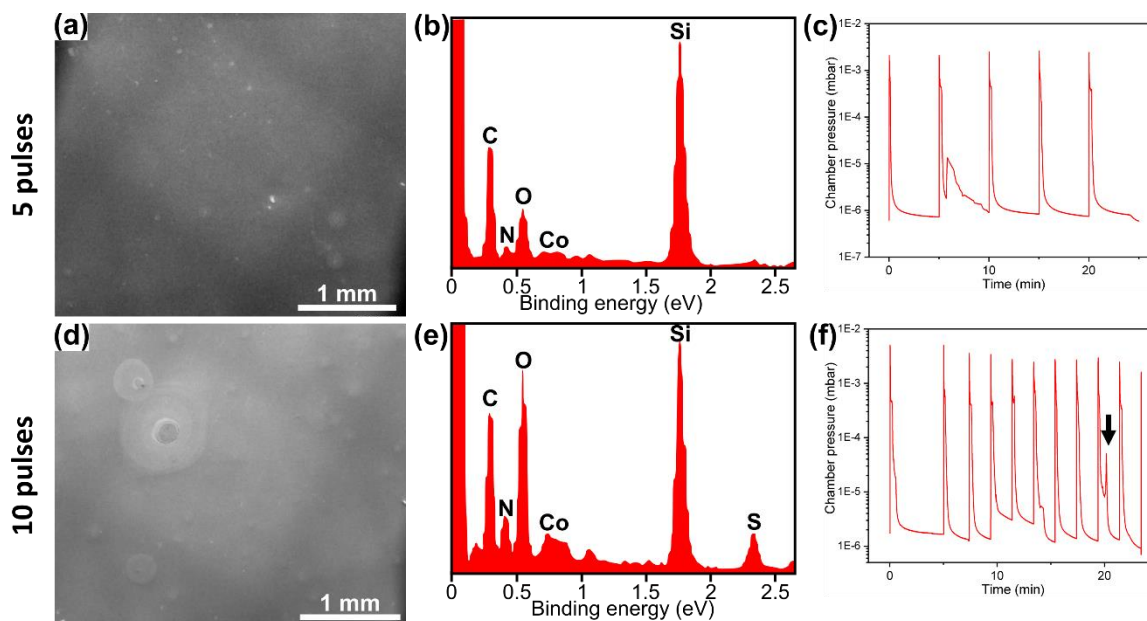


Figure 3.19: SEM images of ALI depositions of DMSO suspension of particles on Si substrates using different pulse's length: (a) 5 pulses of 5 ms and (d) 10 pulses of 5 ms. EDX on both samples are respectively shown (b and e). Respective ALI Chamber pressures along each deposition are shown in (c) and (f). All other parameters remained unchanged: pressure of 800 mbar and room temperature.

- Temperature effect

As DMSO has a quite high boiling point, larger temperatures were applied in the chamber in order to obtain drier samples. SEM images of samples obtained at room temperature and at 80°C show that number and size of droplets seem to be independent on the applied temperature as similar depositions are obtained in both samples (Figure 3.20a and c). The main difference raised on the wettability of the substrate. When applying 80°C, less contrast is observed when imaging, allowing to identify single particles on top of the substrate (Figure 3.20e). However, a thicker wetting layer on top of the of particles can be still observed (Figure 3.20b). It is noteworthy that thinner peaks are observed in chamber pressure diagram recorded at 80°C than the one seen at room temperature. This faster decrease in the pressure reinforces the faster drying of the pulses as indicated by the SEM images. Taking into account all the aforementioned, large pulses at high temperatures are chosen as optimized conditions for deposition. Further, distance between to ensure the dried deposition of particles onto the substrate.

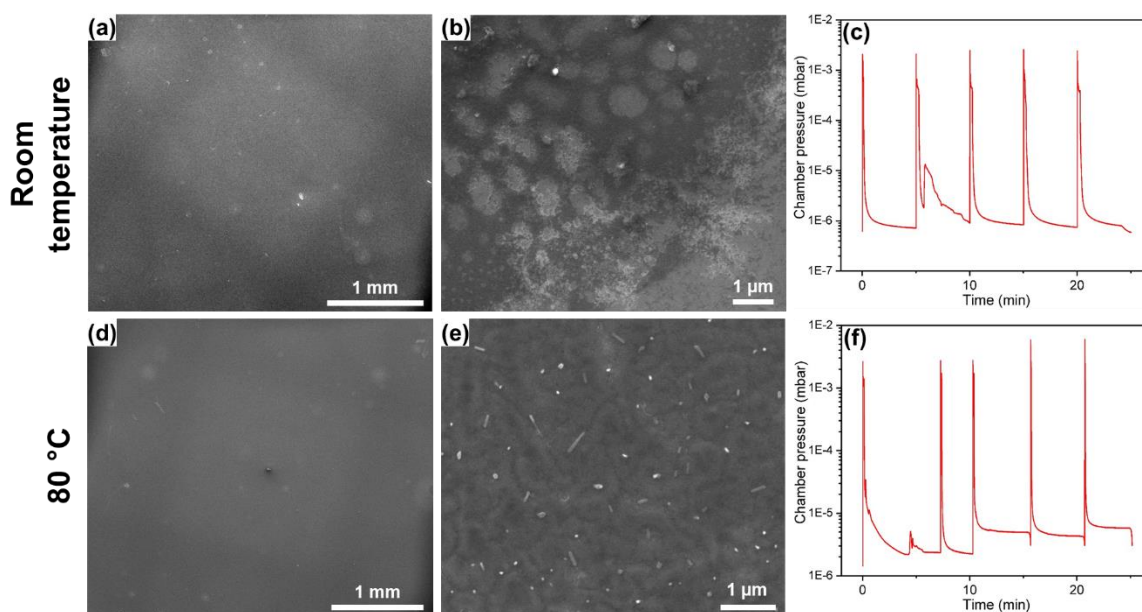


Figure 3.20: SEM images of ALI depositions of DMSO suspension of particles on Si substrates at different temperatures: (a-b) room temperature and (d-e) 80 °C. Respective ALI Chamber pressures along each deposition are shown in (c) and (f). All other parameters remained unchanged: 5 pulses of 5ms at a pressure of 800 mbar.

- Effect of distance between sample and injector

Two samples were prepared using a sequence of 5 pulses of 7 ms at 80°C with different valve to sample distances: 100 mm and 150 mm. SEM images showed smaller droplets in samples prepared at 150 mm than at 100 mm (Figure 3.21a and d), suggesting that longer distances are needed between the valve and the sample to ensure the drying of the microdroplets during its ballistic trajectory after injection. Remarkably, densely packed droplets were obtained in both samples due to the long-time pulse. However, samples prepared at 100 mm seem to have a wetting layer covering the of particles which is not present at samples prepared at 150 mm (Figure 3.21b and e). EDX confirmed the presence of sulfur coming from DMSO traces in the sample prepared at 100 mm whereas no sulfur is detected in the sample prepared at 150 mm. Therefore, we can conclude that long sample to valve distances are the needed optimized values along with long pulses and large temperature to obtain particles onto substrates in large amounts through ALI deposition. Being these the optimized values, characterization of samples prepared in the optimized conditions is required.

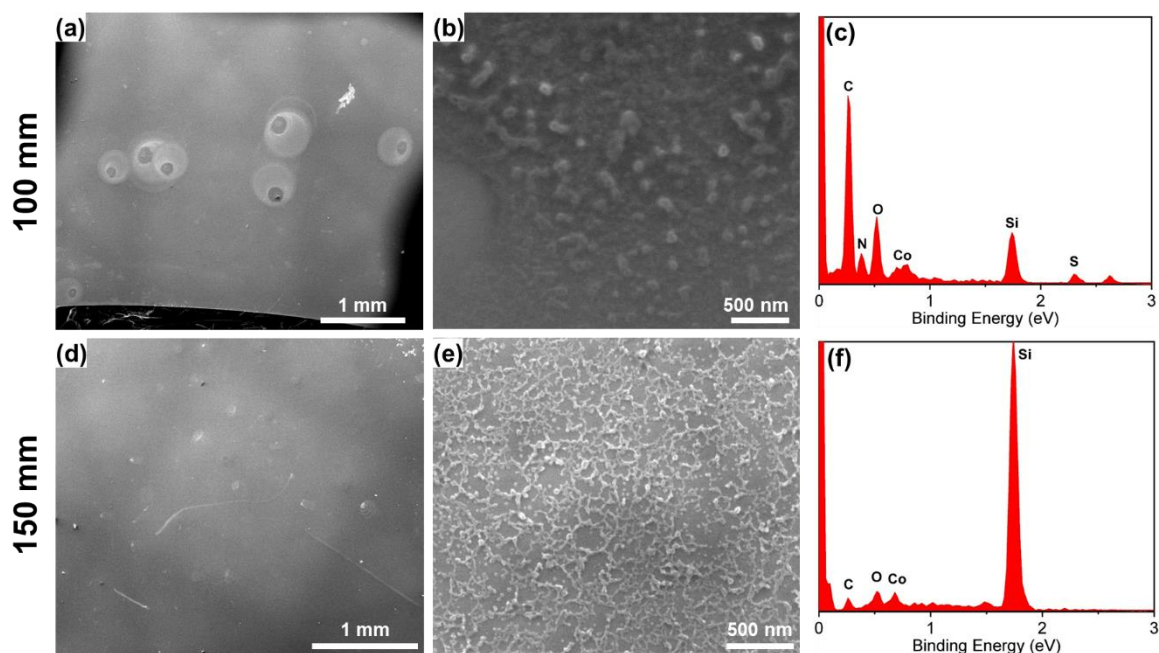


Figure 3.21: SEM images of ALI depositions of DMSO suspension of particles on Si substrates using different injector to sample distances: (a-b) 100 mm and (d-e) 150 mm. EDX on both samples are respectively shown (c and f). All other parameters remained unchanged: 5 pulses of 7 ms, a pressure of 800 mbar and 80 °C.

Suspensions in DMSO have allowed us to explore the parameters of the UHV ALI deposition technique due to the large colloidal stability of particles in DMSO. Optimization on the technique has indicated that injections of more diluted suspensions of 0.03 mg/mL using 5 pulses of short injection times (5 ms) are more adequate for the depositions. Moreover, long sample to injector distances and harsh conditions as large temperatures are needed due to the large boiling point of DMSO. This has also hindered the large deposition of particles with DMSO as wetting layers arise when applying longer or numerous pulses. Further, the large boiling point of DMSO leads to the need of long waiting times between pulses to recover UHV conditions, enlarging the deposition time process. Thus, use of another solvent with lower boiling point was sought to avoid these effects using the learned variations of the ALI deposition parameters.

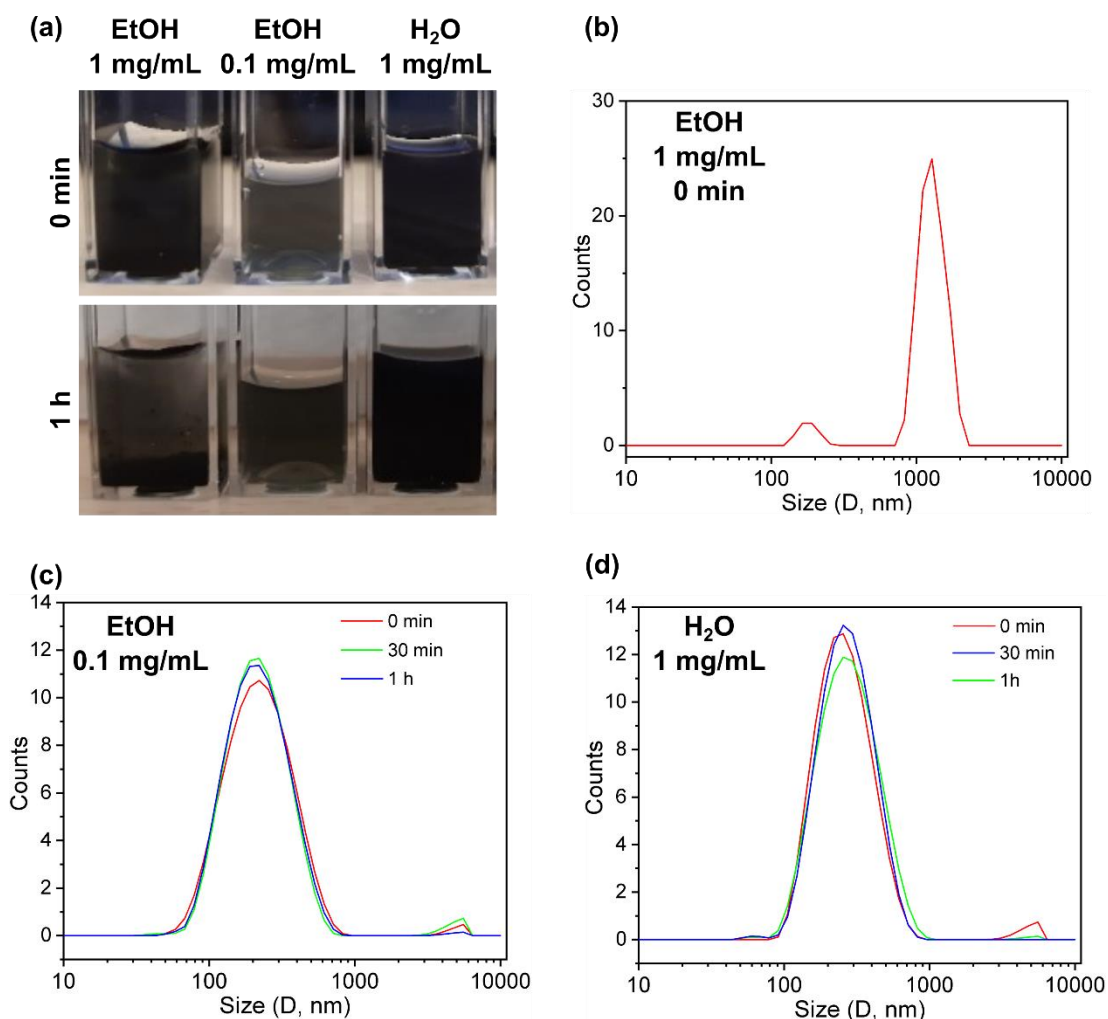


Figure 3.22: (a) Images of $\text{Co}_3(\text{HITP})_2$ suspensions over time in Ethanol (EtOH) and Water (H_2O); (b-d) DLS measurements of the suspensions at different times.

Based on the previous results on optimization of ALI deposition, aggregation during the injection may lead to irregular and few covering of the substrate. Hence, stability of the $\text{Co}_3(\text{HITP})_2$ particles was studied over an hour in ethanol and water using DLS measurements, aiming for a colloidal stable suspension suitable for the deposition (Figure 3.22). The suspensions were prepared at similar concentrations after washing of the synthesized $\text{Co}_3(\text{HITP})_2$ particles. Notoriously, upon resuspension in ethanol (EtOH) two populations arise immediately: a large population of micrometre long aggregates and a small population of stabilized $\text{Co}_3(\text{HITP})_2$ particles (Figure 3.22b). These two populations can even be identified by naked eye since after one hour a large precipitate is observed at the bottom of the DLS cuvette while a more diluted colloidal stable suspension remains (Figure 3.22a). In fact, when ten times more diluted suspension is prepared, the measured DLS size distribution matches the

one observed during the MOF characterization in Figure 3.22c, showcasing few negligible aggregates. Besides, this distribution is stable over an hour and no aggregation nor precipitate at naked eye is observed. Therefore, diluted ethanolic suspension of **Co₃(HITP)₂** particles could be a candidate to be subjected to ALI. However, aqueous suspension at 1 mg/mL concentration showcased similar size distribution and stability being hence a valuable candidate as well. As previously depicted, concentration of the suspension plays a key role in ALI deposition as injection of more concentrated samples will lead to larger amounts of material on the surface. For this reason, water was selected as the optimized solvent for the UHV deposition of this **Co₃(HITP)₂** particles synthesized according to the reported protocol.

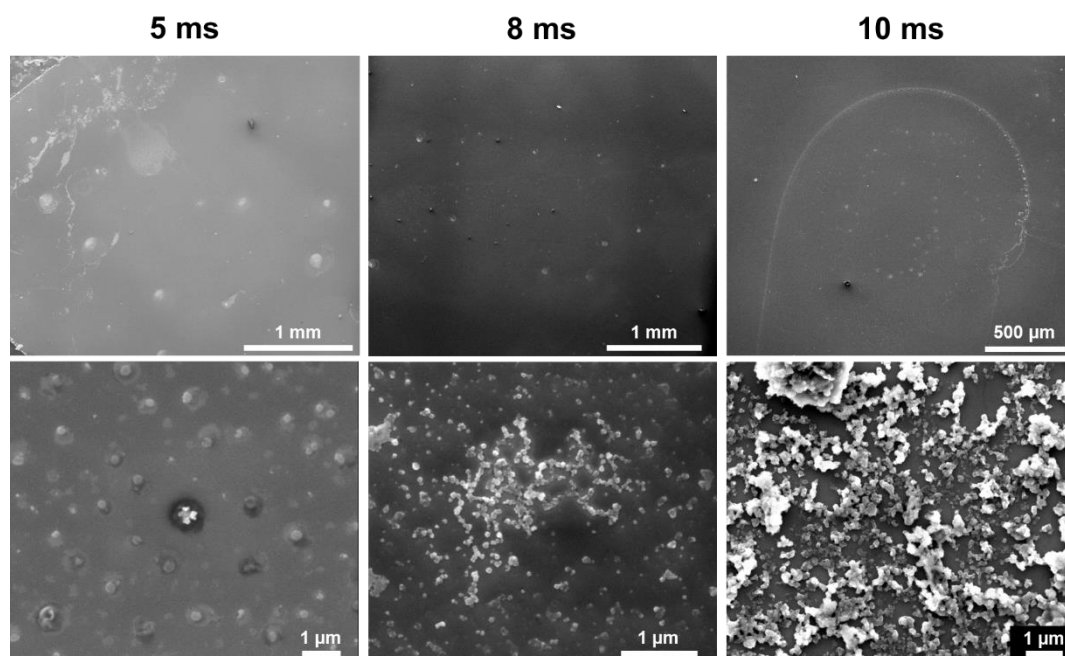


Figure 3.23: SEM images of ALI depositions of aqueous suspension of **Co₃(HITP)₂** particles on Si substrates using different pulse's length: 10 pulses of 5 ms, 8ms and 10 ms respectively. All other parameters remained unchanged: pressure of 800 mbar and room temperature.

Different essays on ALI deposition were performed using aqueous suspensions of **Co₃(HITP)₂** particles. To avoid possible obstruction of the valve as previously observed, the suspension was diluted to a 0.2 mg/mL concentration. Further, the pre-injection chamber was kept at 800 mbar and 10 pulses were set to ensure larger amounts of material on the surface. Different pulse times were hence tried. SEM images on ALI depositions using 5 ms, 8 ms and 10 ms show that at longer pulse times a larger on-surface density of particles was obtained (Figure 3.23). However, large aggregates seem to be obtained when using 10 ms pulses, which

may hinder some magnetic signals or create inter-particle interactions. On the other hand, individual particles can be identified in samples obtained employing 5 ms and 8 ms pulses. Nonetheless, a thin wetting layer seemed to be obtained when using short injection times. Thus, medium pulse times of 8 ms were chosen as optimized pulse time to ensure a dense deposition of particles as dry as possible. Sample to distance injector was optimized as an attempt to obtain drier depositions. SEM images on samples obtained at a distance of 150 mm indicated a less dense deposition of $\text{Co}_3(\text{HITP})_2$ particles showcasing smaller droplets than the sample obtained at 100 mm using similar conditions (Figures 3.24a and c). Moreover, droplets seem to have a lower payload in when placing the sample far from the injector, since some droplets do not show the presence of $\text{Co}_3(\text{HITP})_2$ particles within them. On the other hand, a large density of individual particles can be observed in the sample obtained at 100 mm. Thus, short sample to valve distances were used for the optimized deposition.

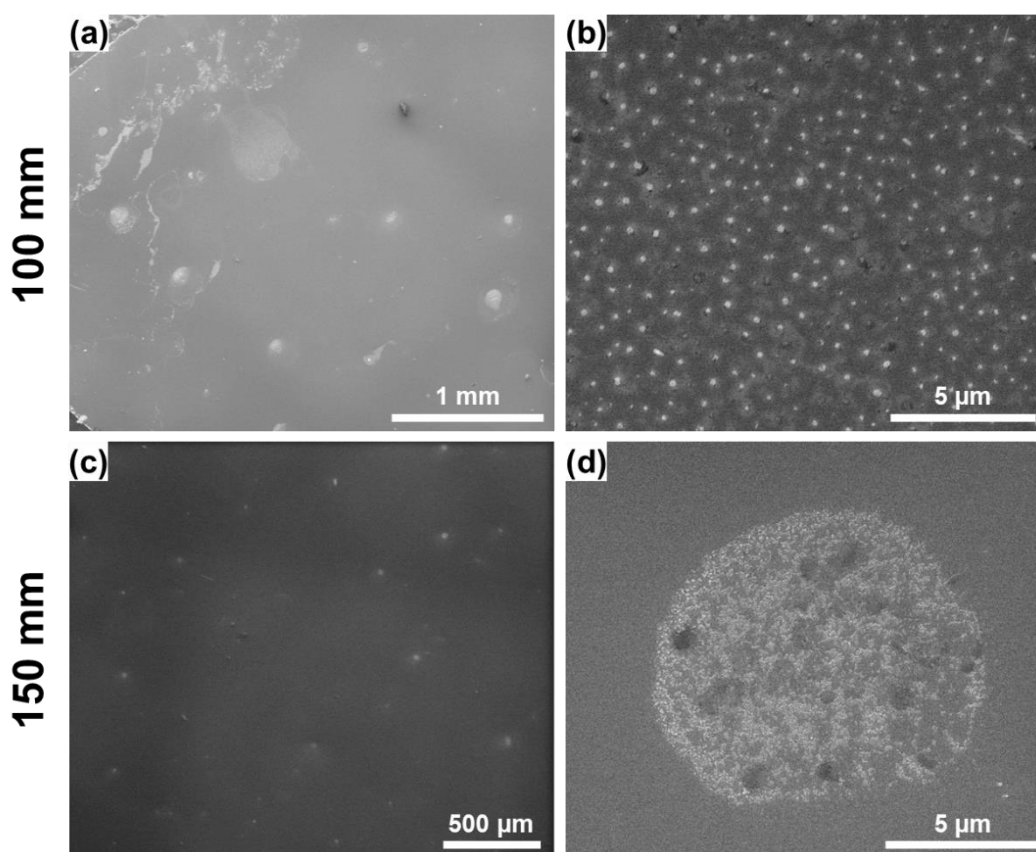


Figure 3.24: SEM images of ALI depositions of aqueous suspension of $\text{Co}_3(\text{HITP})_2$ particles on Si substrates using different injector to samples distances: (a-b) 100 mm and (d-e) 150 mm. All other parameters remained unchanged: 10 pulses of 5 ms at a pressure of 800 mbar and room temperature.

Time constraints of the ALI equipment schedule did not allow to improve the UHV deposition of $\text{Co}_3(\text{HITP})_2$ particles using water suspensions. Hence, optimized conditions chosen were: 10 pulses of 8 ms at a 100 mm sample to valve distance, at a pre-injection chamber pressure of 800 mbar and room temperature.

3.2.4. Synthesis of monolayers using UHV

HATP·6HCl ligand synthesized with the previously optimized parameters was thermally evaporated in a UHV chamber and co-deposited with a sputtered metal into a gold substrate, as schematically depicted in Figure 3.25 (this work was done by Dr. Amina Kimouche from Prof. Mugarza's group). Afterwards coordination was achieved through thermal annealing, forming a single layer of MOF catalyzed by the substrate. This methodology led to different monolayers of 2D MOF depending on the used evaporated metallic center being cobalt and iron.

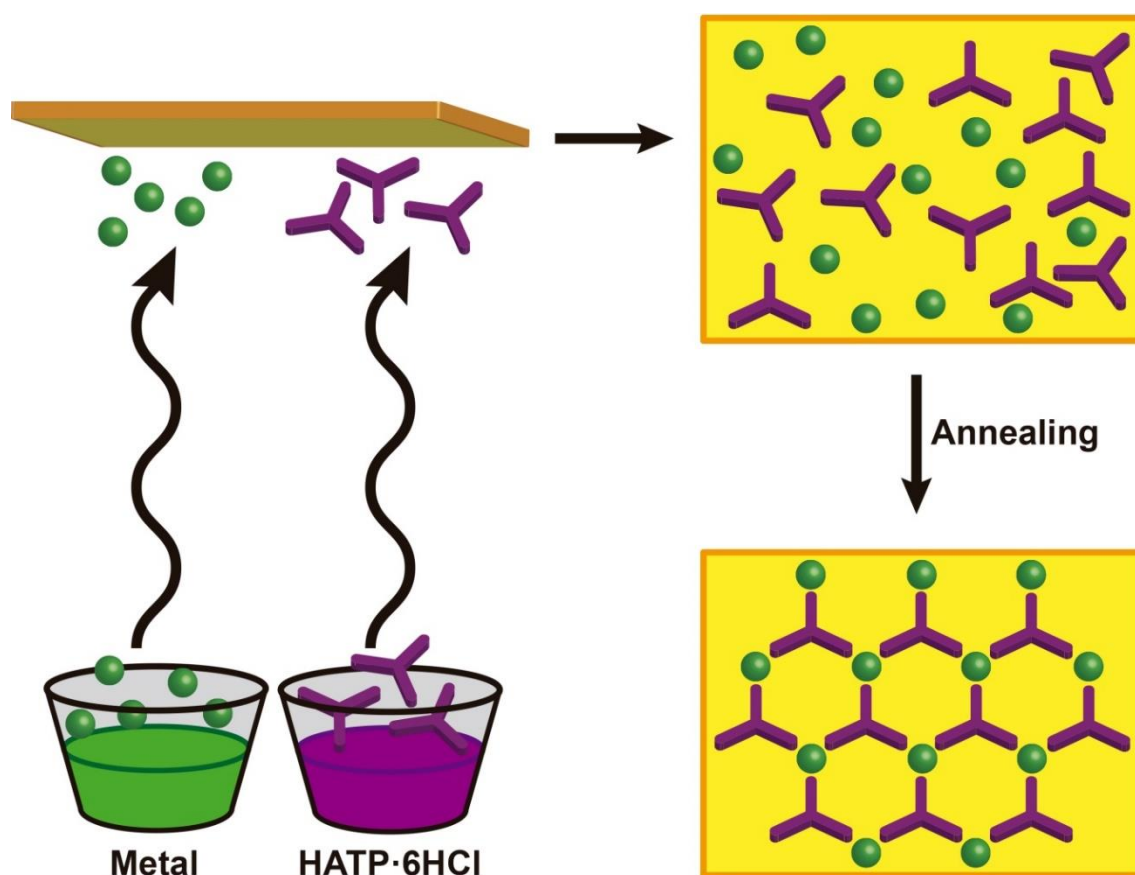


Figure 3.25: Schematic illustration of synthesis of 2D $\text{M}_3(\text{HITP})_2$ monolayers through UHV evaporation.

Co-deposition with cobalt provided long range ribbons of **Co₃(HITP)₂** monolayers that could be imaged by STM (Figure 3.26). Characteristic honeycomb lattices can be observed all over the sample. High-resolution STM image in Figure 3.27a shows the position metallic centers (seen as bright spots) and the organic molecules (less bright) matching the structure of other layered **M₃(HITP)₂** structures. X-ray Photoelectron Spectroscopy (XPS) was used to study the chemical bonds of the generated structure (Figure 3.27b).

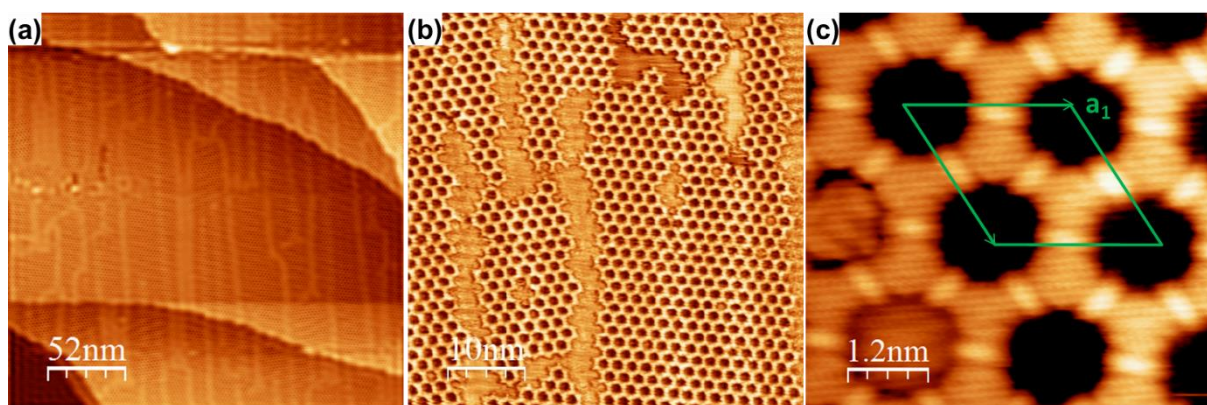


Figure 3.26: (a) (b) and (c) STM images of **Co₃(HITP)₂** ribbons synthesized through UHV evaporation. Characteristic honeycomb lattice is evidenced with unit cell as labelled in image (c). Imaging conditions: (a) 0.83V, 0.65nA; (b) 0.83V, 0.65nA; (c) -0.83V, 0.65nA.

Presence of cobalt and nitrogen was confirmed with the appearance of bands at ~780 eV and ~400 eV corresponding to 2p Co and 2p N atoms respectively. High-resolution curve-fitting was performed in order to assess the bonds present in the structure. Hence, two peaks were fitted for the C1s band, attributed to aromatic C-C at 284 eV and single C-N at 287 eV corresponding to the **HATP** bonds. However, shifting of the C-N peak suggest a progressive deprotonating of the ligand. This is supported by the fitting in the 2p N band, since the strong peak shifted at lower energies indicate the deprotonating of the amino groups and its coordination to the metallic center. Interestingly, a small shoulder at 402 eV can be observed corresponding to few protonated and non-coordinating -NH_2 groups at the edges of the material. Finally, the Co 2p spectrum shows a very tiny signal which is proportional to the coverage of Co per monolayer (1.8%).

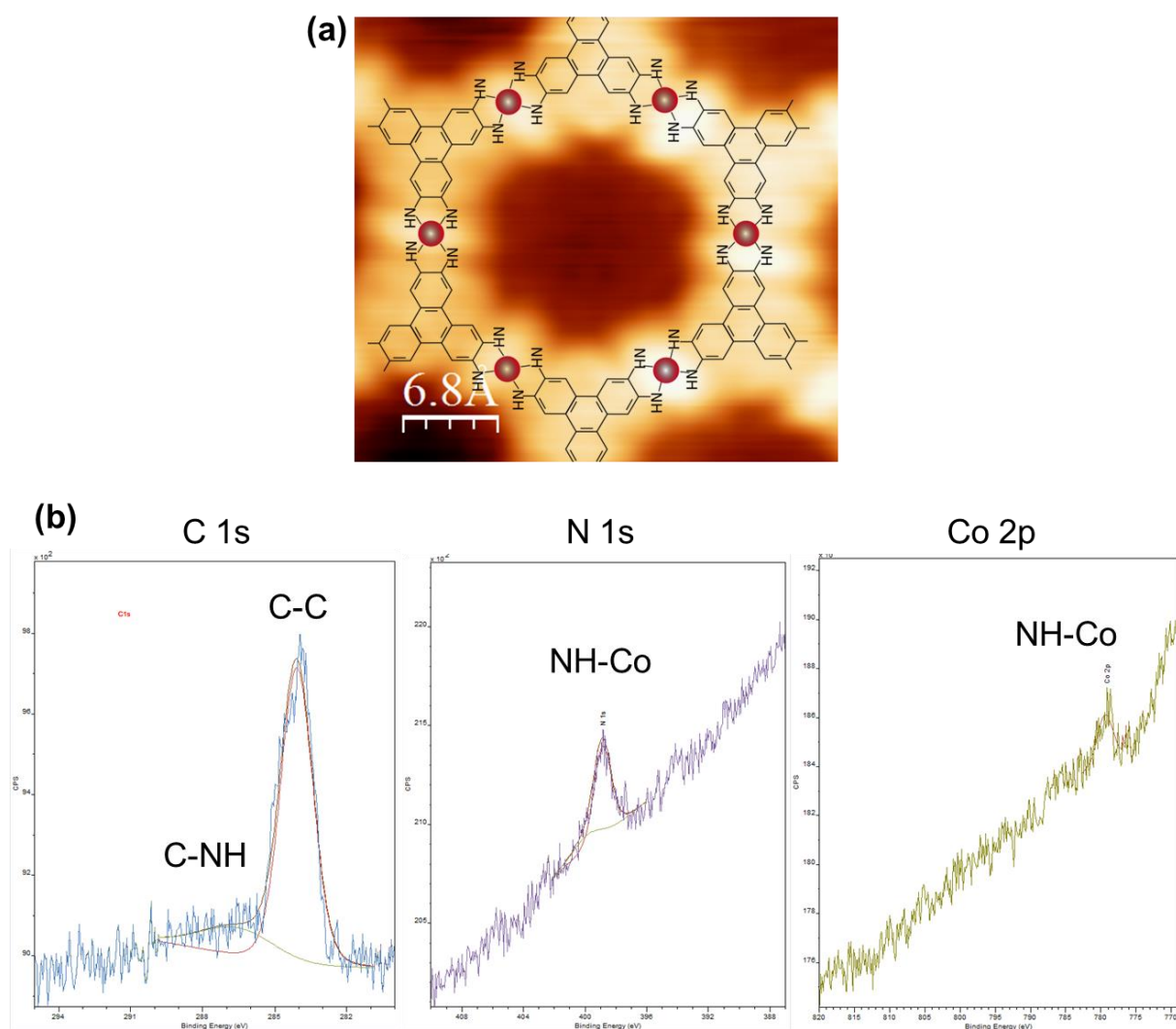


Figure 3.27: (a) High resolution STM image with chemical structure of $\text{Co}_3(\text{HITP})_2$ layer overlapped. (c) XPS spectra for carbon, nitrogen and cobalt.

Having confirmed the successful formation of $\text{Co}_3(\text{HITP})_2$ monolayers, Scanning Tunneling Spectroscopy (STS) was performed at different positions to record its electronic states (Figure 3.28). The measurements show a dominant contribution to density of states from the Co metallic center at negative bias (corresponding to energies from -1 eV to the E_F) whereas at positive bias contribution arises mainly from the ligand (corresponding to energies from the E_F to 1 eV). Interestingly, this is in agreement with the predicted PDOS from the DFT calculations (Figure 3.3). Thus, anti-ferromagnetic coupling between the Co ions is expected in this material as indicated by the theoretical simulations.

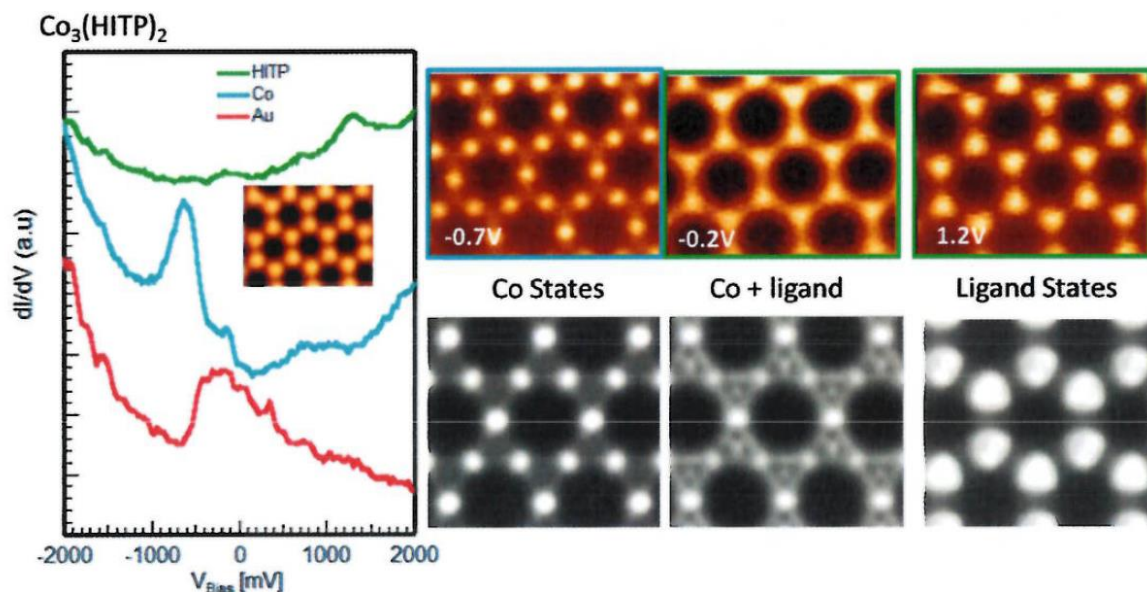


Figure 3.28: STS spectra at different locations of the sample. Experimental (top) and calculated (bottom) constant dI/dV maps at the indicated bias.

Analogously to the formation of $\text{Co}_3(\text{HITP})_2$ monolayers, $\text{Fe}_3(\text{HITP})_2$ monolayers were successfully synthesized and characterized. STM images revealed domains of monolayers. STS on $\text{Fe}_3(\text{HITP})_2$ monolayers indicated similar contribution as in the case of $\text{Co}_3(\text{HITP})_2$ ribbons, matching the predicted PDOS as well (Figure 3.29). However, as small domains are obtained, XMCD measurements could not be performed, as boundary states would be predominant.

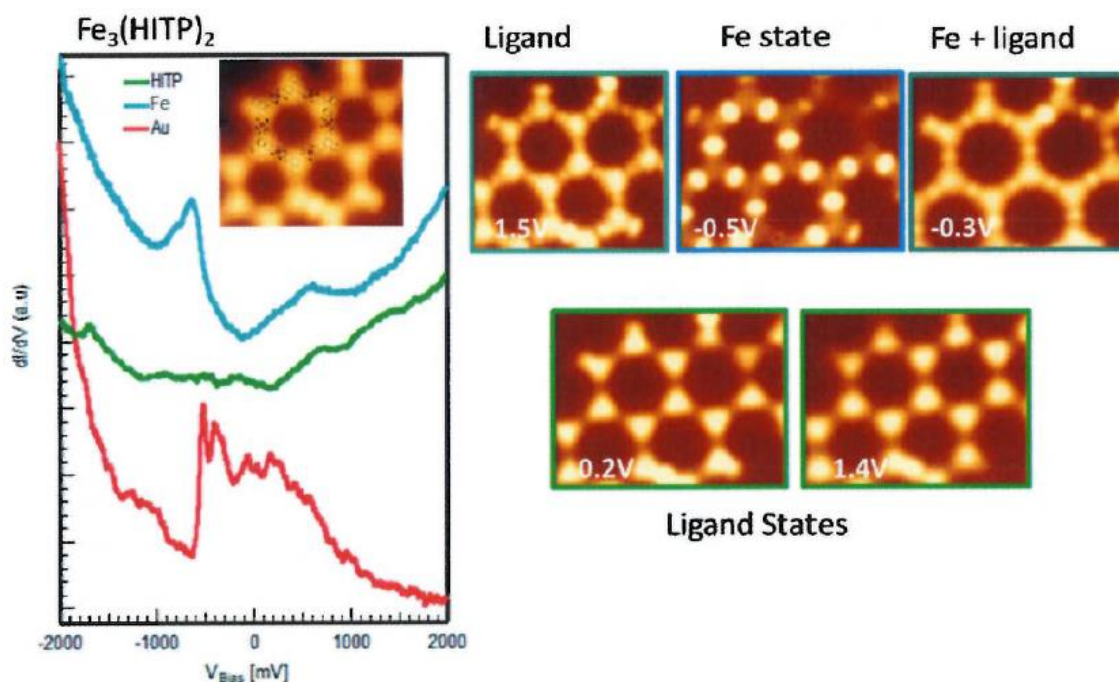


Figure 3.29: STS spectra at different locations of the sample. Experimental (top) and calculated (bottom) constant dI/dV maps at the indicated bias.

3.3 Conclusions

The synthetic methodology previously described for the synthesis of **HATP·6HCl** has been successfully modified to ensure a product of high purity for the synthesis of MOF under UHV conditions by the group of Prof. Mugarza. Single layers of **Co₃(HITP)₂** and **Fe₃(HITP)₂** with porous honeycomb hexagonal lattices were successfully obtained. Notoriously, large nanoribbons of width ~50 nm were achieved in the case of **Co₃(HITP)₂**.

For comparison purposes, the related cobalt-based MOF was also obtained in bulk as microcrystals that were successfully deposited on silicon surfaces after optimization of the different key parameters involved in the ALI process. Optimum conditions were found to be by injection of aqueous suspensions of **Co₃(HITP)₂** bulk particles at 0.2 mg/mL concentrations in 10 pulses of 8 ms at room temperature with sample to injector distances of 100 mm.

In addition, given the success of the materials obtained, these were transferred to Prof. Mugarza's group, which are being meticulously studied even at the time of writing this report. This is so in spite the fact that this characterization began more than a year and a half ago given the complexity of the system and the limited access to the synchrotron facility.

3.4 Materials and methods

3.4.1 Chemicals and materials.

Hexabromotriphenylene, and (±)-2,2'-Bis(diphenylphosphino)-1,1'-binaphthalene (rac-BINAP) were obtained from Cymit (Cymit Química S.L., Barcelona, Spain). All other chemicals were obtained from Sigma Aldrich (Merck, Madrid, Spain). All solvents were synthesis grade solvents with >99% purity purchased in Scharlab (Scharlab,S.L., Sentmenat, Spain). Aqueous solutions were prepared filtered, deionized and decalcified water.

3.4.2 Synthesis

3.4.2.1 Synthesis of HATP·6HCl with the optimized protocol

2,3,6,7,10,11-hexaaminotriphenylene hexahydrochloride, **HATP·6HCl**, was prepared adapting procedure published elsewhere. An anhydrous toluene solution (50 mL) of tris(dibenzylideneacetone)dipalladium(0) (0.448 g, 0.49 mmol) and rac-BINAP (0.607

g, 0.98 mmol) was degassed by five freeze-pump-thaw cycles, purged with Ar, and stirred at 110 °C for 30 min. After cooling at room temperature, the mixture was added with benzophenone imine (3.05 mL, 18.18 mmol), 2,3,6,7,10,11-hexabromotriphenylene (1.419 g, 2.02 mmol), and sodium tert-butoxide (1.747 g, 18.18 mmol), and the mixture was stirred at 110 °C overnight. The mixture was cooled at room temperature, diluted with CH₂Cl₂, filtered through a pad of Celite, and evaporated to dryness. The residue was subjected to column chromatography on alumina gel with AcOEt/hexane (1:4) as eluent. The last fraction was collected and evaporated to dryness, to give 2,3,6,7,10,11-hexabenzophenoneimine-triphenylene (2.001 g, 1.53 mmol) as yellow solid in 75% yield. To a THF solution (10 mL) of 2,3,6,7,10,11-hexabenzophenoneimine-triphenylene (0.219 g, 0.17 mmol) was added a 2.0 M aqueous HCl solution (0.5 mL, 1.0 mmol) and the mixture was stirred at room temperature for 0.5 h. The precipitate was isolated by centrifugation, washed with hexane (5.0 mL × 3), and dried under vacuum, to give 2,3,6,7,10,11-hexamino-triphenylene hexachloride (0.076 g, 0.14 mmol) as light yellow solid in 84% yield.

3.4.2.2 Attempts of synthesis of bulk Co₃(HITP)₂ through ammonia diffusion in DMSO

A stock solution of metallic salt was prepared by dissolving 13.3 mg (0.056 mmol) of CoCl₂·6H₂O in 10 mL of synthesis grade DMSO. 4 mg (0.0074 mmol) of **HATP·6HCl** ligand were dissolved in 2 mL of dry synthesis grade DMSO. The reaction mixture was prepared by adding 2 mL of the stock solution of CoCl₂ to the **HATP·6HCl** solution. The mixture was then placed in an ammonia-saturated gas ambience overnight. The ammonia-saturated ambience was prepared with a concentrated ammonia bath (25%) freshly prepared, 5 minutes before. The resulting black powder was recovered by dilution and precipitation in ethanol. The powder was washed with ethanol three times under centrifugation steps and posterior ambient evaporation.

3.4.2.3 Synthesis of bulk Co₃(HITP)₂ through acetate addition in water

Synthesis was performed as reported previously.¹⁶ 162.66 mg of Co(NO₃)₂·6H₂O (62.1 mmol·L⁻¹, 10 eq.) in 9 mL of DMF was preheated at 65 °C, to which was added 12 mL of NaOAc aqueous solution (2 mol·L⁻¹). To this was added a solution of 30 mg (0.0558 mmol, 1 eq.) of **HATP·6HCl** in 9 mL of water, and this mixture was heated in a 250 mL open glass vial with stirring for 2 hours at 65 °C. The resulting black powder was

filtered, and washed with large amounts of water and methanol, and dried under ambient conditions.

Centrifugation and solvent exchange: Aqueous suspensions were prepared at 1-1.2 mg/mL concentration, similar to the as synthesized mixture, after the washing steps. For solvent exchange, aliquots of the aqueous suspension were centrifuged at 4°C at 13300 rpm for 10 min. The removed water was afterwards replaced with an equivalent volume of ethanol, methanol or isopropanol.

3.4.2.4 ALI depositions

Native Si substrates were previously washed by 10 min sonication in acetone, followed by 10 min sonication in ethanol and N₂ blow-drying. Then, the substrates were loaded in the UHV chamber of the ALI equipment. Atomic Layer Injection was performed with model ALI-1000 from BihurCrystal S.L. (San Sebastián, Spain). Optimization on the injection parameters can be found on the main text.

3.4.3 Characterization

3.4.3.1 Characterization of HATP•6HCl

Proton Nuclear Magnetic Resonance H-NMRs were performed dissolving 10 mg of powder in 0.7 mL of *d*-DMSO and using a Bruker DPX360 MHz NMR spectrometer (Bruker).

UV-vis absorbance spectroscopy UV-vis spectrum of **HATP•6HCl** aqueous solution at 50 ppm was recorded in transmission mode using Cary 60 spectrophotometer and in a 1 mm quartz cuvette.

Thermogravimetric analysis TGA was performed in a NETZSCH -STA 449 F1 Jupiter equipment in argon atmosphere, applying a heating ramp of 25 to 700 °C at a constant rate of 10 °C/min.

Fourier-Transform Infrared Spectroscopy FT-IR was performed with Tensor 27 FT-IR spectrometer (Bruker) in transmittance mode. The instrument is equipped with a room temperature detector and a mid-IR source (4000 to 400 cm⁻¹). The samples were prepared grinding a mixture of small amount of crystal and KBr powder, which does not absorb IR radiation. A pure KBr disc was used to create the background spectra for

all measurements. The spectra were recorded and treated with OPUS (Bruker) data collection software.

Matrix-Assisted Laser Desorption/Ionization Mass Spectroscopy MALDI-MS was performed with Bruker MALDI-TOF Ultraflex extreme equipment (Bruker).

3.4.3.2 Characterization of bulks $\text{Co}_3(\text{HITP})_2$

Proton Nuclear Magnetic Resonance H-NMRs were performed dissolving 10 mg of powder in 0.7 mL of *d*-DMSO and 0.05 mL of DCl solution (35 wt. % in D_2O) and using a Bruker DPX360 MHz NMR spectrometer (Bruker).

Wide-Angle X-Ray Scattering WAXS patterns were measured at the NCD-SWEET beamline at the ALBA synchrotron using 12.4 keV radiation and a Rayonix LX255HS detector and integrated into one-dimensional patterns.

Scanning Electron Microscopy SEM images of the crystals were obtained with SEM FEI Quanta 650F microscope. The samples were prepared by drop-casting of the crystals suspensions onto metallic sample holders. After evaporation of the solvent under ambient conditions, the previously suspended crystals remained on the holders. Afterwards, the particles were imaged with high acceleration voltages, between 10 to 20 kV at a working distance of 10 mm.

Transmission Electron Microscopy HR-TEM was performed with FEI Tecnai G2 F20 S-Twin HRTEM at acceleration voltages of 200 kV. Samples were prepared by drop-casting crystals suspensions onto ultrathin carbon on lacey carbon holders. Elemental analysis color maps were obtained performing Electron Energy Loss Spectroscopy with super ultra-thin window X-ray detector with 136 eV resolution.

Fourier-Transform Infrared Spectroscopy FT-IR for bulk material was performed with Tensor 27 FT-IR spectrometer (Bruker) in transmittance mode. The instrument is equipped with a room temperature detector and a mid-IR source (4000 to 400 cm^{-1}). The samples were prepared grinding a mixture of small amount of crystal and KBr powder, which does not absorb IR radiation. A pure KBr disc was used to create the background spectra for all measurements. The spectra were recorded and treated with OPUS (Bruker) data collection software.

Dynamic Light Scattering Size distribution in colloidal suspension was studied by DLS with Zetasizer Nano 3600 equipment (Malvern Instruments) at room temperature (20-25°C). The data was collected with the Zetasizer 7.04 software. The samples were introduced in disposable 1 cm plastic cuvettes and afterwards measured.

UV-vis absorbance spectroscopy UV-vis spectra of suspensions were recorded in transmission mode using Cary 60 spectrophotometer and in a 1 mm quartz cuvette.

3.4.3.3 Characterization of $\text{Co}_3(\text{HITP})_2$ on surface depositions (ALI).

Scanning Electron Microscopy SEM images of the spin-coating and ALI depositions were obtained with SEM FEI Quanta 650F microscope. The samples were imaged as obtained, stuck onto metallic holders with carbon tape. Low magnification images were taken with low acceleration voltages Afterwards, the samples were imaged with low acceleration voltages, between 10 to 20 kV at a working distance of 10 mm. EDX spectra were collected using an Inca 250 SSD XMax20 detector.

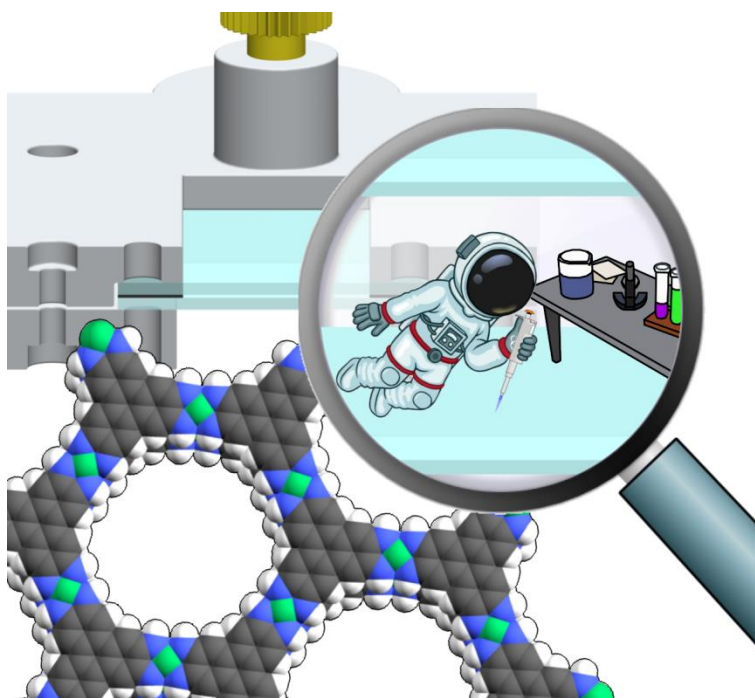
3.5 References

1. L. Yu, Z. B. Li, D. Wang, *Chem. Commun.* **2016**, 52, 13771.
2. Z. Gao, Y. Gao, M. Hua, J. Liu, L. Huang, N. Lin, *J. Phys. Chem. C* **2020**, 124, 27017.
3. S. Zint, D. Ebeling, S. Ahles, H. A. Wegner, A. Schirmeisen, *J. Phys. Chem. C* **2016**, 120, 1615.
4. L. Giovanelli, O. Ourdjini, M. Abel, R. Pawlak, J. Fujii, L. Porte, J.-M. Themlin, S. Clair, *J. Phys. Chem. C* **2014**, 118, 14899.
5. N. A. A. Zwaneveld, R. Pawlak, M. Abel, D. Catalin, D. Gigmes, D. Bertin, L. Porte, *J. Am. Chem. Soc.* **2008**, 130, 6678.
6. C. Liu, Y. Yu, W. Zhang, Q. Zeng, S. Lei, *Chem. - A Eur. J.* **2016**, 22, 18412.
7. M. Lischka, R. Dong, M. Wang, N. Martsinovich, M. Fritton, L. Grossmann, W. M. Heckl, X. Feng, M. Lackinger, *Chem. – A Eur. J.* **2019**, 25, 1975.
8. Z. Gao, C.-H. Hsu, J. Liu, F.-C. Chuang, R. Zhang, B. Xia, H. Xu, L. Huang, Q. Jin, P. N. Liu, N. Lin, *Nanoscale* **2019**, 11, 878.
9. L. Yang, X. He, M. Dincă, *J. Am. Chem. Soc.* **2019**, 141, 10475.
10. Y. Misumi, A. Yamaguchi, Z. Zhang, T. Matsushita, N. Wada, M. Tsuchiizu, K. Awaga, *J. Am. Chem. Soc.* **2020**, 142, 16513.
11. X. Song, X. Wang, Y. Li, C. Zheng, B. Zhang, C. Di, F. Li, C. Jin, W. Mi, L. Chen, W. Hu, *Angew. Chemie* **2020**, 132, 1134.
12. H. Zhang, *ACS Nano* **2015**, 9, 9451.
13. M. Caputo, M. Panighel, S. Lisi, L. Khalil, G. Di Santo, E. Papalazarou, A. Hruban, M. Konczykowski, L. Krusin-Elbaum, Z. S. Aliev, M. B. Babanly, M. M. Otrokov, A. Politano, E. V. Chulkov, A. Arnau, V. Marinova, P. K. Das, J. Fujii, I. Vobornik, L. Perfetti, A. Mugarza, A. Goldoni, M. Marsi, *Nano Lett.* **2016**, 16, 3409.
14. A. Lerch, L. Fernandez, M. Ilyn, M. Gastaldo, M. Paradinas, M. A. Valbuena, A. Mugarza, A. B. M. Ibrahim, J. Sundermeyer, U. Höfer, F. Schiller, *J. Phys. Chem. C* **2017**, 121, 25353.

15. A. Lodi Rizzini, C. Krull, A. Mugarza, T. Balashov, C. Nistor, R. Piquerel, S. Klyatskaya, M. Ruben, P. M. Sheverdyayeva, P. Moras, C. Carbone, C. Stamm, P. S. Miedema, P. K. Thakur, V. Sessi, M. Soares, F. Yakhou-Harris, J. C. Cezar, S. Stepanow, P. Gambardella, *Surf. Sci.* **2014**, *630*, 361.
16. T. Chen, J.-H. Dou, L. Yang, C. Sun, N. J. Libretto, G. Skorupskii, J. T. Miller, M. Dincă, *J. Am. Chem. Soc.* **2020**, *142*, 12367.
17. L. Chen, J. Kim, T. Ishizuka, Y. Honsho, A. Sacki, S. Seki, H. Ihee, D. Jiang, *J. Am. Chem. Soc.* **2009**, *131*, 7287.
18. J. Park, M. Lee, D. Feng, Z. Huang, A. C. Hinckley, A. Yakovenko, X. Zou, Y. Cui, Z. Bao, *J. Am. Chem. Soc.* **2018**, *140*, 10315.

Chapter 4: Synthesis of 2D TP MOF Thin Films under simulated microgravity conditions

In the following Chapter, an easy and highly efficient method is shown to achieve space-like experimentation conditions on Earth employing custom-made microfluidic devices to fabricate 2D porous crystalline MOFs. Experimentation under these simulated microgravity conditions has unprecedented effects on the orientation, compactness and crack-free generation of 2D porous crystalline molecular frameworks.



*Work presented in this chapter was published and accepted as front cover in
Advanced Materials, 2021, 2101777.*

4.1 Introduction

4.1.1 Conductive triphenylene-based 2D MOFs thin films

Conductive porous 2D MOFs have recently opened the way to a new family of functional electronic materials.¹ This premise has not been proven only with enhanced conductivity in MOF by infiltration of doping agents into the pores² but also with the arise of novel applications for these materials such as field-effect transistors,³ chemiresistive gas sensors⁴ including e-textiles,⁵ electrochemical oxygen reduction catalysts⁶ or supercapacitors.⁷

However, issues in the synthetic routes hinder the potential of these materials.⁸ Reactions are frequently conducted under vigorous stirring to improve the mass transport of reagents and to increase the reaction efficiency via turbulent flows. Nonetheless, turbulent conditions lead to a poor control of convective transport processes which may prompt the precipitation of reaction products and significantly affect the reaction performance. This scenario is especially critical during the synthesis of 2D and 3D functional crystals with controlled sizes and shapes. For example, 3D crystalline porous molecular frameworks such as MOFs are often synthesized using turbulent mixing,⁹ and/or solvothermal methods,^{10,11} among others.¹² In these synthetic conditions, the formation of MOF crystals depletes the surrounding monomer solution, thus creating buoyancy-driven convection, which generates uneven growth rates and the precipitation (sedimentation) of crystals in solution. Precipitation can significantly affect the reaction performance, for example, by leading to a noncontrolled and non-uniform growth rate of MOF crystals in solution. Other methods that are particularly suitable for the generation of functional 2D porous crystalline molecular frameworks (*e.g.* 2D MOFs) are surface-templated growth methods^{13,14} or interfacial synthetic approaches (*e.g.* liquid/air or liquid/liquid interfaces).^{15–17} Certainly, these methods can also suffer noncontrolled convective transport processes (*e.g.* surface-tension-driven convection (Marangoni convection)) and precipitation leading to fragmentation of the MOF films as well as to a poor control over their orientation, compactness, roughness profile, and/or morphology, features that greatly impact their function and performance.^{15,16}

4.1.2 Microfluidics as simulated microgravity synthetic conditions

Recently, groundbreaking studies at the International Space Station clearly confirmed the favorable effect of microgravity on the growth of crystalline matter.¹⁸ It has been

demonstrated that the convection-free mass transport occurring in microgravity conditions can greatly favor the synthesis of materials with larger crystalline domain sizes, lower defect densities and new morphologies.¹⁹ However, the high costs and restricted access to experimentation in space have hindered efforts to study and control the engineering of MOF crystals as well as other functional and porous crystalline materials under these synthetic conditions. Herein, we show that microfluidic devices can simulate on Earth the effect of the microgravity in space experimentation.

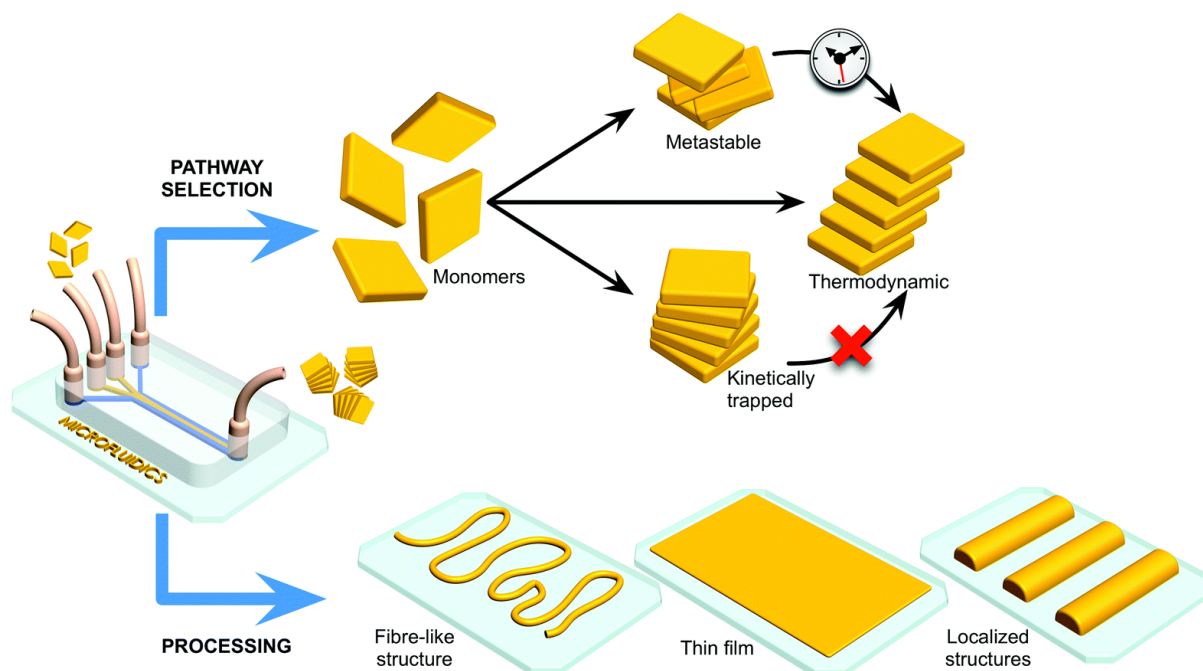


Figure 4.1: Microfluidic approaches allow the pathway selection of crystalline phases during self-assembly syntheses, enabling the metastable or kinetically trapped assemblies unavailable in typical thermodynamic methodologies. Moreover, use of microfluidics enables the processing of self-assembled structures onto substrates and designable shape. Reproduced from ref. 21.

Microfluidic devices have been already proposed as on Earth simulators of the microgravity effect in space experimentation.²⁰ Low Grashof numbers are common characteristics of microgravity and microfluidic conditions, where buoyancy forces are heavily suppressed. Recently, Puigmartí and co-workers proved a high control on the synthesis of peptide-based MOFs through the use of microfluidics, mimicking growth conditions of reported biomineralizations in microgravity. Notoriously, they reported millimeter long single crystals of peptide-based MOFs aside the control on the shape and growth direction of the crystals giving rise to non-equilibrium morphologies. Further, controlled diffusion of reagents in microfluidics give rise to out-standing properties in the

technique such as pathway selection (obtaining novel intermediate crystalline species) or processing of the final material into a desired shape (Figure 4.1). Thus, microfluidics can open the way to unprecedented growth of MOF thin films mimicking microgravity conditions.

This premise has been corroborated with some first attempts on synthesizing MOF thin films with microfluidics in-situ in fibers or capillaries. Notoriously, Nair and collaborators reported the interfacial microfluidic membrane processing technique (IMMP) in 2014 which allowed to synthesize ZIF-8 thin films supported on Torlon hollow fibers.²² The synthesis relied on a two-solvent interface occurring at the porous fiber wall and a microfluidic flow inside the fibers themselves. Detailer, an alcoholic solution of zinc salt was flowed within the fibers while these ones were immersed in an aqueous solution of imidazole ligand (Figure 4.2a). The organic ligand would diffuse through the fibers' porous wall and meet the metallic ion at the fibers' inner shell, where growth of the MOF occurred. The obtained ZIF-8 films showcased thicknesses in the range of microns and remarkable H₂ and C₃H₆ separation properties. Deeper studies on the synthesis control of this technique have been reported in 2016 by the same group proving the relevance of parameters as reagents ratio, flow of the metallic container solution or temperature on the film's properties such as the gas separation performance, allowing two-stage separations of ternary gas mixtures.^{23,24}

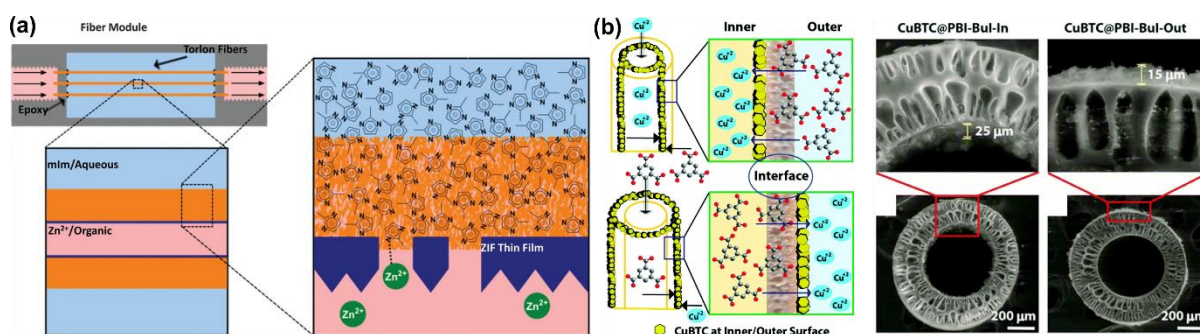


Figure 4.2: (a) Synthesis of ZIF-8 thin films on Torlon hollow fibers using IMMP technique. Image extracted from ref. 22. (b) HKUST-1 thin films grown on polybenzimidazole hollow fibers. Image extracted from ref. 25.

Remarkably, the technique has been exported to other groups expanding the potential of the technique. In 2015, Kharul *et al.* reported the synthesis of ZIF-8 and HKUST-1 thin films on either the inner or outer surface of polybenzimidazole hollow fibers.²⁵ Since the organic ligand was the one migrating through the porous wall, if the metal containing solution flowed inside the fiber and the ligand solution remained outside, the two-solution interface and therefore the reaction occurred at the inner wall of the fiber (Figure 4.2b). On

the other hand, if the ligand solution was the one flowed inside the fiber, the thin films grew on the outer surface of the fiber.

Further, the MOF thin film growth on fibers using microfluidics was extrapolated to synthesis other than interfacial. In 2015, Coronas and co-workers introduced the synthesis of micrometered thick and thermally stable ZIF-7 and ZIF-8 films on polysulfonate hollow fibers by simultaneously flowing the solutions containing the metallic and organic precursors in a microfluidic system.²⁶ Analogously, capillary systems have been also used in order to grow MOF thin films using microfluidic flows. In a work published by Zhang et al. a homochiral pillared $\text{Cu}_2(\text{D-cam})_2\text{P}$ was grown on capillaries functionalized with hydroxyl groups or poly(L-DOPA) by liquid phase epitaxy, flowing alternatively solution containing the copper salt or the organic ligands²⁷ (Figure 4.3b). In this work, the relevance of the substrate is highlighted as different crystalline orientation on the MOF thin film were obtained depending on the capillary's functionalization and enantiomer separation was achieved when using poly(L-DOPA) based MOF thin films in gas chromatography. Furthermore, recently, Jeong et al reported the synthesis of sub-micron thick ZIF-8 thin films on polymeric hollow fibers using microwave-assisted seeding and microfluidic-based secondary growth combined.²⁸ As shown in Figure 4.3a, a first step of metal saturation of the fiber was followed by the injection of ligand solution in the fiber while heating the fiber with microwaves. Subsequently, a mixture of metal and ligand solution was flowed through the fiber leading to ultrathin films. All these premises seeded the way to microfluidic growth of MOF thin films. However, these reported methods are constrained to hollow fibers or capillaries acting as reactor with micrometered diameters and non-flat supporting substrates.

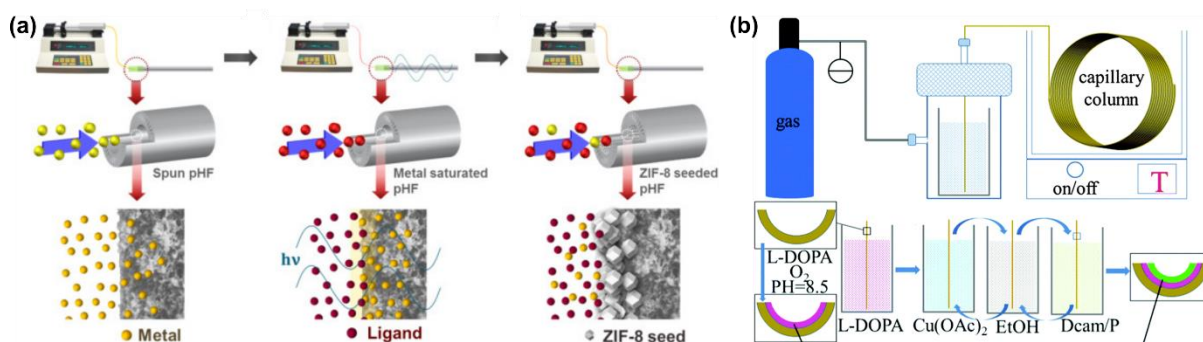


Figure 4.3: (a) ZIF-8 growth in capillary systems using microwave heating. Image extracted from 28. (b) Growth of $\text{Cu}_2(\text{D-cam})_2\text{P}$ on functionalized capillary with hydroxyl or poly(L-DOPA). Image extracted from 27.

Noteworthy, Puigmartí-Luis *et al.* recently achieved the spatiotemporal controlled generation of HKUST-1 thin films employing the in-flow MOF lithography method.²⁹ Detailer, a diffusion of benzene-tricarboxylate (BTC) ligand solution was performed through microfluidic channel patterned on a polydimethylsiloxane (PDMS) chip pressed on top of a metal-containing reactive substrate (Cu_2O). Control on the reagent diffusion proved to be key to obtain continuous and homogeneous films. As shown in Figure 4.4a-b, BTC ligand solution was flowed in the microfluidic chip along with a pure ethanol solution. The flow rate ratio of the two solutions determined the position of the interface of these. Modifying the ratio allowed to expose different areas of the Cu_2O substrate for different times (Figure 4.4c), which lead to different degrees of HKUST-1 covering on top of the substrate (Figure 4.4d-e). Notoriously, this method allowed patterning the thin film into several microstructures by shaping the polymeric device (Figure 4.4 f-g).

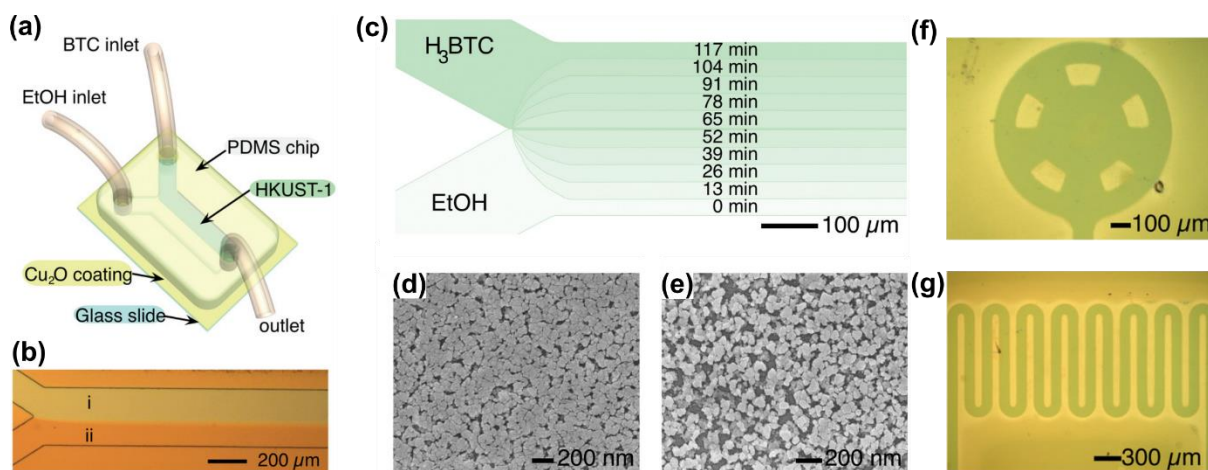


Figure 4.4: (a) and (b) Schematic illustration and OM of the microfluidic in-flow MOF lithography device respectively. (c) Schematic of the controlled exposure of the Cu_2O substrate to the BTC for different times. (d) and (e) SEM images of areas where BTC flowed 100 and 60 min respectively. (f) and (g) Shape patterning of the thin film. Images adapted from ref. 29.

4.1.3 Our microfluidic approach

Hence, using flat surfaces as part of the reaction chamber can open the way to supported thin film growth assisted by microfluidics, simulating microgravity conditions on down-Earth set-up. Thus, in this Chapter, a newly-engineered microfluidic device that consists of two substrates sandwiched with a thin silicone film with variable thicknesses (from 80 μm to 200 μm) to create a microfluidic environment 6 cm in length and 1.5 cm in width (see Figure 4.5a). One of the surfaces has two machined inlet ports that allow the

injection and complete filling of the microfluidic environment preventing the appearance of air bubbles (Figure 4.5b and 4.5c). For more details on the microfluidic device see Figure 4.51 in Materials and Methods section. The device was designed and developed by the group of Prof. Josep Puigmartí-Luis from *ETH Zürich* and the *University of Barcelona* since 2020. Therefore, this project has been performed in collaboration with his groups, including a research stay of three months in the *ETH Zürich*.

We chose to synthesize $\text{Ni}_3(\text{HITP})_2$ as an exemplar case for three main reasons: i) $\text{Ni}_3(\text{HITP})_2$ is a MOF whose growth has been difficult to control – $\text{Ni}_3(\text{HITP})_2$ precipitates quickly in solution due to its fast coordination reaction in alkaline media and when exposed to oxidation conditions (*e.g.* atmospheric oxygen). In fact, $\text{Ni}_3(\text{HITP})_2$ precipitates as unprocessable black particles dispersed in the reaction media due to an uncontrolled oxygen diffusion,³⁰ a result that has hampered the harnessing of its growth as well as its direct integration to read-out components. ii) $\text{Ni}_3(\text{HITP})_2$ is a conductive 2D MOF with extended π -conjugation, analogous to graphene, but whose conductivity properties have been derived mainly from pressed pellets and from randomly oriented polycrystalline $\text{Ni}_3(\text{HITP})_2$ thin films.³¹ iii) $\text{Ni}_3(\text{HITP})_2$ can be synthesized following a two-step vapor induced crystallization approach. Yet, a controlled two-step vapor induced crystallization of $\text{Ni}_3(\text{HITP})_2$, first with volatile alkaline vapors and subsequently with oxidant gasses, cannot be systematically done employing common synthetic approaches.¹⁵

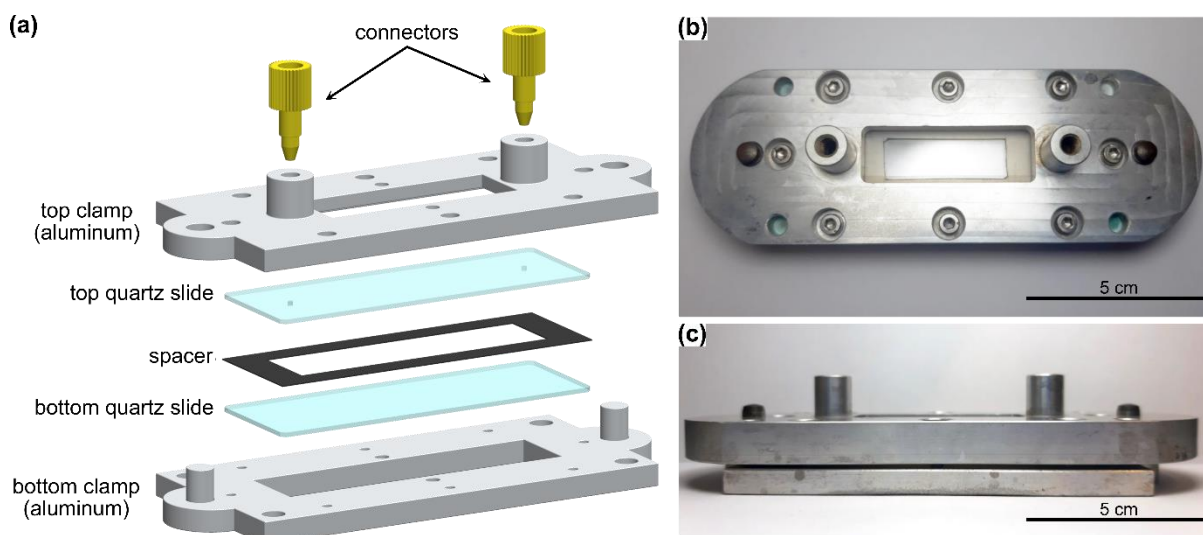


Figure 4.5: (a) Illustration showing an expanded view of the microfluidic device. (b) and (c) Top and side view photographs of the microfluidic device, respectively.

Computational fluid dynamics approach based on finite volume method were done to shed more light into the transport phenomena inside the microfluidic device. This part was done by the group of Prof. Tiago Sotto Mayor from *SIMTECH Laboratory* (Portugal). Two scenarios were considered in our numerical analyses: i) the conventionally used vapor-assisted conversion method,³² where $\text{Ni}_3(\text{HITP})_2$ is generated from a hypothetical droplet of precursors when exposed to volatile alkaline gas and atmospheric oxygen, and ii) the synthesis of $\text{Ni}_3(\text{HITP})_2$ inside our custom-made microfluidic device, where a controlled diffusion of the volatile reactive species in the reaction media can be easily achieved (see Figure 4.6). Anhydrous DMSO was chosen as the solvent of reaction in both scenarios as it is one of the solvents tried in the syntheses using the microfluidic device (see *vide infra*).

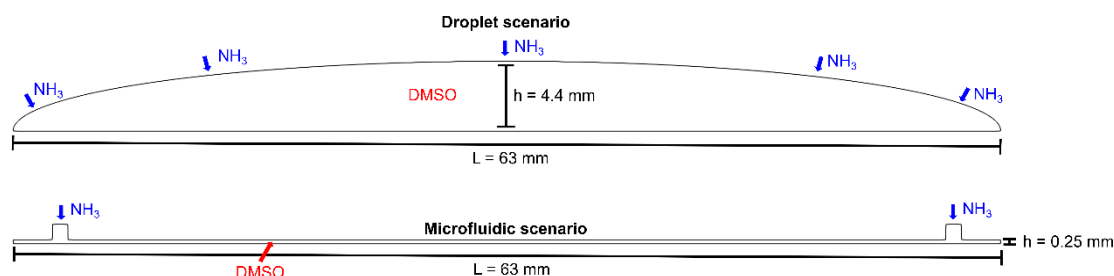


Figure 4.6 Representation of the droplet and microfluidic scenarios considered in the numerical analyses. There is solute (NH_3 , blue) moving from the gas phase to the liquid phase (DMSO, red) through the liquid-gas interface. This interface is considered to be the arc of the droplet in the droplet scenario, and the cross-section of the inlet tubes in the microfluidic device scenario.

The velocity and the concentration maps in the droplet and the microfluidic device after 1 minute are shown in Figure 4.7, whereas the maps after 30 minutes are shown in Figure 4.8. The concentration-driven density difference between the lighter solute (NH_3) and the denser liquid phase (DMSO) generates buoyancy forces that overcome the viscous forces, leading to the onset of buoyancy-driven convection within the liquid phase. This is observed in both the droplet and the microfluidic scenarios, though with vastly different intensity and impact over the associated transport processes.

Interestingly, we observed that in the droplet scenario, there are two counter-rotating vortices spanning most of the droplet diameter (see Figure 4.7a) where fluid elements move inwards along the droplet upper free surface (*i.e.* the gas-liquid interface) and outwards near the substrate. In agreement with this, there is an evident accumulation of the less dense ammonia solute in the upper part of the droplet (Figure 4.8c), and a horizontal concentration front moving downwards towards the substrate (*i.e.* in the direction of gravity), see Figure

4.8c. In this scenario, the precursors can mix and react in the upper part of the droplet, before the solute concentration front reaches the substrate. During this time, $\text{Ni}_3(\text{HITP})_2$ powders may start to form in the upper part of the droplet due to the oxidation reaction with atmospheric oxygen, and the $\text{Ni}_3(\text{HITP})_2$ precipitate will be pulled down by gravity, adding to the already existing convective currents inside the droplet. In sharp contrast, and as shown in Figure 4.7b, the microfluidic device used in our investigations allows to dramatically reduce the effect of convective mass transport during the reaction process. Indeed, much smaller/weaker vortices are observed (and only near the device inlets), whose velocities (in the $\mu\text{m/s}$ range) are ca. 1000 times smaller (at 1 min) and ca. 25 smaller (at 30 min) than those observed inside the droplet (see Figure 4.7 and Figure 4.8). In agreement with this, the concentration profile is also vastly different from that in the droplet scenario, with the microfluidic device having a vertical concentration front moving horizontally along the substrate length (i.e. perpendicular to the direction of gravity), see Figure 4.8d. The clearly different synthetic conditions generated with our microfluidic approach enables the vapor-assisted synthesis of $\text{Ni}_3(\text{HITP})_2$ in a reaction environment that induces the convection-free mass transport conditions achieved in space experimentation.

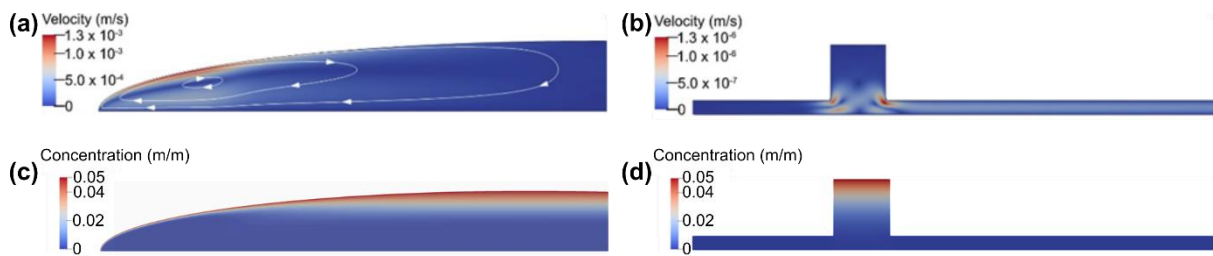


Figure 4.7: (a) and (b) Velocity maps after 1 min of simulation time for the droplet and the microfluidic device, respectively. The images are zoomed in to allow the visualization of the flow details. Streamlines are also shown in the droplet velocity map to highlight the motion of the fluid elements. (c) and (d) Concentration maps after 1 min of simulation time for the droplet and the microfluidic device, respectively. The concentration maps are shown with ranges of 0 – 0.05 (m/m).

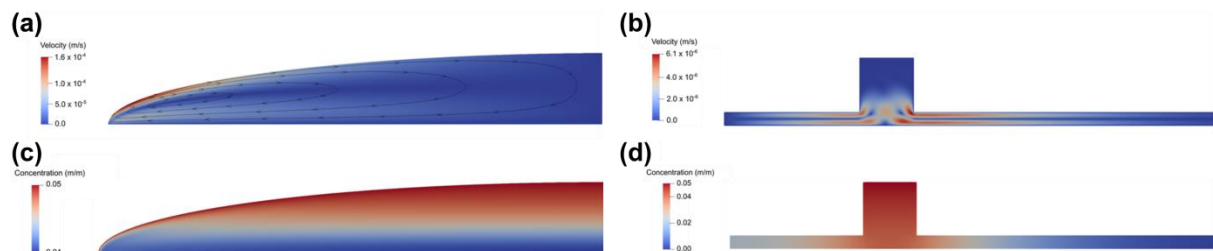


Figure 4.8: (a) and (b) Velocity maps after 30 min of simulation time for the droplet and the microfluidic device, respectively. The images are zoomed in to allow the visualization of the flow details. Streamlines are also shown in the droplet velocity map to highlight the motion of the fluid elements. (c) and (d) Concentration maps after 30 min of simulation time for the droplet and the microfluidic device, respectively. The concentration maps are shown with ranges of 0.04-0.05 and 0 – 0.05 (m/m) respectively.

4.1.4 Scope of this chapter

Considering the support of the theoretical calculations to the high control of synthesis using the designed microfluidic devices, the specific objectives of this Chapter are:

- To study the synthesis of **Ni₃(HITP)₂** thin films using the newly described microfluidic device, attempting its crystallization with different solvents (water and DMSO).
- To characterize the obtained thin films studying the impact of simulated microgravity environment the morphology and crystalline properties and control over them.
- To assess the compatibility of the microfluidic device to a wide variety of substrates.
- To study the effect of microgravity synthetic environments into the electrical properties of the thin films.

4.2 Results and discussion

As previously commented, the synthesis using the microfluidic device was studied using different solvents for the crystallization. Solvent will not only determine the diffusion of reagents in the gas phase (ammonia and oxygen) but also define the crystallization rate. Thus, water was firstly tried out as in analogous bulk crystallizations.

4.2.1 Aqueous synthesis of **Ni₃(HITP)₂** thin films

a.- Aqueous synthesis of **Ni₃(HITP)₂** thin films with the microfluidic device

First attempts in synthesizing **Ni₃(HITP)₂** thin films in aqueous media with the microfluidic device resulted in irregular depositions. For the synthesis, two glass slides are inserted in the chamber and separated with a spacer of 1 mm thickness, acting thus as the sides of the chamber. The inlet and outlet allowed to fill the chamber with an aqueous solution of **HATP·6HCl** and **NiCl₂·6H₂O**. Afterwards, the chamber was left overnight in a saturated ammonia ambience. The **Ni₃(HITP)₂** thin films grew supported on the glass slides (see Figure 4.9).

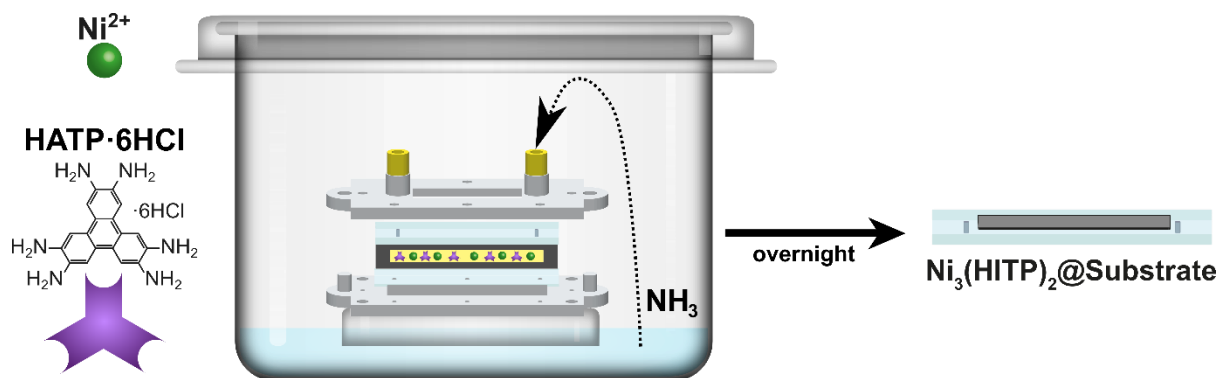


Figure 4.9: Schematic illustration of aqueous synthesis of $\text{Ni}_3(\text{HITP})_2$ thin films with two slide confined spaces. The confined space between the two glass slides is filled with an aqueous solution of $\text{HATP} \cdot 6\text{HCl}$ and $\text{NiCl}_2 \cdot 6\text{H}_2\text{O}$. Then, the chamber is placed in an ammonia saturated ambiance for slow diffusion into the chamber. The $\text{Ni}_3(\text{HITP})_2$ thin film is grown supported on the top and bottom glass slides.

A centimeter long light blue iridescent $\text{Ni}_3(\text{HITP})_2$ thin film on top of glass was obtained (Figure 4.10a). Nonetheless, the film exhibited already irregular coloring suggesting an irregular coverage of the substrate. Larger opacity at the edges of the substrate indicated larger deposition while transparency at the center of the film suggested the contrary.

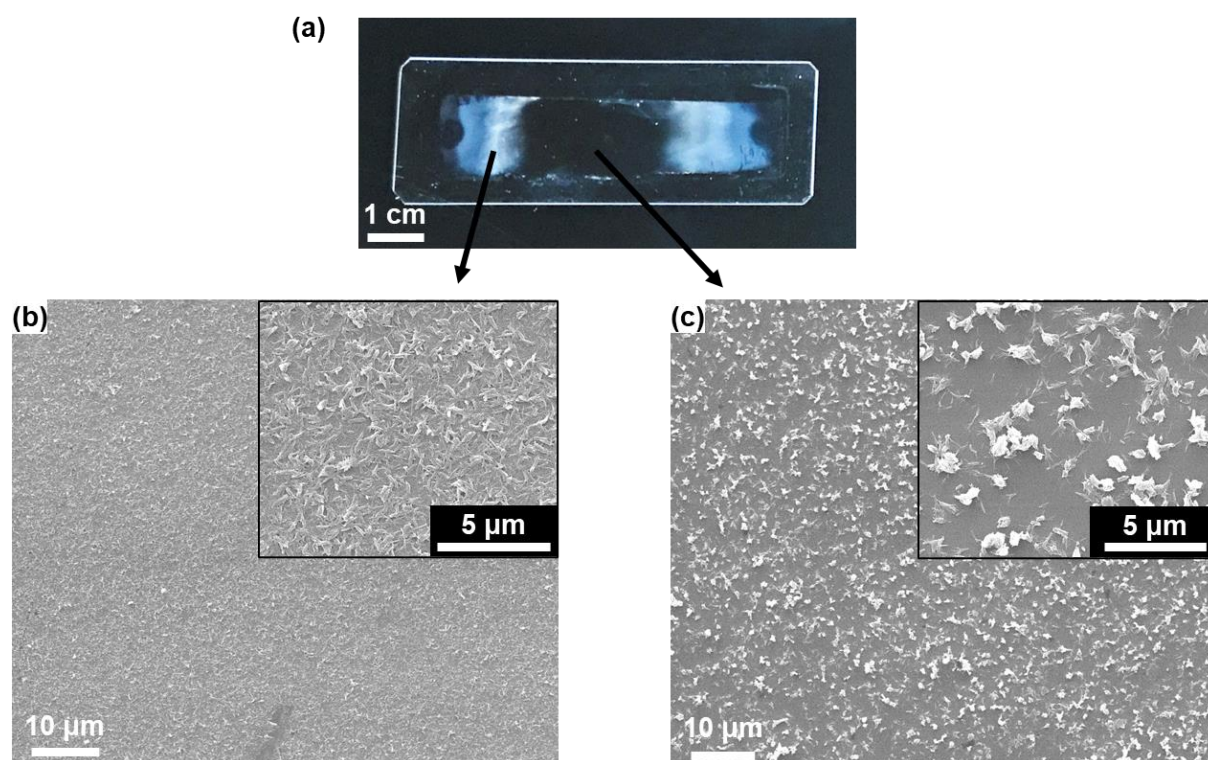


Figure 4.10: (a) Image of the obtained $\text{Ni}_3(\text{HITP})_2$ thin films on glass substrates with aqueous synthesis in confined spaces. Larger deposition on the sides of the substrate (corresponding to the inlet position) is already observed by naked eye. (b) SEM image on the edge of the film showing a large and compact deposition of fiber like particles. Inset shows a higher magnification image of the particles (c) SEM image at the center of the film showing an inhomogeneous and low degree of deposition of fiber like particles. Inset shows a higher magnification image of the particles.

The premise was confirmed by electron microscopy (Figure 4.10b and 4.10c). SEM images on the **Ni₃(HITP)₂** thin film revealed a dense and compact deposition of fiber-like structures with mean lengths of $0.8 \pm 0.2 \mu\text{m}$ (N=120) forming large and crack-free areas. However, at the center of the substrate, the thin film is discontinuous as the few deposited fiber-like structures form isolated aggregates. Interestingly, only long needle like structures can be observed over all the film in contrast with the **Ni₃(HITP)₂** crystalline powder synthesized through ammonia diffusion, that shows disk-like form crystallites (see *vide infra*). Thus, besides the partial growth of a supported **Ni₃(HITP)₂** thin film, a novel morphology of crystallites is obtained with confined spaces proving the potential of convection free synthesis.

Crystallinity of the deposited rod-like particles was evaluated by 2D Grazing Incident Wide-Angle X-ray Scattering (GIWAXS) at the edge of the **Ni₃(HITP)₂** thin film (Figure 4.11a). 2D GIWAXS on this film showcased the crystalline reflections of **Ni₃(HITP)₂** at $q_r = 3.4 \text{ nm}^{-1}$ (100), $q_r = 6.7 \text{ nm}^{-1}$ (200), $q_r = 8.9 \text{ nm}^{-1}$ (130), $q_r = 11.7 \text{ nm}^{-1}$ (240) and $q_z \sim 18 \text{ nm}^{-1}$ (002) in an isotropic fashion, indicating a random orientation of the crystallites.³³ UV-vis spectrum of the film at its edge was performed in transmission mode (Figure 4.11b). The typical **Ni₃(HITP)₂** strong UV absorption could not be fully observed because of the large UV absorbance of the glass substrate underneath 275 nm. Nonetheless, the large band at $\sim 650 \text{ nm}$ indicates the coordination of the **HATP** ligand to the metal.

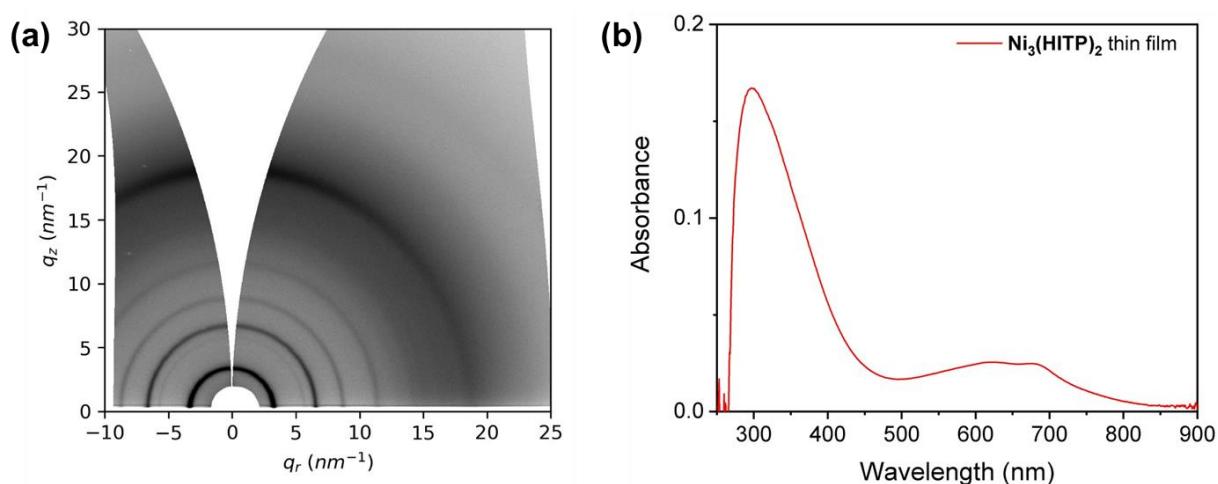


Figure 4.11: (a) 2D GIWAXS on the edge of the **Ni₃(HITP)₂** thin films. (b) UV-vis spectrum of the **Ni₃(HITP)₂** thin film measured in transmittance.

Thickness of the edge of the thin film was assessed by stylus profilometry. Measurements indicated a thickness of ~400 nm at the edges of the $\text{Ni}_3(\text{HITP})_2$ thin film. However, thicknesses of few nanometers are obtained only measuring few millimeters away from the edge.

Conductance spectroscopy was carried out at the edge and at the center of the $\text{Ni}_3(\text{HITP})_2$ thin film. At its center, the lack of continuity of the film made it too resistive, being thus isolating. Remarkably, the edge of the $\text{Ni}_3(\text{HITP})_2$ thin film was highly resistant despite the high compactness of particles at that area. This may arise from the narrowing thickness of the film in that area. Very thin thickness and micrometer long contacts can provide large resistances difficult to measure. Thus, inhomogeneity of the thin film did not allow the study of the electronic properties of the thin film.

b.- $\text{Ni}_3(\text{HITP})_2$ crystals synthesized according to the published protocol.

$\text{Ni}_3(\text{HITP})_2$ is typically obtained by coordination of deprotonated $\text{HATP} \cdot 6\text{HCl}$ and Ni^{2+} ions in an aqueous solution and further oxidation.³³ Ammonia and oxygen are commonly used for the $\text{Ni}_3(\text{HITP})_2$ formation for as base and oxidant agent either by their addition or diffusion. The synthesis between $\text{NiCl}_2 \cdot 6\text{H}_2\text{O}$ and $\text{HATP} \cdot 6\text{HCl}$ in water was performed at 60°C as reported in order to compare crystal morphology to the one obtained in microfluidic environments. To an aqueous solution of $\text{HATP} \cdot 6\text{HCl}$ and aqueous solution of $\text{NiCl}_2 \cdot 6\text{H}_2\text{O}$ with ammonia was added. After stirring at 60°C for 2h and washing steps, black nanoscale crystals of $\text{Ni}_3(\text{HITP})_2$ were obtained (Figure 4.12).

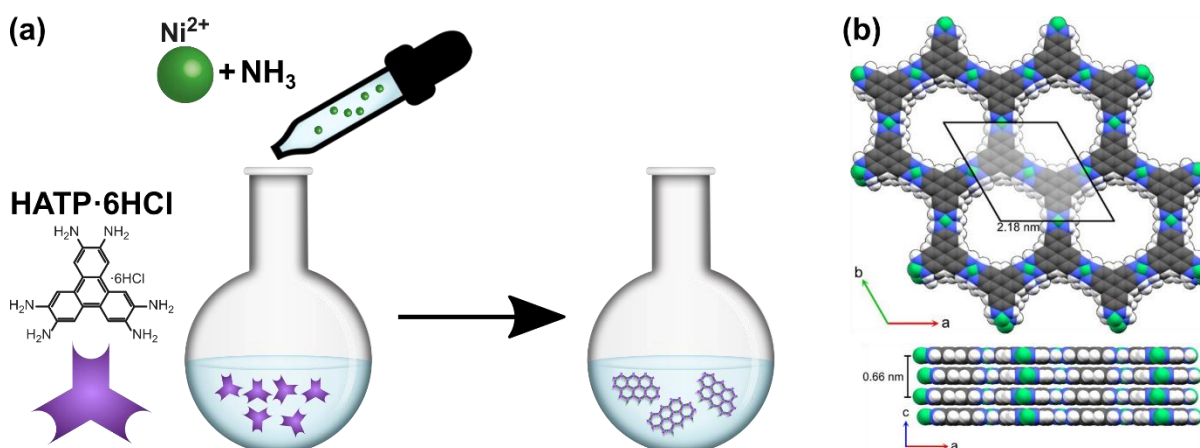


Figure 4.12: (a) Schematic illustration of the bulk synthesis of $\text{Ni}_3(\text{HITP})_2$ crystals following the reported protocol. (b) $\text{Ni}_3(\text{HITP})_2$ structure. Top view, the unit cell is highlighted, showing its size in the a and b directions. Side view, the unit cell dimension along the c -axis is shown, the interlayer distance is half that value: 0.33 nm. Element colors: C: grey, H: white, N: blue, Ni: green.

After drying, nanocrystals of were collected as a shiny fine black powder (Figure 4.13a). SEM of crystals revealed a disk like morphology of these with diameters between 300-400 nm and thicknesses of 40 nm (Figure 4.13b). Aggregation of the crystals during sample preparation hindered the measurement of crystals for size distribution. This morphology is in high contrast with the one obtained in microfluidic environments previously observed.

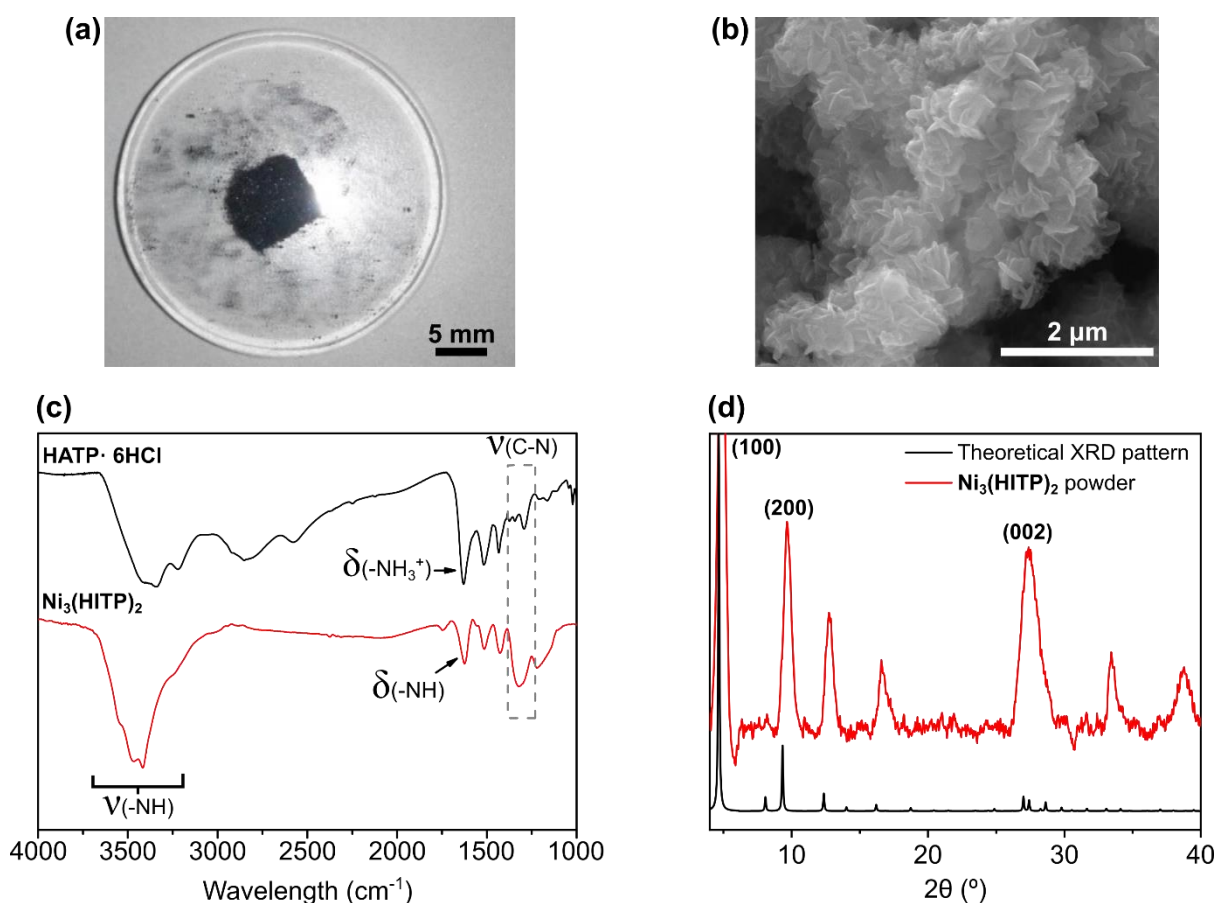


Figure 4.13: (a) Image of the $\text{Ni}_3(\text{HITP})_2$ powder after drying. (b) SEM images of the $\text{Ni}_3(\text{HITP})_2$ powder. (c) Comparison of FT-IR spectra of $\text{HATP} \cdot 6\text{HCl}$ and $\text{Ni}_3(\text{HITP})_2$ crystals. Characteristic peaks from the $\text{HATP} \cdot 6\text{HCl}$ ligand are labelled on the image. (d) Comparison of PXRD pattern of the $\text{Ni}_3(\text{HITP})_2$ crystals and the theoretical XRD pattern from structure simulation.

FT-IR spectroscopy on crystals synthesized with the reported methods was performed (Figure 4.13c). When compared to the FT-IR spectrum of $\text{HATP} \cdot 6\text{HCl}$, a $\sim 30 \text{ cm}^{-1}$ red shift on the peaks at 1300 and 1600 cm^{-1} , corresponding to the $\delta\text{C-N}$ and $\delta\text{N-H}$ vibrations, is observed confirming the coordination to the metallic center. Further, crystallinity of $\text{Ni}_3(\text{HITP})_2$ powder was assessed with Powder X-ray Diffraction (PXRD) (Figure 4.13d). The measured PXRD pattern matches with the theoretical structure of $\text{Ni}_3(\text{HITP})_2$. High

intensity of peaks at $2\theta = 4.8^\circ$, 9.6° , 12.7° and 16.6° corresponding to *ab*-planes suggest a large crystallinity along the 2D layers. On the other hand, the broad peak at $2\theta \sim 27^\circ$ corresponds to the (002) directions and thus to *out-of-plane* diffraction. Remarkably, broad peaks are obtained as a consequence of the nanometered size of the crystals.

Electronic characterization of the **Ni₃(HITP)₂** crystals was performed by compressing the crystalline powder into a pressed pellet applying pressures of 0.44 GPa. Afterwards, electronic contacts were deposited in Van der Pauw geometry with silver paste spaced of 1 mm (Figure 4.14a). Copper wires were imbedded in the paste before dryness and wire-bonded to a plastic leaded chip carrier. Four-wire conductance spectroscopy was performed obtaining a conductivity of $2.6 \pm 0.4 \text{ S}\cdot\text{cm}^{-1}$ which is in accordance with the reported values.³³ Two-wire I-V curves were measured in the pellet (Figure 4.14b) to assess percolation of charge carriers. Non-linear I-V curves indicate a large presence of grain boundaries creating energetic barriers which may arise from the low applied pressure during pelletization. Thus, electronic conduction in the randomly oriented pellet seems to be performed by hopping effect of the charge carriers through the crystalline domains.

Hence, **Ni₃(HITP)₂** powder synthesis has proven to be highly reproducible providing highly crystalline and conductive disk-like nanoparticles in sharp contrast to the needle-like crystals obtained with the microfluidic device. Pressing the crystals in pellets has enabled charge carrier conduction despite the presence of grain boundaries. For a better comparison of the electronic properties of **Ni₃(HITP)₂** synthesized under conventional synthesis and with our microfluidic devices, thin film morphologies were sought.

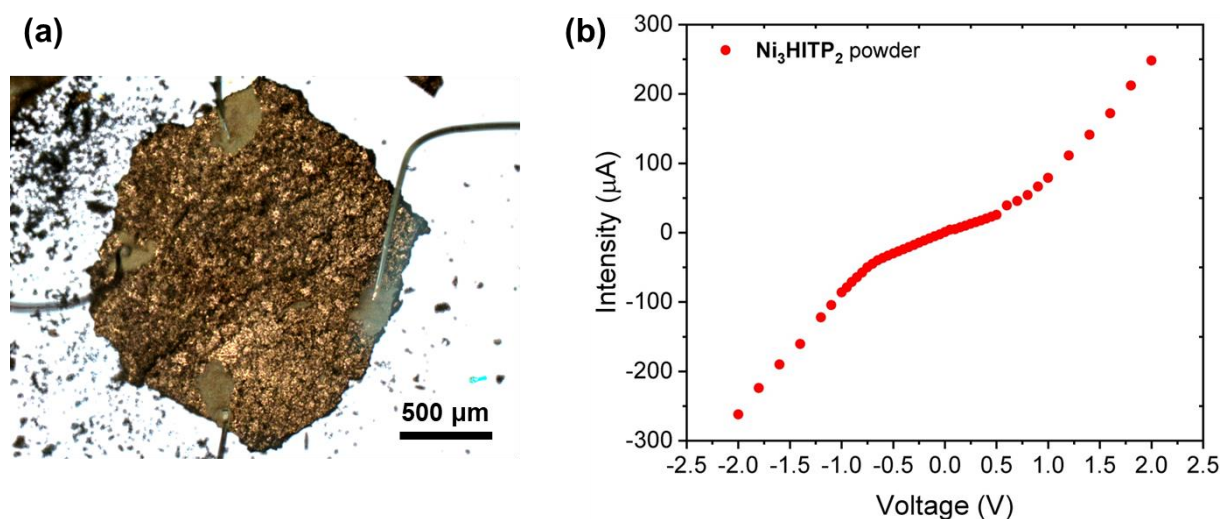


Figure 4.14: (a) OM of a pressed pellet of **Ni₃(HITP)₂** crystals with electronic contacts. (b) I-V curve of the pressed pellet

c.- **Ni₃(HITP)₂** thin films synthesized by diffusion of ammonia

Interfacial synthesis **Ni₃(HITP)₂** thin film was proposed for comparison purposes with films obtained with our microfluidic device. An aqueous solution of **HATP·6HCl** and $\text{NiCl}_2 \cdot 6\text{H}_2\text{O}$ was placed in an ammonia saturated ambiance (Figure 4.15) and left overnight. **Ni₃(HITP)₂** thin film grown at the water-air interface was recovered by stamping onto a SiO_2/Si substrate and left to dryness to air ambiance.

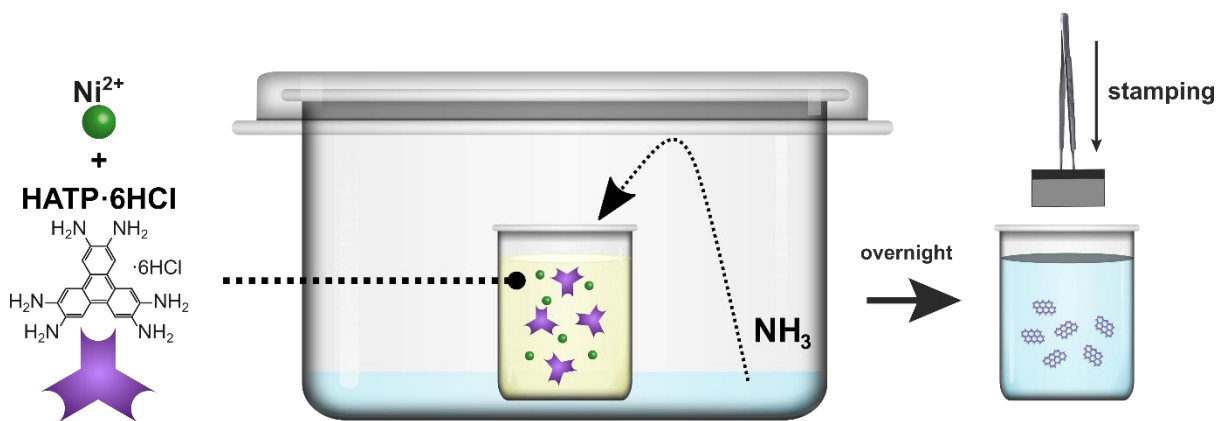


Figure 4.15: Schematic illustration of synthesis of **Ni₃(HITP)₂** thin films through ammonia diffusion. The film is formed at the water-air interface and recovered by stamping a 300 nm SiO_2/Si .

During the sample drying, water surface tension leads to cracking of the **Ni₃(HITP)₂** thin films, obtaining low degree of coverage of the SiO_2/Si substrate (Figure 4.16a). The sub-centimeter long films are formed by an irregular aggregation of nanoscale **Ni₃(HITP)₂** disk-like particles (Figure 4.16b) showcasing high roughness. Low degree of coverage hindered the FT-IR spectroscopy (Figure 4.16c) performed in reflectance mode. Nevertheless, vibrations corresponding to N-H and C-N bonds at 1600 cm^{-1} and 1300 cm^{-1} respectively, previously recorded in the **HATP·6HCl** and **Ni₃(HITP)₂** bulk powder can be seen.

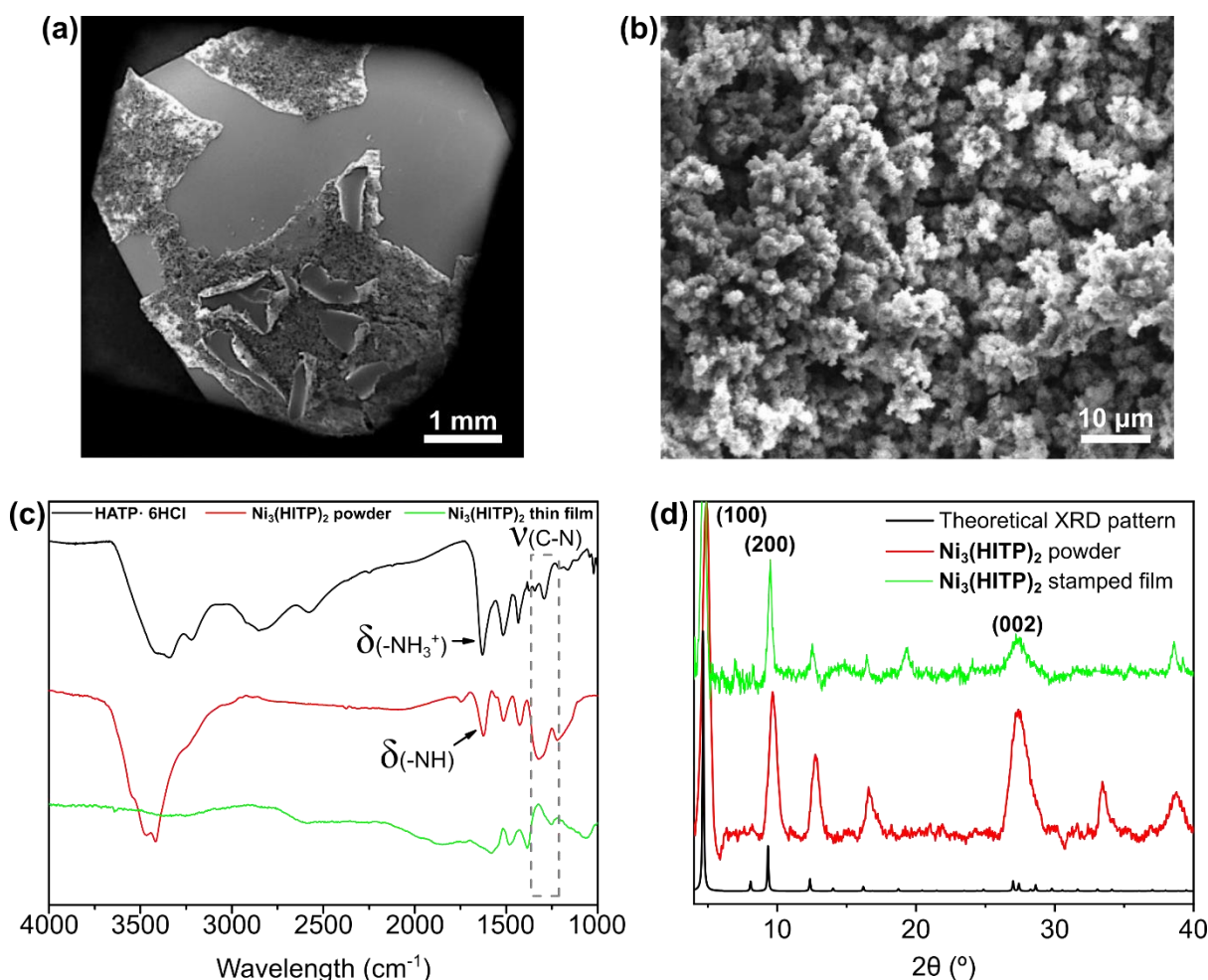


Figure 4.16: (a) SEM image of the stamped $\text{Ni}_3(\text{HITP})_2$ thin film onto the SiO_2/Si substrate showing the low degree of coverage (b) Magnified SEM image of the $\text{Ni}_3(\text{HITP})_2$ thin film showing the nanoparticulated character of the film and the high roughness. (c) Comparison of FT-IR spectra of the $\text{HATP} \cdot 6\text{HCl}$ ligand (black), $\text{Ni}_3(\text{HITP})_2$ powder from bulk synthesis (red) and $\text{Ni}_3(\text{HITP})_2$ thin film (green). (d) Comparison of PXRD spectra of the $\text{HATP} \cdot 6\text{HCl}$ ligand (black), $\text{Ni}_3(\text{HITP})_2$ powder from bulk synthesis (red) and GIXRD of $\text{Ni}_3(\text{HITP})_2$ thin film (green).

Crystallinity of the films was assessed by Grazing Incident X-Ray Diffraction (GIXRD) (Figure 4.16d). GIXRD pattern of the $\text{Ni}_3(\text{HITP})_2$ thin film indicated a high crystallinity, matching the pattern of the $\text{Ni}_3(\text{HITP})_2$ powder obtained with reported methods. Noteworthy, peaks corresponding to ab -planes as well as peaks corresponding to (002) direction appear, indicating an isotropic orientation of crystals.

Cracking of the $\text{Ni}_3(\text{HITP})_2$ thin film allowed to estimate the thickness of the film with SEM (Figure 4.17) being of the order of 1-2 μm. As seen in the images, the cracked films showcase a large flexibility as they can be bended over the substrate before breaking. Bended pieces of the thin film suggest a Janus character of the film regarding their roughness as the bottom side of the film seems smooth (corresponding to the air-side of the interface)

and homogenous. Essays on recovering the film by fishing techniques to expose the smooth side were unsuccessful as no coverage was obtained due to interface breaking.

Electronic characterization on the $\text{Ni}_3(\text{HITP})_2$ thin films was performed to evaluate possible presence of grain boundary (Figure 4.18a). Four wire DC measurements provided a conductivity of $0.12 \pm 0.05 \text{ S} \cdot \text{cm}^{-1}$, which is significantly lower than for the pressed pellet. However, it is noteworthy that linear two wire I-V curves are obtained (Figure 4.18b) at different contact distance, indicating a high degree of percolation of charge carriers.

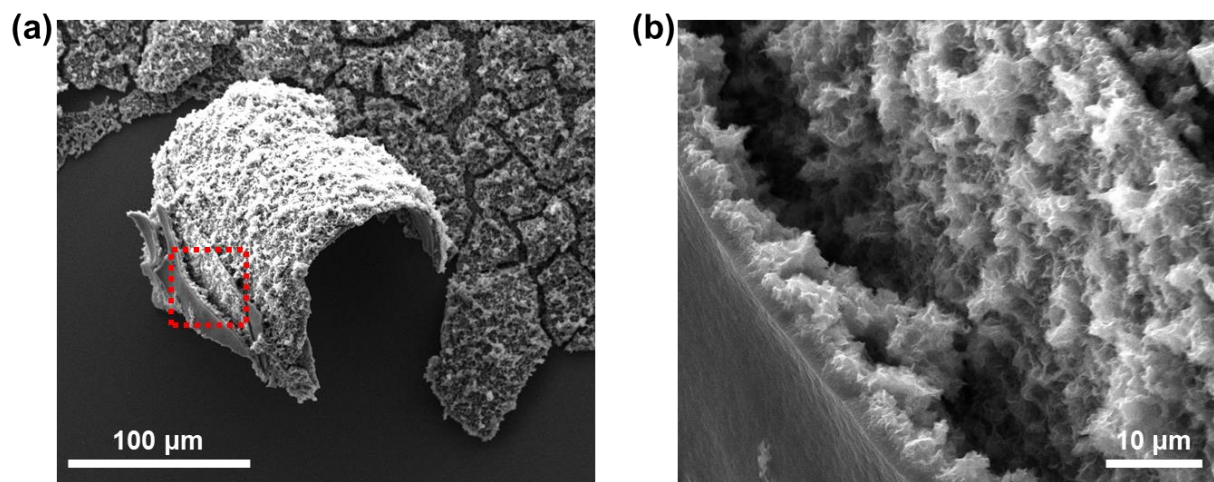


Figure 4.17: (a) SEM image of the stamped $\text{Ni}_3(\text{HITP})_2$ thin film onto the SiO_2/Si substrate showing film cracking and bending. (b) Magnified SEM image of the $\text{Ni}_3(\text{HITP})_2$ thin film from the selected area in image a showing the film's thickness.

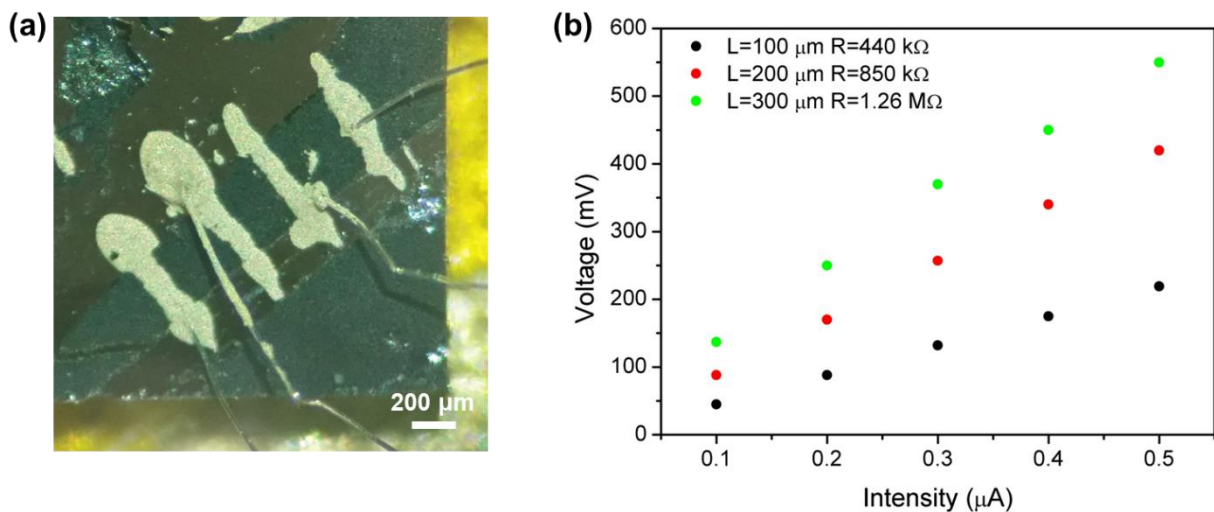


Figure 4.18: (a) OM image of stamped $\text{Ni}_3(\text{HITP})_2$ thin film with electric contacts. (b) Two-wire I-V curves measured in the thin film with three different distances between contacts.

Thus, $\text{Ni}_3(\text{HITP})_2$ thin films obtained with interfacial synthesis presented irregular coverage of the substrates due to convection flows present in water. Further, both conventional and microfluidic approaches have provided highly crystalline isotropic thin films. However, the introduction of simulated microgravity environments has already presented novelties in the crystallization $\text{Ni}_3(\text{HITP})_2$ as needle-like shaped crystallites were obtained in high contrast to disk-like morphologies obtained with conventional methods. This effect suggests that different preferential growth directions are obtained in simulated microgravity environments.

Similarities on the low degree of coverage in thin films using microfluidics point towards solvent effects during the thin film formation. Convection flows in water inside or microfluidic device cannot arise from solvent evaporation thus possible heterogeneity of $\text{Ni}_3(\text{HITP})_2$ crystallization was hypothesized as source of buoyancy forces. Effectively, when adding ammonia to an aqueous solution of $\text{HATP} \cdot 6\text{HCl}$ a pink precipitate is obtained immediately (Figure 4.19). FT-IR spectroscopy showed a slight redshift of the peak corresponding to the $\delta(\text{N-H})$ vibration ($\sim 1630 \text{ cm}^{-1}$) and an increase of the intensity of the $\nu(\text{C-N})$ ($\sim 1300 \text{ cm}^{-1}$), proving the deprotonation of the ligand into HATP which is still not soluble after 4 days in solution. Therefore, the unprotonated HATP is not soluble in water leading to a heterogeneous reaction during the $\text{Ni}_3(\text{HITP})_2$ formation in aqueous media.

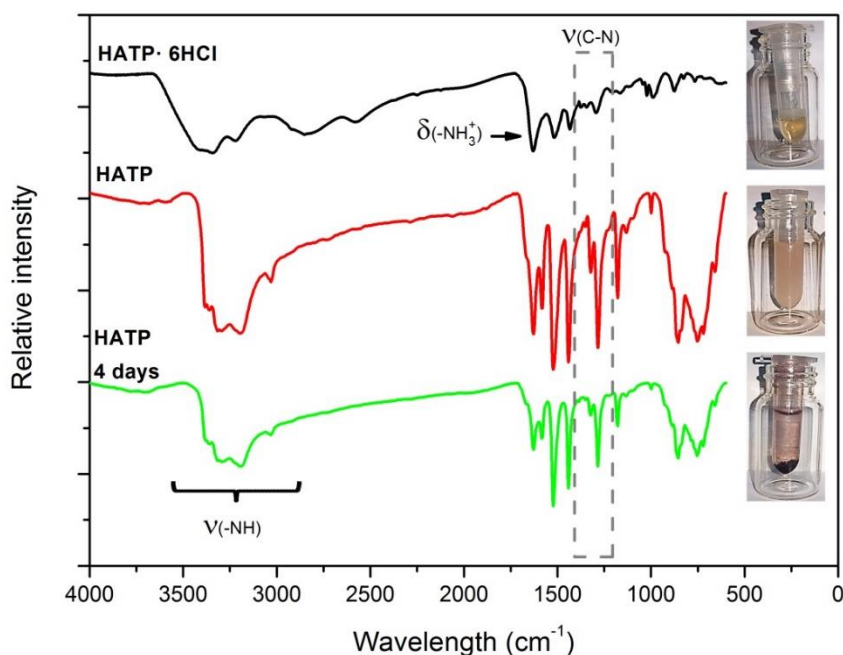


Figure 4.19: FT-IR measurements of $\text{HATP} \cdot 6\text{HCl}$ (black), HATP (red) and HATP after 4 days in water (green). Pictures of each molecule in water are added as insets. HATP was obtained by dissolution in water of $\text{HATP} \cdot 6\text{HCl}$ and addition of a stoichiometric amount of ammonia. The pink precipitate was immediately recovered by centrifugation and dried for its analysis.

4.2.2 Synthesis in DMSO of $\text{Ni}_3(\text{HITP})_2$ thin films with confined spaces

To ensure the homogeneity during the crystallization in the microfluidic device, DMSO was proposed as solvent for the synthesis. To confirm the correct crystallization of $\text{Ni}_3(\text{HITP})_2$ in DMSO, powder syntheses were studied first.

a.- $\text{Ni}_3(\text{HITP})_2$ powder bulk synthesis in DMSO

$\text{Ni}_3(\text{HITP})_2$ powder synthesis was modified with respect of the previous interfacial approach. In a few words, a stoichiometric mixture of $\text{HATP} \cdot 6\text{HCl}$ and NiCl_2 were dissolved in dry DMSO and subjected to ammonia and oxygen gas diffusions. After being in an ammonia saturated ambiance for 24h, the initial yellowish solution becomes pink (Figure 4.20) without any precipitate ensuring the homogeneity of the synthesis. Further, once in air ambiance a black precipitate appears within a minute at the liquid-air interface. By the end of the oxygen diffusion the precipitate is over the entire vial (Figure 4.20).

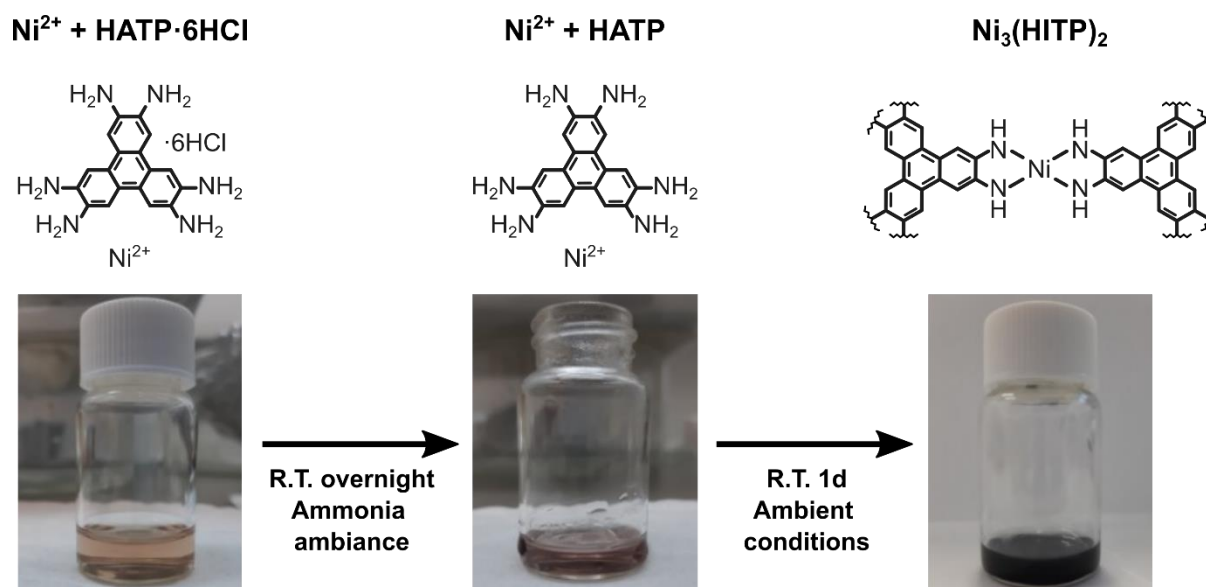


Figure 4.20: Images of the different steps of the $\text{Ni}_3(\text{HITP})_2$ bulk synthesis in dry DMSO with ammonia diffusion. Scheme of the state of the components at each state can be found on top of the pictures. The initial $\text{HATP} \cdot 6\text{HCl}$ and NiCl_2 mixture in dry DMSO has yellow color. After diffusion of ammonia, deprotonated HATP form and Ni^{2+} provide a pink color to the solution. After oxygen diffusion, a black precipitate appears indicating the formation of the MOF.

After centrifugation and washing, a black powder could be isolated. PXRD of the obtained solid proved the synthesis of high crystalline $\text{Ni}_3(\text{HITP})_2$ in agreement with the literature (Figure 4.21b). Besides, SEM suggests the retention of the crystal morphology with

respect to the crystals obtained with the reported protocol (Figure 4.21a) presenting disk-like crystals of sizes around 100 nm. Further, HR-TEM images of the MOF showed typical hexagonal honeycomb-like structures when imaged along the *c*-axis of the crystal (Figure 4.21c) measuring 2.0 ± 0.1 (N=10), matching the **Ni₃(HITP)₂** porous size. This confirms the formation of high-quality **Ni₃(HITP)₂** bulk material with identical properties than the previously reported despite the newly introduced synthesis conditions.

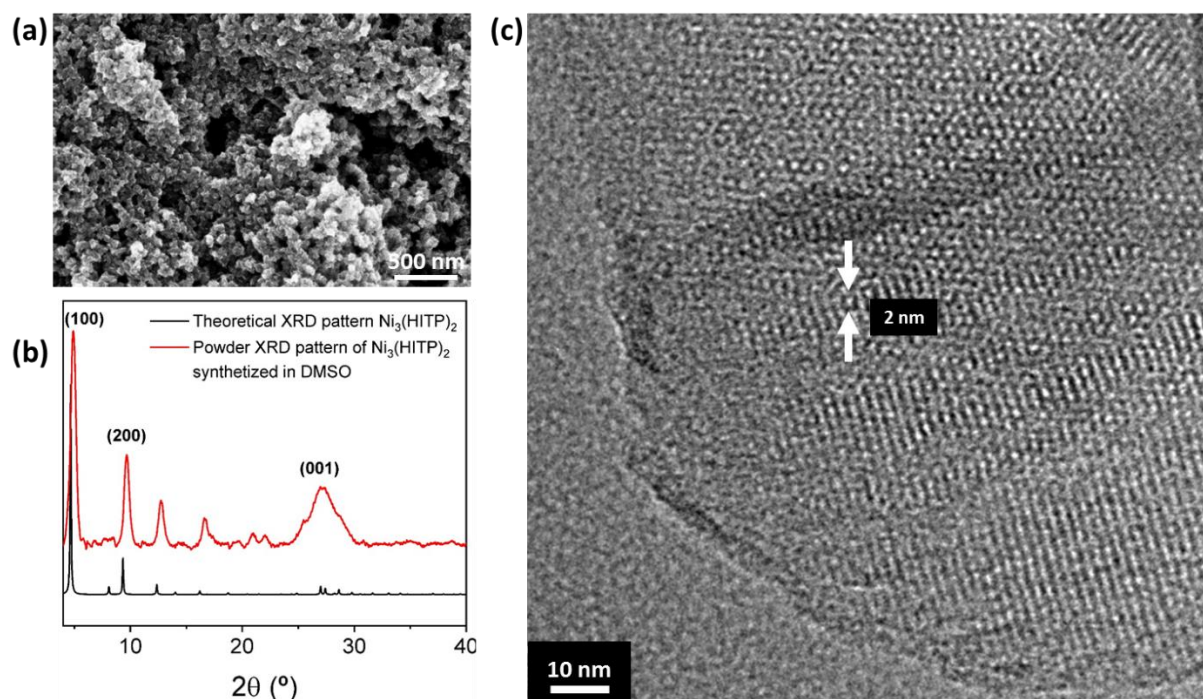


Figure 4.21: (a) SEM image of bulk **Ni₃(HITP)₂** crystals synthesized in DMSO with ammonia diffusion. Nanodisks of 100nm diameter are obtained. (b) PXRD of the bulk **Ni₃(HITP)₂** crystals after centrifuge and washing. The pattern matches the previously reported. (c) High magnification HR-TEM image of **Ni₃(HITP)₂** showing large crystallinity and porosity in a honeycomb lattice structure.

Having proved the efficacy on synthesis of **Ni₃(HITP)₂** crystals in DMSO and its homogeneity, control on the evolution of the synthesis was studied by UV-vis-Near Infrared (UV-vis-NIR) spectroscopy. **HATP·6HCl** and **NiCl₂** were dissolved in dry DMSO in a quartz cuvette. Addition of ammonia was resulting into an immediate formation of the **Ni₃(HITP)₂** crystals not allowing to perform any measurement. Thus, tetrabutylammonium hydroxide was used as a softer base in order to record the absorption spectra during the **Ni₃(HITP)₂** formation upon exposure to air (Figure 4.22a). After deprotonation of **HATP·6HCl**, a strong absorption band at 1000 nm appears. Control experiments prove that this band is not characteristic of the deprotonated **HATP** or the **NiCl₂** salt by themselves (Figure 4.22b). Therefore, it might correspond to some charge transfer between the **HATP** ligand and the metallic center. Upon exposure to air, within minutes, the band at 1000nm

decreases while the characteristic $\text{Ni}_3(\text{HITP})_2$ charge transfer appears at 600 nm. Besides, the $\text{Ni}_3(\text{HITP})_2$ black powder can be seen by naked eye as a black precipitate in the quartz cuvette.

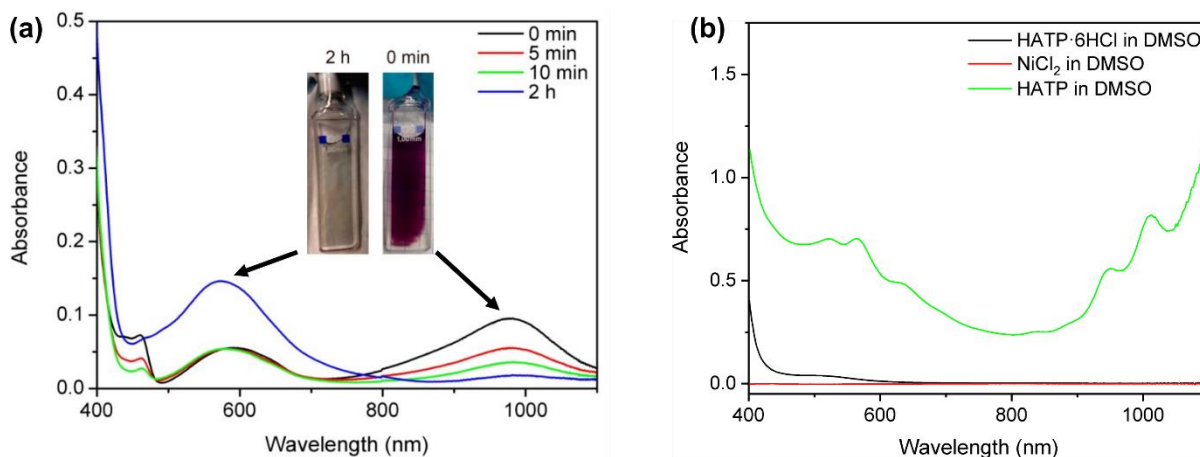


Figure 4.22: (a) UV-vis-NIR absorption spectra of the reaction mixture at different stages. (black) Spectrum of $\text{HATP} \cdot 6\text{HCl}$ and NiCl_2 mixture in dry DMSO immediately after tetrabutylammonium hydroxide addition (red, green, blue) Spectra after 5 min, 10 min and 2 h respectively of oxidation. Images of 0 min and 2 h of oxidation can be found as an inset. (b) UV-vis-NIR absorption spectra of $\text{HATP} \cdot 6\text{HCl}$, HATP and NiCl_2 in DMSO.

b.- Control on the synthesis of $\text{Ni}_3(\text{HITP})_2$ thin films in double slide confined spaces

Having proved the homogeneous crystallization of $\text{Ni}_3(\text{HITP})_2$ in DMSO, use of this solvent in microgravity conditions is now faced. In order to experimentally confirm the controlled two-step vapor induced crystallization of $\text{Ni}_3(\text{HITP})_2$ inside our microfluidic environment, we firstly assembled the microfluidic device with two quartz slides as top and bottom walls. This configuration was preferred as it enables following the reaction progress of $\text{Ni}_3(\text{HITP})_2$ both optically and spectroscopically. Anhydrous DMSO was chosen as the solvent of reaction as it can solubilize all the reactants (NiCl_2 and $\text{HATP} \cdot 6\text{HCl}$), including intermediate species, thus preventing convection induced by the movement of precipitates inside the microfluidic device. Next, the two-step vapor induced crystallization approach of $\text{Ni}_3(\text{HITP})_2$ was accomplished by controlling the diffusion of ammonia gas (step 1) and air (step 2) inside the microfluidic device through its inlets (see Figure 4.23a).

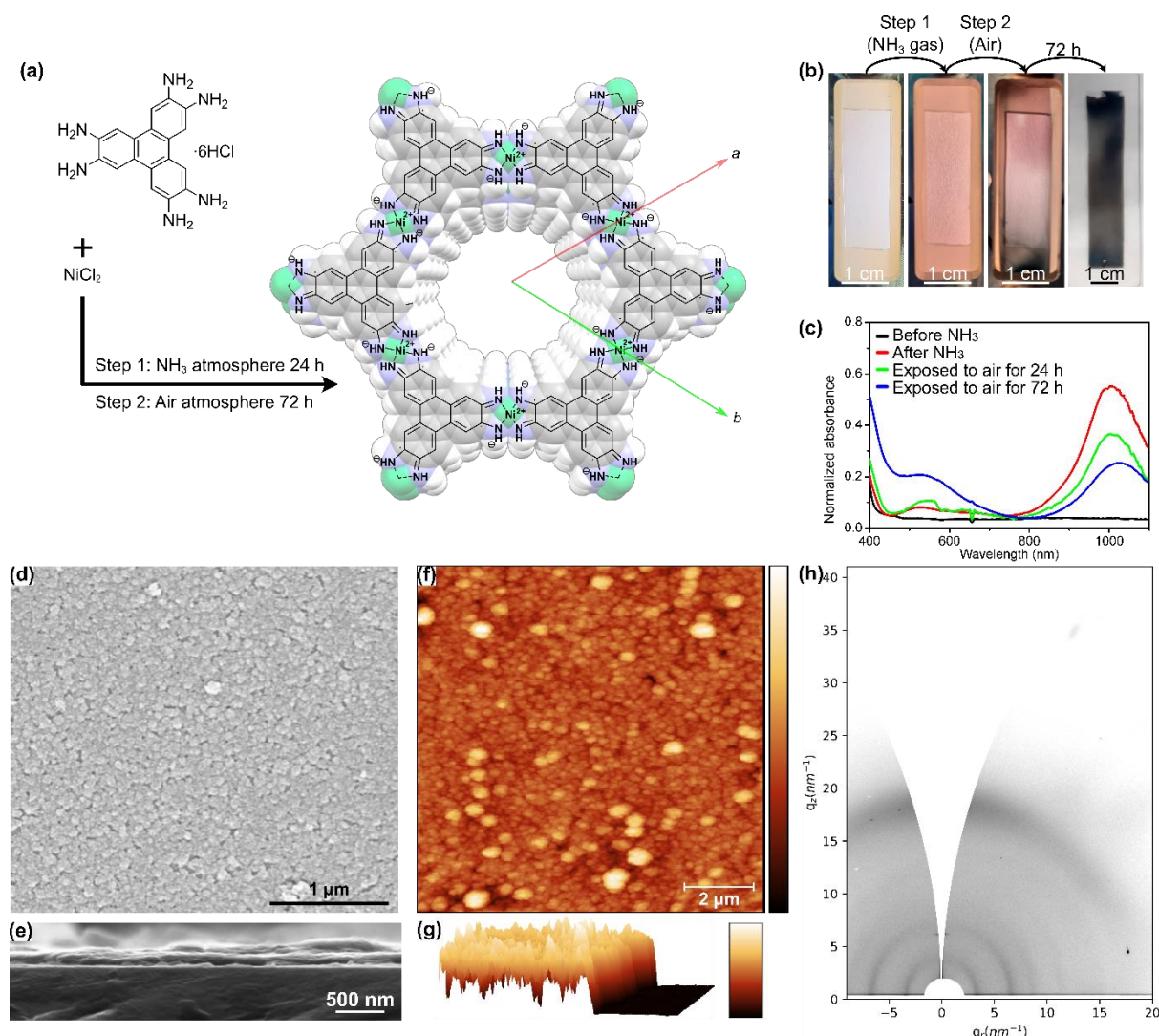


Figure 4.23: (a) Schematic synthesis and final structure of $\text{Ni}_3(\text{HITP})_2$. (b) Photographs of the microfluidic environment at the different stages during the synthesis of $\text{Ni}_3(\text{HITP})_2$. The initial colorless solution becomes pink upon exposure to ammonia vapors for 24 h. Afterwards, the pink solution progressively becomes black from the inlets towards the center of the chamber upon exposure to air. After 72 h, a black thin film supported on quartz can be observed. Scalebars underneath all images correspond to 1 cm. (c) UV-vis-NIR spectra acquired in situ (*i.e.* in the microfluidic environment) and during the synthesis of $\text{Ni}_3(\text{HITP})_2$. Color changes are reflected in the changes in the spectra. An absorption band at 1000 nm rises after the exposure to ammonia. Upon exposure to air, this band decreases and a band at 530 nm is formed. (d) Top-view SEM image of $\text{Ni}_3(\text{HITP})_2$ @Quartz. (e) Cross-section SEM image of $\text{Ni}_3(\text{HITP})_2$ @Quartz. (f) AFM image of $\text{Ni}_3(\text{HITP})_2$ @Quartz. The colorbar goes from 0 to 180 nm. (g) 3D AFM image of $\text{Ni}_3(\text{HITP})_2$ @Quartz profile. The colorbar goes from 0 to 140 nm. (h) 2D GIWAXS pattern of $\text{Ni}_3(\text{HITP})_2$ @Quartz.

As shown in Figure 4.23b, the initially colorless solution composed by a stoichiometric mixture of NiCl_2 and $\text{HATP} \cdot 6\text{HCl}$ turns pink during step 1, *i.e.* when the microfluidic device is introduced in a chamber full of ammonia vapor for 24 h. Subsequently, this pink solution turns black at the inlet ports in step 2, *i.e.* upon exposure to air. After 72 h, the substrate is completely covered with a black film that can readily be analyzed as

Ni₃(HITP)₂, see Figure 4.23b. The UV-Vis spectra in Figure 4.23c clearly shows these color changes. An intense absorption band at 1000 nm tentatively attributed to the non-oxidized complex between non-protonated **HATP** and the metal cation is detected right after taking the device out of the ammonia atmosphere. Then, when the device is exposed to air, the band at 1000 nm starts to decrease while the characteristic band of **Ni₃(HITP)₂** at 530 nm appears and increases as the film is formed.³³ In contrast to this controlled two-step vapor induced crystallization of **Ni₃(HITP)₂** inside the microfluidic device, performing the same reaction in bulk conditions (*e.g.* a vial) results in a fast precipitation of black particles at the air/DMSO interface characterized as **Ni₃(HITP)₂** as previously seen. This rapid progress of the reaction in bulk, without the appearance of the two distinct stages, showcases the lack of control on the oxygen diffusion when conventional synthetic conditions are in place.

The slow diffusion of gases and long reaction times allowed the crystallization of **Ni₃(HITP)₂** into large scale black thin films supported on quartz (here after referred as **Ni₃(HITP)₂@Quartz** films) with lateral sizes of 2-6 cm (Figure 4.23b) supported on the quartz substrate. The final formed **Ni₃(HITP)₂** thin film shows a strong UV absorption, a band at 600 nm and a broad absorption band over the NIR region (Figure 4.23c).

The black **Ni₃(HITP)₂@Quartz** films were initially characterized by SEM, which revealed a smooth, compact and crack-free continuous film with a homogeneous thickness of 100 nm (Figure 4.23d and 4.23e), which was further corroborated by profilometry (Figure 4.23g). AFM confirmed the low roughness of the film showcasing root mean square (RMS) roughness of 14.9 ± 0.5 nm (Figure 4.23f). The crystallinity and structure of the **Ni₃(HITP)₂@Quartz** films were assessed by 2D GIWAXS. The reflections corresponding to the **Ni₃(HITP)₂** structure at $q_r = 3.4 \text{ nm}^{-1}$ (100), $q_r = 6.7 \text{ nm}^{-1}$ (200), $q_r = 8.9 \text{ nm}^{-1}$ (130), $q_r = 11.7 \text{ nm}^{-1}$ (240) and $q_z \sim 18 \text{ nm}^{-1}$ (002) are clearly observed in Figure 4.23h, where they appear with an anisotropic distribution. That is, plotting the intensities in an azimuthal representation (Figure 4.24) clearly shows that the (hk0) peaks have higher intensity in the *in-plane* direction, while the (002) peak is mainly localized in the *out-of-plane* direction. These data suggest that the **Ni₃(HITP)₂** structure is preferentially oriented with its *c*-axis perpendicular to the substrate.

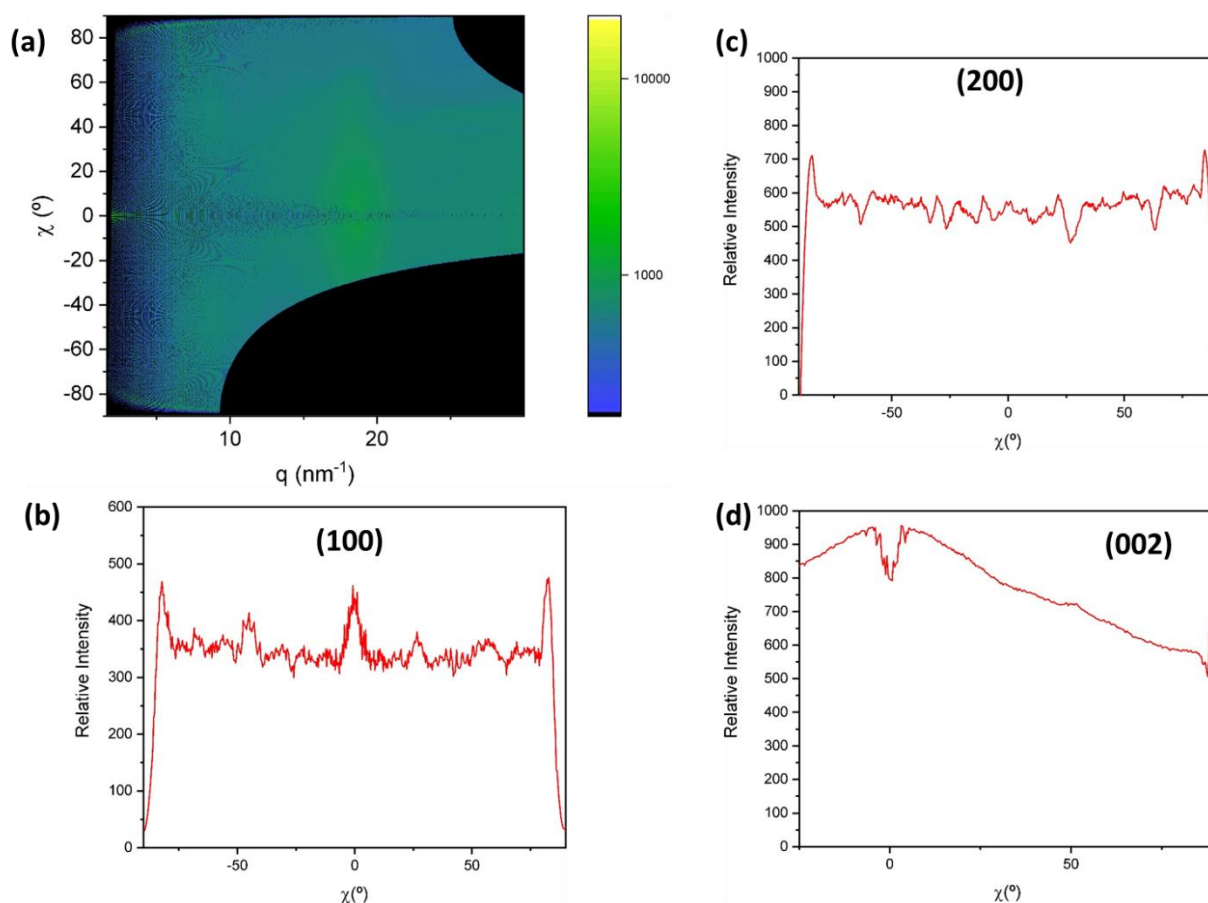


Figure 4.24: (a) 2D GIWAXS pattern of $\text{Ni}_3(\text{HITP})_2@ \text{Quartz}$ thin films represented as azimuthal angle versus q . (b) Cut of (a) along the $q=3.32 \text{ nm}^{-1}$ position corresponding to the (100) plane. (c) Cut of (a) along the $q=6.64 \text{ nm}^{-1}$ position corresponding to the (200) plane. (d) Cut of (a) along the $q=18 \text{ nm}^{-1}$ position corresponding to the (002) plane. Signals for every cut were averaged from values of the cuts at $\pm 0.05 \text{ nm}^{-1}$ at each given position. Cuts in (b) and (c) show a larger intensity at $\chi = 90^\circ$ (*out-of-plane*) while cut in (d) proves a larger intensity at $\chi = 0^\circ$ (*in-plane*) proving the c -axis orientation.

It is worth noting that performing the experiment in the presence of buoyancy-driven convections using the same reaction mixture, $\text{Ni}_3(\text{HITP})_2$ can be generated but the resulting coverage of the substrate is not compact and homogeneous, in this case $\text{Ni}_3(\text{HITP})_2$ does not have a preferential orientation (Figure 4.25). To reinforce the relevance of our device an analogous synthesis was performed by immersing a 1x1 cm quartz (001) substrate into the bulk reaction mixture (in the presence of buoyancy-driven convection). Without removing the substrate, the mixture was subsequently exposed to ammonia for 24 h and air for three days (Figures 4.25a and 4.25b). After this, the substrate was removed and gently rinsed in ethanol. To avoid material depositions driven by gravity, we focused on the film grown on the bottom face of the substrate. As seen in the inset of Figure 4.25c, a navy-blue thin film supported on quartz is obtained. Noticeably, the coverage is not uniform showing areas with large and low

deposition. SEM images of the thin film (Fig. 4.25c) indicated an irregular compact deposition of disk-like structures. 2D GIWAXS on this film showcased the crystalline reflections of $\text{Ni}_3(\text{HITP})_2$ in an isotropic fashion, confirming the random orientation of the crystallites (Fig. 4.25d). This underlines the relevance of our microfluidic device in order to control the on-surface growth of $\text{Ni}_3(\text{HITP})_2$ films.

These results clearly highlight the importance of avoiding convective mass transport during the synthesis of $\text{Ni}_3(\text{HITP})_2$ thin films. Undoubtedly, with our microfluidic device, we allow the growth of $\text{Ni}_3(\text{HITP})_2$ in a quiescent environment that ensures the generation of compact, smooth and crack-free $\text{Ni}_3(\text{HITP})_2$ thin films.

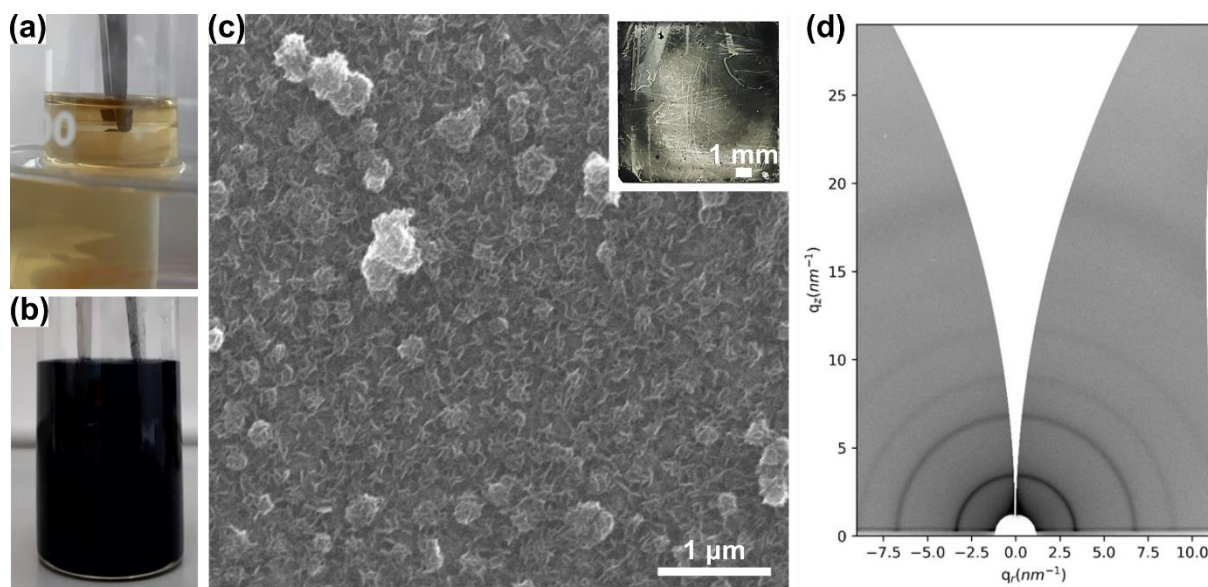


Figure 4.25: $\text{Ni}_3(\text{HITP})_2$ thin films synthesized in a bulk environment: (a) and (b) Initial and final images of the synthesis of $\text{Ni}_3(\text{HITP})_2$ thin film on quartz by immersion in the reaction media. (c) SEM image of the $\text{Ni}_3(\text{HITP})_2$ thin film grown on the bottom face of the quartz substrate. The picture on the inset shows the irregular deposited film grown on that face. (d) 2D GIWAXS pattern of the $\text{Ni}_3(\text{HITP})_2$ thin film on quartz.

Further, control on the thickness of $\text{Ni}_3(\text{HITP})_2$ thin films grown in confined spaces was assessed. For this, the device was mounted in three different occasions with two glass slides as top and bottom walls and filled with the same reaction mixture as previously. After the diffusion of ammonia, the devices are exposed to air for different times on each occasion, being these one, two or three days respectively. Notoriously, the films grown after one and two days of exposure to air showcase irregular coverage with larger thicknesses on the sides

of the film, corresponding to the positions of the inlets. Only the thin film obtained after three days has a homogeneous thickness. Tapping AFM images were acquired at the middle of films obtained with one, two and three days of oxygen diffusion respectively (Figure 4.26). Images at the middle of the edge revealed thicknesses of 30 nm, 60 nm and 100 nm for thin films grown after one, two and three days of oxidation respectively. Therefore, linear increase of the thickness is obtained with increasing oxidation time. Interestingly, RMS remained of the same order despite the increasing reaction times. This suggests a homogeneous deposition of $\text{Ni}_3(\text{HITP})_2$ crystallites at the center of the substrate.

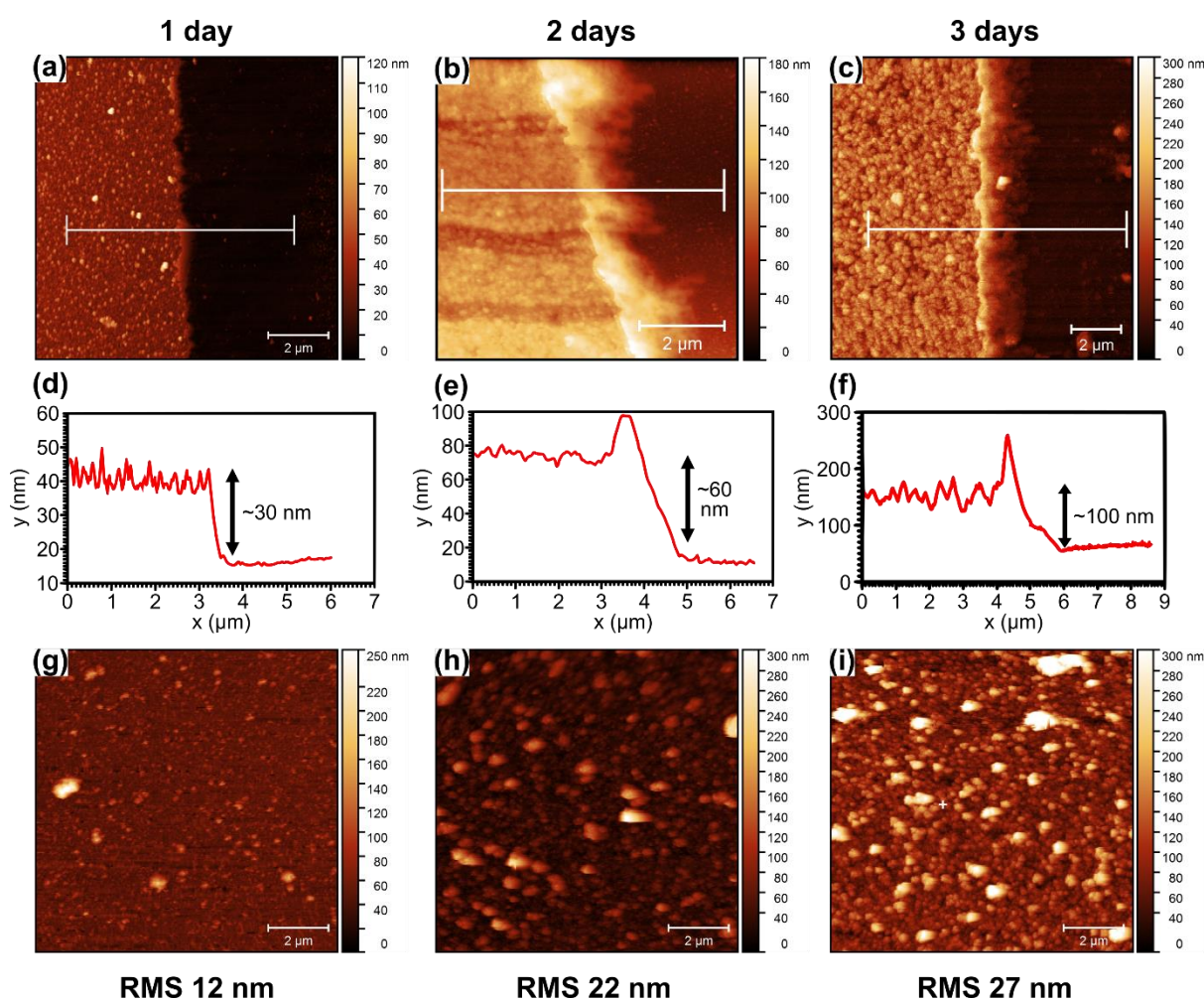


Figure 4.26: AFM images at the middle of the edge of $\text{Ni}_3(\text{HITP})_2$ thin films grown after (a) one day, (b) two days and (c) three days of exposure to atmospheric oxygen. (d), (e) and (f) Cross-section profiles obtained from lines shown in images (a), (b) and (c) respectively. AFM topography images at the center of $\text{Ni}_3(\text{HITP})_2$ thin films grown after (g) one day, (h) two days and (i) three days of exposure to atmospheric oxygen.

Such control on the growth of $\text{Ni}_3(\text{HITP})_2$ thin films with the newly introduced conditions paves the way to possible epitaxial or oriented growth of the films. Hence, synthesis onto substrates with different surface chemistry is aimed now with the purpose of evaluating its impact in convection free systems.

c.- Synthesis and characterization of $\text{Ni}_3(\text{HITP})_2@ \text{Glass}$, $\text{Ni}_3(\text{HITP})_2@ \text{Quartz}$ and $\text{Ni}_3(\text{HITP})_2@ \text{Glass-SAM}$ thin films

To evaluate the impact of surface in our system, $\text{Ni}_3(\text{HITP})_2$ thin films are grown on top of three substrates of similar chemical composition to quartz but with different surface chemistry. These are amorphous glass slide (**Glass**) and chemically modified glass with amino terminated groups (**@Glass-SAM**). Correct functionalization with a Self-Assembled Monolayer (SAM) of the last one was assessed by contact angle measurements (Figure 4.27).

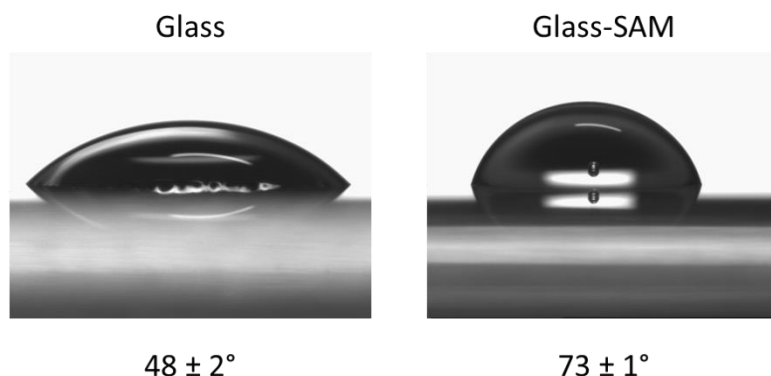


Figure 4.27: Representative images of water droplets for contact angle measurements in Glass and Glass-SAM substrates previously and after the surface chemical modification respectively.

Thus, synthesis was performed as previously described using two identical substrates as slides of the confined chamber and filling it with a dry DMSO solution of $\text{HATP} \cdot 6\text{HCl}$ and NiCl_2 solution. After 24 h ammonia diffusion and exposure to air ambiance for three days, centimeter-scale large black $\text{Ni}_3(\text{HITP})_2$ thin films are obtained on top of each substrate, henceforth labelled $\text{Ni}_3(\text{HITP})_2@ \text{Glass}$, $\text{Ni}_3(\text{HITP})_2@ \text{Quartz}$ and $\text{Ni}_3(\text{HITP})_2@ \text{Glass-SAM}$ thin films respectively (Figure 4.28a, 4.28b and 4.28c).

Top view SEM images of the different thin films revealed different degrees of compactness among them (Figures 4.28d-f). $\text{Ni}_3(\text{HITP})_2@ \text{Glass}$ thin films present a random

distribution of particles irregularly compacted in the form of thin film. Contrary to previously characterized $\text{Ni}_3(\text{HITP})_2@ \text{Quartz}$, $\text{Ni}_3(\text{HITP})_2@ \text{Glass-SAM}$ thin films showcased densely packed nanoplates attached edge-on to the substrate. Comparison between the images suggested different arrangement of $\text{Ni}_3(\text{HITP})_2$ nanoparticles leading to different crystalline orientations. All films present similar thicknesses of around 100 nm as shown in the cross-sections SEM images (Figures 4.18g-i).

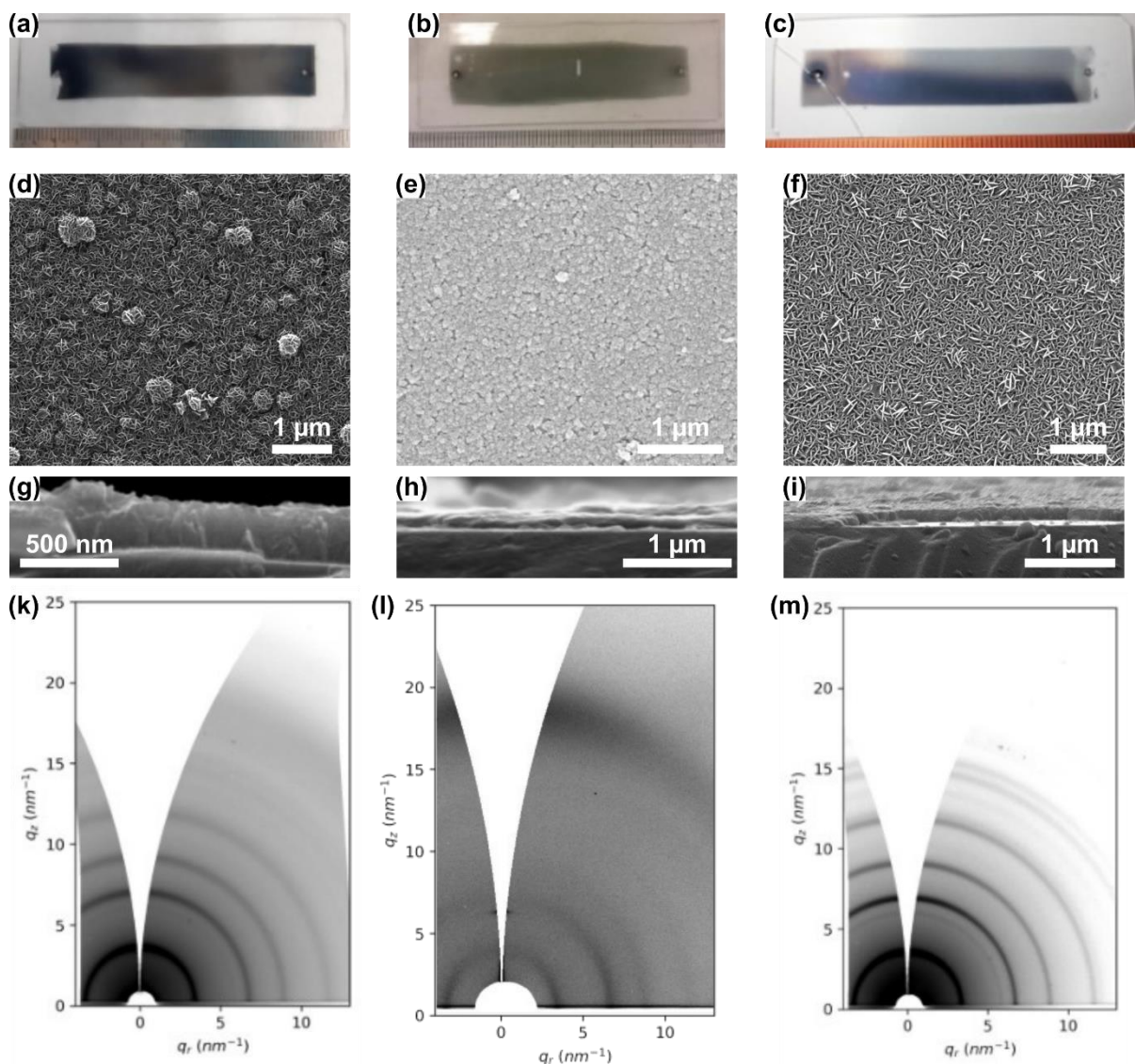


Figure 4.28: (a), (b) and (c) Images of the $\text{Ni}_3(\text{HITP})_2@ \text{Glass}$, $\text{Ni}_3(\text{HITP})_2@ \text{Quartz}$ and $\text{Ni}_3(\text{HITP})_2@ \text{Glass-SAM}$ thin films respectively. (d), (e) and (f) Top view SEM images of the $\text{Ni}_3(\text{HITP})_2@ \text{Glass}$, $\text{Ni}_3(\text{HITP})_2@ \text{Quartz}$ and $\text{Ni}_3(\text{HITP})_2@ \text{Glass-SAM}$ thin films respectively. (g), (h), and (i) Cross-section SEM images of the $\text{Ni}_3(\text{HITP})_2@ \text{Glass}$, $\text{Ni}_3(\text{HITP})_2@ \text{Quartz}$ and $\text{Ni}_3(\text{HITP})_2@ \text{Glass-SAM}$ thin films respectively. (k), (l) and (m) 2D GIWAXS spectra of the $\text{Ni}_3(\text{HITP})_2@ \text{Glass}$, $\text{Ni}_3(\text{HITP})_2@ \text{Quartz}$ and $\text{Ni}_3(\text{HITP})_2@ \text{Glass-SAM}$ thin films respectively

Thus, crystallinity of the thin films was assessed by means of 2D GIWAXS (Figures 4.28k-m). All obtained patterns demonstrate the formation of $\text{Ni}_3(\text{HITP})_2$ as the observed reflections correspond to the ones expected for its structure. Interestingly, 2D GIWAXS confirms the different orientation from substrate to substrate. In the case of $\text{Ni}_3(\text{HITP})_2@\text{Glass}$ thin films the observed reflections are observed as full broad semi-circles confirming the random orientation of crystallites. Remarkably, regarding $\text{Ni}_3(\text{HITP})_2@\text{Quartz}$ samples, the reflections at $q_r = 3.4 \text{ nm}^{-1}$ (100), $q_r = 6.7 \text{ nm}^{-1}$ (200), $q_r = 8.9 \text{ nm}^{-1}$ (130), $q_r = 11.7 \text{ nm}^{-1}$ (240) are more intense in the *in-plane* component of the 2D GIWAXS pattern, while a broad diffuse arch at $q_z \sim 18 \text{ nm}^{-1}$ corresponding to the (002) reflection is observed in the *out-of-plane* direction. On the other hand, 2D GIWAXS pattern of $\text{Ni}_3(\text{HITP})_2@\text{Glass-SAM}$ thin films showed reflections at $q_r = 3.4 \text{ nm}^{-1}$ (100), $q_r = 6.7 \text{ nm}^{-1}$ (200), $q_r = 8.9 \text{ nm}^{-1}$ (130), $q_r = 11.7 \text{ nm}^{-1}$ (240) with higher intensity in the *out-of-plane* component of the pattern. This indicates an orientation with *c*-axis parallel to the substrate. Hence, epitaxial growth of $\text{Ni}_3(\text{HITP})_2$ thin films was achieved depending on the surface chemistry of the substrate.

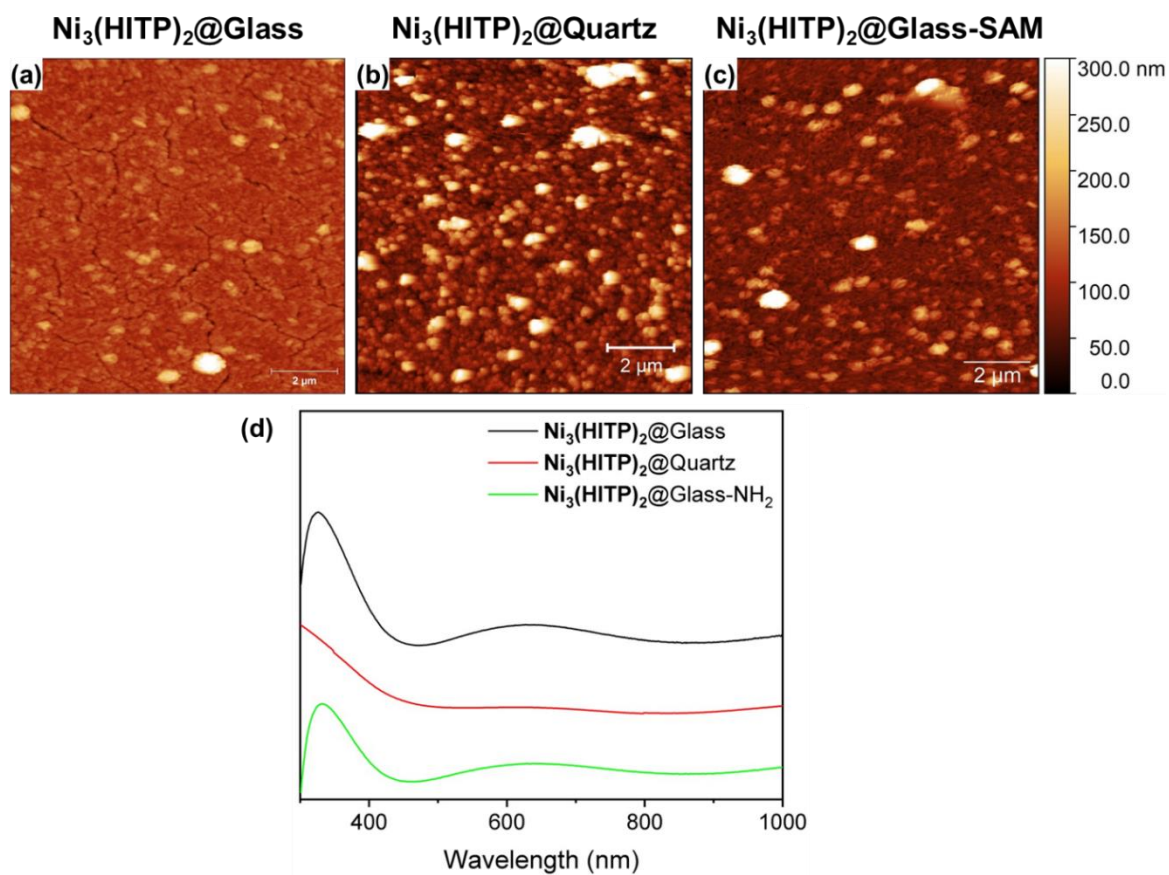


Figure 4.29: AFM images of (a) $\text{Ni}_3(\text{HITP})_2@\text{Glass}$, (b) $\text{Ni}_3(\text{HITP})_2@\text{Quartz}$ and (c) $\text{Ni}_3(\text{HITP})_2@\text{Glass-SAM}$ thin films respectively. (d) Comparison of the UV-vis spectra of $\text{Ni}_3(\text{HITP})_2@\text{Glass}$, $\text{Ni}_3(\text{HITP})_2@\text{Quartz}$ and $\text{Ni}_3(\text{HITP})_2@\text{Glass-SAM}$ thin films respectively.

UV-vis spectroscopy confirmed the correct growth of the **Ni₃(HITP)₂** thin films on the different substrates, showcasing the typical charge transfer at 600 nm (Figure 4.29d). AFM images of the three obtained thin films proved the nanoparticulated character of all sample with similar roughness independently of the different crystalline preferential orientations (Figure 4.29a-c), obtaining RMS 16.6, 14.9 and 27.1 nm for **Ni₃(HITP)₂@Glass**, **Ni₃(HITP)₂@Quartz** and **Ni₃(HITP)₂@Glass-SAM** thin films respectively.

d.- Synthesis and characterization of **Ni₃(HITP)₂@Au** and **Ni₃(HITP)₂@Au-SAM** thin films

Since **Ni₃(HITP)₂** is a promising conductive material that will have to be interfaced with electrodes in order to build functional devices, we extended our synthetic microfluidic approach to gold substrates. The use of gold was twofold: i) on the one hand, it provides a conductive surface to analyze the electronic properties of the as-prepared **Ni₃(HITP)₂** thin films. On the other hand, ii) it facilitates the rational surface engineering of the microfluidic environment. Gold can be readily functionalized with thiols, forming SAMs, a feature that can be exploited to trigger a controlled orientation of **Ni₃(HITP)₂** films during their growth in the simulated microgravity conditions achieved with our microfluidic device as previously observed with glass-based substrates.

Assembling the microfluidic device with two glass slides sputtered with gold as top and bottom walls and performing the synthesis of **Ni₃(HITP)₂** as indicated above, yielded a large centimeter-scale **Ni₃(HITP)₂** film, hereafter called **Ni₃(HITP)₂@Au** film (Figure 4.30a). The morphology of the **Ni₃(HITP)₂@Au** films is again compact, smooth and crack-free with a thickness of *ca.* 100 nm (Figure 4.30b and 4.30c). HR-TEM of the material removed from **Ni₃(HITP)₂@Au** films shows the high quality of the **Ni₃(HITP)₂** crystals generated, in which the interlayer distance of 0.33 nm can be observed directly from the images, while selected area electron diffraction (SAED) patterns show peaks matching the (100) and (200) crystallographic planes (Figure 4.31b). Finally, the 2D GIWAXS images are very similar to those reported for **Ni₃(HITP)₂@Quartz** films, with the (hk0) peaks displaying a higher intensity in the *in-plane* direction, indicating that **Ni₃(HITP)₂@Au** films are also preferentially oriented with the *c*-axis perpendicular to the substrate (Figure 4.30d-g).

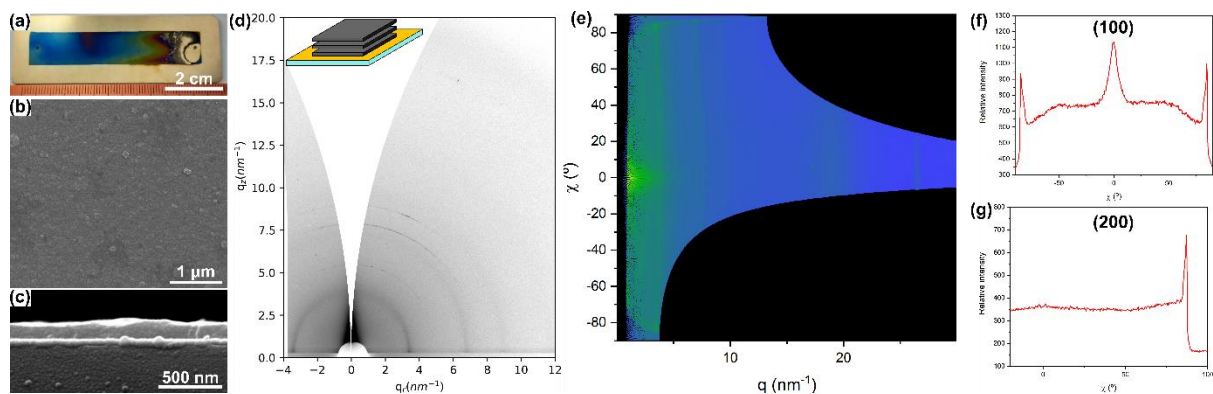


Figure 4.30: (a) Top-view SEM image of the MOF thin film obtained on top of a gold substrate. Inset: MOF thin film on a gold substrate. (b) Cross-section image of the MOF thin film obtained on top of a gold substrate, (c) 2D GIWAXS pattern of $\text{Ni}_3(\text{HITP})_2@Au$ film proving a high crystallinity and orientation. (e) 2D GIWAXS pattern of $\text{Ni}_3(\text{HITP})_2@Au$ thin films represented as azimuthal angle versus q . (f) Cut of (e) along the $q=3.32 \text{ nm}^{-1}$ position corresponding to the (100) plane. (g) Cut of (e) along the $q= 6.64 \text{ nm}^{-1}$ position corresponding to the (200) plane. Cuts in (f) and (g) show a larger intensity at $\chi = 90^\circ$ (*out-of-plane*) proving the c -axis orientation.

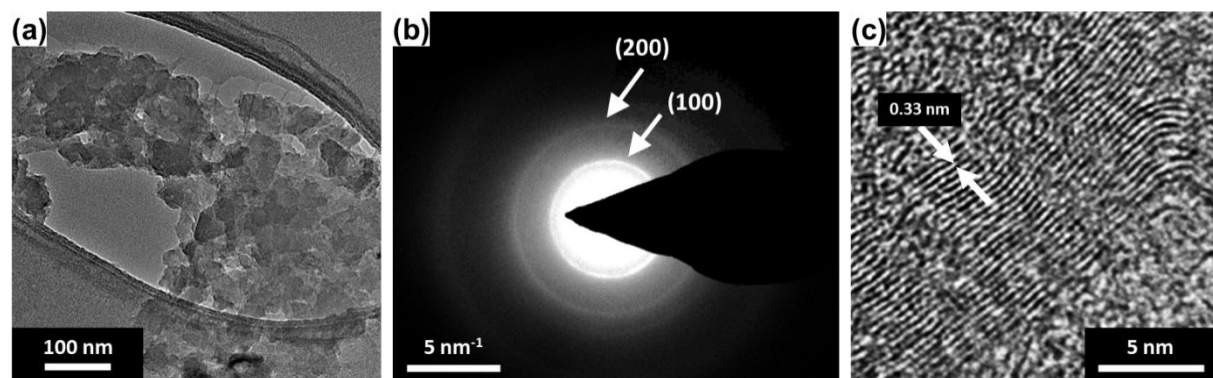


Figure 4.31: (a) Low magnification HR-TEM images of material removed from $\text{Ni}_3(\text{HITP})_2@Au$ thin films proving a high homogeneity in particle size. (b) SAED pattern obtained from (a). Diffraction shows highly crystalline $\text{Ni}_3(\text{HITP})_2$ as peaks match the reported positions of (100) and (200) planes. (c) High magnification HR-TEM image of material removed from $\text{Ni}_3(\text{HITP})_2@Au$ thin film imaged perpendicularly to the c -axis. The pattern measurements match the interlayer distance of $\text{Ni}_3(\text{HITP})_2$.

Next, we decided to functionalize the gold surface with an amino terminated SAM to study if the nature of the substrate with the presence of anchoring groups can have some influence in the growth of $\text{Ni}_3(\text{HITP})_2$ when a convection-free mass transport condition is achieved. Note that gold surfaces functionalized with chemical groups mimicking those of linkers have been used to grow conductive 2D MOFs under convective mass transport processes and employing a layer-by-layer approach.³⁴ Therefore, the amino groups of our SAM are expected to have strong directional interactions with the building blocks of $\text{Ni}_3(\text{HITP})_2$, either by coordination to the nickel cations or through hydrogen bonds with the ligand. Accordingly, a completely different microfluidic-based synthetic environment was

designed in these studies to perform the two-step vapor induced crystallization of $\text{Ni}_3(\text{HITP})_2$ films under the convection-free mass transport condition achieved in our microfluidic device when compared to the film grown onto bare gold substrates.

Gold substrates were functionalized with amino terminated groups that can coordinate to the metallic center. The formation of the amino terminated SAM was confirmed by means of contact angle (Figure 4.32b). The as-sputtered gold substrates showcase contact angles with water of $77 \pm 4^\circ$ whereas the functionalized gold substrates with SAM show lower contact angles around $51.7 \pm 0.7^\circ$. The high reproducibility of the contact angle measurement along the substrate suggests a high homogeneity and quality of the SAM. Further, FT-IR spectroscopy carried out in reflection mode on top of the functionalized substrates (Figure 4.32a) revealed the presence of the characteristic peaks of 11-Amino-1-undecanethiol. A broad band at $\sim 3100 \text{ cm}^{-1}$ corresponding to the $\nu(\text{N-H})$ vibration is observed along with the bending vibration of the same bond $\delta(\text{N-H})$ at 1630 cm^{-1} . Besides, a highly intense absorption at 1260 cm^{-1} indicates the presence of the $\nu(\text{C-N})$ vibration. Remarkably, no signal between 2500 and 2600 cm^{-1} corresponding to the $\nu(\text{S-H})$ can be seen indicating that the SAM is effectively formed with the thiol group linked to the gold substrate.

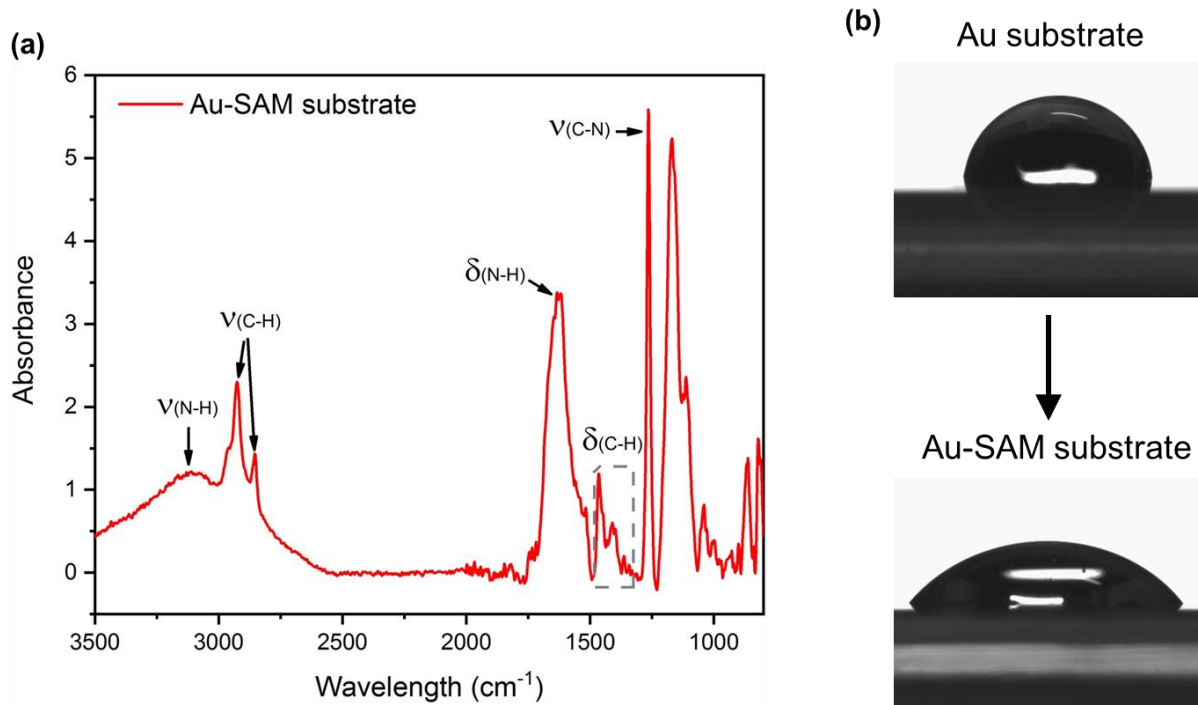


Figure 4.32: (a) FT-IR spectrum of the Au-SAM substrate to check the chemical modification. Characteristic vibrational bands are labelled on the spectrum. (b) Representative images of water droplets for contact angle measurements in Au and Au-SAM substrates previously and after the surface chemical modification respectively.

Thus, Au-SAM substrates were used now as substrates in the double slide cell. Even though the films grown on bare gold and on Au-SAMs substrates looked similar to the naked eye (Figure 4.30a and Figure 4.33a, respectively), the **Ni₃(HITP)₂@Au-SAM** films showed a very different morphology when observed by SEM. As shown in Figure 4.33b and 4.33c, the **Ni₃(HITP)₂@Au-SAM** films consist of densely packed nanoplatelets attached edge-on to the Au-SAM substrate, while the thickness remains at *ca.* 100 nm. This striking morphological change was also corroborated by AFM, which also allowed to assess the significant difference in roughness between **Ni₃(HITP)₂@Au** and **Ni₃(HITP)₂@Au-SAM** films (Figures 4.34 and 4.35). From the AFM images, RMS of **Ni₃(HITP)₂@Au** films is 7.2 ± 0.5 nm while the RMS for **Ni₃(HITP)₂@Au-SAM** films is 24.1 ± 0.6 nm. More interestingly, 2D GIWAXS measurements showed that this morphological change arises from a change in the orientation of the **Ni₃(HITP)₂** crystals generated. As seen in Figure 4.33d-g, the (hk0) peaks acquired from the 2D GIWAXS patterns of **Ni₃(HITP)₂@Au-SAM** films are more intense in the *out-of-plane* direction, which agrees with a preferential orientation of the **Ni₃(HITP)₂@Au-SAM** films parallel to the substrate. These results are in sharp contrast to the earlier observations where **Ni₃(HITP)₂@Au** films were grown with an orientation perpendicular to the substrate. HR-TEM images of the material removed from **Ni₃(HITP)₂@Au-SAM** films reveal hexagonal patterns with periodicities of 2 nm, matching the pores of the **Ni₃(HITP)₂** structure. Additionally, SAED patterns also show the (100) and (200) reflections of **Ni₃(HITP)₂** crystals as for **Ni₃(HITP)₂@Au** films (Figure 4.36). Altogether, these results show the versatility of our approach to prepare compact and crack-free **Ni₃(HITP)₂** thin films both in conductive and insulating substrates, *i.e.* on quartz and/or gold substrates, respectively. Strikingly, it was also demonstrated that the simulated microgravity conditions achieved with our microfluidic device can trigger the growth of compact, smooth and crack-free **Ni₃(HITP)₂** thin films with controlled preferred orientations, either perpendicular or parallel to the substrate, avoiding time-consuming, labor-intensive, and non-controlled fluid flow layer-by-layer approaches.

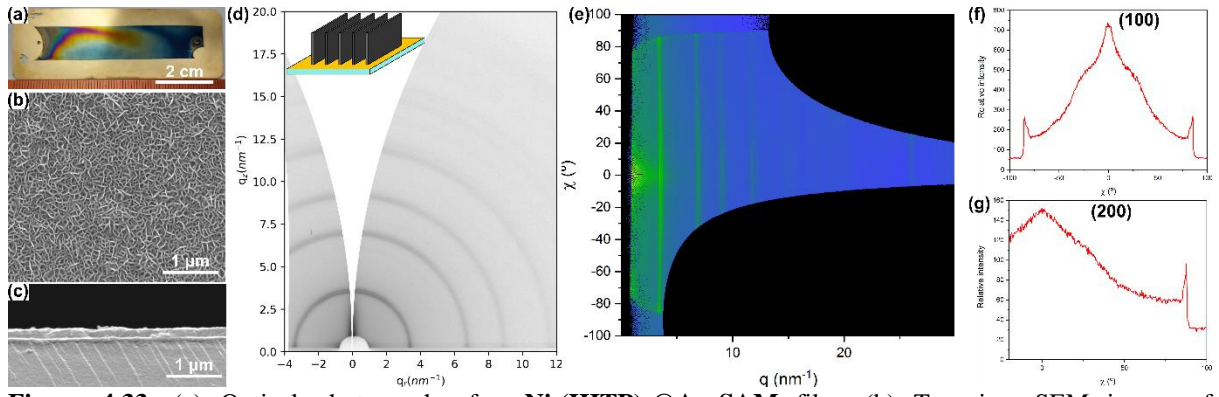


Figure 4.33: (a) Optical photograph of a $\text{Ni}_3(\text{HITP})_2@Au\text{-SAM}$ film. (b) Top-view SEM image of $\text{Ni}_3(\text{HITP})_2@Au\text{-SAM}$ film. (c) Cross-section SEM image of a $\text{Ni}_3(\text{HITP})_2@Au\text{-SAM}$ film. (d) 2D GIWAXS pattern of a $\text{Ni}_3(\text{HITP})_2@Au\text{-SAM}$ film. (e) 2D GIWAXS pattern of $\text{Ni}_3(\text{HITP})_2@Au\text{-SAM}$ thin films represented as azimuthal angle versus q . (f) Cut of (e) along the $q=3.32 \text{ nm}^{-1}$ position corresponding to the (100) plane. (g) Cut of (e) along the $q= 6.64 \text{ nm}^{-1}$ position corresponding to the (200) plane. Cuts in (f) and (g) show a larger intensity at $\chi = 0^\circ$ (*in-plane*) proving the *ab*-axis orientation.

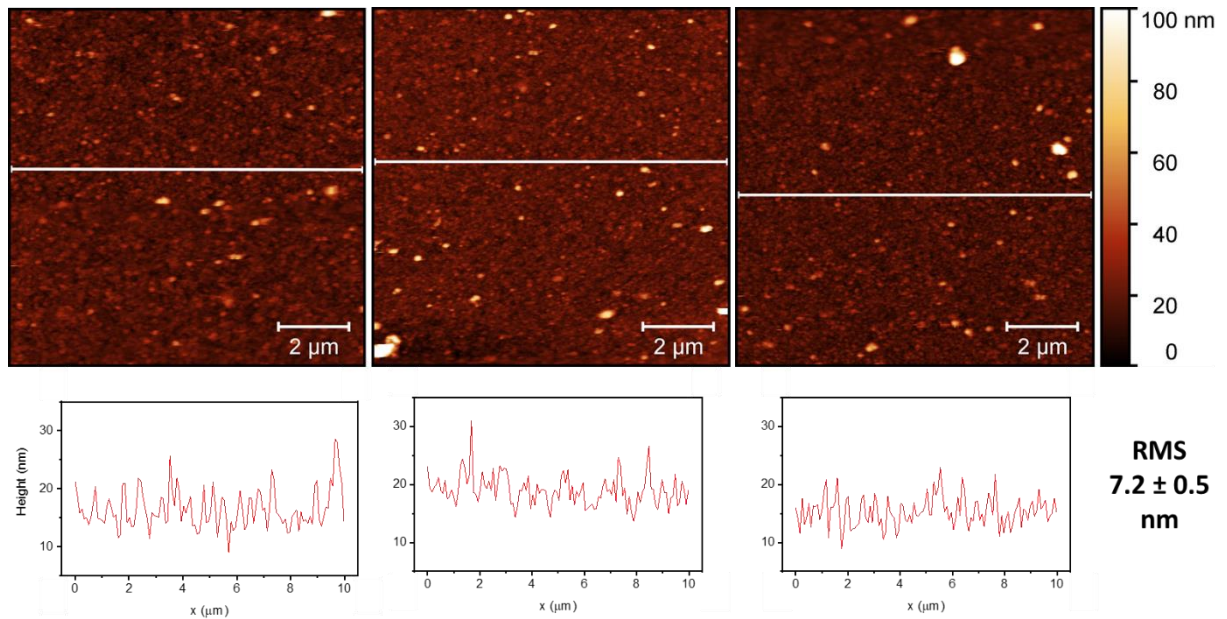


Figure 4.34: AFM images of $\text{Ni}_3(\text{HITP})_2@Au$ film at different areas for statistics on roughness. Profiles indicated for each image can be found below it. High resemblance between images indicates the high homogeneity of the sample. Color scale bars are the same for all images.

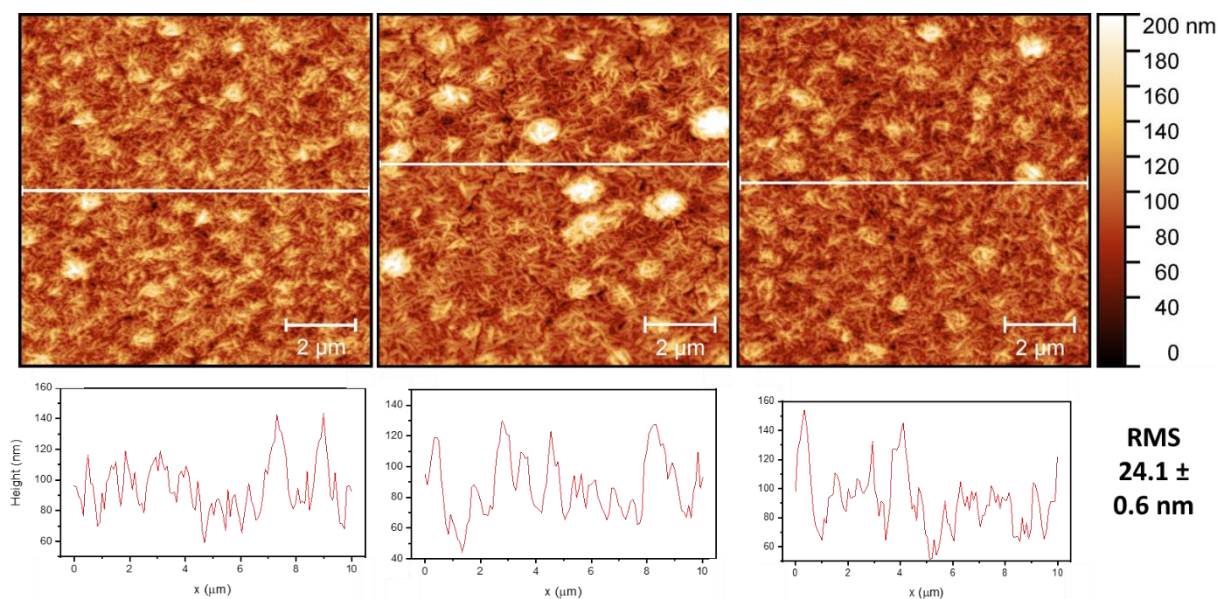


Figure 4.35: AFM images on $\text{Ni}_3(\text{HITP})_2@ \text{Au-SAM}$ film at different areas for statistics on roughness. Profiles indicated for each image can be found below it. High resemblance between images indicates the high homogeneity of the sample. Color scale bars are the same for all images.

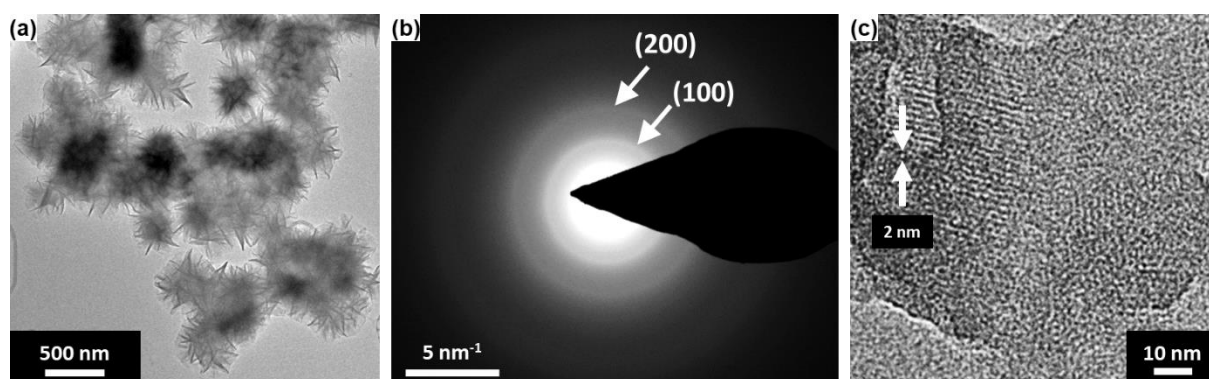


Figure 4.36: (a) Low magnification TEM images of material removed from $\text{Ni}_3(\text{HITP})_2@ \text{Au-SAM}$ thin films proving a high homogeneity in particle size. (b) SAED pattern obtained from (a). Diffraction shows highly crystalline $\text{Ni}_3(\text{HITP})_2$ as peaks match the reported positions of (100) and (200) planes. (c) High magnification HR-TEM image of material removed from $\text{Ni}_3(\text{HITP})_2@ \text{Au-SAM}$ thin film imaged parallel to the c-axis. The pattern measurements match the interlayer distance of $\text{Ni}_3(\text{HITP})_2$.

FT-IR on $\text{Ni}_3(\text{HITP})_2@Au$ and $\text{Ni}_3(\text{HITP})_2@Au\text{-SAM}$ thin film show identical spectra (Figure 4.37). Both thin films have the characteristic fingerprint between 1300 and 1600 cm^{-1} also seen in the $\text{Ni}_3(\text{HITP})_2$ powder spectrum obtained with the previously reported method which corresponds to the $\delta(\text{C-N})$ and $\delta(\text{N-H})$ vibrations.

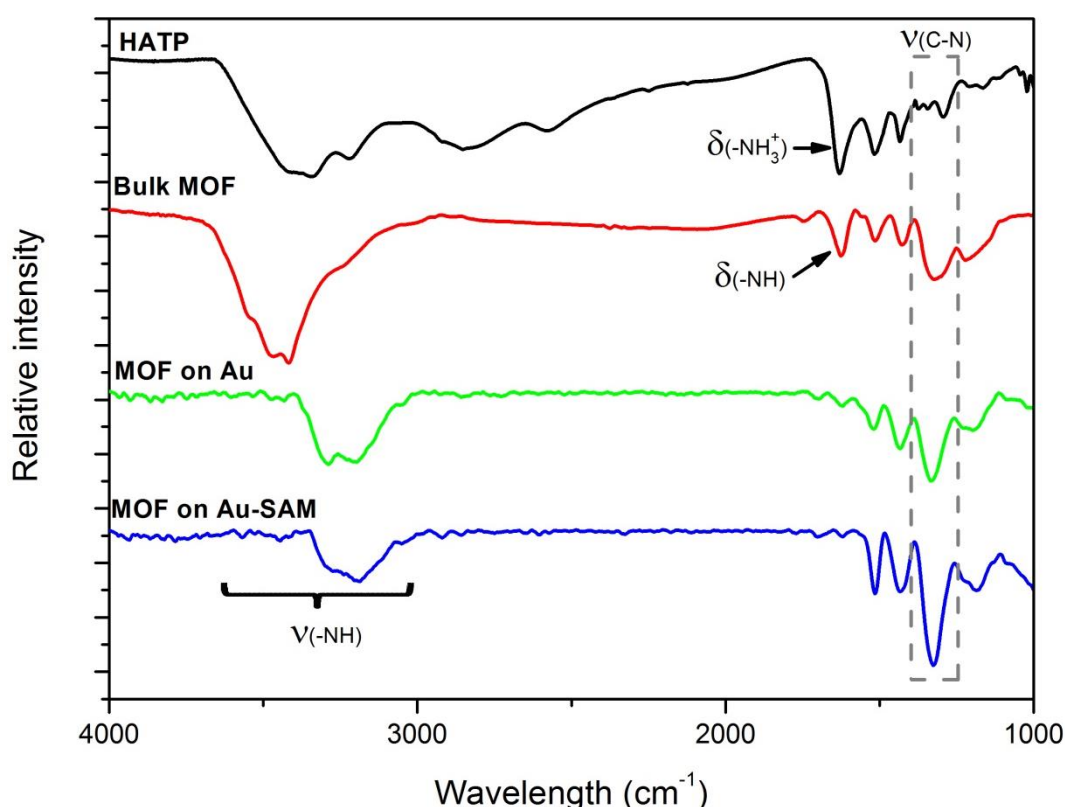


Figure 4.37: Comparison of FT-IR spectra of **HATP·6HCl** molecule (black), $\text{Ni}_3(\text{HITP})_2$ bulk material (red) measured in transmission mode and spectra of $\text{Ni}_3(\text{HITP})_2@Au$ thin film (green) and $\text{Ni}_3(\text{HITP})_2@Au\text{-SAM}$ thin film (blue) measured in reflectance mode. Characteristic vibrations bands are labelled on the spectra.

Difference on the surface roughness was analyzed by contact angle measurements as well (Figure 4.38). Differences on water uptake on these porous structures can have a deep impact on differences on the electronic properties since gas uptake has proven to change measured conductivities on conductive 2D MOFs thin films³⁵ due to swelling effect. Noticeably, contact angle with water diminishes around 30° in 20 minutes for both thin films. Thus, water uptake kinetics in this porous material remains unchanged despite the change of preferential orientation and hence direction of the porous in the thin film from one sample to another.

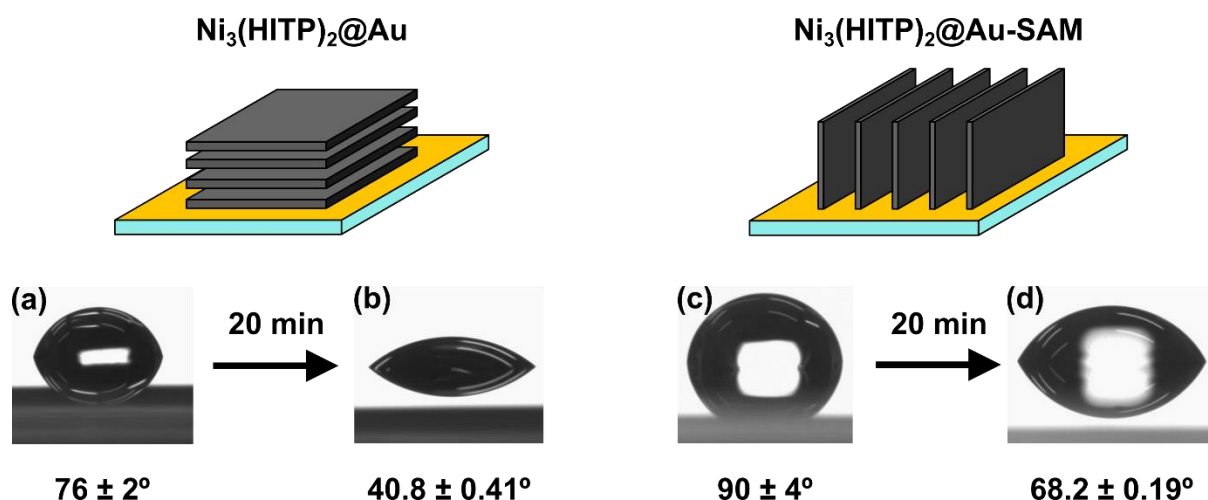


Figure 4.38: Water droplets from contact angle measurements from (a) $\text{Ni}_3(\text{HITP})_2@Au$ and (c) $\text{Ni}_3(\text{HITP})_2@Au\text{-SAM}$ films respectively. Larger values in $\text{Ni}_3(\text{HITP})_2@Au\text{-SAM}$ films are obtained due to larger roughness. (b) and (d) Decreasing of contact angle of $\approx 30^\circ$ in 20 min after deposition show similar water uptake kinetics in both films.

All in all, two main differences arise when comparing the characterization of $\text{Ni}_3(\text{HITP})_2@Au$ and $\text{Ni}_3(\text{HITP})_2@Au\text{-SAM}$ films: crystallite orientation and surface roughness. Other parameters as particle size, crystallinity and composition of the films have proven to remain unmodified despite the change on the MOF growth.

e.- Electronic anisotropy

Hence, conductance spectroscopy is faced now aiming to study the impact of preferential orientation into electronic properties of $\text{Ni}_3(\text{HITP})_2$ thin films. For this purpose, different sets of metallic gold contacts were sputtered on top of each sample. Two wire I-V curves were recorded in N_2 atmosphere from each sample using different contacts with the same width-to-length ratio W/L summarized in Table 4.1.

Table 4.1: Width and length from each set of sputtered gold contacts.

Width		Length
L/W = 20	50 μm	1 mm
	100 μm	2 mm
	150 μm	3 mm
	200 μm	4 mm
	250 μm	5 mm
	400 μm	8 mm

Values on the electronic resistance on each the sample, which can be extracted from the slope of the I-V curves, depend inherently on the geometry of the contacts as expressed in equation 1. Thus, as the ratio W/L is maintained, resistances measured on a same sample with different set of contacts will depend only on its thickness and conductivity.

$$R = \frac{1}{\sigma} \cdot \frac{W}{L \cdot t} \quad \text{Eq. 1}$$

(where σ is the conductivity of the sample, L is length of the contacts, W is width between contacts, and t is the thickness of the sample).

Linear I-V curves were obtained in measurements with all set of contacts indicating good ohmic contacts and high metallic behavior of the sample (Figure 4.39). This suggests a high percolation degree of charge carriers between crystallites independently of the crystalline preferential orientation of the films. Similar resistances were extracted from each set of contacts for each sample indicating a high homogeneity in thickness and compactness along each. Resistances obtained from one film to another remained also of the same order of magnitude. For instance, resistances extracted from I-V curves obtained with contacts spaced of 250 μm were $146 \pm 61 \Omega$, $174 \pm 9 \Omega$ and $130 \pm 12 \Omega$ in the case of $\text{Ni}_3(\text{HITP})_2@\text{Glass}$, $\text{Ni}_3(\text{HITP})_2@\text{Quartz}$ and $\text{Ni}_3(\text{HITP})_2@\text{Glass-SAM}$ thin films respectively (Figure 4.41).

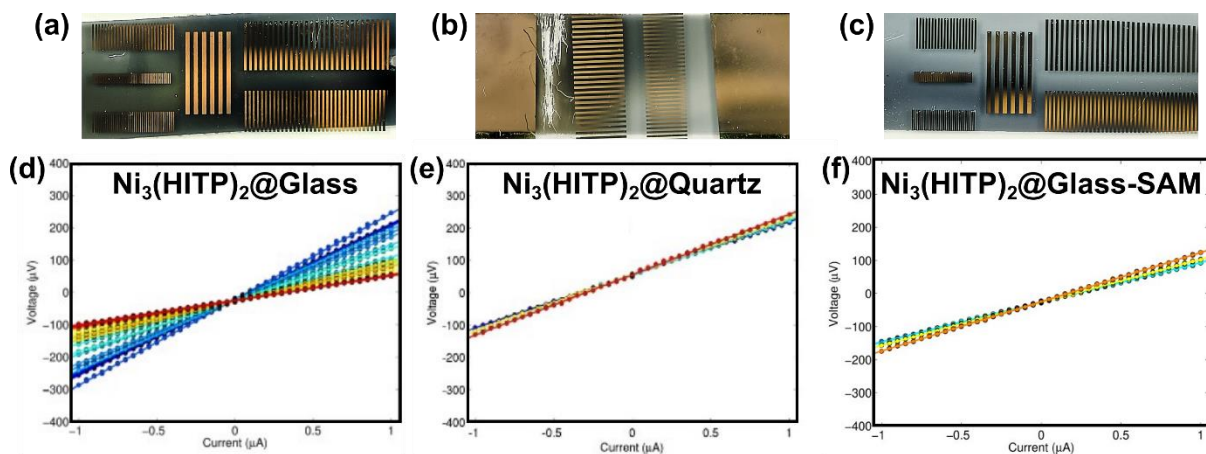


Figure 4.39: (a-c) Photographs of the deposited contacts for each sample. (d-f) I-V linear curves obtained using 5 mm long contacts spaced of 250 μm for all three films.

Notoriously, samples grown on glass showcased a larger distribution of measured resistances whereas films supported on quartz or functionalized glass showcased quite reproducible slopes from device to device. Thus, we can conclude the random crystalline orientation in samples as **Ni₃(HITP)₂@Glass** thin films can lead to a variance in the electronic properties within the sample, as different local crystalline orientations may arise. On the other hand, crystalline uniformity in oriented samples as **Ni₃(HITP)₂@Quartz** and **Ni₃(HITP)₂@Glass-SAM** thin films lead to a uniformity on the conductivity along the sample. Worth-to-mention, taking into account the 100 nm thickness of all three films, conductivities of 34 ± 14 , 29 ± 2 and 39 ± 4 S·cm⁻¹ are obtained for **Ni₃(HITP)₂@Glass**, **Ni₃(HITP)₂@Quartz** and **Ni₃(HITP)₂@Glass-SAM** thin films respectively. Hence, microgravity reactors have proven to successfully obtain centimeter-long homogenous and highly conducting **Ni₃(HITP)₂** thin films with different crystalline orientations, opening the way to new and disruptive applications. However, due to the polycrystalline character and random *in-plane* orientation of the samples, these measurements do not allow to assess the anisotropy of conduction in **Ni₃(HITP)₂**. For this, another set-up was considered.

Since the **Ni₃(HITP)₂** films have the same crystallographic orientation on quartz and gold, a microfluidic device assembled with quartz slides sputtered with gold electrodes was considered as the best-case scenario to study the electrical anisotropy of the **Ni₃(HITP)₂** films generated (Figure 4.40). Accordingly, quartz substrates with pre-patterned gold electrodes were used to grow **Ni₃(HITP)₂@Electrodes** films with their *c*-axis perpendicular to the substrate. This electrode configuration, represented as geometry (i) in Figure 4.40b, allowed the direct characterization of the *in-plane* conductivity of **Ni₃(HITP)₂@Electrodes** films right after their generation inside our microfluidic device. However, the *out-of-plane* conductivity properties of **Ni₃(HITP)₂@Electrodes** films required a second set of electrodes on top of the **Ni₃(HITP)₂@Electrodes** films. Taking into account that the thermal evaporation or the sputtering of top electrode contacts onto the generated **Ni₃(HITP)₂@Electrodes** films will facilitate the intercalation of metal atoms into the film altering its electrical properties and eventually leading to electrical shortcuts, we conducted a different approach.³⁶ First, 50 nm of gold was thermally evaporated on polyimide substrates and these were mechanically pressed on top of the 100 nm thick **Ni₃(HITP)₂@Electrodes** films, resulting in the contact geometry (ii) shown schematically in Figure 4.40c. All these geometries allowed characterizing two relevant charge transport channels in the as-synthesized **Ni₃(HITP)₂@Electrodes** films. While geometry (i) allows to study charge

transport horizontally (*i.e.* σ_{\parallel}), hence along the **Ni₃(HITP)₂@Electrodes** films, geometry (ii) gives access to vertical charge transport (σ_{\perp}), *i.e.* perpendicular to the **Ni₃(HITP)₂@Electrodes** films. Note that performing this vertical measurement through the extremely **Ni₃(HITP)₂@Electrodes** thin films is challenging using standard direct current (DC) measurement techniques because of the non-negligible contribution of contact resistances, so a Lock-in alternating current (AC) amplifier in A-B mode was used to efficiently filter DC contact voltages. In order to calibrate the electrical measurement setup and to determine its resolution two different commercially available copper wires with different length were employed. Figure 4.41 shows the I-V characteristics, phase and resistance as function of cable length and multiplicity exhibiting resistivity values for copper comparable with literature. Thus, the employed system allows to measure sub-microvolt resolution suitable to characterize **Ni₃(HITP)₂**.

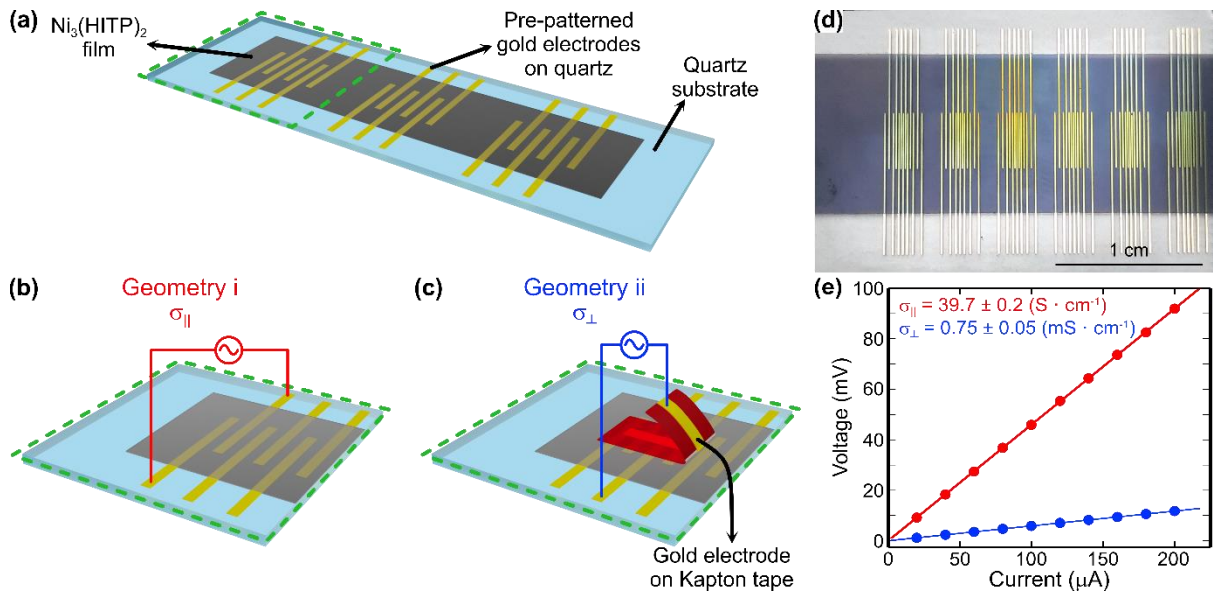


Figure 4.40: Electrical characterization of **Ni₃(HITP)₂** thin films. (a) Schematic view of the pre-patterned gold electrodes below the **Ni₃(HITP)₂@Electrodes** film. (b) and (c) Schematic views of the area highlighted in green in (a) showing the contact geometries employed to measure the electrical anisotropy of a **Ni₃(HITP)₂@Electrodes** film. (b) shows the contact used for in-plane conductivity, while (c) shows the gold contact thermally evaporated on a polyimide substrate and subsequently pressed on top of the sample to measure the out-of-plane conductivity. (d) **Ni₃(HITP)₂@Electrodes** film (dark region in the center) grown on top of pre-patterned gold electrodes deposited by sputtering on a quartz substrate, analogously to the scheme in (a). (e) Lock-in AC V-I measurements of a **Ni₃(HITP)₂@Electrodes** film measured in-plane (red, geometry (i)) and vertical directions (blue, geometry (ii)).

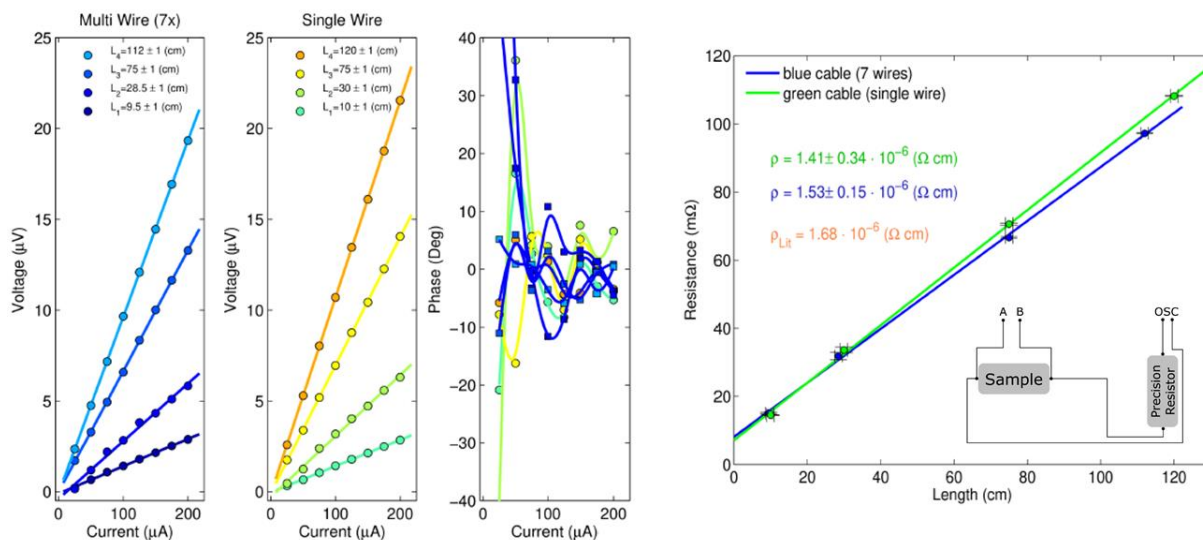


Figure 4.41: Calibration measurements of Lock-in AC system employing commercial copper cables with different length. By using a Lock-in amplifier in A-B mode it is possible to efficiently filter DC contact voltages caused by contact resistances. In order to minimize parasitic effects from cables, the frequency was fixed at 73.5 Hz while the AC voltage of the lock-in oscillator was varied from 0 – 2000 mV. A precision resistor, chosen in agreement with the electrical conductivity of the sample (Copper wire in this case), was used to apply a current from 0 – 200 μA . Both tested copper cables exhibited resistivity values well in agreement with literature values of copper.

As shown in Figure 4.40c, the I-V plots obtained for both geometries are highly linear, which indicates good ohmic contacts³⁷ and negligible Fermi level pinning³⁸ along all directions of the **Ni₃(HITP)₂@Electrodes** films. Moreover, the phase during the measurements remains close to zero, showcasing a very low capacitive coupling in all geometries (Figure 4.42). Linear fits of the I-V plots provided conductivities of $39.7 \pm 0.2 \text{ S}\cdot\text{cm}^{-1}$ for horizontal measurements under ambient temperature and pressure. Interestingly, such high conductivities close to $40 \text{ S}\cdot\text{cm}^{-1}$ in triphenylene-based MOFs are normally only obtained under inert atmosphere or vacuum rather than in ambient conditions, as water uptake diminishes the conductivity.³⁵ It should be noted here that in order to achieve similar values in ambient conditions, only pelletization at high pressures has proved efficient, *i.e.* pelletization at ca. 1 GPa.³⁹ Again, these results clearly showcase the good packing of the **Ni₃(HITP)₂** crystallites obtained with our microfluidic approach. On the other hand, the vertical conductivities obtained from geometry (ii) is $0.75 \pm 0.05 \text{ mS}\cdot\text{cm}^{-1}$, which leads to a high anisotropy factor of $5\cdot 10^4$. Note that the same high anisotropy factor has only been reported for graphite so far.^{40–42} To ensure the good contact and measurement in geometry (ii), vertical I-V plots were acquired again using thinner gold contacts on the polyimide substrate. Notoriously, same values on the vertical conductivity were obtained ($0.78 \pm 0.05 \text{ mS}\cdot\text{cm}^{-1}$) confirming the veracity of the measurements.

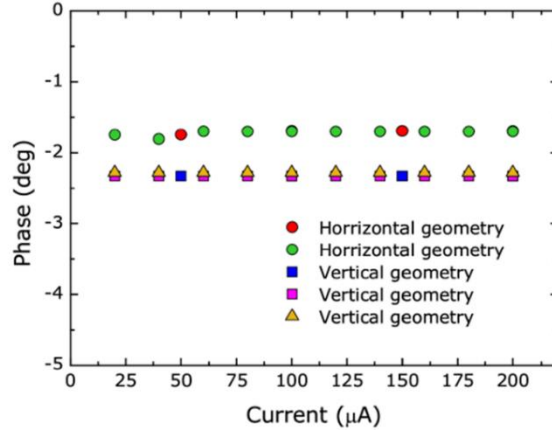


Figure 4.42: The phase difference between current and voltage was found to be very close to zero, indicating good Ohmic contacts and negligible capacitive coupling in all measured geometries.

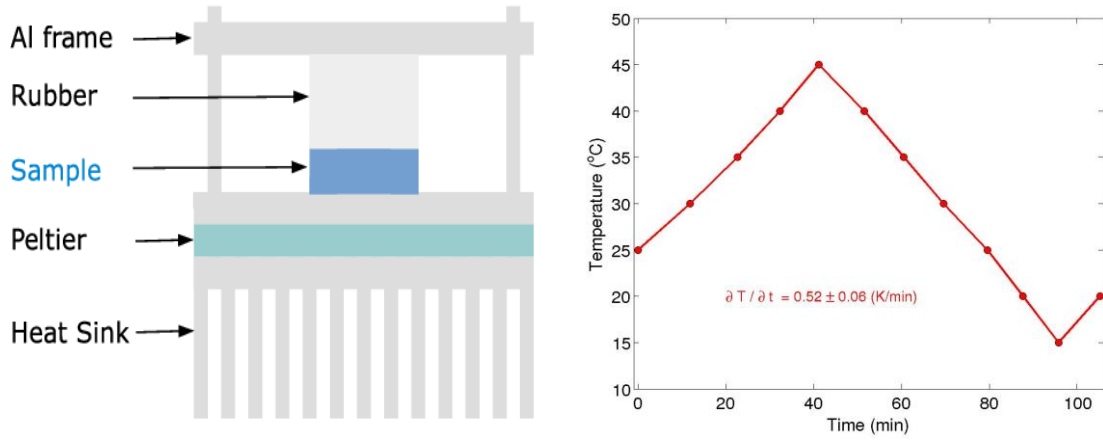


Figure 4.43: (a) Schematic illustration of Aluminum frame including Peltier to thermally stabilize the sample at a given temperature setpoint. (b) Typical heating/cooling cycle with a slow rate of about 0.52 ± 0.06 K/min to guarantee thermal equilibrium of the sample and minimize heating/cooling induced mechanical stress.

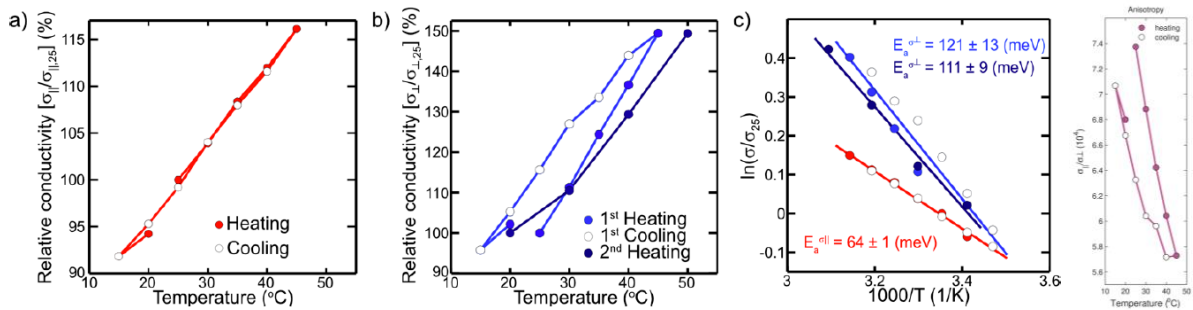


Figure 4.44: Temperature dependent conductivity of a $\text{Ni}_3(\text{HITP})_2@ \text{Electrodes}$ films measured in (a) geometry (i) and (b) geometry (ii). two heating cycles are conducted in the vertical geometry. (c) Arrhenius plot for the heating and cooling cycles in (a) and (b). $R^2 = 0.995, 0.893$ and 0.987 for the red, blue and deep blue plots, respectively. (d) Electrical anisotropy as function of temperature. As expected, conductivity measured perpendicular to the substrate shows a higher temperature dependence compared to the horizontal direction. This is clearly reflected in the temperature dependent anisotropy.

In addition to the electrical characterization at room temperature, we also studied the temperature dependence of the electrical conductivity, since it provides further insights into the transport properties of the material. Geometries (i) and (ii) were used to probe the horizontal and vertical charge transport, respectively. Samples were mounted on an aluminum support with temperature regulation⁴³ between $T = 15$ and 50 °C (Figure 4.43). As shown in Figure 4.44a and Figure 4.44b, both geometries display thermally activated transport with a very small hysteresis between heating and cooling. The temperature dependence fits nicely to an Arrhenius type of response, as shown in Figure 4.44c, from which activation energies (E_a) of 64 ± 1 , 121 ± 13 and 111 ± 11 meV can be extracted for $\sigma_{||}$ and σ_{\perp} in the first and second heating ramps, respectively. These values are in good agreement with theoretical values predicted in the literature.⁴³ It is worth noting that, as expected, the activation energy in the vertical direction is higher than horizontally, which results in a decrease of the conductivity anisotropy at higher temperatures (Figure 4.44d).

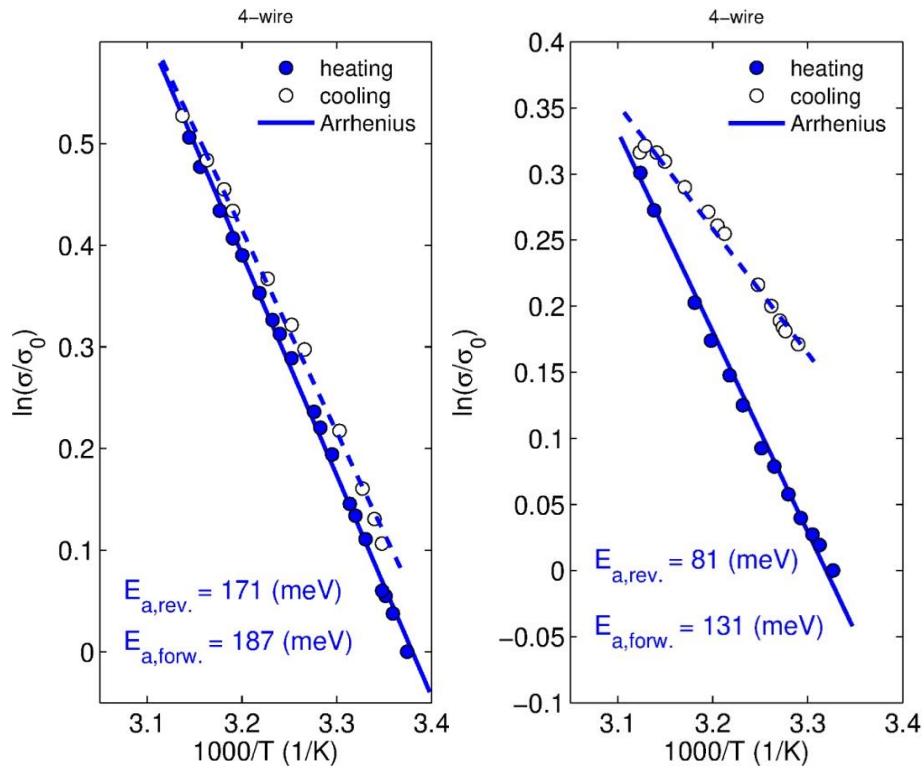


Figure 4.45: Arrhenius plot $\text{Ni}_3(\text{HITP})_2@\text{Glass}$ measured under ambient conditions (*i.e.* $T = 25 \pm 1$ °C and relative humidity (RH) $\text{RH} = 62 \pm 5$ %), and under inert conditions within a nitrogen glovebox ($\text{H}_2\text{O} < 5$ ppm, $\text{O}_2 < 1$ ppm).

Remarkably, when probing randomly oriented $\text{Ni}_3(\text{HITP})_2@\text{Glass}$ thin films in a four-probe DC configuration, the temperature dependence in this sample in ambient conditions shows larger activation energies than in the preferentially oriented thin film, being

within 171-187 meV (Figure 4.45). It is only when placing the $\text{Ni}_3(\text{HITP})_2@ \text{Glass}$ thin films within a nitrogen glovebox that activation energies come closer to the previously measured with values between 81-131 meV. This along with the conductivity values suggest that the use of microgravity conditions for the synthesis of oriented and high degree compact thin films strongly suppresses the effects of humidity and ambient conditions on $\text{Ni}_3(\text{HITP})_2$ thin films. The control on the growth and the orientation allows a diminishing of the porosity and exposed surface area which are critical for the interacting interface of the thin film with its surroundings. Thus, microgravity mimetic syntheses pave the way to new or enhanced applications of $\text{Ni}_3(\text{HITP})_2$ thin films in ambient conditions.

f.- Synthesis and characterization of $\text{Ni}_3(\text{HITP})_2@ \text{PDMS}$

After proving the control on the synthesis and the crystalline orientation, compatibility with transferring techniques was studied. For this, previously described peeling method¹⁵ was applied on $\text{Ni}_3(\text{HITP})_2@ \text{Au}$ thin films (Figure 4.46). Transfer of the $\text{Ni}_3(\text{HITP})_2$ thin film into a flexible PDMS substrate was successful yielding centimeter $\text{Ni}_3(\text{HITP})_2@ \text{PDMS}$ large thin films (see Figure 4.47a). SEM images of the obtained $\text{Ni}_3(\text{HITP})_2@ \text{PDMS}$ (Figure 4.47a) show a homogenous coverage of the flexible substrate. Absorption spectrum after peeling was performed in transmission mode across the $\text{Ni}_3(\text{HITP})_2@ \text{PDMS}$ film (Figure 4.47c). A strong absorption in the UV range and a broad band at 600 nm indicate the presence of the $\text{Ni}_3(\text{HITP})_2$ MOF. The films showed high flexibility and integrity upon bending and twisting (Figure 4.48).

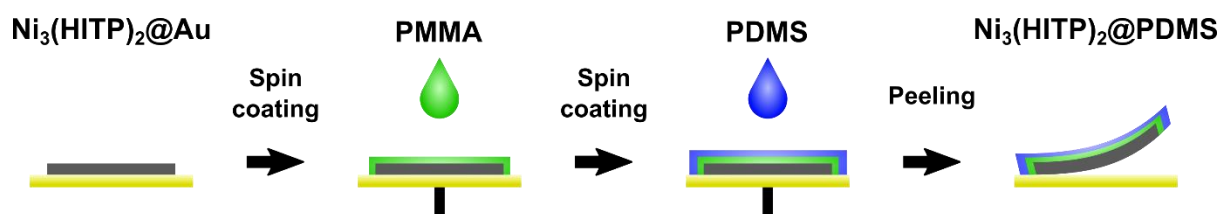


Figure 4.46: Scheme of the peeling method used to obtain $\text{Ni}_3(\text{HITP})_2@ \text{PDMS}$ thin film from $\text{Ni}_3(\text{HITP})_2@ \text{Au}$ films.

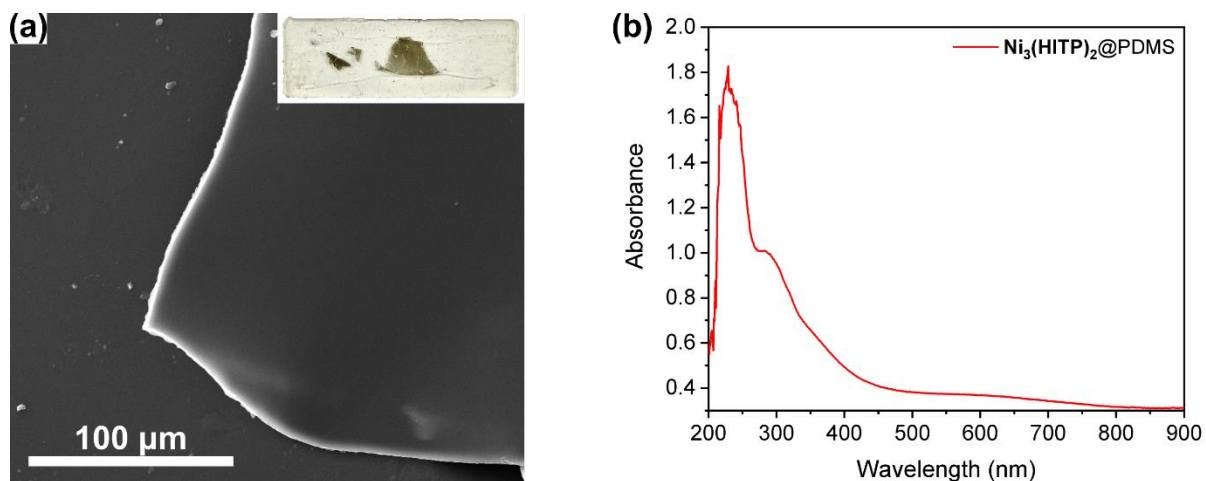


Figure 4.47: (a) SEM image of the $\text{Ni}_3(\text{HITP})_2@\text{PDMS}$ thin film. (b) UV-vis spectrum measured in transmittance of the $\text{Ni}_3(\text{HITP})_2@\text{PDMS}$ thin film. Inset: Image of the $\text{Ni}_3(\text{HITP})_2@\text{PDMS}$ thin film.

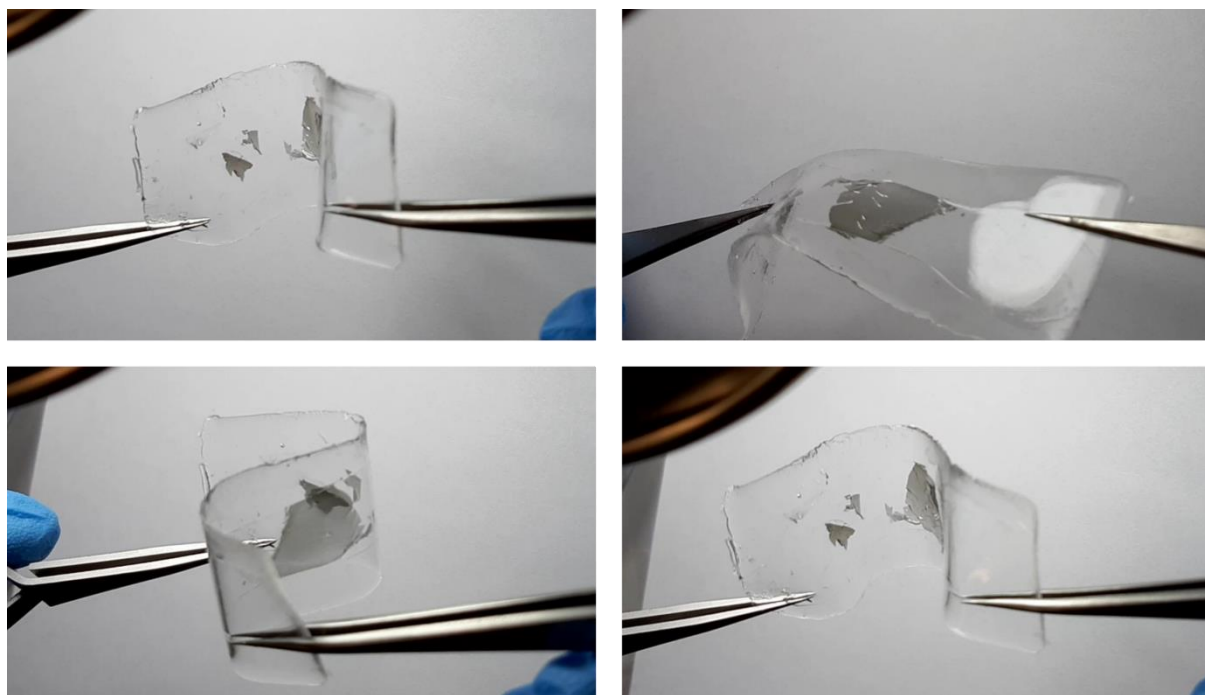


Figure 4.48: $\text{Ni}_3(\text{HITP})_2@\text{PDMS}$ thin film under different bendings.

Linear I-V curves under N_2 ambiance of the peeled thin film were taken after sputtering gold contacts, providing conductivities of order of **2 S/cm** (Figure 4.49). This similar value to the reported pellet conductivity proves a high compactness of the crystallites in the thin film, allowing charge percolation and conduction, even after the peeling process.

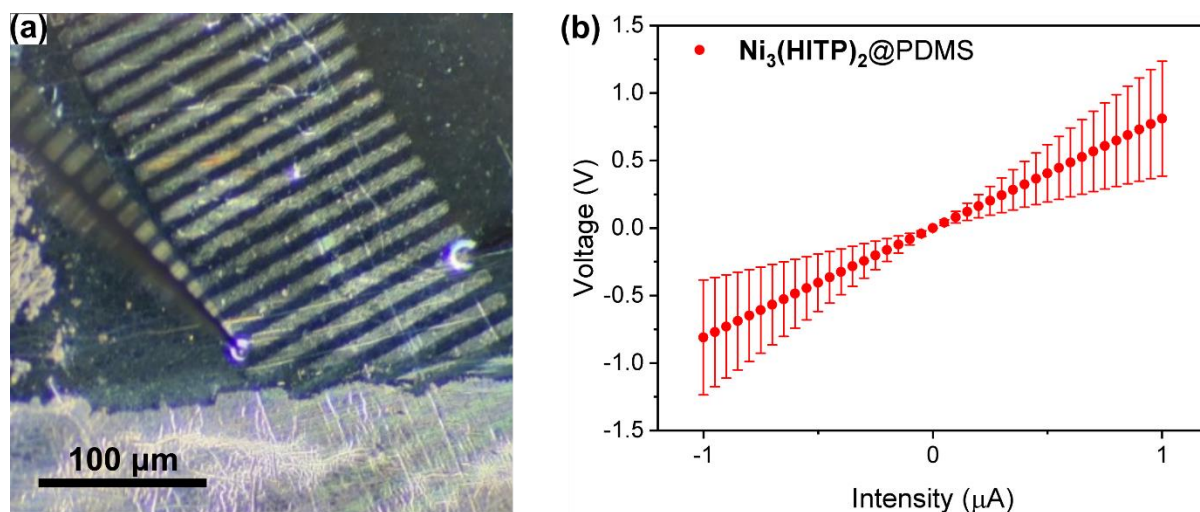


Figure 4.49: (a) OM image of the $\text{Ni}_3(\text{HITP})_2@PDMS$ thin film with gold contacts evaporated on top. Needles from the probe station are contacting the gold electrodes for measuring. (b) Two wire linear I-V curve of the $\text{Ni}_3(\text{HITP})_2@PDMS$ thin film. Error bars correspond to standard deviation. Statistics were performed by measuring on different pairs of contacts.

g.- Synthesis and characterization of $\text{Ni}_3(\text{HITP})_2@Graphene$

Further, control of synthesis under microgravity conditions on epitaxial growth and compatibility with different substrates opened the way to the growth of hybrid materials containing conductive MOF onto other layered materials. Thus, crystallization of $\text{Ni}_3(\text{HITP})_2$ on graphene is faced now. Accordingly, we designed a new microfluidic device that can accommodate a large variety of commercially and technologically relevant surfaces with a standard 1 cm x 1 cm size (*e.g.* silicon (111) and/or graphene). This new microfluidic device consists of a machined polyether ether ketone (PEEK) piece with a 1 cm square cavity in which the desirable commercial surface is placed. Then, a stainless-steel part (bottom clamp) is clamped pressing the surface against a 200 μm thick sealing groove to create the microfluidic environment presented in Figure 4.52 from Materials and Methods.

Hence, convection-free chamber was prepared using graphene supported onto 300 nm SiO_2/Si . Quality of the graphene was studied previous to the $\text{Ni}_3(\text{HITP})_2$ growth with Raman spectroscopy, taking spectra every 1 mm over the substrate. Presence of G and 2D bands at 1578 cm^{-1} and 2755 cm^{-1} respectively indicated the presence of a continuous and defect-free graphene over the whole substrate. Thus, the substrate was mounted into the confined space

reactor. As previously, the reactor filled with the DMSO solution of **HATP·6HCl** and NiCl_2 and exposed sub-sequentially to ammonia and atmospheric oxygen.

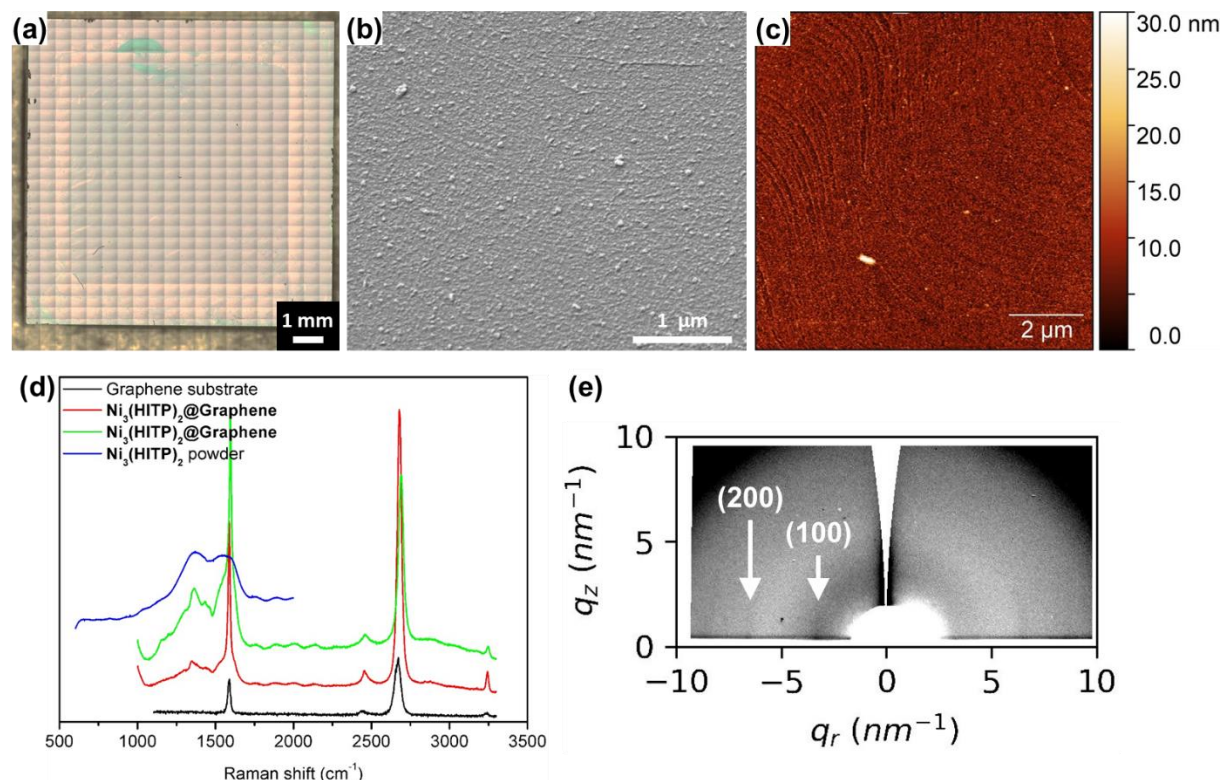


Figure 4.50: (a) Optical microscopic image of $\text{Ni}_3(\text{HITP})_2@ \text{Graphene}$ thin film with blue iridescence. (b) Top view SEM image of $\text{Ni}_3(\text{HITP})_2@ \text{Graphene}$ thin film. (c) AFM image of $\text{Ni}_3(\text{HITP})_2@ \text{Graphene}$ thin film. (d) Raman spectra of (black) graphene substrate previous to growth, (red and green) $\text{Ni}_3(\text{HITP})_2@ \text{Graphene}$ thin film and (blue) of $\text{Ni}_3(\text{HITP})_2$ powder drop-casted onto a Si/SiO₂ substrate.

As a result, a millimeter scale squared blue iridescent $\text{Ni}_3(\text{HITP})_2@ \text{Graphene}$ thin film was obtained (Figure 4.50a). Top view SEM and AFM images revealed a crack-free thin film formed by a homogenous deposition of particles and very low roughness around 2.7 nm (Figure 4.50b and 4.50c). Thickness of the $\text{Ni}_3(\text{HITP})_2@ \text{Graphene}$ film could not be assessed by profilometry due to its very low thickness but was estimated to be within the nanometer range. Raman spectroscopy was carried at different positions of the film to evaluate the presence and deposition of $\text{Ni}_3(\text{HITP})_2$ growth. Two broad bands at $\sim 1300 \text{ cm}^{-1}$ and $\sim 1550 \text{ cm}^{-1}$ overlapping the G band of graphene in the thin film can be observed matching the bands from $\text{Ni}_3(\text{HITP})_2$ powder spectrum. Further, 2D GIWAXS pattern of the film showed the reflections corresponding to the $\text{Ni}_3(\text{HITP})_2$ structure at $q_r = 3.4 \text{ nm}^{-1}$ (100), $q_r = 6.7 \text{ nm}^{-1}$ (200). Interestingly, the peaks are only observed in plane, indicating a similar c -axis orientation as the one measured in quartz. Raman spectroscopy confirmed the presence

of **Ni₃(HITP)₂** on top of graphene as two broad bands corresponding to the **Ni₃(HITP)₂** powder are seen at 1300 and 1600 cm⁻¹ aside the G and 2D bands of graphene (Figure 4.50d).

4.3 Conclusions

Here, synthesis under simulated microgravity conditions was developed and optimized, using confined space reactors and newly introduced synthesis conditions. Decrease of turbulences and convection flows had significant effects on the final material, allowing an unprecedented control over the synthesis of **Ni₃(HITP)₂** and its crystallization into centimeter-large scale homogeneous thin films. The deposition of **Ni₃(HITP)₂** could be followed by means of UV-vis spectroscopy and AFM measurements which proved a control over the thickness of the films with reaction time.

Further, convection-free reactors have proven to be compatible with a large variety of substrates, as well isolating as conducting, obtaining thin films of similar lateral dimensions and thicknesses regardless of the supporting substrate. Electronic characterization of thin films grown on top of glass under microgravity reactors proved the high conductivity and fast response leading to novel future applications.

Moreover, confined space reactors have proven to be highly dependent on the chemistry surface of the substrate enabling epitaxial growth and control over crystalline orientation. Hence, *c*-axis oriented polycrystalline thin films are obtained on quartz and gold substrates whereas *c*-axis is oriented parallel to the substrate when these substrates are functionalized with amino-terminated chains serving for metal anchorage.

Taking advantage of similar orientations, anisotropy of conductivity of this highly promising MOF could be assessed and its transfer to flexible substrates. The measurements confirm higher conductivity in the in-plane direction of the 2D layers of the material with anisotropy factors of the order of graphitic materials (10⁴).

Finally, the high control and versatility of the synthesis of thin films in convection free reactors allowed the synthesis of hybrid materials growing **Ni₃(HITP)₂** on top of single layer graphene opening the way to hybrid materials.

4.4 Materials and methods

Chemicals and materials. N-(2-Aminoethyl)-11-Aminoundecyltrimethoxysilane was purchased in Cymit (Cymit Química S.L., Barcelona, Spain). **HATP·6HCl** was synthesized according to the optimized protocol described in Chapter 3. All other reagents were purchased in Merck (Merck Life Science S.L.U., Madrid, Spain). All solvents were synthesis grade solvents with >99% purity purchased in Scharlab (Scharlab,S.L., Sentmenat, Spain). Aqueous solutions were prepared filtered, deionized and decalcified water.

The microfluidic device used for the synthesis of **Ni₃(HITP)₂** thin films (Figure 4.51) was designed using a 3D computer-aided design software (SOLIDWORKS 2018) to mechanically clamp a spacer (*e.g.* 200-500 μm -thick silicone sheet) between two quartz slides (75.5 mm x 25.5mm), hence to form a reaction area (15 mm x 60 mm) confined. This work was performed by the group of Prof. Josep Puigmartí-Luis (*UB*, Spain). Note that, the top quartz slide includes 2 holes (1 mm in diameter) enabling to fill the confined space with precursor solution once the reactor is assembled. While the top and bottom parts of the clamp were machined from aluminum, the windows in the center of the metallic clamps enable looking inside the reaction chamber. Moreover, the top clamp also includes input/output ports for microfluidic connectors (10-32 Coned for 1/16" OD, IDEX Health & Science, LLC, USA) to connect PTFE tubing (1/16" OD, IDEX Health & Science, LLC, USA).

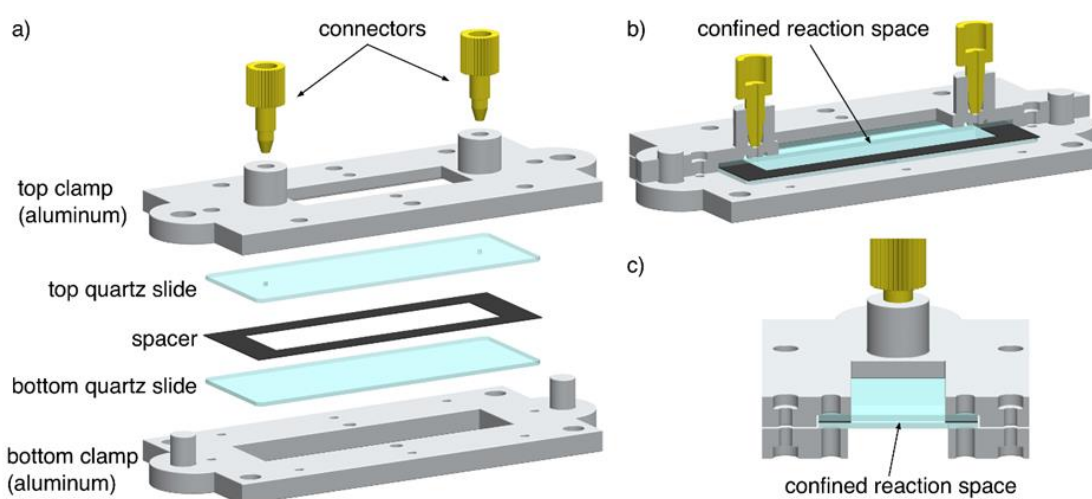


Figure 4.51: 3D schematic drawings showing (a) the split version of 1st type confined space reactor prior to its assembly to represent each part separately, and its assembled version with a section-cut (b) along the long-axis in the top part and (c) along the short-axis to demonstrate the confined reaction space formed with a spacer between two quartz slides.

The microfluidic device used for the synthesis of **Ni₃(HITP)₂@Graphene** (Figure 4.52) was designed to mechanically clamp a square shaped (10 mm x 10 mm) substrate (graphene coated Si wafer) between the top and bottom parts, respectively machined from PEEK and stainless steel. Whereas the top clamp contains both the inlet/outlet ports for microfluidic connectors and the confined gap circumscribed by a sealing groove, the bottom acts as a support to press the substrate towards the PEEK part. The tinny PEEK groove (500 µm in width) machined on the top clamp not only behaves as a sealing element to border a reaction area (7 mm x 7 mm) and avoid leakage, but also defines the confined gap (200 µm) between the substrate and PEEK part.

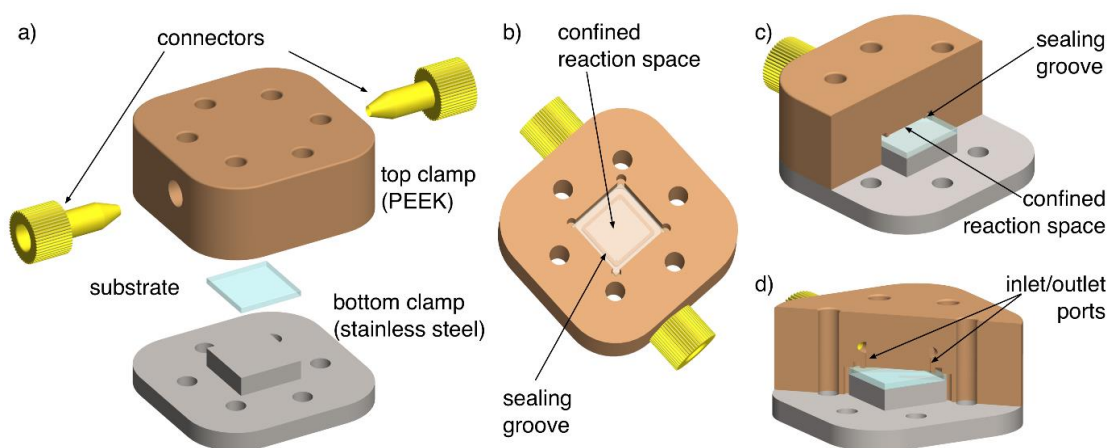


Figure 4.52: 3D schematic drawings showing (a) the split version of 2nd type confined space reactor prior to its assembly to represent each part separately, (b) the bottom view after inserting the substrate inside the top clamp to form square-shaped (7 mm x 7 mm) confined (200 µm in height) reaction space circumscribed by sealing groove, (c-d) the assembled version of the device with a section-cut in the top part (b) along the middle-axis to demonstrate the confined space shaped by sealing groove between top clamp and substrate, and (c) along the diagonal-axis to show the inlet/outlet ports.

Aqueous synthesis of thin film in confined spaces Aqueous synthesis of thin films of **Ni₃(HITP)₂** was performed with a double glass slide confined space chamber with an interlayer space of 1 mm and two inlets. A stock solution of metallic salt was prepared by dissolving 13.3 mg of NiCl₂·6H₂O in 10 mL of water. 2 mg of **HATP·6HCl** ligand were dissolved in 1 mL of water. The reaction mixture was prepared by adding 1 mL of the stock solution of NiCl₂ to the **HATP·6HCl** solution. The mixture was slowly introduced into the chamber with a syringe making sure that no air bubbles are introduced. The chamber was then placed in an ammonia-saturated gas ambience

overnight. After growth, the cell was opened and both slides were rinsed under a flux of ethanol and blow dried softly with nitrogen.

Aqueous bulk synthesis following reported protocol A solution of 6.6 mg (0.028 mmol) of $\text{NiCl}_2 \cdot 6\text{H}_2\text{O}$ in 5 mL of water and 0.3 mL of concentrated aqueous ammonia (NH_4OH , 14 $\text{mol} \cdot \text{L}^{-1}$) was added to a solution of 10 mg (0.019 mmol) of **HATP·6HCl** in 5 mL of water. This mixture was stirred in an open beaker for 2 hours at 65 °C. The resulting black powder was centrifuged, filtered, and then washed in water under reflux for a total of 36 hours (the water was refreshed 2 times during this washing step, for a total of 3 steps, 12 hours each). Finally, the solid was heated at reflux in neat acetone for another 3 h. The solid was then dried under vacuum.

Aqueous bulk synthesis with ammonia diffusion A solution of 6.6 mg (0.028 mmol) of $\text{NiCl}_2 \cdot 6\text{H}_2\text{O}$ in 5 mL of water was added to a solution of 10 mg (0.019 mmol) of **HATP·6HCl** in 5 mL of water in a glass vial. The above-mentioned solution was placed overnight in an ammonia saturated gas ambiance for its slow diffusion in the solution.

Thin film created at the water-air interface of the vial was recovered by stamping onto SiO_2/Si substrates and left to dryness at ambient conditions. The substrates were cleaned previously by sonication 10 min in acetone and 10 min in ethanol. Afterwards, the substrates were blown dried with a N_2 flux.

Bulk synthesis in DMSO solution A stock solution of metallic salt was prepared by dissolving 13.3 mg (0.056 mmol) of $\text{NiCl}_2 \cdot 6\text{H}_2\text{O}$ in 10 mL of dry synthesis grade DMSO. 2 mg of **HATP·6HCl** ligand were dissolved in 1 mL of dry synthesis grade DMSO. The reaction mixture was prepared by adding 1 mL of the stock solution of NiCl_2 to the **HATP·6HCl** solution. The mixture was then placed in an ammonia-saturated gas ambiance overnight. The ammonia-saturated ambiance was prepared with a concentrated ammonia bath (25%) freshly prepared, 5 minutes before. Afterwards, the mixture was left in air ambiance for one day for oxygen diffusion. The resulting black powder was centrifuged and subjected to three washing in water at 13000 rpm for 5 min and an additional one in acetone.

Substrate preparation

a- Glass substrates: Glass substrates were purchased in Labbox (Labbox Labware, S.L., Barcelona, Spain). Top glass surfaces were drilled with 1 mm diameter diamond drill. The drilled holes were matching the positions of the inlets in the microfluidic cell. Substrates were cleaned with ethanol and blow dried with nitrogen previously to the thin film growth.

b- Quartz substrates: Monocrystalline quartz substrates with (001) orientation were purchased in Siegertwafer (SIEGERT WAFER GmbH, Aachen, Germany). Top quartz surfaces were drilled with 1 mm diameter diamond drill. The drilled holes were matching the positions of the inlets in the microfluidic cell. Substrates were cleaned with ethanol and blow dried with nitrogen previously to the thin film growth.

c- Glass substrates functionalized with amines: Previously drilled glass substrates were cleaned with acetone and IPA. After being blow dried under nitrogen, they were placed in oxygen plasma cleaner PVA TePla Inc PS210 for one minute at 400W power and immediately placed under vacuum next to a vial with N-(2-Aminoethyl)-11-Aminoundecyltrimethoxysilane. Substrates were left overnight under vacuum. Then, the substrates were rinsed with copious amounts of ethanol and blow dried with nitrogen.

d- Gold substrates: Eight drilled glass slides (Thermo Scientific Menzel 76x26 cm) were cleaned by sonication in acetone for 10 min, followed by sonication in IPA for 10 min and were blow dried with nitrogen. The samples were introduced in AJA International Inc. ATC-8E Orion E-Beam evaporator. 5 nm layer of titanium as an adhesion layer and 50 nm of gold were deposited with e-beam evaporation under high vacuum onto the glass slides. After evaporation, the substrates were cleaned with ethanol and blow dried with nitrogen previously to the thin film growth.

e- Gold substrates functionalized with amines: Three of the previously prepared gold substrates were cleaned with acetone and IPA. After being blow dried under nitrogen, they were placed in oxygen plasma cleaner PVA TePla Inc PS210 for one minute at 400W power and immediately immersed in a 1 mM ethanoic solution of 11-Amino-1-Undecanethiol hydrochloride. The gold substrates were left overnight in the solution.

Then, the substrates were rinsed with copious amounts of ethanol and blow dried with nitrogen.

f- Quartz substrates with pre-patterned gold contacts substrates: Drilled quartz slides were cleaned by sonication in acetone for 10 minutes, followed by sonication in IPA for 10 minutes and were blown dried with nitrogen. Sets of electrodes of various channel lengths ($L = 200, 300, 500$ and $1400\ \mu\text{m}$) were fabricated by lithography using a copper mask. A 5 nm layer of titanium as an adhesion layer and 50 nm of gold were deposited with an AJA International Inc. ATC-8E Orion E-Beam evaporator under high vacuum onto the quartz slides. After evaporation, the mask was removed and the substrates were cleaned with ethanol and blown dried with nitrogen previous to thin film growth.

g- Graphene substrates: Graphene substrates were purchased to Graphenea (Graphenea Inc., Graphenea Headquarters, San Sebastián, Spain). Substrates consisted of monolayer graphene on $10\times 10\ \text{mm}\ \text{SiO}_2/\text{Si}$ (300 nm). Graphene was produced by chemical vapor deposition and transferred by a wet transfer process. Quality of the as-received graphene was assessed by RAMAN spectroscopy. The substrates were used as received for the synthesis.

h- Polyimide supported contacts: Au contacts were evaporated with a Univex 350G, thermal evaporator with base pressure below 10^{-6} mbar.

Synthesis in DMSO of thin film in double slide confined spaces $\text{Ni}_3(\text{HITP})_2$ thin films were obtained with a double slide confined space chamber with an interlayer silicon spacer of 1 mm and two inlets. The chamber was mounted with identical substrates in all cases right after their treatment. A stock solution of metallic salt was prepared by dissolving 13.3 mg of $\text{NiCl}_2\cdot 6\text{H}_2\text{O}$ in 10 mL of dry synthesis grade DMSO. 2 mg of **HATP·6HCl** ligand were dissolved in 1 mL of dry synthesis grade DMSO. The reaction mixture was prepared by adding 1 mL of the stock solution of NiCl_2 to the **HATP·6HCl** solution. The mixture was slowly introduced into the chamber with a syringe making sure that no air bubbles are introduced. The chamber was then placed in an ammonia-saturated gas ambiance overnight. The remaining mixture solution was placed with the chamber in the ammonia bath as a blank and bulk reference. The ammonia-saturated ambiance was prepared with a concentrated ammonia bath (25%) freshly prepared, 5 minutes before the insertion of the cell.

Afterwards, the chamber and the blank were left in air ambiance for three days for oxygen diffusion. After growth, the cell is opened and both slides were rinsed under a flux of ethanol and blow dried softly with nitrogen.

Synthesis in DMSO of thin film in one slide confined spaces ($\text{Ni}_3(\text{HITP})_2@\text{Graphene}$) A stock solution of metallic salt is prepared by dissolving 13.3 mg of $\text{NiCl}_2 \cdot 6\text{H}_2\text{O}$ in 10 mL of dry synthesis grade DMSO. 2 mg of **HATP·6HCl** ligand are dissolved in 1 mL of dry synthesis grade DMSO. The reaction mixture is prepared by adding 1 mL of the stock solution of NiCl_2 to the **HATP·6HCl** solution. A 1 cm x 1 cm confined space reactor with a 100 μm thick PEEK spacer and a graphene substrate was filled with the above solution using a syringe. The chamber was then placed in an ammonia-saturated gas ambiance overnight. The ammonia-saturated ambiance was prepared with a concentrated ammonia bath (25%) freshly prepared, 5 minutes before the insertion of the cell. Afterwards, the chamber was left in air ambiance for three days for oxygen diffusion. After growth, the chamber is opened and the film was rinsed under a flux of ethanol and blow dried softly with nitrogen.

Peeling method The PMMA anisole solution was spin-coated on to the $\text{Ni}_3(\text{HITP})_2@\text{Au}$ thin films. The program of spin was 500 rpm for 5 s and 1500 rpm for 30 s. The second layer consisted of PDMS was prepared by mixing the prepolymer gel and crosslinker at the weight ratio of 10:1. The PDMS was spread on the fresh PMMA layer. The whole film was stored for one day at 60 °C for 10 h. Finally, the film was carefully peeled off.

UV-visible Spectroscopy $\text{Ni}_3(\text{HITP})_2$ formation in the cell with UV-vis-NIR spectroscopy was performed with a AvaSpec-ULS2048CL-EVO-RS optical fiber with an Avalight DHS light source. UV-vis-NIR final spectrum of $\text{Ni}_3(\text{HITP})_2@\text{Quartz}$ was measured with UV-vis spectrometer Cary 500. UV-vis spectra of $\text{Ni}_3(\text{HITP})_2@\text{Glass}$, $\text{Ni}_3(\text{HITP})_2@\text{Glass-SAM}$, and $\text{Ni}_3(\text{HITP})_2@\text{PDMS}$ was collected using a UV-vis spectrometer Cary 6000 in transmission mode.

Scanning Electron Microscopy (SEM) Images were obtained with a FEI Quanta 650F microscope at acceleration voltages between 10 to 20 kV at a working distance of 10 mm. A 5 nm Pt layer was sputtered with Leica EM ACE600 on top of the samples. Samples of powder materials were prepared by drop-casting ethanolic

suspensions of them onto metallic sample holders. Cross-section images of the films were acquired by cutting the sample with a Precision Diamond Wire Saw-Well 3242. Cross-section images were taken tilting the sample 90°.

Atomic Force Microscopy (AFM) Images were acquired with a Nano-Observer AFM (CSI) in a non-contact imaging mode. FORT-A (CSI) cantilevers with a nominal spring constant of 1.6 N/m, a resonant frequency of 61 kHz and tip radius of 10 nm were employed.

2D Grazing Incident Wide-Angle X-ray Scattering (2D GIWAXS) Synchrotron patterns of all samples were recorded at the NCDSWEET beamline at the ALBA synchrotron, Cerdanyola del Vallès, Spain. An X-ray beam of 8 keV (or 12.4 keV) was set using a Si (111) channel cut monochromator, further collimated using an array of Be lenses. The beam size at the sample position was ca. 50×100 (V \times H) μm^2 . The scattering vector q was calibrated using Cr_2O_3 as standard, obtaining a sample to detector distance of 198 [or 147] mm. The 2D scattering pattern was recorded using a Rayonix LX255HS detector, which consists of a pixel array of 5760×1929 (V \times H) with a pixel size of 44.27×44.27 (V \times H) μm^2 , used with a binning mode of 2×2 .

Fourier Transform Infrared (FT-IR) Spectra of the as-grown $\text{Ni}_3(\text{HITP})_2@Au$ and $\text{Ni}_3(\text{HITP})_2@Au\text{-SAM}$ thin films was performed with Hyperion 2000 FT-IR microscope (Bruker) working in reflection mode. The instrument is equipped with a room temperature detector and a mid-IR source (4000 to 600 cm^{-1}). The spectra were recorded and treated with OPUS data collection software.

Transmission Electron Microscopy (TEM) Images were acquired with FEI Tecnai G2 F20 S-Twin HRTEM at acceleration voltages of 200 kV. Samples were prepared by carefully removing the film from the substrate with a razor blade, dispersing the resulting powder in ethanol and drop-casting the obtained suspensions onto ultrathin carbon on lacey carbon holders.

Static contact angle Measurements were performed with an EasyDrop contact angle meter (KRÜSS GmbH, Hamburg, Germany) using 15 μL water droplets. Each substrate was measured at five different points for obtaining an average of the whole surface. The measurements were performed approximately one minute after the

droplet deposition. Measurements on water uptake were performed by measuring the same droplet at 1, 5, 10, 15 and 20 minutes after deposition.

Contacts deposition Au contacts were evaporated on **Ni₃(HITP)₂@Glass**, **Ni₃(HITP)₂@Glass-SAM**, and **Ni₃(HITP)₂@Quartz** thin films with a Univex 350G, thermal evaporator with base pressure below 10⁻⁶ mbar and a copper mask.

Electrical characterization Measurements on **Ni₃(HITP)₂@Glass**, **Ni₃(HITP)₂@Glass-SAM**, and **Ni₃(HITP)₂@Quartz** thin films were performed with a 2612 SourceMeter Keithely in a N₂ glovebox. The electrical characterization of of **Ni₃(HITP)₂@ Electrodes** was carried out employing a Signal Recovery Lock-in Amplifier model 5209, using a precision resistor of $R = 10.002 \pm 0.005 \text{ k}\Omega$. The system was set a constant frequency of $f = 73.5 \text{ Hz}$ and a voltage up to 2000 mV. This allows performing AC current sweeps from 0 to 200 μA , low enough to prevent Joule Heating of the samples. The voltage drop on the sample was measured with a resolution down to 100 nV, the resistance was extracted and using the geometrical dimensions the conductivity was calculated.

Raman spectroscopy Raman measurements were performed using an inverted Raman microscope (XploRA INV, Horiba Europe GmbH, Belgium) equipped with 532 and 785 nm lasers.

4.5 References:

1. M. Ko, L. Mendecki, K. A. Mirica, *Chem. Commun.* **2018**, 54, 7873.
2. A. Sengupta, S. Datta, C. Su, T. S. Herng, J. Ding, J. J. Vittal, K. P. Loh, *ACS Appl. Mater. Interfaces* **2016**, 8, 16154.
3. G. Wu, J. Huang, Y. Zang, J. He, G. Xu, *J. Am. Chem. Soc.* **2017**, 139, 1360.
4. M. G. Campbell, S. F. Liu, T. M. Swager, M. Dincă, *J. Am. Chem. Soc.* **2015**, 137, 13780.
5. M. K. Smith, K. A. Mirica, *J. Am. Chem. Soc.* **2017**, 139, 16759.
6. E. M. Miner, T. Fukushima, D. Sheberla, L. Sun, Y. Surendranath, M. Dincă, *Nat. Commun.* **2016**, 7, 10942.
7. D. Sheberla, J. C. Bachman, J. S. Elias, C. J. Sun, Y. Shao-Horn, M. Dincă, *Nat. Mater.* **2017**, 16, 220.
8. L. Sun, M. G. Campbell, M. Dincă, *Angew. Chemie Int. Ed.* **2016**, 55, 3566.
9. A. R. Millward, O. M. Yaghi, *J. Am. Chem. Soc.* **2005**, 127, 17998.
10. M. Latroche, S. Surblé, C. Serre, C. Mellot-Draznieks, P. L. Llewellyn, J.-H. Lee, J.-S. Chang, S. H. Jung, G. Férey, *Angew. Chemie Int. Ed.* **2006**, 45, 8227.
11. M. Kandiah, M. H. Nilsen, S. Usseglio, S. Jakobsen, U. Olsbye, M. Tilset, C. Larabi, E. A. Quadrelli, F. Bonino, K. P. Lillerud, *Chem. Mater.* **2010**, 22, 6632.
12. S. H. Jung, J.-H. Lee, J. W. Yoon, C. Serre, G. Férey, J.-S. Chang, *Adv. Mater.* **2007**, 19, 121.
13. Z.-G. Gu, S.-C. Chen, W.-Q. Fu, Q. Zheng, J. Zhang, *ACS Appl. Mater. Interfaces* **2017**, 9, 7259.
14. B. Sen, J. C. C. Santos, R. Haldar, Q. Zhang, T. Hashem, P. Qin, Y. Li, F. Kirschhöfer, G. Brenner-Weiss, H. Gliemann, L. Heinke, C. Barner-Kowollik, A. Knebel, C. Wöll, *Nanoscale* **2020**, 12, 24419.
15. K. Yuan, T. Song, X. Zhu, B. Li, B. Han, L. Zheng, J. Li, X. Zhang, W. Hu, *Small* **2019**, 15, 1804845.

16. V. Rubio-Giménez, M. Galbiati, J. Castells-Gil, N. Almora-Barrios, J. Navarro-Sánchez, G. Escorcia-Ariza, M. Mattera, T. Arnold, J. Rawle, S. Tatay, E. Coronado, C. Martí-Gastaldo, *Adv. Mater.* **2018**, *30*, 1704291.
17. T. Kambe, R. Sakamoto, K. Hoshiko, K. Takada, M. Miyachi, J.-H. Ryu, S. Sasaki, J. Kim, K. Nakazato, M. Takata, H. Nishihara, *J. Am. Chem. Soc.* **2013**, *135*, 2462.
18. A. McPherson, L. J. DeLucas, *npj Microgravity* **2015**, *1*, 15010.
19. R. L. Kroes, D. Reiss, *J. Cryst. Growth* **1984**, *69*, 414.
20. A. Sorrenti, L. Jones, S. Sevim, X. Cao, A. J. DeMello, C. Martí-Gastaldo, J. Puigmartí-Luis, *J. Am. Chem. Soc.* **2020**, *142*, 9372.
21. S. Sevim, A. Sorrenti, C. Franco, S. Furukawa, S. Pané, A. J. DeMello, J. Puigmartí-Luis, *Chem. Soc. Rev.* **2018**, *47*, 3788.
22. A. J. Brown, N. A. Brunelli, K. Eum, F. Rashidi, J. R. Johnson, W. J. Koros, C. W. Jones, S. Nair, *Science* **2014**, *345*, 72.
23. K. Eum, A. Rownaghi, D. Choi, R. R. Bhave, C. W. Jones, S. Nair, *Adv. Funct. Mater.* **2016**, *26*, 5011.
24. K. Eum, C. Ma, A. Rownaghi, C. W. Jones, S. Nair, *ACS Appl. Mater. Interfaces* **2016**, *8*, 25337.
25. B. P. Biswal, A. Bhaskar, R. Banerjee, U. K. Kharul, *Nanoscale* **2015**, *7*, 7291.
26. F. Cacho-Bailo, S. Catalán-Aguirre, M. Etxeberria-Benavides, O. Karvan, V. Sebastian, C. Téllez, J. Coronas, *J. Memb. Sci.* **2015**, *476*, 277.
27. Z.-G. Gu, W.-Q. Fu, X. Wu, J. Zhang, *Chem. Commun.* **2016**, *52*, 772.
28. M. J. Lee, M. R. Abdul Hamid, J. Lee, J. S. Kim, Y. M. Lee, H.-K. Jeong, *J. Memb. Sci.* **2018**, *559*, 28.
29. S. Sevim, C. Franco, H. Liu, H. Roussel, L. Rapenne, J. Rubio-Zuazo, X. Chen, S. Pané, D. Muñoz-Rojas, A. J. DeMello, J. Puigmartí-Luis, *Adv. Mater. Technol.* **2019**, *4*, 1800666.
30. R. W. Day, D. K. Bediako, M. Rezaee, L. R. Parent, G. Skorupskii, M. Q. Arguilla, C. H. Hendon, I. Stassen, N. C. Gianneschi, P. Kim, M. Dincă, *ACS Cent. Sci.* **2019**, *5*, 1959.
31. L. S. Xie, G. Skorupskii, M. Dincă, *Chem. Rev.* **2020**, *120*, 8536.
32. A. Mähringer, A. C. Jakowetz, J. M. Rotter, B. J. Bohn, J. K. Stolarczyk, J. Feldmann, T. Bein, D. D. Medina, *ACS Nano* **2019**, *13*, 6711.
33. D. Sheberla, L. Sun, M. A. Blood-Forsythe, S. Er, C. R. Wade, C. K. Brozek, A. Aspuru-Guzik, M. Dincă, *J. Am. Chem. Soc.* **2014**, *136*, 8859.
34. M.-S. Yao, X.-J. Lv, Z.-H. Fu, W.-H. Li, W.-H. Deng, G.-D. Wu, G. Xu, *Angew. Chemie* **2017**, *129*, 16737.
35. V. Rubio-Giménez, N. Almora-Barrios, G. Escorcia-Ariza, M. Galbiati, M. Sessolo, S. Tatay, C. Martí-Gastaldo, *Angew. Chemie - Int. Ed.* **2018**, *57*, 15086.
36. Y. Liu, J. Guo, E. Zhu, L. Liao, S.-J. Lee, M. Ding, I. Shakir, V. Gambin, Y. Huang, X. Duan, *Nature* **2018**, *557*, 696.
37. M. Farmanbar, G. Brocks, *Adv. Electron. Mater.* **2016**, *2*, 1500405.
38. Y. Liu, P. Stradins, S.-H. Wei, *Sci. Adv.* **2016**, *2*, e1600069.
39. T. Chen, J.-H. Dou, L. Yang, C. Sun, N. J. Libretto, G. Skorupskii, J. T. Miller, M. Dincă, *J. Am. Chem. Soc.* **2020**, *142*, 12367.
40. K. S. Krishnan, N. Ganguli, *Nature* **1939**, *144*, 667.
41. A. K. Dutta, *Phys. Rev.* **1953**, *90*, 187.
42. O. J. Guentert, C. A. Klein, *Appl. Phys. Lett.* **1963**, *2*, 125.
43. S. Chen, J. Dai, X. C. Zeng, *Phys. Chem. Chem. Phys.* **2015**, *17*, 5954.

Chapter 5

Melanin-inspired HHTP-based thin films for wearable on-skin electronics

In the following chapter, synthesis of melanin-inspired HHTP-based free-standing thin films is established. Synthetic methodology is optimized by exploring the use of different amine to react with HHTP and used approach. The obtained thin film showcased good conductivities with dual charge carriers (electrons and ionic) under different wet conditions, pure water and simulated sweat buffers. Large biocompatibility, adhesion and conformability to skin were obtained as well, allowing to implement the film in wearable electronic on-skin (e-skin) devices on porcine skin. Measurements in wearable devices indicated large sensitivity towards sweat-like conditions, body motion and temperature.

Manuscript in preparation

5.1 Introduction

5.1.1. e-skin: state-of-the-art

In the recent years, bioelectronics have emerged as ground-breaking application of electronics, more notably electronic on-skin devices (henceforth referred as e-skin devices).¹ Conformability and strain-related conductivities of e-skin devices have opened the way to remarkable applications as tactile sensors or monitoring of bodily electrical signals as electromyography or electrocardiography (ECG).² Furthermore, multimodal sensitivity to body motion, temperature, respiratory and humidity among others can arise. Notoriously, the wide range of physiological recording is giving rise to human-machine interfaces for artificial intelligence and prosthetics movement³ upon using machine learning process (Figure 5.1).^{4,5} Thus, this area devoted to wearable electronics is living its expansion gaining further interest upon the scientific community.

Commercial skin electrodes are commonly used nowadays in medical treatment. However, their characteristics do not fill the ideal e-skin device requirements. First, conventional electrodes are conformed of rigid metal electrodes implemented on the skin surface with aggressive gels and adhesives.⁶ Further than the possibility of causing skin or allergic irritation, these electrodes lack of skin conformability: skin has a rough and wrinkled surface and hence its interface with the planar commercial electrodes can be irregular with voids between the skin and the electrode.^{3,7} This does not only lead to a large electronic impedance between the electrode and the skin, hindering thus the electronic monitoring application, but also implies a very low adhesion of the electrodes to the skin pointing consequently to short-term recording. Moreover, current commercial electrodes can be hardly used during intensive body performance as they have proven to not be water or sweat resistant. Thus, novel materials for e-skin devices have been sought. Said materials should meet several characteristics as for instance a large adhesion of the skin⁸ preferably with a large conformability to the skin surface or large elasticity to adapt to body shapes and movements.^{1,6} Furthermore, water-proof materials with invariable adhesion to skin under wet conditions are require to withstand sweat conditions of high intense body activity. Moreover, e-skin devices should have low electronic impedance with skin (below 20 k Ω) to ensure good electrical contact during the bodily signal measurement.^{3,6}

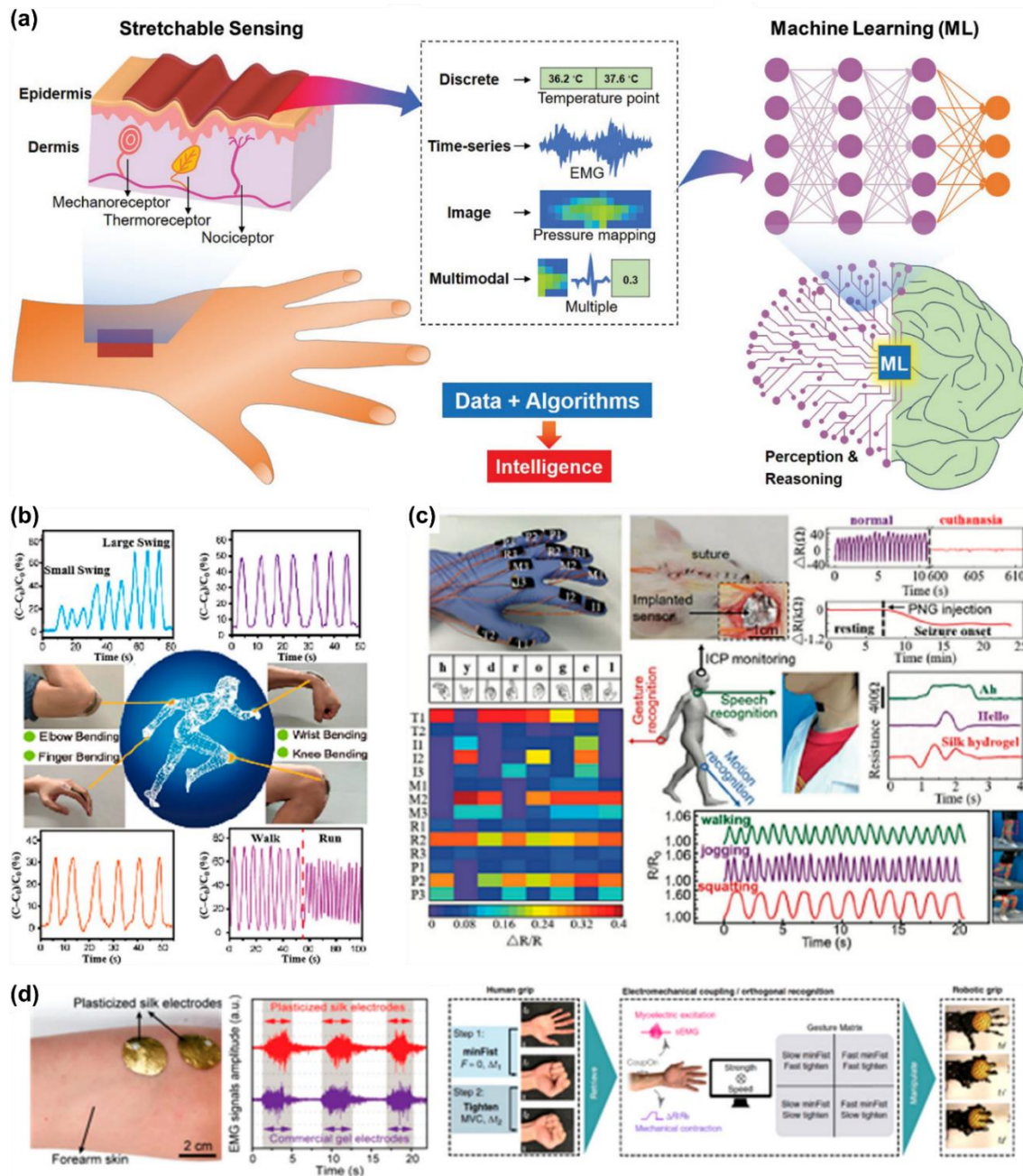


Figure 5.1: Examples and application of wearable electronic devices. (a) Schematic of stretchable e-skin device emulating the sensing functionalities of human skin. Sensing data of multiple signals can be recorded (discrete, time-dependent, imaging through pressure or multimodal). The collected data can be used for artificial intelligence with machine learning process. Image extracted from ref. 6. (b) Examples of different body movement recording upon resistance monitoring in real-time. (c) Multifunctional health sensor for motion, vocal and gesture recognition. Images extracted from ref. 2. (d) E-skin electrode for electromyography recording. E-skin devices allow to transmit hand gestures from human to prosthetics interface. Image extracted from ref. 8.

First materials to be exploited in the area were conductive hydrogels due to their considerable withstand of large strains aside their large uptake of water arising from their large hydrophilicity.⁷ Hydrogels typically showcase large stiffness modulus within the range of 0.1

and 100 kPa conferring them a large stretchability optimal for body movement. Further, many examples of natural hydrogels with bioadhesive and self-healing properties have been reported making them thus interesting for health care applications. However, hydrogels rarely have inherent electric charge carrier conduction requiring of doping.² Four main strategies arise for obtaining conductive hydrogel based sensors: introduction of ionic salts, direct gelation of conductive moieties, polymerization of conductive fillers with hydrogel precursors during gelation and doping with conductive fillers of the already synthesized hydrogel.³ Other techniques rely on the direct physicochemical doping with conductive agents as for instance carbon nanotubes, Ag nanowires or polypyrrol nanoparticles.^{4,8}

Aside the need of doping, hydrogels present another great disadvantage regarding electronic device fabrication: a physical and mechanical mismatch with the rigid metallic electrodes arising from the difference of Young's modulus between the two materials, resulting in a poor connection of the interface.⁴ Some techniques have been recently reported to overcome this limitation as mechanical interlocking or chemical bonding of the electrodes to the hydrogel.⁸ Nonetheless, this represents still a disadvantage due to the extra-processability needed for device fabrication. Hence, free-standing conductive thin films compatible with current device fabrication techniques represents a great alternative for e-skin devices.

5.1.2. Thin films

Several examples of thin film-like materials have been reported in the recent years for e-skin devices. In 2019, Huo and co-workers presented a natural leather-based e-skin watch-band device as a pressure sensor for arterial pulse recording.⁹ Electronic conductive leather was obtained by infiltration of doping agents as carbon nanotubes or conductive nanoparticles into the leather. Further, Ding and co-workers developed last year an all-fiber structured, highly elastic and breathable e-skin device exhibiting a large pressure sensibility within a 0-175 kPa range (Figure 5.2a).¹⁰ The device was obtained by the superposition of different fiber structures performing each a different function required in e-skin applications: a highly elastic polyurethane fibrous layer, a conductive carbon fiber layer and a polyvinylidene fluoride triboelectric sensing layer. In another example, Chen and co-workers introduced a bubble-like stretchable Janus thin film with high adhesion to the skin surface that enabled body motion,

breathing and pneumatic monitoring (Figure 5.2b).¹¹ The film showcased a hydrophilic/hydrophobic interphase as it consisted of a PDMS layer introduced over a carbon nanotube thin film. Similar devices were reported by Xue and co-workers.¹² The material synthesized at liquid-air interface consisted on a carbon nanotube thin film coated by a thermoelastic polymer on its upside layer and by PDMS on the water-side layer (Figure 5.2c). The PDMS coating enhanced the hydrophobicity of the film whereas the thermoelastic polymer conferred it a large strain resistance. The device was used as pulse and movement sensor. Notoriously, the film showcased large and stable performance under different wetting conditions, pHs and presence of salts or alkali, suggesting a possible sweat resistance during body motion.



Figure 5.2: Examples of multifunctional thin films for e-skin devices. (a) All-fiber structure elastic e-skin device. The different fibrous layers perform a functionality required for e-skin devices: elasticity, conductivity and waterproof respectively. The inset is a photograph of the device. Image adapted from ref. 10. (b) Janus thin film formed by PDMS with an underneath carbon nanotube thin film. The black film possessed large skin adhesion with a large conformability, reproducing the skin surface. Image adapted from ref. 11. (c) E-skin device conformed by the superposition of thermoelastic polymer, carbon nanotubes and PDMS. Image extracted from ref. 12.

Most of the thin film devices for e-skin electronics previously described have been proposed by the combination of materials each one of them with a specific functionality (adhesion, conductivity, ...) resulting in interface challenges and long processability of the e-skin devices. Up to our knowledge, multifunctional devices for wearable electronics conformed by a unique single material have not been reported. Herein, we hypothesize that melanin-inspired thin films can arise as suitable candidates with this aim.

5.1.3. Eumelanin-like approach

The interest of eumelanin and related bioinspired materials for this work is manifold, as detailed below:

1. Melanin is a natural pigment present in nature and human body responsible.¹³ Five main types of melanin can be found in nature depending on the starting precursor: eumelanin, pheomelanin, neuromelanin, allomelanin, and pyromelanin. Eumelanin is principally responsible of skin and hair coloration, proof that skin seems to be compatible with melanin-like structures. Hence, the large biocompatibility of melanin could prevent allergic reactions towards wearable artificial skin devices.
2. Second, catechol groups contained in melanin-like materials confer them large adhesive properties to a wide variety of surfaces, reminiscent of mussel-inspired adhesives and coatings.¹³ Furthermore, melanin-like mussel adhesives present interesting properties like large adhesion under humid conditions as sought in artificial skin devices.
3. And third, the key feature of melanin-inspired materials conferring them the suitability for wearable active devices is the inherent electron and proton charge conduction exemplified by eumelanin with predominant ionic conduction in the wet state and electronic one in the dry state.^{13–15} Hydration not only enhances proton effects in electronic conduction but also reduces catechol moieties to semi-quinones inducing the formation of free-radicals.¹⁴ Accordingly, natural eumelanin typically showcases semiconducting conductivity values of 10^{-2} - 10^{-3} S·cm⁻¹ under dry conditions even over long millimetric distances.^{13,15} The chemical and structural disorder of melanin conferring it multiple charge transfer pathways has complicated the determination of the conduction mechanism. However, several ways of melanin conductivity modulation have been reported. First, eumelanin can generate photocurrent upon its irradiation under UV and visible light.¹³ The absorbed photon induces the redox generation of semi-quinone radicals and protons enhancing both the electrical and protonic conduction. Further, presence of metallic ions as Cu(II) within eumelanin can modulate the free proton concentration inducing a higher proton conduction.¹⁶

Motivated by the advantages previously described, electrical devices have already been described by imbedding natural melanin nanoparticles into Polyvinyl alcohol (PVA) either using layer-by-layer methods¹⁷ or by dry-casting of the mixture and subsequential annealing¹⁸ obtaining supported and free-standing films respectively. The large aggregation degree in these films allowed to have enhanced conductivity under dry conditions reaching values of after annealing treatment in the case of the free-standing film, since annealing enabled large percolation degree. Beyond natural melanin, synthetic conductive melanin-like materials have been obtained in a wide variety of morphologies and through different synthetic methods. Worth-to-mention, Kim and co-workers used synthetic polydopamine nanoparticles as active layer in a skin-inspired hydrogel-elastomer hybrid material for light and free-dopamine detection material.¹⁹ However, nanoparticle-based devices seem unlikely suitable for e-skin devices as they lack of adhesive properties. So, regarding thin film morphologies, several synthetic approaches arise to obtain melanin-inspired thin films as for instance solvothermal²⁰ and solid-gas interfacial syntheses²¹ though electrical performances remained within the range of natural melanin. Remarkably, spin-coating techniques arise as well. In a work performed by Gethin and co-workers, melanin synthesized and dispersed in DMSO was spin-coated on top of graphene electrodes.²² The use of DMSO as solvent allows to spin-coat the melanin over both hydrophilic and hydrophobic substrates. Worth-to-mention, four-point resistances proved that upon the deposition of melanin on top of graphene resistances increased only slightly, going from $2.61 \pm 0.105 \, \Omega$ to $8.42 \pm 0.988 \, \Omega$ suggesting a very high melanin conductivity. This may arise from the change of solvent during the synthetic procedure. During the synthesis in DMSO, sulfonate groups are generated, which protect the phenolic groups of catechol moieties and avoid their polymerization. This could lead hence to an enhanced aromaticity in the structure.²³ Similar observations were performed in polydopamine thin films synthesized by oxidative chemical vapor deposition in the gas state.²⁴ The lack of water during the formation of polydopamine lead to an enhanced C-C coupling allowing to obtain four-probe conductivities of $0.4 \, \text{S} \cdot \text{cm}^{-1}$.

On the other side, potential of polydopamine thin films for bioelectronics have also crystallized in examples of in-vitro cell adhesion and culturing of electrical-sensitive neuron cells and their electrical stimulation.^{25,26} Notoriously, inclusion of catechol moieties in wearable electronics has already been explored both in hydrogels^{27,28} and multifunctional thin films (Figure 5.3).^{29,30} Exemplarily, tannic acid was included in an acrylamide and cellulose based hydrogel (doped with silver ions for its body motion detection) proving to be a good

adhesive towards both hydrophobic and hydrophilic.²⁷ On the other hand, polydopamine derived polymers were used as adhesive layer of on-skin electrodes for ECG monitoring.^{29,30} Conductivity on these electrodes was achieved by depositing a conductive gold layer on top of the polydopamine-based polymer, coated by a hydrophobic polymer. Notoriously, the inclusion of this catechol-based polymeric layer allowed not only a high skin conformability but also a long-term heartbeat recording, including monitoring during intense exercise³⁰ and under-water activity.²⁹ However the need of large electronic coupling to the skin requires of an enhanced and controlled conductivity, hindering thus the application of some polydopamine-like materials.

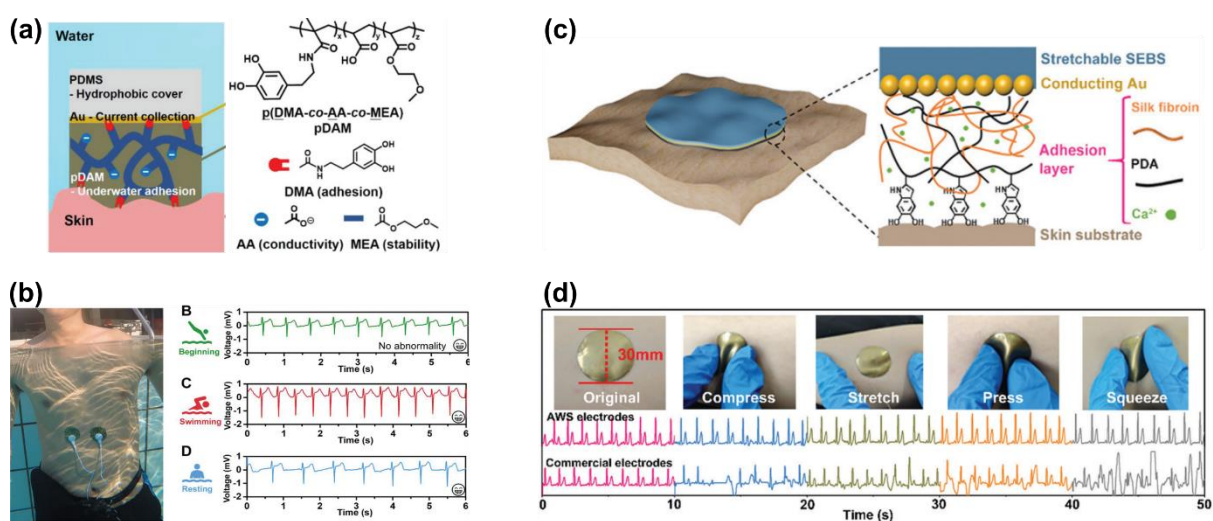


Figure 5.3: Examples of e-skin devices using polydopamine derivatives for enhanced adhesion. (a) Structure elastic e-skin device with the polydopamine derivative structure. (b) Electrocardiogram real-time monitoring underwater during swimming activity. Images extracted from ref. 29. (c) Structure of e-skin electrode using polydopamine-doped silk fibroin for enhanced skin adhesion. (d) Electrocardiogram monitoring of the electrode introduced in (c) and a commercial electrode under different skin deformations. The e-skin device proved an enhanced performance with respect to the commercial one. Images extracted from ref. 30.

As previously described, melanin and derived synthetic products have been used to make, on the one hand, conductive films and, on the other, as primers in electronic devices whose objective is to promote adhesion. However, as far as we know, the combination of both properties in a single film has been described to us to date despite the enormous scientific and technological interest that this would have. In this Thesis we hypothesize that the fabrication of films from the **HHTP** ligand could achieve this objective thanks to its duality, on the one hand favoring stimulating conductive properties and on the other its tris-catechol character that can favor adhesion on surfaces, specifically on the skin.

5.1.4 Scope of this chapter

Considering the aforementioned, the following objectives were set for this Chapter:

- To develop and optimize a methodology for the synthesis of free-standing **HHTP**-based melanin-like thin films.
- To perform a full physico-chemical characterization including water-proof consistency and electrical conduction.
- To study the cytotoxicity and adhesion to skin of the free-standing films.
- To assess the potential of the free-standing films as artificial electrical on-skin wearable devices.

5.2 Results and Discussion

5.2.1 Attempts to obtain **HHTP**-based thin-films by reaction with different amines

a.- Ammonia

First attempts to obtain thin films were tested with ammonia. However, direct dissolution of **HHTP** in aqueous ammonia would result into heterogeneous reactions due to the low solubility of **HHTP** in water, leading to an uncontrolled growth while avoiding the optimal formation of large thin films. Thus, the reaction was performed by adding methanolic ammonia to a methanolic solution of **HHTP** (see Figure 5.4a). After addition, the brown solution became black and opaque (see Figure 5.4a), indicating a fast reaction of the **HHTP** molecule with ammonia. Worth-to-mention, stamping of a flat substrate on the liquid-air interface after 15 min of reaction resulted on the deposition of a brittle black thin film (Figure 5.4b). However, longer reaction times did not lead to a thickening of the thin film but to a colloidal suspension of particles. The particles grew leading to a brown precipitate could be seen by naked eye after six days.

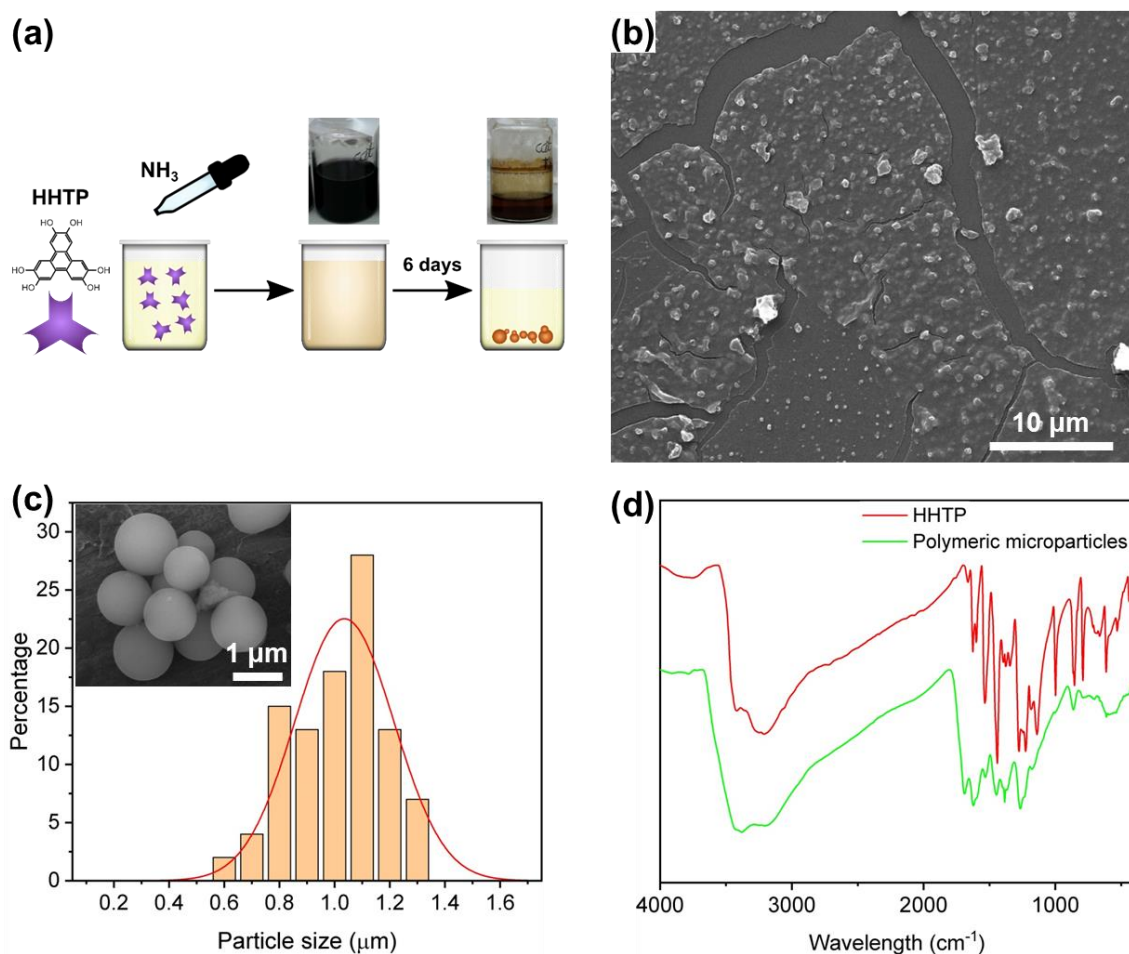


Figure 5.4: (a) Schematic illustration of the synthesis of polymeric microparticles and images of the microparticle synthesis vial at its beginning and end. (b) SEM image of the stamping of a silicon wafer substrate at the liquid-air interface after 15 minutes of reaction. (c) Size distribution histogram of the microparticles according to SEM images with a normal distribution fitting. Inset: SEM images of the microparticles. (d) Comparison of FT-IR spectra of commercial **HHTP** and microparticles.

SEM images of the washed precipitate revealed microsized particles with a smooth surface (Figure 5.4c). The microparticles showcase good size distribution with mean sizes of $1.0 \pm 0.2 \mu\text{m}$ (Figure 5.4c). FT-IR of microparticles proved the polymerization of **HHTP** since the peak corresponding to the $\nu(\text{C-O})$ in the spectrum of **HHTP** ($\sim 1600 \text{ cm}^{-1}$) is slightly shifted with respect to the free ligand (Figure 5.4d). This suggests that polymerization occurs through the hydroxyl groups. Electronic properties on these particles were firstly assessed pressing them into a pellet and depositing silver paste contacts (Figure 5.5a). The measured four wire conductivity under dry conditions provided values around $0.5 \cdot 10^{-6} \text{ S} \cdot \text{cm}^{-1}$. The low values can be attributed to the presence of grain boundaries, as sustained by the two-wire I-V curves measured in the pellet as they showcase semi-conducting non-linear behavior (Figure 5.5b).

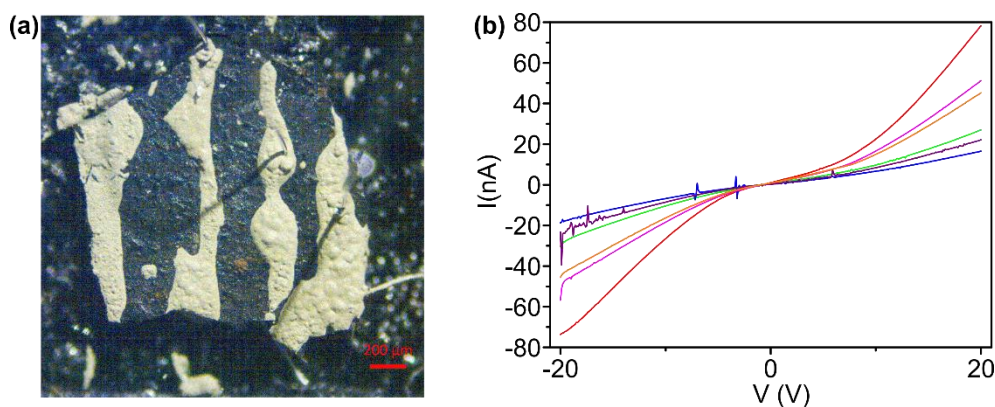


Figure 5.5: (a) OM of a pressed pellet of polymeric microparticles with electronic contacts. (b) I-V curve of the pressed pellet using different pairs of contacts.

To facilitate the obtaining of thin films, slower reactions were tested by slow diffusion of ammonia into a methanolic solution of **HHTP** instead of direct addition (Figure 5.6). However, once more diffusion also led to a brown precipitate observed over the whole mixture. SEM images of the washed precipitate revealed the formation in large yield of polymeric nanoparticles with smooth surface (Figure 5.6a). Interestingly, these nanoparticles can react with each other through their surfaces since some polymerization can be observed between particles (see inset of Figure 5.6b). The nanoparticles showcase quite narrow distribution of sizes with mean diameters of 151 ± 24 nm ($N=107$) (Figure 5.6c). FT-IR spectrum of nanoparticles shows a shift on the peak at 1600 cm^{-1} corresponding to the $\nu(\text{C-O})$ vibration with respect to the **HHTP** spectrum. As described previously described in the introduction, post-synthetic approaches for the encapsulation of natural melanin nanoparticles into PVA films have been described. One of the reported studies revealed that this approach leads to the coalescence of conductive nanoparticles allowing interparticle charge transfer.¹⁸ Thus the same protocol was followed aiming for the aggregation of the polymeric nanoparticles into compact conductive layers. For this, the obtained polymeric nanoparticles seen in Figure 5.7b were dispersed in a 2% aqueous solution of PVA under sonication for 30 min. Further, the suspension was drop-casted in a plastic mold and left to dryness under ambient conditions. The obtained film can be seen in Figure 5.7a. The nanoparticles@PVA film proved to be highly transparent with a light brown color. SEM images (Figure 5.7b) proved the incorporation of the nanoparticles in the PVA film as well as the UV-vis absorbance spectrum since it showcases a large absorption in the UV range corresponding to the TP moieties. However, the resulting nanoparticles@PVA film seemed to be highly insulating when performing conductive spectroscopies suggesting a low cargo of nanoparticles is obtained, not ensuring the formation of a continuous conducting layer.

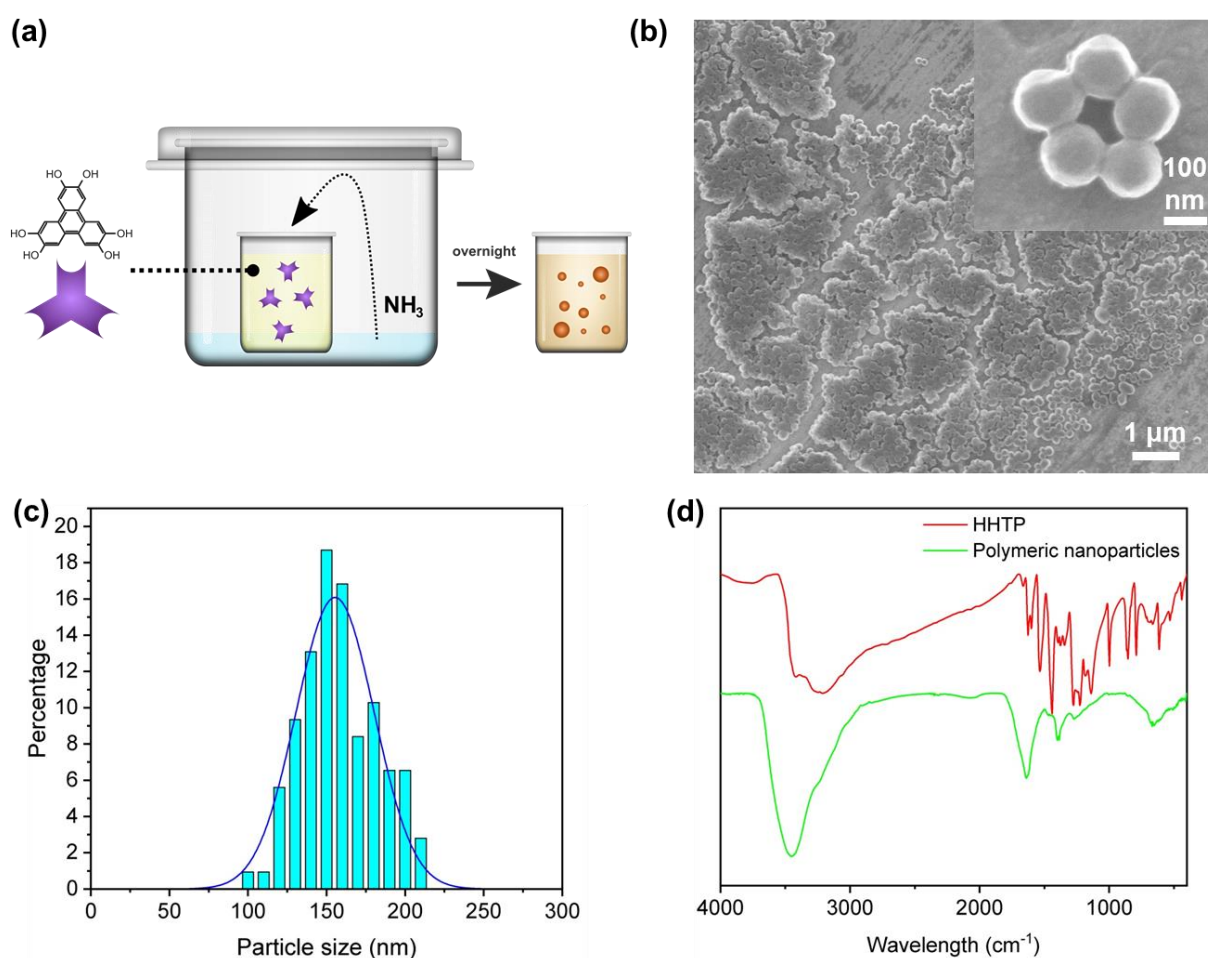


Figure 5.6: (a) Schematic illustration of synthesis of polymeric nanoparticles through ammonia diffusion. (b) SEM image of nanoparticles. (c) Size distribution histogram of the nanoparticles according to SEM images. (d) Comparison of FT-IR spectra of commercial **HHTP** and nanoparticles.

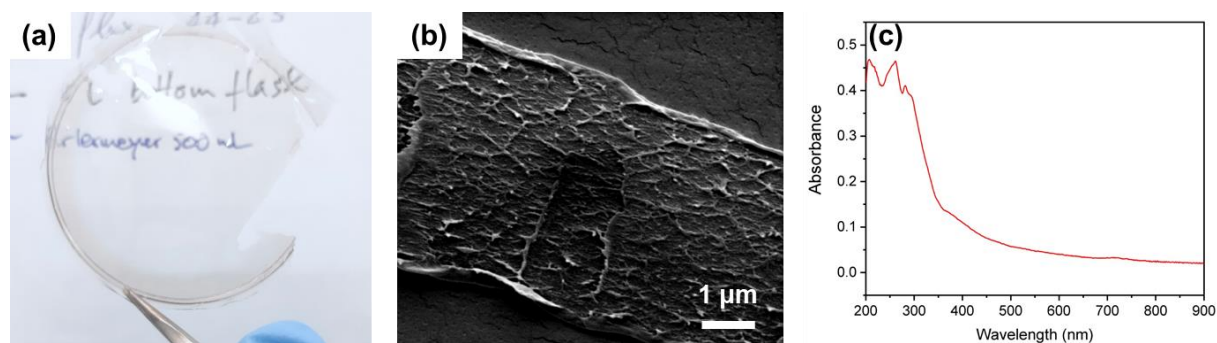


Figure 5.7: (a) Photograph of nanoparticles@PVA thin film in front of a written paper to show the large transparency of the film. (b) SEM image of the nanoparticles@PVA thin film. (c) UV-vis of nanoparticles@PVA thin film measured in transmission.

b.- Flexible amines

Due to the hindrances of implementing the **HHTP**-based polymeric micro and nanoparticles into polymeric films, free-standing thin films were sought using amine long molecules for an extended polymerization. In a first approach, aliphatic flexible amines were used: hexamethylenediamine and tris(3-aminopropyl)amine (Figures 5.8a and 5.8c). Analogously to previous experiments, a methanolic solution of amine was added to a methanolic solution of **HHTP**. Both reactions concluded to an immediate precipitation of plate-like microparticles in the case of hexamethylenediamine and needle-like in the case of tris(3-aminopropyl)amine (Figures 5.8b and 5.8d). The large degree of flexibility may allow the fast interaction between TP moieties inducing the precipitation. Thus, more rigid amines were further employed to avoid the fast particle precipitation.

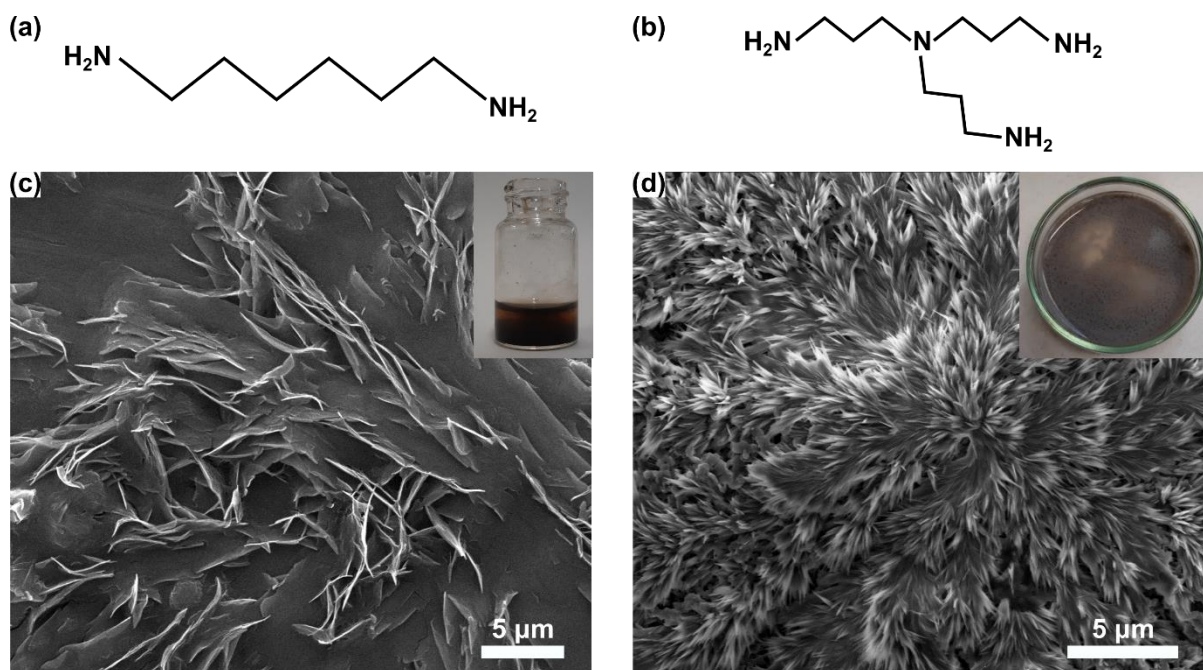


Figure 5.8: (a) Hexamethylenediamine; (b) SEM image of plate-like particles obtained in the precipitate of reaction between **HHTP** and hexamethylenediamine. Inset: photograph of the precipitate obtained. (c) tris(3-aminopropyl)amine (d) SEM image of needle-like particles obtained in the precipitate of reaction between **HHTP** and tris(3-aminopropyl)amine. Inset: photograph of the precipitate obtained.

c.- Rigid amines

p-Phenylenediamine (PPD) was used as rigid diamine for a more controlled reaction. For this, methanolic solutions of **HHTP** and PPD were mixed (Figure 5.9a). A brownish color

was immediately obtained after mixture, though no film nor precipitation was observed at naked eye not even after 24 h. However, upon drop-casting of the solution micrometer long pieces of films were observed under SEM (Figure 5.9c). Notoriously, if spin-coating of the solution is used instead, large covering of substrates is obtained (Figure 5.9d) proving that solvent evaporation effects can have a deep impact in the formation of thin films. Thus, the one-pot reaction was now repeated using water as solvent to avoid fast evaporation of the solvent. For an enhanced solubility of the **HHTP** ligand an aqueous carbonate buffer (pH~9) was used. **HHTP** and PPD were dissolved in the aqueous buffer as shown in Figure 5.9b and the overall was left in an open vial. Within minutes, sub-millimeter sized thin films were already observed in the water-air interface and remained of similar sizes after 24 h. These results confirmed the interfacial character of the reaction. Still, the synthesis is characterized by a fast reaction concluding to small lateral areas of thin films, hindering their manipulation. Thus, more controlled interfacial approaches were tried in an attempt to obtain larger thin films.

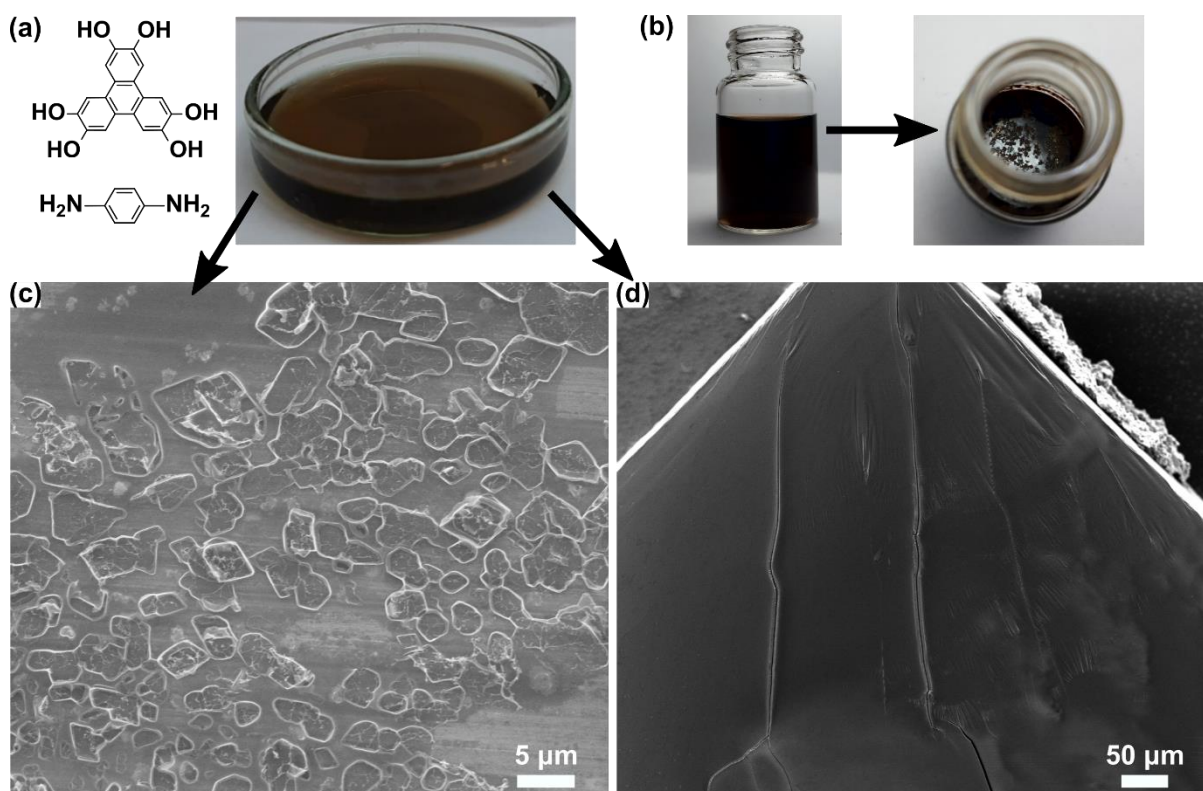


Figure 5.9: (a) Photographs of the methanolic reaction between **HHTP** and PPD after 24 h. No film nor precipitated is seen at naked eye. (b) Photographs of reaction between **HHTP** and PPD in carbonate buffer at initial state (left) and after 24 h. (c) SEM image of the product of methanolic reaction between **HHTP** and PPD upon drop-casting after solvent evaporation. Micrometer-long thin-like materials are observed. (d) SEM image of the product of methanolic reaction between **HHTP** and PPD upon spin-coating. Large and homogeneous coverage is obtained.

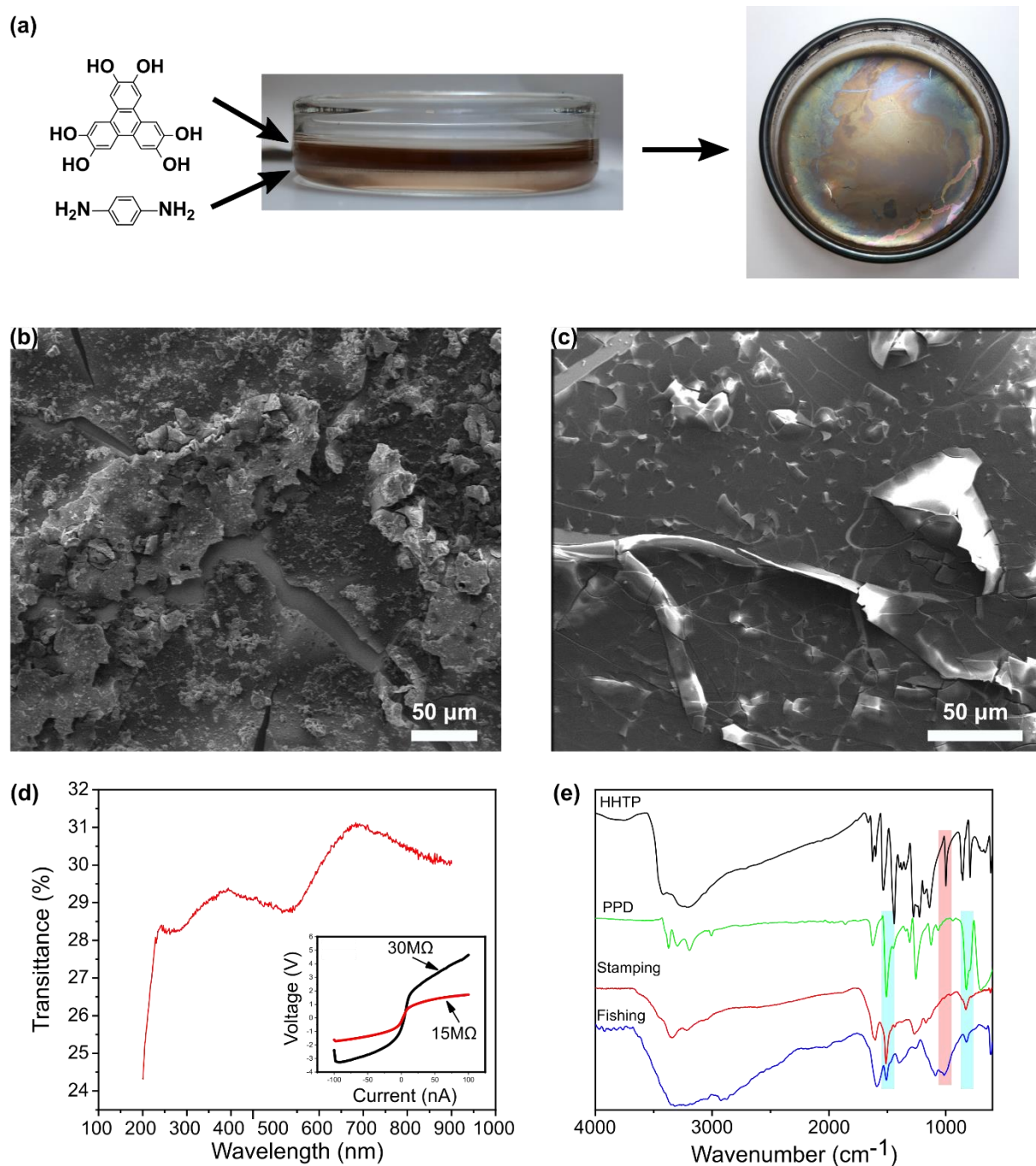


Figure 5.10: (a) Scheme and photographs of the liquid-liquid interfacial reaction. (b) and (c) SEM images of the thin film recovered by stamping and fishing respectively, showing the Janus character of the water-side and air-side faces of the film. (d) UV-vis transmittance spectrum of a thin film fished on quartz substrates. Inset: Four-wire I-V curves of a stamped thin film onto silicon substrates. Very large resistivities and non-linear curves were obtained arising of the discontinuous and broken film. (e) Comparative of IR spectra of **HHTP** (black), **PPD** (green), stamped (red) and fished (blue) thin films.

For this, liquid-liquid methodology was employed, for a controlled diffusion of the reagents (Figure 5.10a). In this experiment, a solution of **HHTP** in ethyl acetate was poured on top of an aqueous solution of PPD. The two-phase system was left closed for three days for a slow diffusion of the **HHTP** into the aqueous phase and afterwards the system was opened and exposed to ambient conditions. After evaporation of the ethyl acetate phase, a centimeter-large thin film was obtained at the water-air interface (Figure 5.10a right). The obtained thin film was very brittle and difficult to manipulate, though it was at least partially recovered by stamping and fishing onto silicon wafer substrates (Figure 5.10b and 5.10c).

Interestingly, SEM revealed a Janus character. The water face of the thin film presented a rough surface with several particles occluded (Figure 5.10b) whereas the air face was thin and smooth (Figure 5.10c). UV-vis transmittance of films recovered by fishing on quartz substrates proved a large absorbance in the UV range along with a strong absorption band at 550 nm (Figure 5.10d). FT-IR spectroscopy confirmed the polymerization between **HHTP** and PPD (Figure 5.10e). On one hand, the wide absorption band at $\sim 3300\text{ cm}^{-1}$ corresponding to the largely energetic $\nu(\text{O-H})$, can be observed on the spectra of films recovered by stamping and fishing, indicating **HHTP** is successfully incorporated in the film. Further, $\nu(\text{C-N})$ highlighted in blue at $\sim 1500\text{ cm}^{-1}$ can be seen in spectra from PPD and both films confirming its presence. Moreover, peaks from **HHTP** and PPD spectra corresponding to $\delta(\text{O-H})$ and $\delta(\text{N-H})$ seen at $\sim 1620\text{ cm}^{-1}$ appear shifted to lower wavenumbers ($\sim 20\text{ cm}^{-1}$ shift) in spectra of thin films, indicating that these groups have participated into polymerization. Nonetheless, four-wire electronic conductance spectroscopy performed on stamped thin films provided non-linear I-V curves indicating a weak charge carrier conduction (Figure 5.10d inset). This may arise by the fragility of the thin films as breaks within the material might lead to breaks on the conduction paths, critically affecting the electronic conduction. Thus, an optimization on the liquid-liquid thin film formation was further required.

5.2.2 Film formation optimization

Optimization on the interfacial liquid-liquid reaction was performed by initially modulating two main parameters, named **HHTP** concentration and pH. As the ethyl acetate phase is already saturated of **HHTP**, an increase of the concentration was not feasible so we moved to an increase of the ethyl acetate phase volume. For this, three interfacial reactions were prepared having each one-fold, four-fold and eight-fold the ethyl acetate volume of the

aqueous phase (Figure 5.11a). Three days later, different diffusion degrees were found for each one of them. Notoriously, larger diffusion of **HHTP** was obtained using larger volumes of ethyl acetate so an enchanted film formation was found (Figure 5.11b). Afterwards, optimization of the using basic aqueous phases was tested for an enhanced solubilization of **HHTP** into the aqueous phase. For this, carbonate buffer (pH~9) was used as aqueous phase (Figure 5.11c). Remarkably, after three days, large diffusion of the **HHTP** towards the interface was obtained (Figure 5.11d). Nonetheless, a large polymerization within the aqueous phase was also observed which could possibly arise from the PPD self-polymerization under basic conditions. Thus, neutral aqueous phases were used from now on. Worth-to-mention despite all the conditions tried out, the obtained films were still brittle and not manipulable showcasing a particulated character.

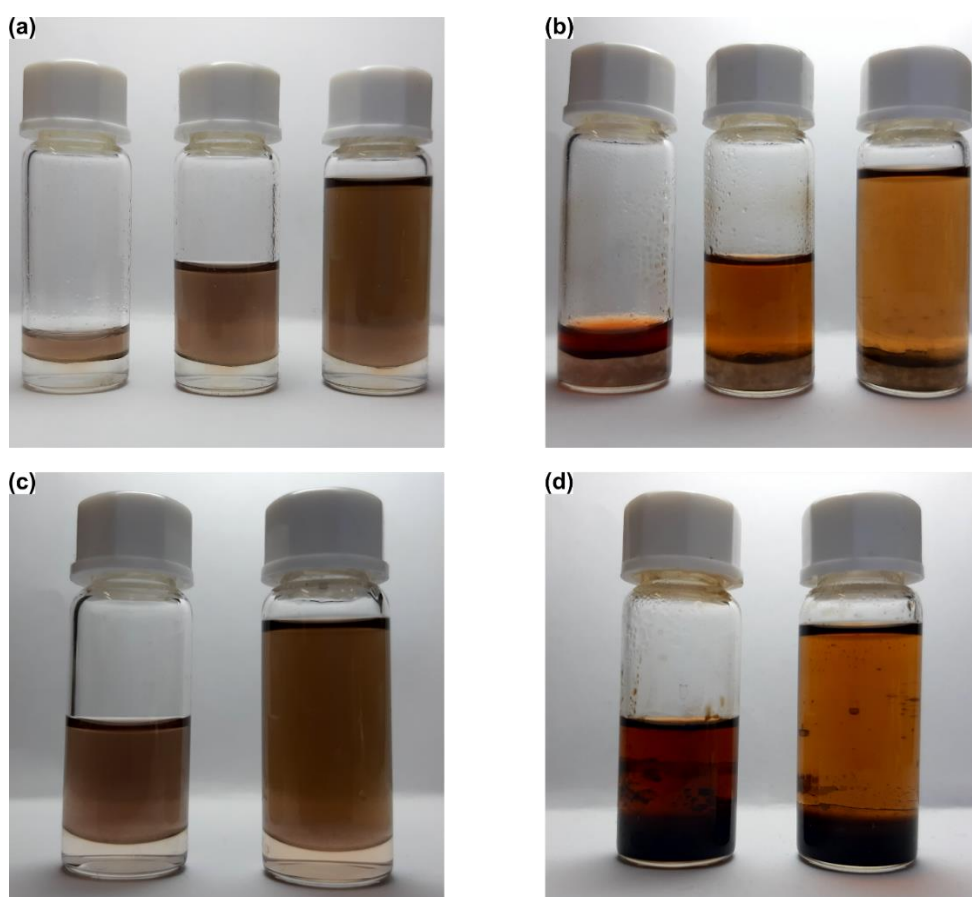


Figure 5.11: Photographs of liquid-liquid interfacial reactions with different liquid stoichiometries at (a) initial stage and (b) after three days. Photographs of liquid-liquid interfacial reactions with different liquid stoichiometries and with carbonate buffer as aqueous phase at (c) initial stage and (d) after three days.

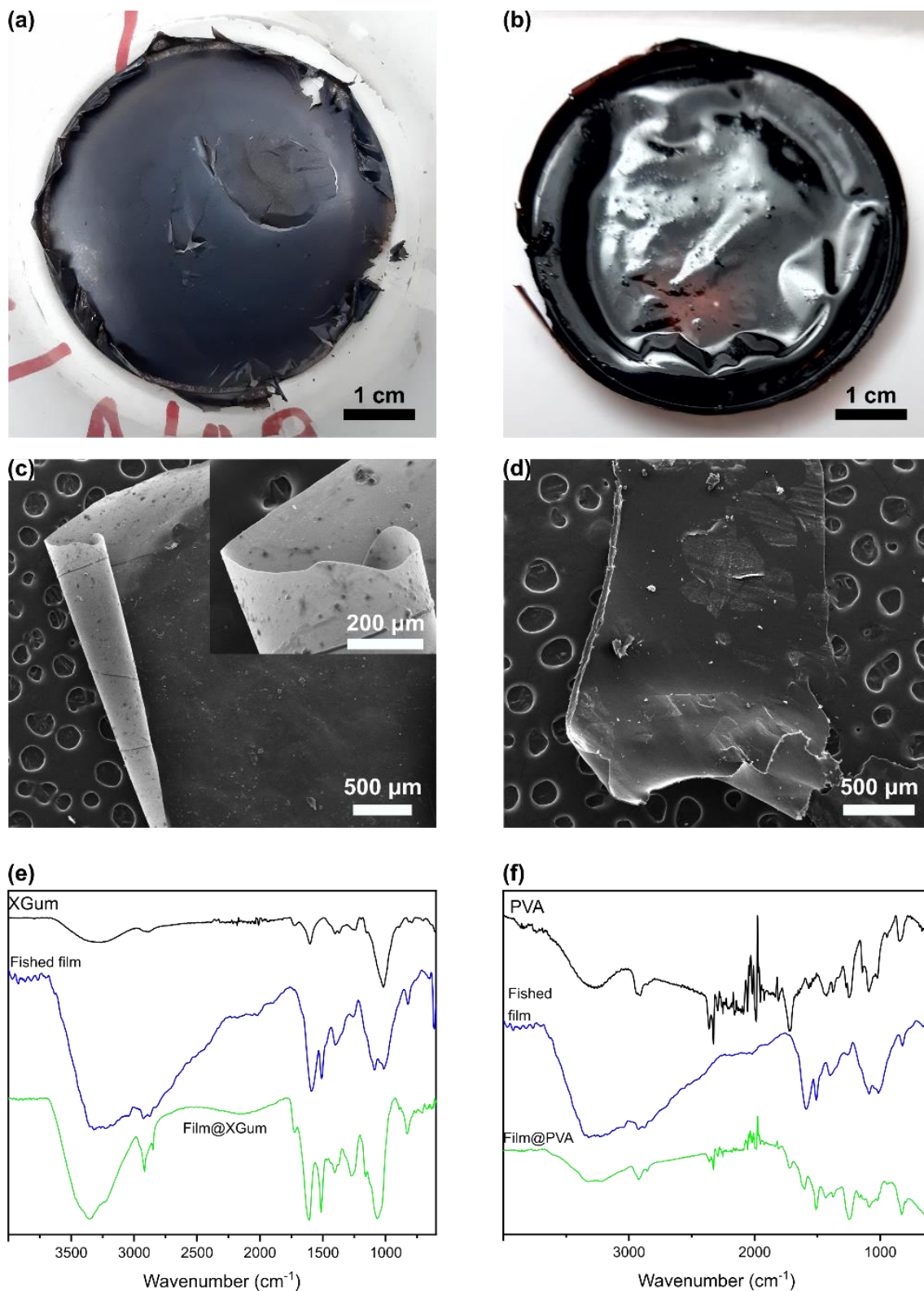


Figure 5.12: (a) and (b) Photographs of **Film@XG** and **Film@PVA** thin films. (c) and (d) SEM images of **Film@XG** and **Film@PVA** thin films. (e) and (f) Comparative IRs of **Film@XG** and **Film@PVA** thin films with the previously obtained fished film and free additives.

Finally, the use of additives that increase the viscosity of the aqueous phase was proposed, aiming for more controlled polymerizations to get free standing thin films. For this liquid-liquid interface syntheses were performed having 0.5% w/w presence of Xanthan Gum (XG) and PVA. Their addition did effectively slow down the diffusion and formation as free-standing thin films. Notoriously, the formed films showcased a larger density than in previous experiments. After washing steps through solvent exchange and drying, free standing thin films were obtained in both cases (Figure 5.12a and 5.12b). Their allure already suggested XG and PVA were included in the thin films, which was further confirmed by FT-IR spectroscopy. Spectra of Figures 5.12e and 5.12f show that characteristic $\nu(\text{C-H})$ vibration at $\sim 2920\text{ cm}^{-1}$ from both XG and PVA can be seen in the newly thin films henceforth labelled **Film@XG** and **Film@PVA**. Worth-to-mention, peaks at 1720 and 1600 cm^{-1} in spectra of XG and PVA corresponding to $\delta(\text{O-H})$ are strongly suppressed indicating that XG and PVA polymerize along with the film doing cross-linking for a more robust film. Morphology of the obtained films was further assessed by SEM (Figures 5.12b and 5.12c). **Film@XG** proved to be considerably thin, with a very large flexibility as they can be twisted (as observed in SEM images) and their surface appears smooth and homogeneous. On the other hand, **Films@PVA** are rather thick, with a rather wrinkled surface.

Remarkably, the capability of polymerization with one or other additive and their different characteristics allowed us to control and tune the film stability in water. **Film@PVA** dissolved within minutes upon exposure to water, whereas **Film@XG** expand over the water-air interface without suffering structural damages (and remain unaltered at water-air interface over weeks). In this way we can achieve films more or less resistant to water according to the desired application, that is to say, that they are easily washed with water or that they hold up under conditions, this being one of the initial objectives. Interestingly, the **Film@XG** films also exhibit a Janus character: the side of the film facing water during the synthesis is highly hydrophilic whereas the air-side face is rather hydrophobic (Figure 5.13). Consequently, after pulling the **Film@XG** out of the interface, it folds itself to avoid exposure of the hydrophilic face to air (Figure 5.12).

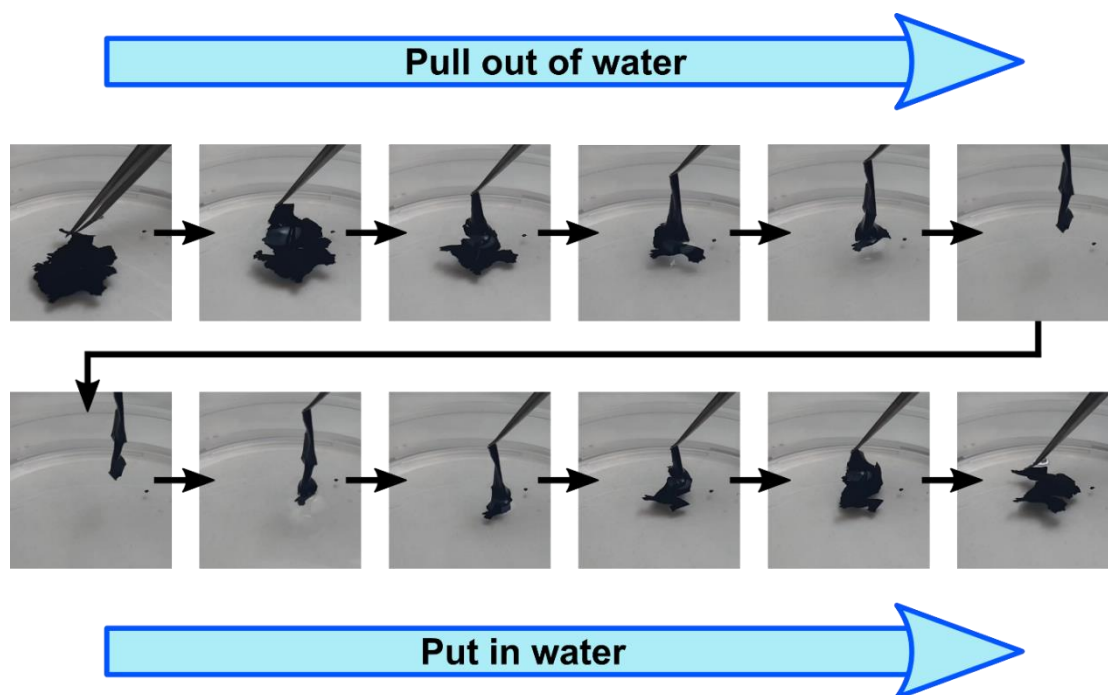


Figure 5.13: Pictures extracted from a video showing the pulling out and putting in the **Film@XG** of water. The film shrinks and folds upon pulling it out of the water-air interface avoiding exposing the hydrophilic face. When putting it back into water, the folded film expands over the water-air interface.

5.2.3 Conductive properties of optimized films

Electrical measurements were performed at the *Institute of Material Sciences of Barcelona (ICMAB)* under the supervision of Dr. Raphael Pfatnner. As both electron and ion conduction are expected, frequency dependent AC measurements were performed using Lock-in amplifier system as in previous chapters (Figure 5.14b) using four-wired indentation contacts (Figure 5.14a). As seen in the Sheet Resistance variation with the frequency (red curve), **Films@XG** at 100% RH showcase two conduction regimes depending on the applied frequency corresponding to the two plateau of the Boltzmann sigmoidal fitting. At low frequencies, higher sheet resistances are obtained converging to $98 \pm 2 \text{ k}\Omega$ as a limit. Worth-to-mention, the sheet resistance at low frequencies converges to the value obtained when measuring the wet thin film in conventional four-wire DC measurements with the same contacts. This regime corresponds to pure electronic conduction as DC currents and similar disable proton conduction through full polarization of water molecules. On the other hand, at high frequencies, the sheet resistance critically decreases, reaching values of $3 \pm 2 \text{ k}\Omega$, confirming the contribution of both electron and proton charge carrier conduction. Observation of a steady plateau at higher frequencies could not be obtained due to the limitations of the

equipment: as observed during calibration of the equipment with high precision commercial resistors, interferences in the signal coming from copper cabling arise over frequencies of 73.5 kHz.

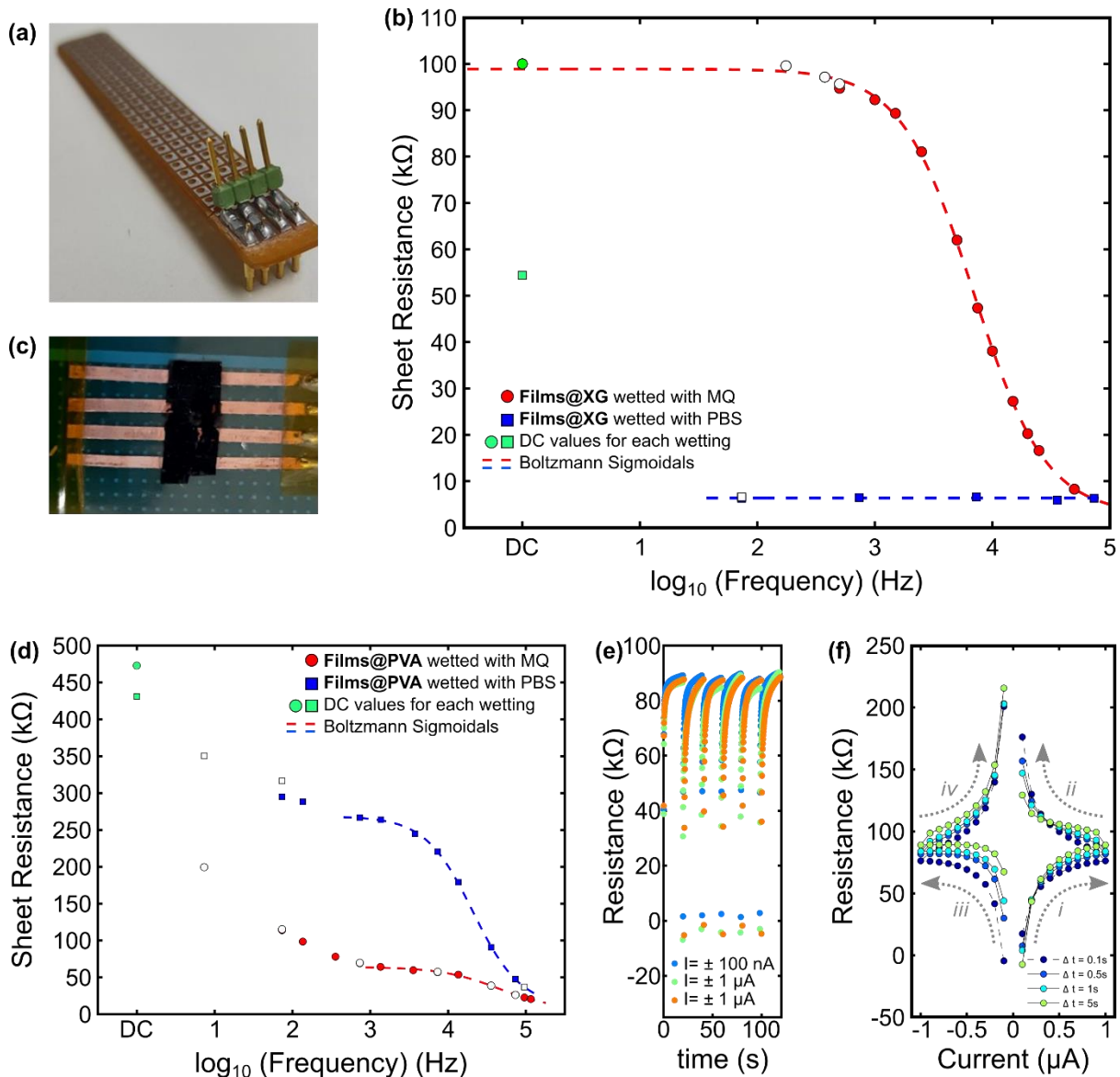


Figure 5.14: (a) Photograph of four-wire indentation electrodes. (b) AC frequency dependence and DC sheet resistances of **Films@XG** wetted with pure water (red curve) and physiological sweat-like PBS buffer (blue curve). (c) Photograph of copper stripped contacts with **Film@PVA** deposited on top. (d) AC frequency dependence and DC sheet resistances of **Films@PVA** wetted with pure water (red curve) and physiological sweat-like PBS buffer (blue curve). (e) Time-transient DC four-wire resistance measurements of **Films@PVA** wetted with pure water. (f) Current increasing dependance of four-wired DC resistance of **Films@PVA** wetted with water.

Considering the thickness of the film of 7 ± 2 μ m as observed in SEM images, conductivity values of 15 ± 4 mS \cdot cm $^{-1}$ and 0.5 ± 0.2 S \cdot cm $^{-1}$ are obtained respectively for low and high frequency values. Remarkably, upon wetting **Films@XG** with Phosphate Buffer

Solution (PBS) in an attempt to mimic physiological sweat-like conditions, the measured sheet resistances proved to be independent of the applied frequency presenting a constant plateau value around $6.6 \pm 0.2 \text{ k}\Omega$ (Figure 5.14b blue curve). This invariability may arise from the large concentration of ions largely contributing to the ionic-charge carrier conduction. DC measurements performed of the thin film under sweat-like conditions are in agreement with this statement since larger sheet resistances of $55 \pm 5 \text{ k}\Omega$ are obtained indicating a large ionic contribution in the AC measurements. Worth-to-mention, similar DC measurements performed in analogous melanin-like thin films made of non-conjugated molecules as a blank led to very large resistances of the order of $\text{M}\Omega$ both under wetting conditions with pure water and sweat-like conditions.

Due to the large solubility of PVA in water, **Films@PVA** were measured using the more flexible four wire cooper stripped contacts on polyimide substrates to adapt to any possible film deformation (Figure 5.14c). Contrarily to **Films@XG**, **Films@PVA** at 100% RH did not showcase a sigmodal dependence of the resistance with the frequency but rather an exponential decrease (Figure 5.14d red curve). Eventually, DC measurements performed in **Films@PVA** samples provided even larger sheet resistances of $470 \pm 10 \text{ k}\Omega$. This behavior is more consistent with conductivity of free water molecules rather than a proton conduction. To further confirm this hypothesis, time transient four-wired DC resistance measurements at different intensities were performed, changing the current direction from one measure to the other (Figure 5.14e). Notoriously, at the beginning of each measurement, very low resistances were obtained which were further increased until reaching a saturation value of $\sim 90 \text{ k}\Omega$. This is in accordance with an enhanced initial conductivity that decreases upon the migration and further saturation of free ionic species from one electrode to another. Consequently, hysteresis on the resistance of the **Film@PVA** samples are obtained when applying increasing currents within short timesteps (Figure 5.14f). When applying 0 to $1 \text{ }\mu\text{A}$ (step *i*), the resistance increases and saturates around $90 \text{ k}\Omega$ as previously seen due to saturation of ionic charge carriers. Then, upon decreasing from 1 to $0 \text{ }\mu\text{A}$ (step *ii*) an increase of the resistance is observed as charge carriers are fully polarized within the material and thus there is no migration despite the variation on the current. Further, when inverting the polarity of the current going from 0 to $-1 \text{ }\mu\text{A}$ (step *iii*), ionic charge carriers migrate from one electrode to another, leading to low resistances that are gradually increased until reaching the saturation value of $90 \text{ k}\Omega$. Analogously to step *ii*, when applying -1 to $0 \text{ }\mu\text{A}$ (step *iv*), an increase of the resistance is observed due to the pre-existent saturation. This free migration of charge carriers might arise

from the large solubility of the **Films@PVA** samples in water which may cause their structural damaging in full RH conditions.

Worth-to-mention similar behaviors are obtained under sweat-like wetting conditions (Figure 5.14 blue curve). The resistance increases exponentially with the decreasing frequency, matching a free ionic conduction. Again, DC values confirm this behavior as very large values of $431 \pm 10 \text{ k}\Omega$ are obtained. Remarkably, the larger resistances obtained in sweat-like conditions in comparison with pure water sustain the hypothesis of uncontrolled free ionic conducting species. The larger ion concentration and ionic strength lead to faster polarization at the electrodes concluding to a lower migration of ionic species. Thus, **Films@PVA** seem less adequate for bioelectronics applications as conduction of charge carriers is hardly measurable.

Thus, **Films@XG** have demonstrated good properties critical for an e-skin device. First, they have proved to be waterproof over long periods, with a very large hydrophilic face suggesting large adhesive properties. Further, high electrical conductivity under wetting and sweat-like conditions has been observed. A switch of the conducting regimes when applying sweat-like buffers suggests as well potential sweat monitoring. To further assess the potential of **Films@XG**, biocompatibility and adhesion towards skin should be assessed along with the electrical performance of the on-skin thin films.

5.2.4 Interaction of the films with skin

Having demonstrated the good electrochemical performance of **Films@XG** under wetting and sweat-like conditions, their use for wearable electronics is now faced. First, cytotoxicity assays in epithelial fibroblasts cells culture were performed in order to corroborate the lack of possible skin irritation. For comparison purposes, the biocompatibility of **Films@PVA** were assessed as well. Fibroblast epithelial cells were cultured in the presence of disks of 3 mm diameter **Films@XG** of culture for 24 h. Afterwards, cell viability was measured to be $90.14 \pm 2.35 \%$ suggesting a very large biocompatibility with skin (Figure 5.15a). On the other hand, **Films@PVA** cultured under same conditions lead to very low cell viability, thus viability at different concentration was assessed to determine the optimal concentration. Large concentrations of $200 \mu\text{g}$ of **Film@PVA** per mL of cell culture resulted in cell viabilities of $60.12 \pm 3.19\%$ indicating that PVA resulted more cytotoxic for epithelial cells (Figure 5.15b).

Notoriously, **Film@PVA** concentration in the cell culture had to be lowered to 25 $\mu\text{g/mL}$ in order to obtain large cell viabilities above 90%. Considering that the thin films would have a large and extended interaction with skin cells during the performance as wearable electronics, cell viability under more concentrated conditions seem more realistic towards our aimed application. Hence, taking into account cytotoxicity and electronic characterization, **Films@XG** were once more suitable candidate for e-skin devices.

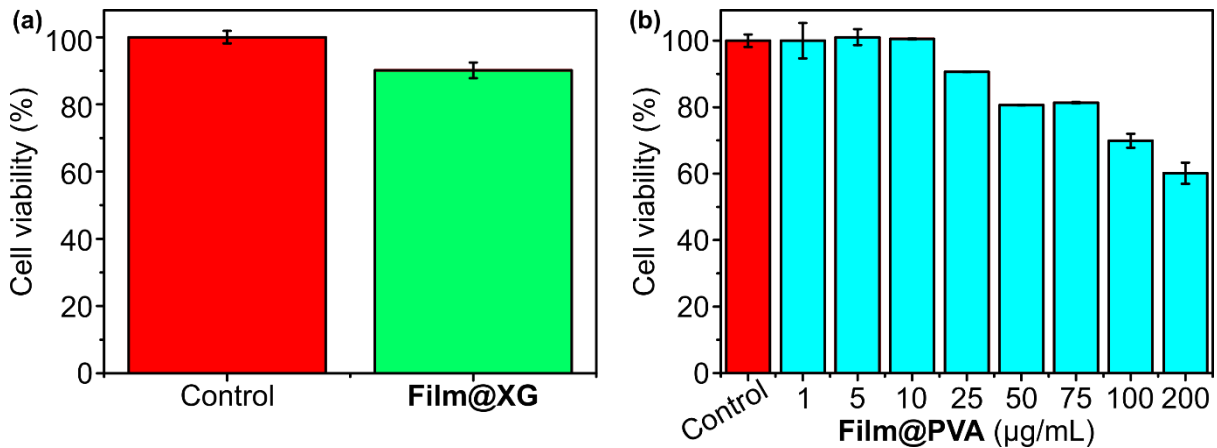


Figure 5.15: Citotoxicity results of (a) **Films@XG** and (b) **Films@PVA** at different concentrations incubated in epithelial fibroblast cells for 24 h.

Table 5.1: Cell viability percentages of **Films@XG** and **Films@PVA** extracted from cell culture.

Control	Film@XG	Film@PVA ($\mu\text{g/mL}$)							
-	-	1	5	10	25	50	75	100	200
100.00	90.14	100.00	101.07	100.51	90.66	80.63	81.33	69.89	60.12
\pm	\pm	\pm	\pm	\pm	\pm	\pm	\pm	\pm	\pm
1.88%	2.35%	5.35%	2.40%	0.17%	0.07%	0.05%	0.22%	2.10%	3.19%

Having confirmed the fibroblast cell viability to the **Films@XG**, adhesion to skin surface was assessed. For this, the film was deposited on top of wetted untreated porcine skin and the excess of water was gently removed with a tissue. Afterwards, the film remained on the skin with high adhesion (Figure 5.17a) both under wet and dry conditions. Notoriously, the film reproduces the complex skin surface adapting to its wrinkles and porosities. Thus, the **Films@XG** seem to have a large conformability to the porcine skin looking like a sticker tattoo. Moreover, allure of the **Films@XG** imitates the natural melanin pigmentation of the skin. Worth-to-mention, the porcine skin could be stretched and deformed reproducing typical skin

stresses with **Films@XG** deposited on top without structural damage or deadhesion of them (Figure 5.17b).

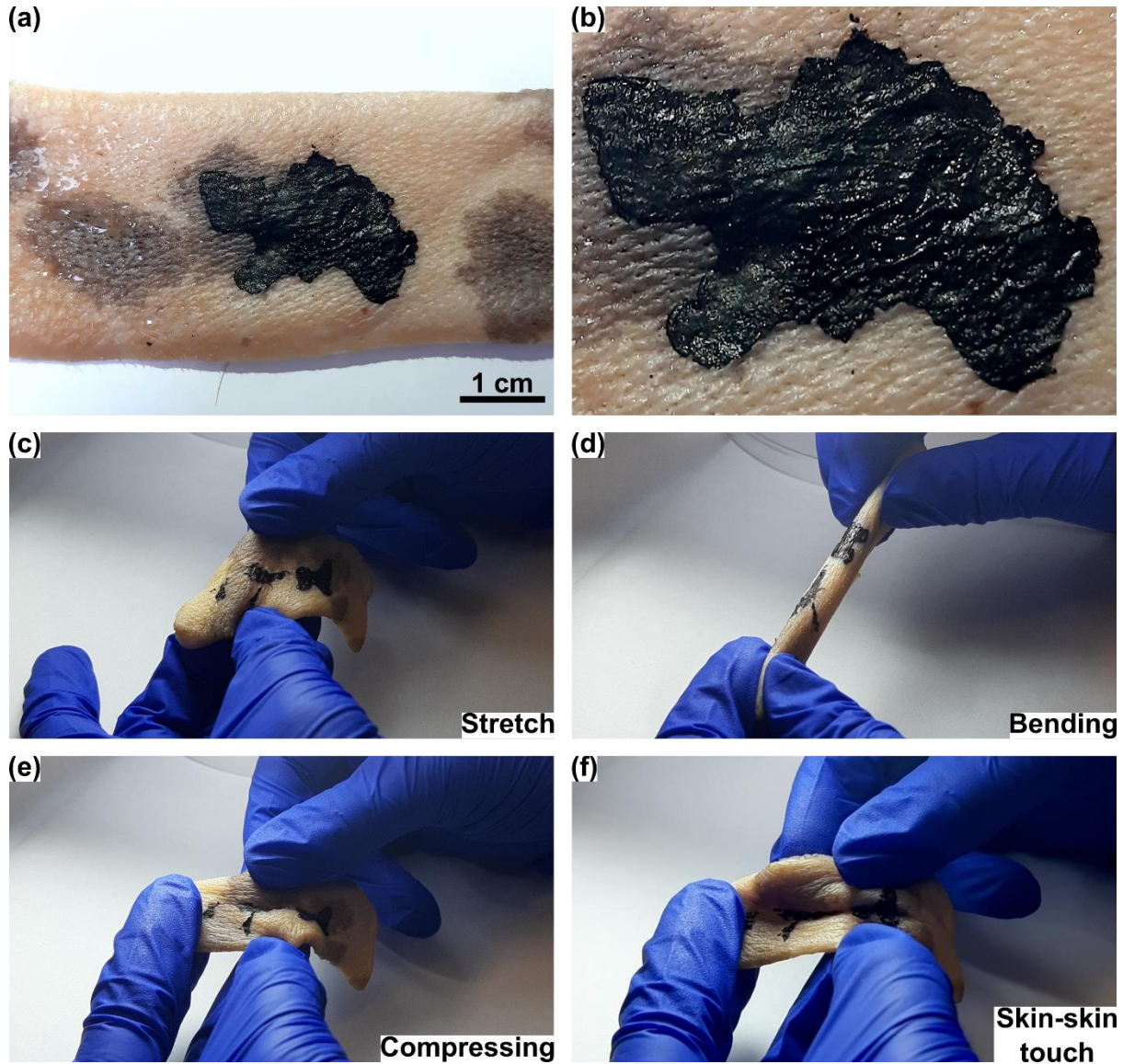


Figure 5.17: (a) Photograph of **Film@XG** adhered on pork skin. The light brown stains correspond to natural melanin pigmentation of the skin. The film imitates with the skin pigmentation. (b) Magnified picture of the **Film@XG** adhered on pork skin showing the large conformability to the skin. Natural wrinkles of the skin are well reproduced (c-f) Photographs of pork skin deformations with e-skin devices of different sizes on top. Skin deformations are indicated on the picture: Stretching, bending and compressing of the skin and skin-skin touch with the film in the middle.

Interestingly, one can shape **Film@XG** in different designs aiming for personalized tattoo-like e-skin electrodes (Figure 5.18). For instance, circular shapes could be obtained upon using a circular puncher cutter (Figure 5.18a). More complex shapes as for instance butterfly forms could be obtained upon manual cutting (Figure 5.18b). Notoriously, the shaping does

not disable the adhesive capabilities of the **Film@XG** nor the conformability to the skin as shown by the inset of Figure 5.18a where the volunteer's wrinkles are reproduced.

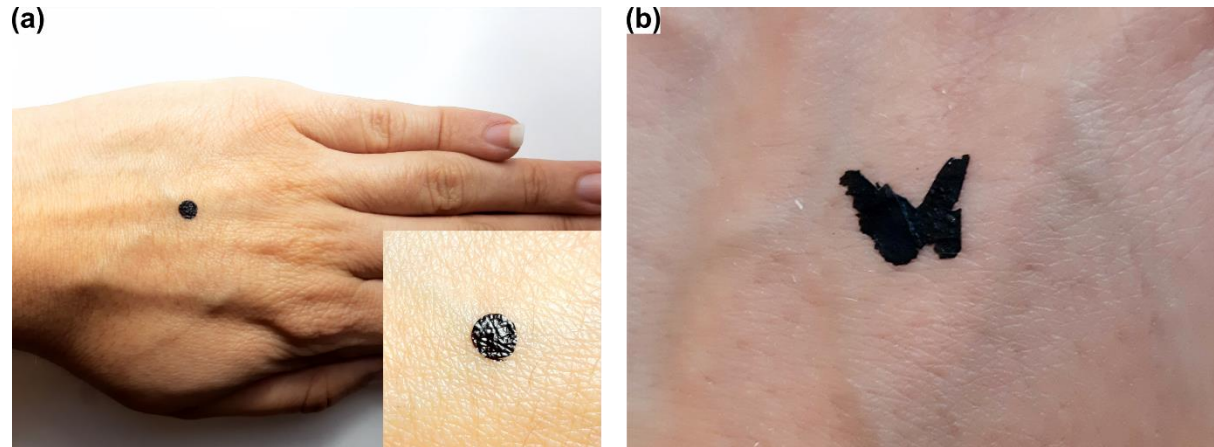


Figure 5.18: Photographs of (a) circular and (b) butterfly-shaped **Film@XG** deposited on a volunteer's hand.

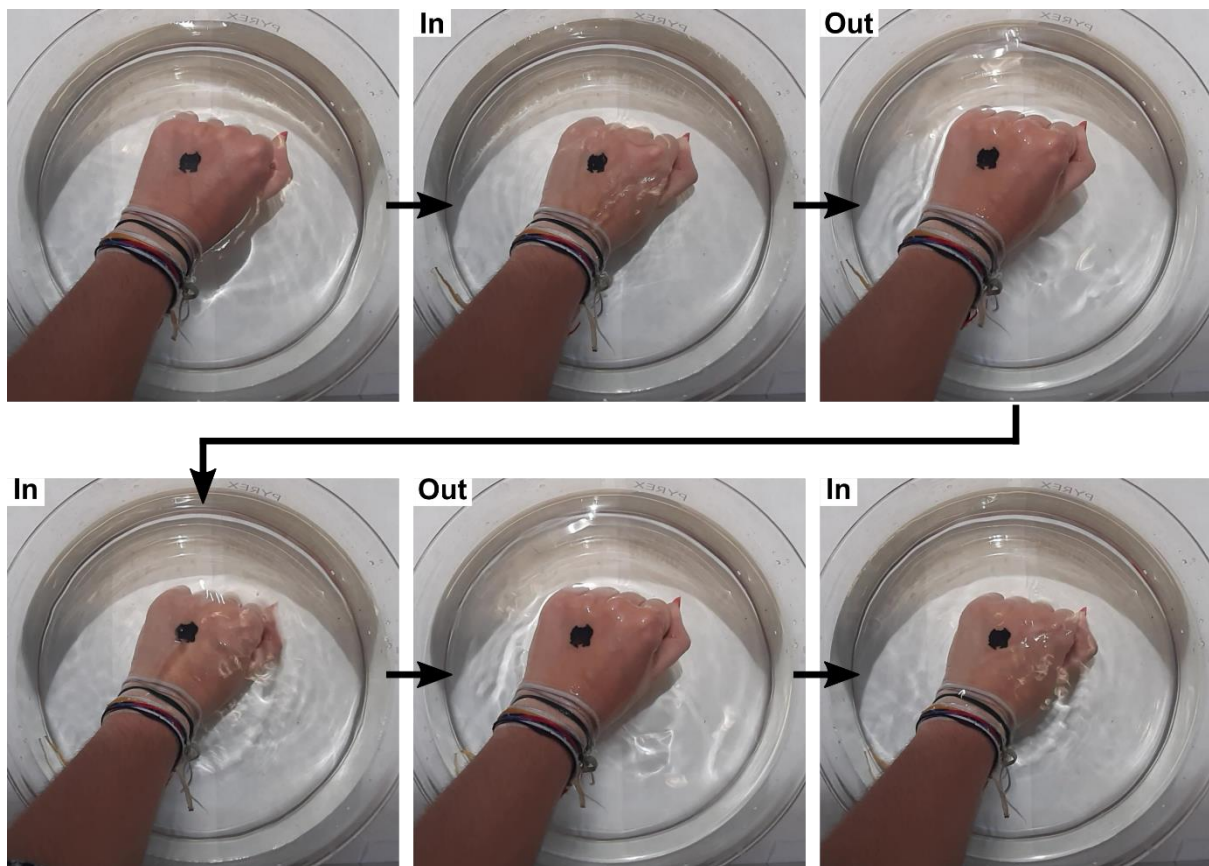


Figure 5.19: Photographs extracted from a video. **Film@XG** was previously deposited on the volunteer's hand. The hand was pulled in and out of a water bath repeatedly. **Film@XG** remained adhered to the skin during the movement.

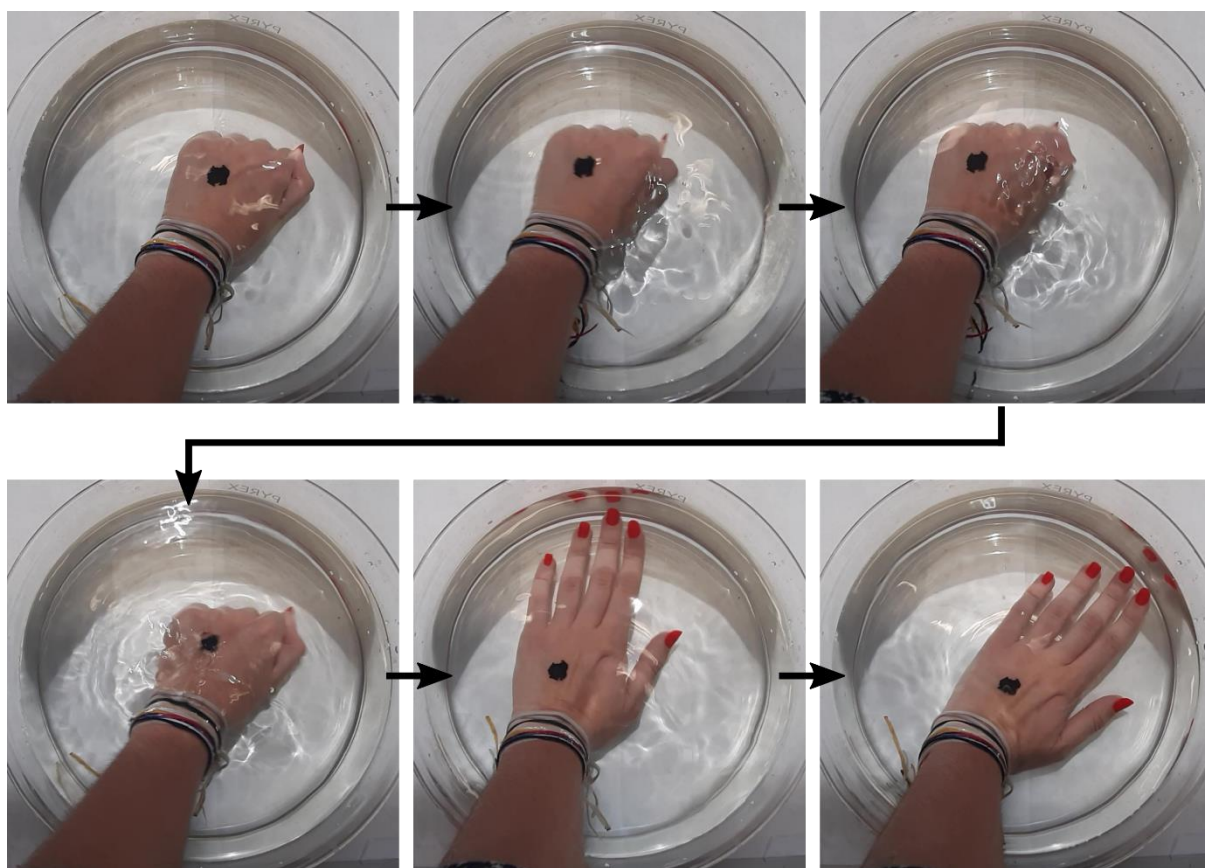


Figure 5.20: Photographs extracted from a video. **Film@XG** was previously deposited on the volunteer's hand. The hand was moved side-to-side in a water bath repeatedly. **Film@XG** remained adhered to the skin during the movement.

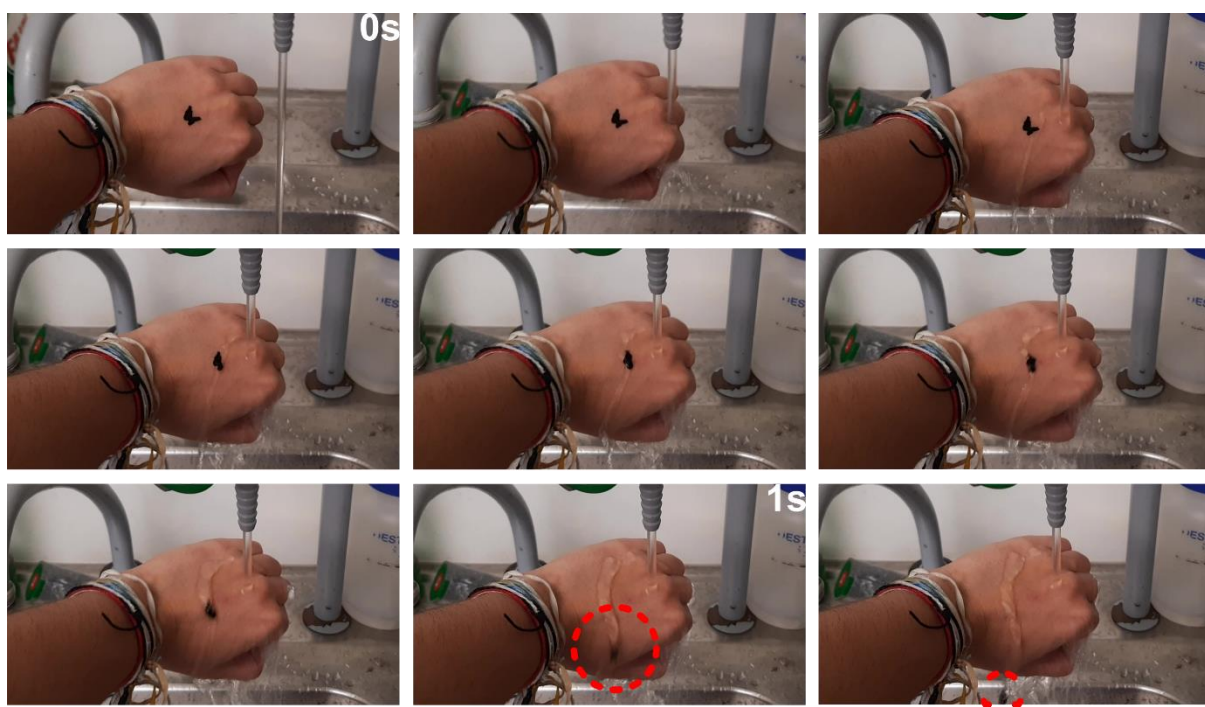


Figure 5.21: Photographs extracted from a one-second video. A butterfly-shaped **Film@XG** was previously deposited on the volunteer's hand. After placing the hand under high flows of water, the film is easily washed off.

Waterproofing of the on-skin adhered **Films@XG** was tested by depositing it on the hand of a volunteer and moving it underneath water. Worth-to-mention, the film remained adhered to the skin when immersing and withdrawing the hand in water repeatedly (Figure 5.19) and also when moving the hand side-to-side underneath steady water (Figure 5.20). Hence e-skin devices formed by **Films@XG** would remain on skin during body performance even at highly intense activity under humid sweat-like conditions of the skin. It should be noted though that thin films can be easily washable under high flows of water for a prolonged period of time. Figure 5.21 shows a series of photographs extracted from a one-second video of the wash-off of butterfly-shaped tattoo-like e-skin film. Under a high flow of current water, the film leaves the skin surface easily.

5.2.5 Use in a wearable e-skin devices

After analyzing the adhesion of the conductive thin films to skin and their biocompatibility, the electrical performance on skin was then faced. For this, a **Film@XG** was deposited on top of humid pork skin. Again, the excess of water was gently removed with a tissue. Copper-tape contacts on polyimide substrates were mechanically deposited on top of the film and DC four-wire resistances were measured. Interestingly, similar sheet resistances to the previously performed in free film measurements were obtained under flat skin conditions obtaining values of $228 \pm 6 \text{ k}\Omega$ (Figure 5.22a) indicating the electrical performance remains on the skin under wetting conditions with pure water.

5.2.5.1 Measurements under pure water: sensitivity to skin-bending

To assess the possible response of the e-skin device to body movement, sheet resistances were measured while bending the skin. To maintain the bending during the measurements, the pork skin was fixed to a flexible substrate. Further, the flexible substrate was bended along a cylindric object of radius 17.5 cm either by bending the skin downwards along the inner radius of the cylinder or upwards along the outer radius of the cylinder as seen in insets of Figure 5.22a. Worth-to-mention the polyimide substrate with the copper contacts has a very large Young modulus, therefore deformations do not arise from strain upon bending it *i.e.* the contact geometry remains unchanged upon bending. Interestingly, sheet resistance of the e-skin device under wet conditions decreased upon bending the pork skin. Similar values were obtained for both upward and downward bending being these $175 \pm 16 \text{ k}\Omega$ and 172 ± 18

k Ω respectively suggesting that sensitivity of the e-skin thin film device depends principally on the bending radius of the pork skin.

5.2.5.2 Measurements sweat-like buffer

a.- Sweat and bending sensitivity

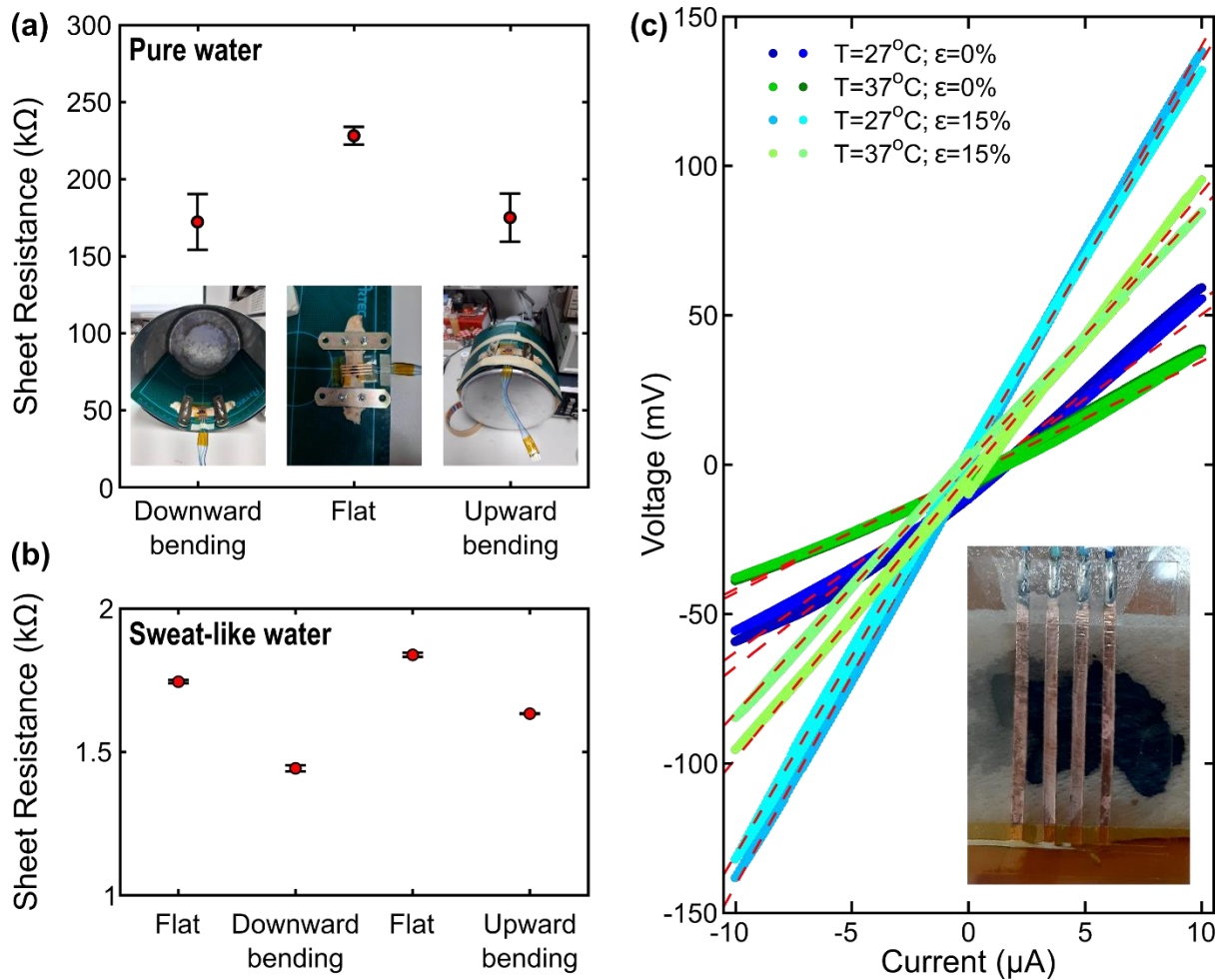


Figure 5.22: (a) Measured four-wired sheet resistance values of **Film@XG** based wearable e-skin devices under pure water wetting conditions and under different bending conditions. Type and photographs of each bending are indicated underneath each measurement; (b) Measured four-wired sheet resistance values of **Film@XG** based wearable e-skin devices under sweat-like wetting conditions and under different bending conditions. Type of each bending is indicated underneath each measurement (c) Four-wire DC I-V curves of **Film@XG** based wearable e-skin devices under sweat-like wetting conditions and under different stretchings and temperature. Room temperature measurements can be found in blue and measurements at body-like temperatures are in green. Lighter colors correspond to stretching the skin at 15%.

To confirm if this behavior would occur in a more realistic scenario, measurements were repeated wetting this time the pork skin with PBS buffer emulating a physiological sweat-like solution (Figure 5.22b). Again, sheet resistances on flat skin were of the same order of magnitude as the previously observed free-standing measurements under sweat-like wet conditions. Worth-to-mention, lower sheet resistances are obtained upon wetting the skin with simulated physiological buffer than with pure water, suggesting that our wearable device is sweat-sensitive. Finally, four-wire DC measurements of the e-skin device wetted with sweat-like buffer were performed in the shown sequence: flat, bended downwards, flat again and bended upwards (Figure 5.22b). The obtained values were 1.743 ± 0.006 , 1.44 ± 0.01 , 1.836 ± 0.007 and 1.632 ± 0.001 k Ω , respectively. Worth-to-mention, the measurements showcase a large reproducibility, with very low standard deviations.

Decreasing of the sheet resistance with the bending remains even when using sweat-like wetting conditions, indicating that body motion sensitivity and sweat degree can be monitored separately.

b.- Sensitivity to skin stretching

To better evaluate the sensitivity of our e-skin devices, we performed four-wire DC I-V measurements in relaxed and linear strained flat positions of pork skin under sweat-like wet conditions at room temperature (27°C) (Figure 5.22c light and dark blue curves). Linear strain was estimated to be 15%. Again, device geometry is unaltered from stressed to relaxed skin positions. Notoriously, highly linear and reproducible I-V curves were obtained for both relaxed and strained e-skin devices (with sheet resistances of 13.8 ± 0.8 and 32 ± 1 k Ω respectively) indicating high conductance of the wetted films regardless their stress condition. As in previous experiments, the device sheet resistance proved to be highly dependent on the strain conditions of the skin as it increases upon applying strain to the e-skin. Thus, Gauge Factor (GF) of our device is estimated to be GF~8.8 indicating a large and good sensitivity of the e-skin device to body movement.

Relaxed and strained measurements under sweat-like conditions were repeated at 37°C emulating body temperature to ensure good GF for possible future application scenarios. Remarkably, linear and reproducible I-V curves are still obtained indicating sheet resistance values of 9.1 ± 0.2 and 21 ± 2 k Ω for relaxed and strained at 15% e-skin devices respectively.

The GF obtained at body-like temperature thus remains of a similar value GF~8.7 as obtained at room temperature. This suggests a high independence of the GF with the body temperature.

c.- Temperature sensing

Analogously, having measured the four-wire sheet resistance under different conditions, we could estimate the e-skin device sensitivity to temperature. Worth-to-mention, sheet resistances decreased for both relaxed and strained conditions upon increasing the temperature due to the activation of charge carriers. The sensitivity to temperature has proven to be of ~3.4%/K for both relaxed and strained conditions. Hence, discrete external monitoring as body temperature could also be performed by our e-skin thin film device. Moreover, temperature sensitivity seems also independent of the stress applied to the e-skin device.

5.3. Conclusions

In summary, we have successfully optimized the synthesis and obtaining of HHTP-based, melanin-inspired, free-standing thin films as multifunctional material for e-skin devices applications. Optimizations regarding the used amine for the melanin-like reaction, the synthetic approach and the use of additives was performed.

Our novel thin films presented many key characteristics needed for wearable e-skin devices:

- i. A good electronic conductivity and performance under wet conditions with dual charge carriers: electrons and protons. Consequently, conductivity proved to be highly dependent on the applied frequency obtaining conductivities of $15 \pm 4 \text{ mS} \cdot \text{cm}^{-1}$ and $0.5 \pm 0.2 \text{ S} \cdot \text{cm}^{-1}$ for low and high frequencies, respectively.
- ii. High electrical performance was obtained upon wetting the thin film with physiological sweat-like buffers.
- iii. A good biocompatibility and interaction with epithelial fibroblast cells.
- iv. Large adhesion and conformability towards porcine and human skin with shaping capabilities emulating sticker like tattooing.
- v. Good on-skin electrical performance even under bending and stretching situations, with large GF~8.7-8.8, temperature 3.4 %/K and sweat sensitivities.

Hence, e-skin devices formed from our thin films could be potentially used for body motion (as for instance electrocardiogram or electromyogram) or temperature monitoring among others. Worth-to-mention, sensitivities to strain and temperature factors seemed to be independent one from the other. Thus, our film would allow to monitor both of them as crosstalk of the sensing would not occur. These results suggest a high dependance of the e-skin device with strain pointing to possible body sensing applications (electrocardiogram, body movement or pressure sensor). Future work of this chapter will include to implement our thin film into wearable e-skin devices in a real case scenario.

5.4 Materials and methods

5.4.1 Chemicals and materials.

HHTP was purchased in Cymit (Cymit Química S.L., Barcelona, Spain). Ammonia at 4M in methanol, hexamethylenediamine, tris(3-aminopropyl)amine, p-Phenylenediamine, Polyvinyl alcohol and Xanthan Gum were purchased in Merck (Merck Life Science S.L.U., Madrid, Spain). All solvents were synthesis grade solvents with >99% purity purchased in Scharlab (Scharlab,S.L., Sentmenat, Spain). Aqueous solutions were prepared filtered, deionized and decalcified water. Porcine skin was obtained from Veterinarian Faculty at Universitat Autònoma of Barcelona.

5.4.2 Synthesis

Synthesis of polymeric HHTP microparticles 6 mL of 4M methanolic ammonia (NH_4OH) was added to a solution of 20 mg (0.062 mmol) of **HHTP** in 6 mL of methanol. The mixture was left in an open beaker for 6 days at room temperature to let the solvent evaporate. The resulting brown powder was centrifuged, and then washed ten times in methanol at 5000 rpm for 5 min. The solid was then dried under vacuum.

Synthesis of polymeric HHTP nanoparticles A solution of 20 mg (0.062 mmol) of **HHTP** in 12 mL of methanol was placed for 6 days in an ammonia saturated gas ambience for its slow diffusion in the solution. The resulting brown powder was centrifuged, and then washed ten times in methanol at 5000 rpm for 5 min. The solid was then dried under vacuum.

Synthesis with flexible amines Hexamethylenediamine: A methanolic solution of 3.245 mg (10 mmol) of **HHTP** in 2 mL was added to a methanolic solution of 1.743 mg (15 mmol) of hexamethylenediamine in 1 mL. A brown precipitate was obtained immediately upon mixture. The powder was centrifuged, washed three times in methanol and dried under ambient conditions.

Tris(3-aminopropyl)amine: A methanolic solution of 19.47 mg (60 mmol) of **HHTP** in 6 mL was added to a methanolic solution of 14.6 mg (77.5 mmol) of tris(3-aminopropyl)amine in 6 mL. A grey precipitate was obtained immediately upon mixture. The powder was centrifuged, washed three times in methanol and dried under ambient conditions.

Synthesis with p-phenylenediamine Methanolic synthesis: a methanolic solution of 9.3 mg (30 mmol) of **HHTP** in 6 mL of methanol were added to a methanolic solution of 8 mg (74 mmol) of PPD in 6 mL. The mixture was left in an open glass petri dish overnight. The unchanged solution was analyzed by drop-casting onto metallic sample holders or spin-coating of the solution onto 300 nm SiO₂/Si commercial wafer substrates. Spin coating was performed using a WS-650MZ-23NPP Spin Coater (Laurell Technologies Corporation, North Wales, PA, USA) at increasing spinning speed from 2000 to 9000 rpm increasing the speed 1000 rpm every 10 seconds. Substrates were cleaned previously by sonication 10 min in acetone and 10 min in ethanol. Afterwards, the substrates were blown dried with a N₂ flux.

Aqueous synthesis: an aqueous solution of 9.3 mg (30 mmol) of **HHTP** in 6 mL of phosphate buffer (pH=9) were added to a methanolic solution of 8 mg (74 mmol) of PPD in 6 mL of phosphate buffer. The mixture was left in an open vial overnight.

Interfacial synthesis: an ethyl acetate solution of 9.3 mg (30 mmol) of **HHTP** in 6 mL of was prepared by sonication and undissolved precipitates were removed by decantation. The resulting solution was gently added to an aqueous solution of 8 mg (74 mmol) of PPD in 6 mL of phosphate buffer creating a liquid-liquid interface. The biphasic mixture was left in a close glass petri dish for three days ensuring the slow diffusion of **HHTP** into the aqueous phase. After this, the petri dish was opened to allow full evaporation of the ethyl acetate resulting in the creation of a thin film at the liquid-air interface. Interfacial synthesis with additives was performed by adding 0.5% w/w of Xanthan Gum or Polyvinyl alcohol to the aqueous phase.

5.4.3 Characterization

Scanning Electron Microscopy SEM images of the particles and the films were obtained with SEM FEI Quanta 650F microscope. Particle samples were prepared by drop-casting of the methanolic suspensions onto metallic sample holders. After evaporation of the solvent under ambient conditions, the previously suspended crystals remained on the holders. Films recovered by stamping or fishing were prepared by pasting of the silicon substrate onto metallic sample holders. Free-standing thin films samples were prepared by pasting of the film onto carbon tape conductive holders and sputtering a 5 nm Pt layer with Leica EM ACE600 on top of the samples. Afterwards, were taken with high acceleration voltages, between 10 to 20 kV at a working distance of 10 mm.

Fourier Transform Infrared (FT-IR) spectroscopy FT-IR for ligands, particles and free-standing films (**Films@XG** and **Films@PVA**) was performed with Tensor 27 FT-IR spectrometer (Bruker) in attenuated total reflection (ATR) mode. The instrument is equipped with a room temperature detector and a mid-IR source (4000 to 400 cm^{-1}). ATR was performed with a single window reflection of diamond model MKII Golden Gate, Specac. The spectra were recorded and treated with OPUS (Bruker) data collection software. Background spectrum in air was performed before the measurements since the instrument is single beam. The dried samples were placed on the window reflection for measurement. FT-IR of the stamped and fished films was performed with Hyperion 2000 FT-IR microscope (Bruker) working in reflection mode. The instrument is equipped with a room temperature detector and a mid-IR source (4000 – 600 cm^{-1}). The spectra were recorded and treated with OPUS data collection software. Samples were prepared by stamping or fishing the films on top of gold substrates.

UV-visible spectroscopy UV-vis spectra of the thin films were collected using a UV-vis spectrometer Cary 6000 under transmittance mode. The stamped film was measured by stamping onto optically transparent quartz substrates.

Electrical measurements Electrical characterization of free and on-skin thin films with DC currents was carried out employing a Keithley 2400 in a four-wire mode. The AC electrical characterization was carried out employing a Signal Recovery Lock-in Amplifier model 5209, using a precision resistor of $R = 1.0077 \pm 0.0005\text{ M}\Omega$. The

system was set at a variable frequency between 7.35 Hz and 73.5 kHz and a voltage up to 1 V. This allows performing AC current sweeps at intensities of 1 μ A. The voltage drop on the samples was measured with a resolution down to 100 nV, the resistance was extracted and using geometrical dimensions of the contacts the sheet resistance and the conductivity were calculated. The four-wired indentation electrodes consisted of four aligned pins with an interspace of 2.54 mm. The stripped copper contacts deposited on polyimide substrates were 11 ± 2 mm long and were separated of 2 ± 0.1 mm.

Cell culture. A fibroblast cell line NIH/3T3 (ATCC® CRL-1658) was used for the cell viability and adhesion tests with the films. The base media (DMEM, Glutamax and glucose) was supplemented with 10% fetal bovine serum, 100 μ L/mL penicillin and 100 μ g/mL streptomycin (Life Technologies, Thermo Fisher Scientific, Waltham, MA, USA). All cell cultures were maintained in a humidified incubator at 37°C under an atmosphere of 10% CO₂.

5.5 References:

1. S. M. A. Mokhtar, E. Alvarez de Eulate, M. Yamada, T. W. Prow, D. R. Evans, *Med. Devices Sensors* **2021**, 4, 1.
2. C. Cui, Q. Fu, L. Meng, S. Hao, R. Dai, J. Yang, *ACS Appl. Bio Mater.* **2021**, 4, 85.
3. L. Pan, P. Cai, L. Mei, Y. Cheng, Y. Zeng, M. Wang, T. Wang, Y. Jiang, B. Ji, D. Li, X. Chen, *Adv. Mater.* **2020**, 32, 1.
4. L. Wang, T. Xu, X. Zhang, *TrAC - Trends Anal. Chem.* **2021**, 134, 116130.
5. X. Duan, S. Taurand, M. Soleimani, *Sci. Rep.* **2019**, 9, 1.
6. M. Wang, T. Wang, Y. Luo, K. He, L. Pan, Z. Li, Z. Cui, Z. Liu, J. Tu, X. Chen, *Adv. Funct. Mater.* **2021**, 2008807, 1.
7. R. Vo, H. H. Hsu, X. Jiang, *Biomater. Sci.* **2021**, 9, 23.
8. C. Wang, T. Yokota, T. Someya, *Chem. Rev.* **2021**, 121, 2109.
9. B. Zou, Y. Chen, Y. Liu, R. Xie, Q. Du, T. Zhang, Y. Shen, B. Zheng, S. Li, J. Wu, W. Zhang, W. Huang, X. Huang, F. Huo, *Adv. Sci.* **2019**, 6, 1801283.
10. Z. Li, M. Zhu, J. Shen, Q. Qiu, J. Yu, B. Ding, *Adv. Funct. Mater.* **2020**, 30, 1.
11. P. Xiao, Y. Liang, J. He, L. Zhang, S. Wang, J. Gu, J. Zhang, Y. Huang, S. W. Kuo, T. Chen, *ACS Nano* **2019**, 13, 4368.
12. Y. R. Ding, C. H. Xue, Q. Q. Fan, L. L. Zhao, Q. Q. Tian, X. J. Guo, J. Zhang, S. T. Jia, Q. F. An, *Chem. Eng. J.* **2021**, 404, 126489.
13. M. d'Ischia, A. Napolitano, A. Pezzella, P. Meredith, M. Buehler, *Angew. Chemie - Int. Ed.* **2020**, 59, 11196.
14. A. B. Mostert, B. J. Powell, F. L. Pratt, G. R. Hanson, T. Sarna, I. R. Gentle, P. Meredith, *Proc. Natl. Acad. Sci. U. S. A.* **2012**, 109, 8943.
15. M. Reali, A. Gouda, J. Bellemare, D. Ménard, J.-M. Nunzi, F. Soavi, C. Santato, *ACS Appl. Bio Mater.* **2020**, 3, 5244.
16. A. B. Mostert, S. B. Rienecker, M. Sheliakina, P. Zierep, G. R. Hanson, J. R. Harmer, G. Schenk, P. Meredith, *J. Mater. Chem. B* **2020**, 8, 8050.
17. T. Eom, K. Woo, W. Cho, J. E. Heo, D. Jang, J. I. Shin, D. C. Martin, J. J. Wie, B. S. Shim, *Biomacromolecules* **2017**, 18, 1908.
18. T. Eom, J. Jeon, S. Lee, K. Woo, J. E. Heo, D. C. Martin, J. J. Wie, B. S. Shim, *Part. Part. Syst. Charact.* **2019**, 36, 1.

19. N. Gogurla, B. Roy, K. Min, J. Y. Park, S. Kim, *Adv. Mater. Technol.* **2020**, 5, 1.
20. M. Sheliakina, A. B. Mostert, P. Meredith, *Mater. Horizons* **2018**, 5, 256.
21. L. Migliaccio, M. Gryszel, V. Derek, A. Pezzella, E. D. Głowacki, *Mater. Horizons* **2018**, 5, 984.
22. Z. Tehrani, S. P. Whelan, A. B. Mostert, J. V. Paulin, M. M. Ali, E. D. Ahmadi, C. F. O. Graeff, O. J. Guy, D. T. Gethin, *2D Mater.* **2020**, 7, 024008.
23. E. S. Bronze-Uhle, A. Batagin-Neto, P. H. P. Xavier, N. I. Fernandes, E. R. de Azevedo, C. F. O. Graeff, *J. Mol. Struct.* **2013**, 1047, 102.
24. H. Coskun, A. Aljabour, L. Uiberlacker, M. Strobel, S. Hild, C. Cobet, D. Farka, P. Stadler, N. S. Sariciftci, *Thin Solid Films* **2018**, 645, 320.
25. C. J. Bettinger, J. P. Bruggeman, A. Misra, J. T. Borenstein, R. Langer, *Biomaterials* **2009**, 30, 3050.
26. C. H. Chen, C. C. Tsai, P. T. Wu, I. K. Wang, J. Yu, W. B. Tsai, *ACS Appl. Bio Mater.* **2019**, 2, 205.
27. S. Hao, C. Shao, L. Meng, C. Cui, F. Xu, J. Yang, *ACS Appl. Mater. Interfaces* **2020**, 12, 56509.
28. Z. Xu, L. Chen, L. Lu, R. Du, W. Ma, Y. Cai, X. An, H. Wu, Q. Luo, Q. Xu, Q. Zhang, X. Jia, *Adv. Funct. Mater.* **2021**, 31, 1.
29. S. Ji, C. Wan, T. Wang, Q. Li, G. Chen, J. Wang, Z. Liu, H. Yang, X. Liu, X. Chen, *Adv. Mater.* **2020**, 32, 1.
30. X. Du, Z. Niu, R. Li, H. Yang, W. Hu, *J. Mater. Chem. C* **2020**, 8, 12257.

Chapter 6:

General conclusions

In the present thesis, the use of novel experimental methodologies for the synthesis of TP-based MOFs and amorphous polymers has resulted in the formation of films ranging from monolayers to free-standing Thin-Films. This challenging objective has been fulfilled completing a deep physico-chemical characterization of all materials obtained. The specific results are summarized next:

1. Organic synthetic procedure for **HATP·6HCl** has been optimized obtaining high degree of purity and synthesis yields of ~65%. This allowed its use by the group of Prof. Aitor Mugraza to obtain **Co₃(HITP)₂** and **Fe₃(HITP)₂** 2D MOFs on a surface as honeycomb structured single layers and widths of 50 nm using UHV deposition techniques.
2. Synthesis and optimization of highly crystalline and pure **Co₃(HITP)₂** has been performed. The large colloidal stability of the resulting microcrystals in water allowed for their deposition in UHV conditions using novel technique Atomic Layer Injection.
3. A double slide microfluidic reactor designed in the group of Prof. Josep Puigmartí that achieves space-like simulated microgravity convection-free environments experimentation conditions has allowed to synthesize unprecedented homogeneous centimeter-large **Ni₃(HITP)₂** thin films.
4. The technique was proved to be very versatile as thin films were grown on a wide variety of substrates: insulating, conductive and in hybrid layered structures, including highly oriented films on both quartz and gold substrates, in the last case assisted by a previous surface functionalization.
5. Oriented **Ni₃(HITP)₂** thin film provided large conductivities of ~40 S·cm⁻¹ in ambient conditions and without post-synthetic treatment because of its large orientation degree and compactness.
6. For the first time, anisotropy of conduction along *in-plane* and *out-of-plane* directions of **Ni₃(HITP)₂** was assessed thanks to the control in the growth orientation. High anisotropy factors of 10⁴ of the order of graphitic materials were obtained.

7. For the first time, HHTP-based melanin-inspired free-standing shapable thin films were obtained upon reaction with diamine p-Phenylenediamine.
8. The free-standing films showcased large conductivities under wetting conditions with dual charge carriers, electrons and protons, as indicated by frequency-dependent measurements. Conductivities of $15 \pm 4 \text{ mS}\cdot\text{cm}^{-1}$ were obtained using low frequencies indicating only electronic conduction. At high frequencies, duality in charge carrier is enabled resulting in conductivities of $0.5 \pm 0.2 \text{ S}\cdot\text{cm}^{-1}$.
9. Sensitivity of the free-standing film towards physiological sweat-like buffers was proved since frequency switching is disabled obtaining high charge carrier conduction at low frequencies.
10. The films presented large skin biocompatibility, adhesion and conformability reproducing the complex skin surface. Shaping capabilities and imitation of natural melanin skin pigmentation conferred to the films emulated tattooing allures.
11. As a proof of concept, films were integrated as wearable e-skin devices on porcine skin. Our film-based wearable device showcased good electrical performance under different skin conditions found in real case scenarios of body activity. First, sweat-sensitivity was proven as lower sheet resistances are obtained upon wetting the skin with physiological sweat-like buffers instead of pure water. Second, electrical performance is maintained but also sensitive to bending and stretching of the skin, showcasing large GF~8.7-8.8. Finally, our wearable devices showcased a good performance under body-like temperatures with sensitivities to temperature of 3.4 %/K.
12. Sensitivity towards multiple factors indicates the strong potential of our melanin-based wearable e-skin devices for multimodal simultaneous monitoring (temperature, body motion, electrocardiogram...). Independence of sensitivity factors between them ensure the lack of cross-talking during bodily recording.